Cranfield University

Athanasios Theos

"Design and Analysis of Welded Aircraft Wing Panels"

College of Aeronautics

This thesis is submitted in fulfilment of the requirement for the Degree of Doctor of Philosophy

Cranfield University

College of Aeronautics

Ph.D

2004-05

Athanasios Theos

Title

"Design and Analysis of Welded Aircraft Wing Panels"

Supervisor: Dr. Xiang Zhang

5 December 2005

Abstract

Nowadays, increasing manufacturing cost effectiveness becomes a vital condition for the commercial success of the next generation of large wide body aircrafts. Welding is a very strong candidate process to be used in manufacturing, allowing both sensible cost reductions and structural efficiency. The main aim of the work is to study the fatigue crack propagation in welded structures. The study is focused on the effect of welding residual stresses to the damage tolerance behaviour of the structure. The welding technique under investigation is the Variable Polarity Plasma Arc (VPPA).

Two stringer panels were designed, one tension panel to simulate the lower wing skin cover and one compression panel to mimic the upper wing skin cover. The main design driving force for the upper stiffened panel is buckling since it is under compression. Damage tolerance is the main design criterion for the lower stiffened panel due tensile fatigue loading. Design of the end-fittings for the tension stiffened panel was also carried out using finite element modelling in order to ensure uniform stress distribution at the cross section of the test area of the structure. A fatigue analysis at the various locations of the bolts and at the weld line has been performed. This is necessary in order to ensure that the crack initiation site comes from the weld line rather than from the fastener holes at the end-fittings during the fatigue testing.

The research was focused on fatigue crack growth behaviour of welded aluminium panels. The FE model of the CCT coupon is the main tool for the comparison of the fatigue crack behaviour between the parent and the welded coupons. Furthermore AFGROW software is used in conjuction with the output of the FE model to compare the experimental and numerical results in terms of fatigue crack growth lives of welded coupons. In welded coupons a faster crack propagation growth was demonstrated at the region of the weld line and the heat affected zone (HAZ) due to the tensile welding residual stresses. Away from this region, a decrease in crack growth took place due to the compressive welding residual stresses in this area.

Finally, a calculation effort in large-scale stiffened panels was made in terms of the stress intensity factor for both welded and non-welded cases. Possible future work was also addressed in such large-scale structures.

Acknowledgements

For these years of my post graduate studies I would like to thank very much all the people who supported me and encouraged me all the way in this journey.

Especially, I would like to thank my supervisor Dr. Xiang Zhang for her support and advice during these years.

Also, I am thankful to all the project participants for the invaluable experience within this project.

Last but not least, this thesis is dedicated to my partner Popy. Without her help and encouragement I would not be able to finish this project.

December 2005
Athanasios Theos

Table of Contents

Chapter 3 Design of 2-Stringer Panels for Fatigue Experiment

Chapter 4 Fatigue Crack Growth Analysis of Welded Centre Crack Tension (CCT) Coupons

List of Figures

Chapter 4

List of Tables

Appendix C

List of Abbreviations

FE	Finite Element
LEFM	Linear Elastic Fracture Mechanics
EPFM	Elastic Plastic Fracture Mechanics
HAZ	Heat Affected Zone
MIG	Metal Inert-Gas
GMA	Gas Metal-Arc
VPPA	Variable-Polarity Plasma Arc
PAW	Plasma Arc Welding
FSW	Friction Stir Welding
SIF	Stress Intensity Factor
VCCT	Virtual Crack Closure Technique
DCPD	Direct Current Potential Drop
CCT	Centre Crack Tension
MPC	Multipoint Constraint

CHAPTER 1

INTRODUCTION

1.1 History and Applications of Aerospace Aluminium Alloys

Although aluminium alloys have dominated the construction of military and civil airframes, it should not be assumed that they are fully developed. A continuous stream of incremental improvements continues to be achieved. These include improved high strength aluminium-zinc based alloys (7000 series) and better damage tolerant aluminium-copper alloys (2000 series).

Step improvements to the performance of the aluminium-zinc-magnesium-copper (7000 series), used primarily in compressively loaded structures (upper wing skins, internal ribs, frames and landing gear), have been achieved by highly sophisticated developments such as:

- Double ageing practices
- Controlled combinations of heating rates
- Mechanical deformation between quenching and ageing

Techniques such as the above have enabled strength, fracture toughness and corrosion resistance to be increased simultaneously.

In aerospace structural applications, where high strength and low density is the first priority, only the strongest 2000 series and 7000 series alloys are used [1]. Generally, the 7000 series alloys have higher strength than the 2000 series alloys but lower fracture toughness. The 2000 series alloys exhibit crack propagation behaviour generally superior to the 7000 series alloys. Fatigue crack growth rates in 2000 series alloys are close to

one-third of those in the 7000 series alloys [2]. In addition, the 2000 series alloys have better fracture toughness and fatigue strength, and their stress-corrosion susceptibility is lower than the 7000 series alloys. Therefore, the 2000 series alloys are typically used in high strength and tension structural applications such as lower wing skin and stringers where fatigue and stress–corrosion cracking is severe. Typical applications for the 7000 series alloys are in the upper wing skin and stringers in order to enhance the buckling resistance. They are also used in spars and ribs, where high tensile strength is required. Properties are given in Table 1.1 for two specific types of aluminium alloys.

It is well known that the upper skin panel of an aircraft is mainly under compression and the lower skin panel is under tension. Due to this loading there is a need for the use of different aluminium alloys. For this study, the material for the upper and the lower skin panel used is 7150-T651 and 2024-T351 respectively. Table 1.1 lists the mechanical properties of these aluminium alloys.

Table 1.1 Mechanical properties of the two aluminium alloys.

Properties	Yield Stress (MPa)	Ultimate Tensile Strength (MPa)	Density ρ (Kg/m^3)	Fracture Toughness (MPa$\sqrt{m}$)
2024-T351	390	520	2800	31
7150-T651	483	534	2800	26

The 2000 series aluminium-copper alloys have been used for applications that require damage tolerance. Damage tolerance, structures have been designed to tolerate some subcritical flaws to remain in a structure. Fracture mechanics provides a rational basis for establishing flaw tolerance limits. The fracture toughness, K_{IC}, which is located at the last column of the Table 1.1, is the indicator for the damage tolerance capacity of the material. A good damage tolerance combination can be considered as the beneficial combination of very high fracture toughness and very low rates of fatigue crack propagation particularly under loading spectra containing the occasional high tensile load.

1.2 The Welding Process in Aerospace Manufacturing

Nowadays, increasing manufacturing cost effectiveness becomes a vital condition for the commercial success of the next generation of large wide body aircrafts [3]. Reduction of manufacturing costs of civil aircraft structures is a key requirement to enhance the competitiveness in the civil aircraft industry. The aircraft industry has therefore extended its interest from the traditional fastening process to alternative and more cost-effective joining processes. Welding is a very strong candidate process to be used in manufacturing, allowing both sensible cost reductions and structural efficiency [4]. The main advantages and disadvantages of the welding process compared to mechanical fastening are given below.

Advantages of Welded Structures

The use of welding could lead to many benefits when compared to the traditional mechanical fastening method.

- Weight benefits

In order to accommodate mechanical fasteners, the sheet metal sections must be overlapped, introducing additional weight. This is not required in welding therefore, weight saving up to 10% for a typical airframe structure [4].

- Manufacturing cost and time

Welding can provide cost savings of up to 30% [4]. Significant cost savings can be achieved since the welding manufacturing process can be automated. Moreover, assembly time and cost will also be reduced due to fewer assembly operations needed.

- Inspection automation and time

Inspection frequencies can be decreased as a result of the lower likelihood of corrosion in welded structures compared with the traditional fastened structures (Bolt holes potential corrosion sites). Using non-destructive techniques the inspection can be automated. This could lead to time and inspection cost savings.

- Quality control

In principal, better quality control can be achieved by welding, since the process can be automated.

- Fretting

The extensive use of mechanical fasteners and related additional overlapping gives rise to fretting fatigue problem. Such a phenomenon could be avoided by means of welding because the different components behave as an integral structure.

- Simple structural design

Joint designs in welded structures can be much simpler than those in riveted structures. In welded structures, members can be simply butted together or fillet welded. In riveted structures, complex joints are required. In addition, there is no thickness limit in welded structures that may be employed provided that the appropriate weld equipment has been developed.

Disadvantages of Welded Structures

- Potential distortion

Distortion is the result of expansion and contraction of the weld occurring during heating and cooling. During the solidification, the weld-melt shrinks transversely and longitudinally. This may results in buckling or other visual evidence of distortion. Areas close to the weld, although not at melting temperature, expand and may distort. In cooling, this distortion may reverses itself and the structure returns to its original configuration, unless its yield strength, which has been lowered by the elevated temperature, has been exceeded and therefore the material has been permanently deformed.

- Residual stresses

Due to local heating, a complex state of residual stresses results after welding. Residual stresses are generated mainly by the restraint of the solidifying and shrinking at the weld

and adjacent heated base metal. These stresses usually occur in local areas of the weld. Residual stress intensity is dependent on several conditions such as the extent and level of heating, strength of the base material, yield temperature, melt-volume in the structure, degree of restraint and cooling rate. The above might be a cause of cracking, fracture, and reduced buckling strength and elastic working range.

- Damage tolerance

The weld itself may be a site of crack initiation. Cracking may result from the thermal expansion of aluminium during welding, followed by solidification shrinkage in localised areas where brittleness or a low strength grain boundary structure exists. The material responds to the stress by cracking rather than yielding or elongating. Once the crack has started it is very difficult to arrest because welding procedure creates integral structures. In contract, in the fastened structures the fastener holes act like crack stoppers on the developed crack. Therefore, crack growth rate is crucial in welded structures. Crack stoppers could be introduced to achieve the desired fatigue life in the form of patches adhered on the structures. This technique is already used in integral structures.

- Weld defects

Typical defects in a weld include cracks, porosity and slag inclusion.

- Reparability

This is one of the main problems related to welding. Once the crack starts, a typical way to repair the component is fusion welding. Otherwise, novel repair techniques must be employed like patches as it was mentioned previously.

- Material

The material used for riveted structures cannot always be used in welded structures. This is because some materials possess higher weld-ability than others. Especially, when it comes to welding aluminium there are particular problems that limit their so-called weld-ability. These problems, include solidification cracking within the fusion zone, liquation cracking at the boundary between the fusion zone and the heat affected zone (HAZ), and

poor corrosion performance. Until suitable welding techniques were developed for aluminium, the use of the material was greatly restricted. Therefore, this limits the material choice.

- Airworthiness requirements

Welded joints must satisfy airworthiness requirements. It is a vital issue. In particular, strength and fracture toughness needs to be investigated since the mechanical properties of the welded area vary from metal to metal. Testing and extensive research needs to be performed.

- Design limitations

Design of a welded joint significantly affects the welding processes that will be used. Many design options permit excellent welding performance. However, designers who are unaware of the range of technology and methods available may fail to realize the welding potential. Since the joint design affects welding processes, the potentials of the available welding process need to be considered when designing a joint. The design must account for the heating produced by welding. Accessibility for the various processes involved is important as well.

1.3 Welding Techniques

Many different welding techniques have been developed [5]. These welding processes, as presently practiced, can be classified into three basic categories:

1) **Fusion welding**, in which the parts to be joined are heated until they melt together. Pressure is not a requisite. Examples are arc welding, gas welding, electron-beam welding, and laser welding.

2) **Electrical-resistance welding**, which involves firstly heating by passage of an electric current through the parts to be welded, and secondly, the application of pressure. Examples are spot welding, and upset welding.

3) **Solid-phase welding**, in which pressure is applied but the metals to be joined do not melt, except for very thin layers near the surfaces to be joined. Examples are forge welding, friction welding and pressure welding.

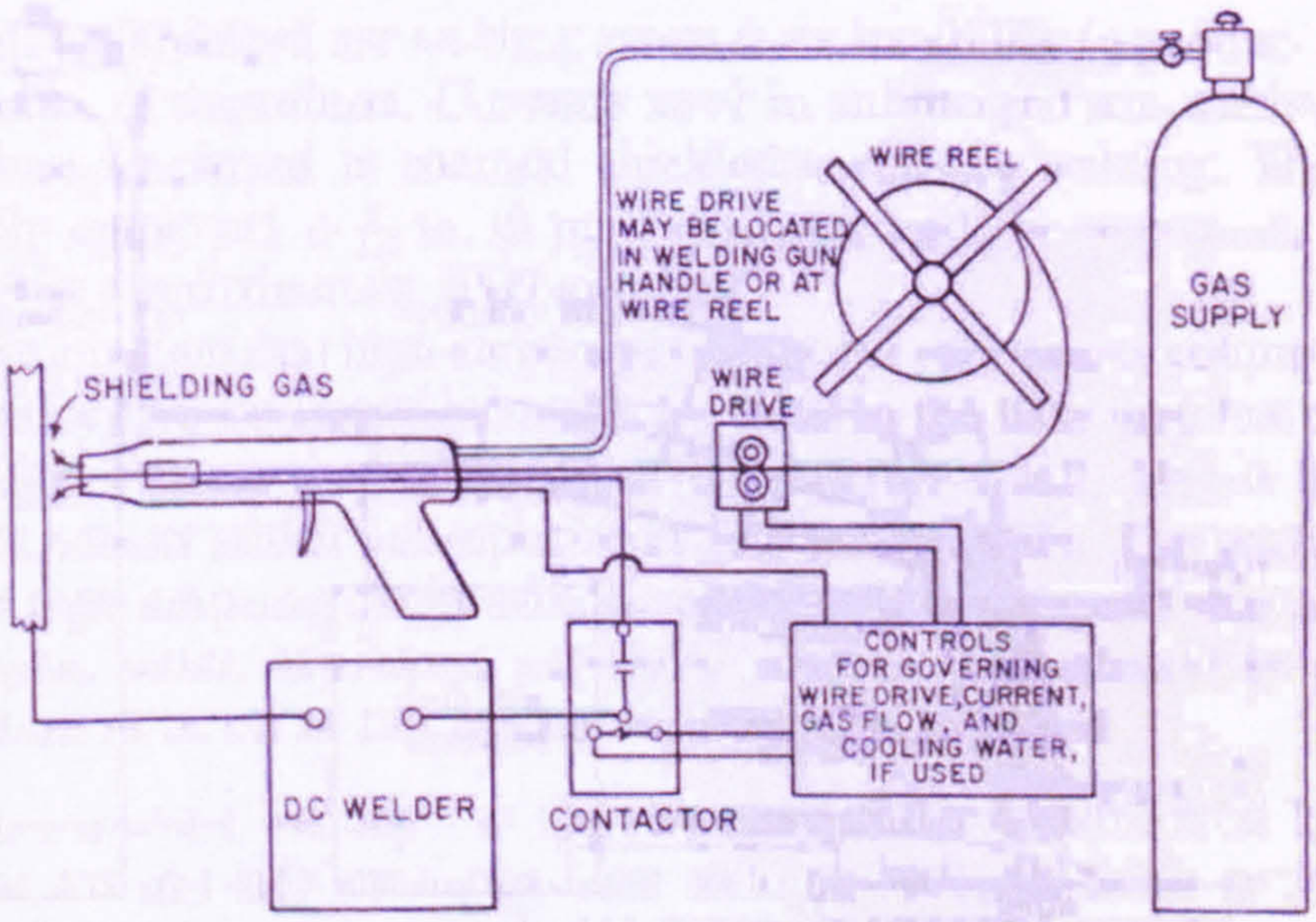

Figure 1.1 Schematic diagram of gas metal-arc welding (MIG). [5]

In this project the fusion welding is under investigation. More specifically, in the fusion welding two welding methods were employed; Metal Inert-Gas (MIG) welding and Gas Metal-Arc (GMA) welding. Figure 1.1 shows basic features of MIG welding. The filler wire, which is manufactured in a coil form, is fed mechanically into the welding arc. The arc travel is controlled manually in the semi-automatic process and mechanically in the automatic process. A bare wire is commonly used for the electrode, but flux-covered wires are also used.

In MIG, shielding is provided by pure inert gas, such as argon and helium. In general, in gas-shielded-arc welding, coalescence is produced by fusion from an electric arc

maintained between the ends of a metal electrode. More specifically, it employs a continuously fed electrode, which melts in the intense arc heat and is deposited as weld metal.

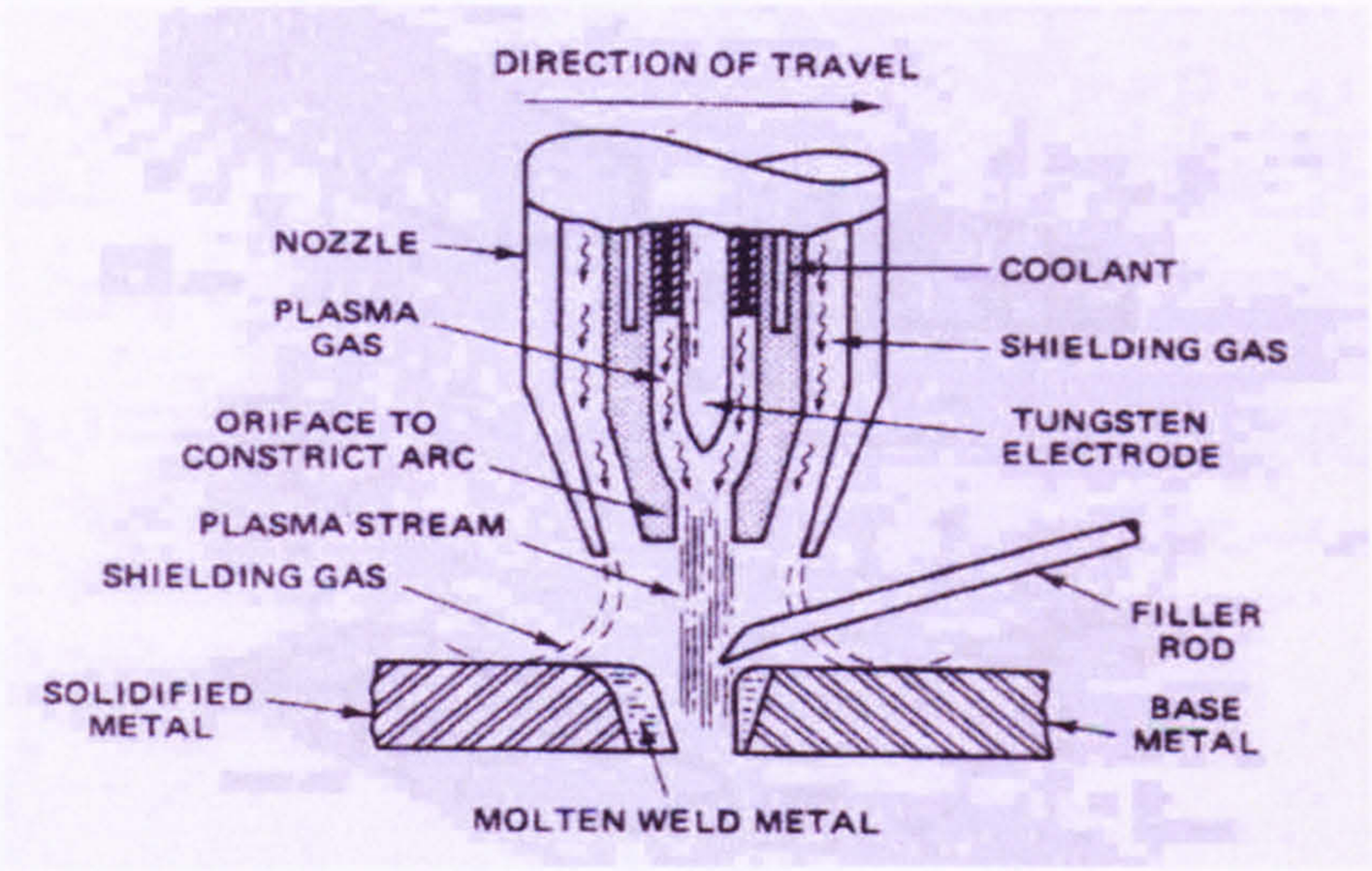

Figure 1.2 Schematic diagram of plasma -arc welding (VPPA). [6]

The variable–polarity plasma arc welding (VPPA) is a latest variation in the category of plasma arc welding (PAW). Figure 1.2 is a schematic presentation of the PAW. This variation was developed by the aerospace industry for welding thicker sections of alloy aluminium. As in gas-shielded-arc welding category (MIG method), VPPA uses a tungsten electrode, but their torches are different. In gas-shielded-arc welding the arc is bell-shaped, unlike the highly focused, strong arc produced with VPPA method.

In a comparison between the MIG and the VPPA method the following points can be made:

- MIG is one of the most popular welding processes due to its flexibility and low cost.
- MIG has a large heat source compared with VPPA and this causes the welds to have poor mechanical properties.
- VPPA's high current densities and energy concentration produces a constricted arc that allows welds with deeper penetration and small heat- affected zone (HAZ). This

is demonstrated in Figure 1.3. It can be observed that the higher the heat intensity the narrower the width of the HAZ.

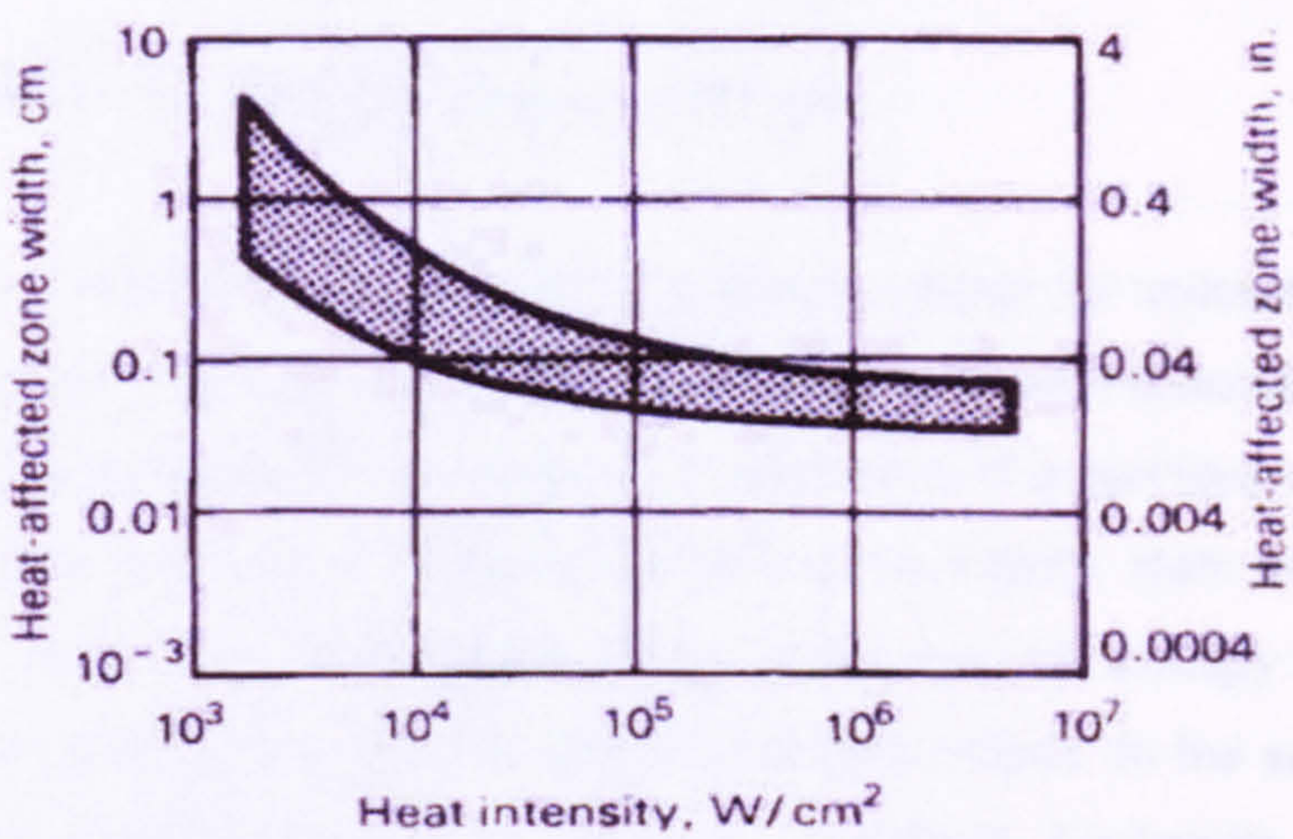

Figure 1.3 Size of the HAZ as a function of intensity of the heat source. [6]

Figure 1.4 presents an advantage of the plasma welding method (VPPA) against the gas shielded arc welding (MIG). The more concentrated heat source in plasma arc welding causes significantly less distortion than the gas shielded arc welding.

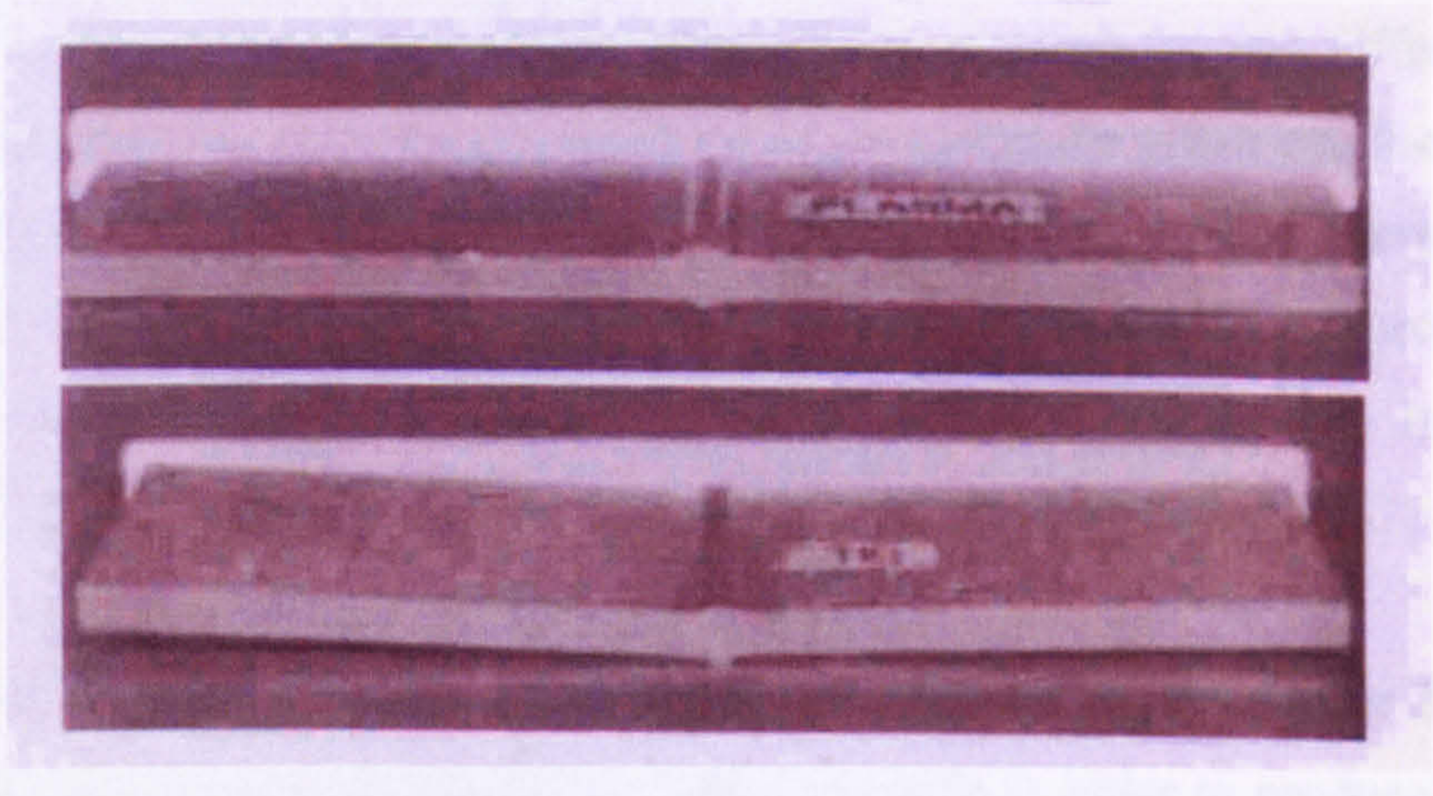

Figure 1.4 Comparison of angular distortion for plasma arc welding (top specimen) and gas shielded arc welding (bottom specimen). [6]

The last point of VPPA when compared with MIG method is related to aluminium alloys. Aluminium has a tendency to form oxides, and this barrier must be removed in order to

produce a good quality weld. The VPPA method manages to remove this layer of aluminium oxide by cathodically etching the metal.

1.4 Description of the WELDES Research Project

At this point a description of the bigger research project is necessary in order to understand the scope of the current work within the consortium's research activities. The name of this project was WELDES and is a continuation of a previous research project CEMWAM, a part of which took place in Cranfield University. Both of these research projects were funded from EPSRC and QinetiQ. Airbus was also strongly involved in this project. ALCOA supplied the required material for this project. In the academic part of WELDES three Universities were involved; Cranfield University, Southampton University and Open University.

Open University's main role within this project was the experimental measurement of the residual stresses due to welding in two groups of structures. The first group was the welded coupons and the second was the two stringer stiffened wing panel. In the first group, residual stress and strain measurements were acquired for two different welding methods MIG and VPPA. In the second group of structures the effort was focused only in one welding method the VPPA since this was judged to be of a more interest especially for the industry sponsors (Airbus). Southampton University's main research effort was focused on micromechanical assessment of crack initiation and growth. In addition, a further effort in development of modelling approaches was undertaken.

Cranfield University's role was divided into three main categories. The first research effort was to develop the necessary knowledge and skill in order to produce high quality welds in both two groups of structures (coupons and stiffened wing panels). The second research effort was both experimental and numerical studies. The experimental part was the fatigue testing of the coupons and the stiffened wing panel in order to establish the behaviour of the welded structures compared with the non-welded structures (parent) in

terms of fatigue life. The numerical effort was focused on the welding technique in order to simulate as closely as possible the welding procedure. The aim was to match the experimental measurements of the residual stress distributions from the Open University. In order to achieve this, a thermoelastic finite element model was employed. These two main roles were undertaken by SIMS department in Cranfield University. The third main role was the research field for this thesis. Two main efforts were undertaken in this study. The first was the design of a stiffened wing panel and end-fittings for the fatigue test machine available in SIMS department in Cranfield University. The second effort was the investigation of welded structures in two levels (coupons & stiffened wing panel) in terms of fatigue life due to the welding residual stresses.

1.5 Overview of the Thesis

The major objectives of this project are:

1) Design of welded upper and a lower wing skin stiffened panels for fatigue testing. These structures are welded by recently developed welding technique known as Variable Polarity Plasma Arc Welding (VPPA).

2) In addition the above task, the design of the end-fittings that are used to grip the welded panels on the fatigue testing machine was perfomed .

3) Fatigue crack growth prediction and damage tolerance design in two levels of welded structures a) coupons and b) stiffened panels. Finite element (FE) methods and fracture mechanics theory were employed for the analysis.

4) Assessment of the effect of residual stresses due to the welding process. Various distributions of measured residual stresses were introduced into the FE models in order to investigate their behaviour under mechanical loading.

A literature review is reported in chapter 2 focusing on the history of welded structures and the main design parameters in this area. In chapter 3 the design of the two-stringer panel is reported together with the design of the end-fittings for the fatigue experiment. In chapter 4 the study of the welded coupon has been performed. Assessment of the impact of the welding residual stresses on small-scale structures (coupons) in terms of fatigue crack propagation life is made. Chapter 5 expands the research in larger structures. Comparison with experimental data is presented in terms of crack length versus load cycles for the stiffened panels. Finally, the work is summarised in chapter 6. The most important findings are discussed and recommendations for future work are made.

CHAPTER 2
LITERATURE REVIEW

2.1 Introduction

The background theory and relevant literature is presented in this chapter in order to address the topic of fracture mechanics of welded structures. A comparison of welded versus riveted stiffened panels is presented first with an attempt to understand the design factors in each of these structures. A more detailed description of weld characteristics is then given, as this is the main interest in the thesis. The generation of residual stresses in welds and their effect on the mechanical behaviour of the structure is discussed. The weld zones and the effect of the welding process on the material properties are also discussed. Next, the fundamental fracture mechanics theory is presented. The Linear Elastic Fracture Mechanics theory (LEFM) and fatigue crack propagation fundamental equations are given. The phenomenon of crack closure due to plasticity at the crack tip is also described. Finally, the effect of welding residual stresses on fatigue strength is discussed.

2.2 Stringer Panel Design and Damage Tolerance Considerations

Traditionally, the majority of the stringer panels in aircraft industry are riveted. Nowadays, riveted panels are not cost efficient for the aircraft industry and that is why aircraft industry is focused on more cost efficient methods of fabrication. The high performance levels in machines and equipment continue to place more exacting demands on the design of the structural components. In aircraft, where weight is always a critical problem, integrally stiffened structural sections have proved particularly effective as a lightweight, high strength construction. From a structural standpoint, appreciable weight

savings are possible through the integral section design, which also develops high resistance to buckling loads. In addition, the reduction in the number of basic assembly attachments gives a smooth exterior skin surface. Another potential advantage of the integrally stiffened structure is the elimination of the attached flanges with a corresponding redistribution of this material for optimum stiffener proportions. However, some production development work is necessary to exploit this advantage fully. In aircraft applications, the most significant advantages of the integrally stiffened structures over comparable riveted panels (skin-stringer panel) have been:

- Absence of fastener holes which are potential sources of fatigue.
- Reduction of the amount of sealing material for pressurized shell structures.
- Increase in allowable stiffener compression loads by elimination of the attached flanges.
- Increase joint efficiencies under tension loads through the use of integral doublers, etc.
- Improved performance through smoother exterior surfaces by reduction in the number of attachments and non-buckling characteristics of the skin.

A disadvantage in the integral stiffened panel, especially for the lower skin panel in which the main design criterion is damage tolerance, is that there is no crack stopper like in the riveted panels. In addition, the main reason for making the fabrication of integral panels with machining unattractive is the significant amount of wasted material in order to produce the desired product. Therefore, the current trend in aircraft industry is the welded fabrication. Using welding technique cost efficiency can be achieved like in machining of integral panels but with a significant saving in material. A crucial role towards the saving of material is the location of the weld. Figure 2.1 illustrates the position of the weld for the wing panel used in this study.

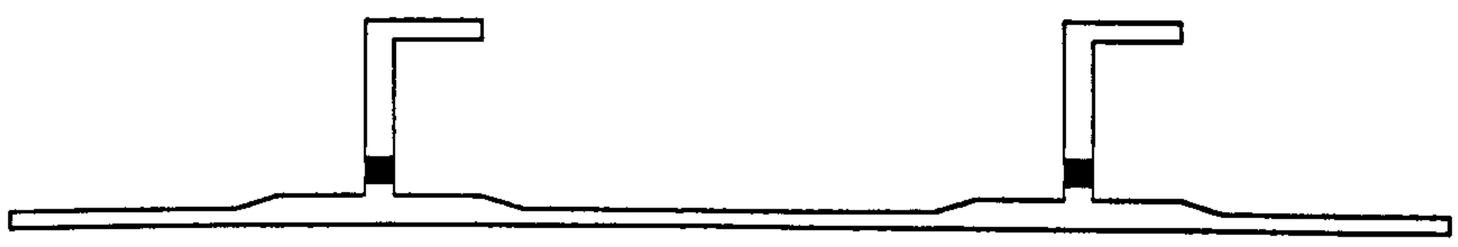

Figure 2.1 Location of the weld on a typical wing stiffened panel.

In the event of a crack appearance on the skin of an integral stiffener panel the stiffeners act as crack stoppers. By varying specific parameters like stiffener to skin area ratio and stiffener spacing it has been proved that the value of the stress intensity factor can be affected and consequently the crack growth rate increased or reduced accordingly [7]. Stiffeners on a stiffened integral panel are the only crack stoppers unlike the riveted panel. The actual rivet on a riveted stiffener panel plays a very crucial role in the damage tolerance concept.

On a riveted panel, in addition to the effect of the stiffeners on the crack growth rate, there is the effect of the rivets themselves. As a crack from the skin is approaching the riveted stiffener the rivets tend to slow down the crack propagation and in some of the cases arrest the crack. Like in the case of the stiffeners, there are specific parameters of the rivets in order to achieve retardation on the crack propagation. Furthermore, the load is transferred from the partially cracked skin to the intact skin. This transition of the load depends on the flexibility of the fasteners. The more flexible the fastener the less load is transferred to the intact stiffener.

2.3 Residual Stresses due to the Welding Process.

Welds are traditionally considered critical in terms of fatigue performance [8]. Porosity, lack of penetration, weld undercutting, inclusions and hot cracking are the most important causes for poor fatigue strength [9]. Joint geometry is a primary factor influencing fatigue strength. Longitudinal butt joints perform generally better than fillet joints and joint misalignment in transverse welds can reduce fatigue strength. In transverse butt welded joints, the bead profile is an important factor that influences fatigue strength. Fatigue cracks typically initiate at the toes of the weld, which are at the junction of the plate surface and the weld, where a stress concentration is associated with the local change in geometry. Residual stresses induced by welding process will also affect fatigue life.

Residual stresses can be induced by thermal, mechanical, or metallurgical processes [5]. Thermal residual stresses are caused by non-uniform permanent (plastic) deformations

when a metal is heated and then cooled under restraint. Restrained expansion and contraction induces permanent deformation (plastic strain) and corresponding residual stresses. Generally, the metal that cools last, is in tension. Mechanically induced residual stresses are caused by non-uniform permanent deformation when a metal is mechanically stretched or compressed under restraint. Therefore, the occurrence of mechanically induced residual stresses requires the presence of both permanent mechanical deformation and restraint that prevents the deformed metal from contracting or expanding to its new unrestrained equilibrium dimension. In general, the sign (tension or compression) of mechanically induced residual stress is opposite to the sign of non-uniform plastic strain that produced the residual stress. This process is used to mechanically curve or straighten components and, in others material treatments like shot-peening [10], to produce a compressive stress layer on the surface of a component in order to improve its fatigue or corrosion behaviour.

Residual stresses are those that exist in a component free from externally applied forces [9]. They are caused by non-uniform plastic deformations in the neighbouring regions. These regions can be small, occurring within weldments, or large, occurring when curving or straightening a beam or a shell during fabrication. Residual stresses are always balanced so that the stress field is in static equilibrium [5]. Consequently, wherever tensile residual stresses occur, compressive residual stresses exist in neighbouring regions.

Development of residual stresses in weldments may be demonstrated by considering the following simplified example of a groove weld shown in Figure 2.2. As the deposited molten filler metal cools, it contracts longitudinally along the weld and transversely across the weld. This contraction is resisted by the stresses as indicated in the Figure 2.2. The combined tensile and compressive stresses are balanced in the neighbouring areas to achieve equilibrium. These stresses may cause distortion, deformation during post-weld machining, stress corrosion cracking and eventually fracture [11].

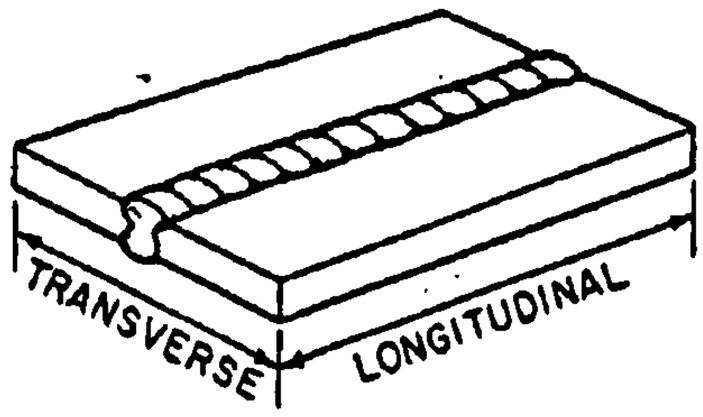

(a) BUTT - WELDED PLATE

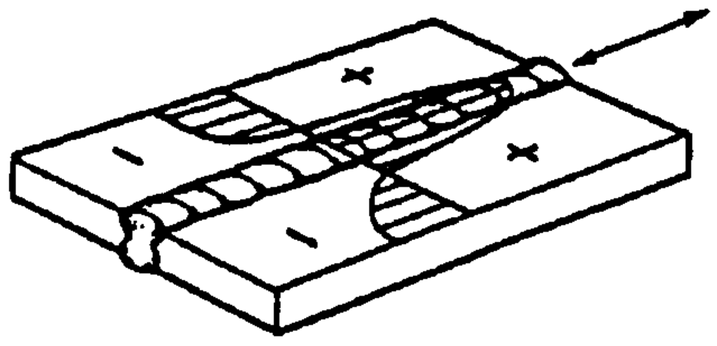

(b) LONGITUDINAL RESIDUAL STRESS

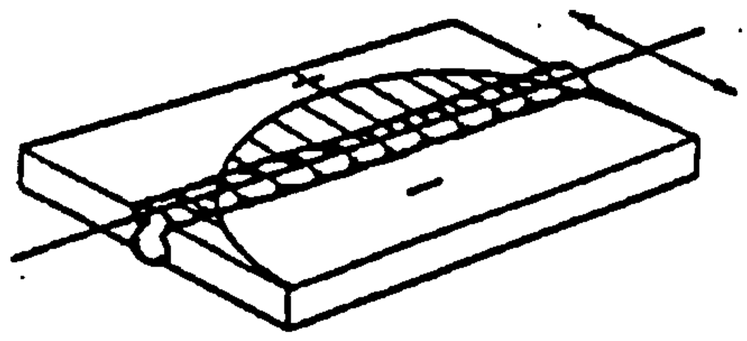

(c) TRANSVERSE RESIDUAL STRESS

Figure 2.2 Residual stresses for a butt-welded plate: (a) butt-welded plate, (b) longitudinal residual stress, and (c) transverse residual stress.

Fabrication by welding usually results in stresses that are locked into the fabricated assembly. These stresses are either residual stresses or reaction stresses or both. Residual stresses are caused by the inability of the deposited molten weld metal to shrink freely as it cools and solidifies [9]. Reaction forces are caused by the inability of the assembly components to move relative to each other during thermal expansion and contraction of the deposited weld metal, or the molten base metal for autogenous welds and surrounding base metal [9]. Contraction of solidifying weld metal is restricted by adjacent materials, resulting in complex three-dimensional residual stresses. The magnitude of these stresses depends on several factors, including size of the deposited weld beads, weld sequence, total volume of the deposited weld metal, weld geometry, strength of the deposited weld metal and of the adjoining base metal as well as other factors. Often, the magnitude of these stresses exceeds the elastic limit of the lowest strength region in the weldment.

The longitudinal residual stresses in a butt-welded component are maximum tensile near the weld in the heat affected zone, then decrease rapidly moving away from the weld line and become compressive [8,12,13]. The magnitude of the tensile stress in the weld may

be equal to the yield stress of the weld metal. The magnitude and distribution of the compressive stresses depend on plate dimensions and must satisfy the equilibrium requirement that the area under the tensile residual stress must be equal to the area under the compressive stress. The application of mechanical tensile stress lower than the yield strength of the parent material can cause plastic straining in the near weld area due to the superposition of these stresses with the tensile welding residual stresses. The magnitude of this plastic strain is equal to the elastic strain in the surrounding elastically stressed material to ensure equilibrium between the two regions. Consequently, in most practical application, the plastic straining of the weld metal is small.

Methods for measuring residual stresses include sectioning, hole drilling, and X-ray diffraction [5,14,15]. The sectioning method is a destructive test in which residual stresses are determined by removing slices from the member and measuring the resulting strain. Hole drilling is a semi-destructive test for measuring residual stresses near the surface of the material; it involves placing strain gages on the surface and measuring strain relaxation as a hole is drilled in the vicinity of the gages. The X-ray diffraction method is a non-destructive test in which surface residual stresses are determined by measuring the change in the lattice spacing of the material; only surface residual stresses are measured in a very localized area.

The mechanical and physical properties of the parent metal have a significant effect on the fatigue strength of the material. However, in welded aluminium structures the presence of a stress concentration or weld defects significantly alters that behaviour [16]. This characteristic fatigue behaviour of welded joints is reflected in the British Standards BS 8118 design curves for aluminium joints. Figure 2.3 shows the fatigue S-N design curves for longitudinal welded joints, transverse butt welded joints and un-welded aluminium structural elements. These design curves are based on the assumption that joint geometry and manufacturing procedure are the dominant factors to determine the fatigue resistance of the joint, and they apply to any weldable structural aluminium alloy.

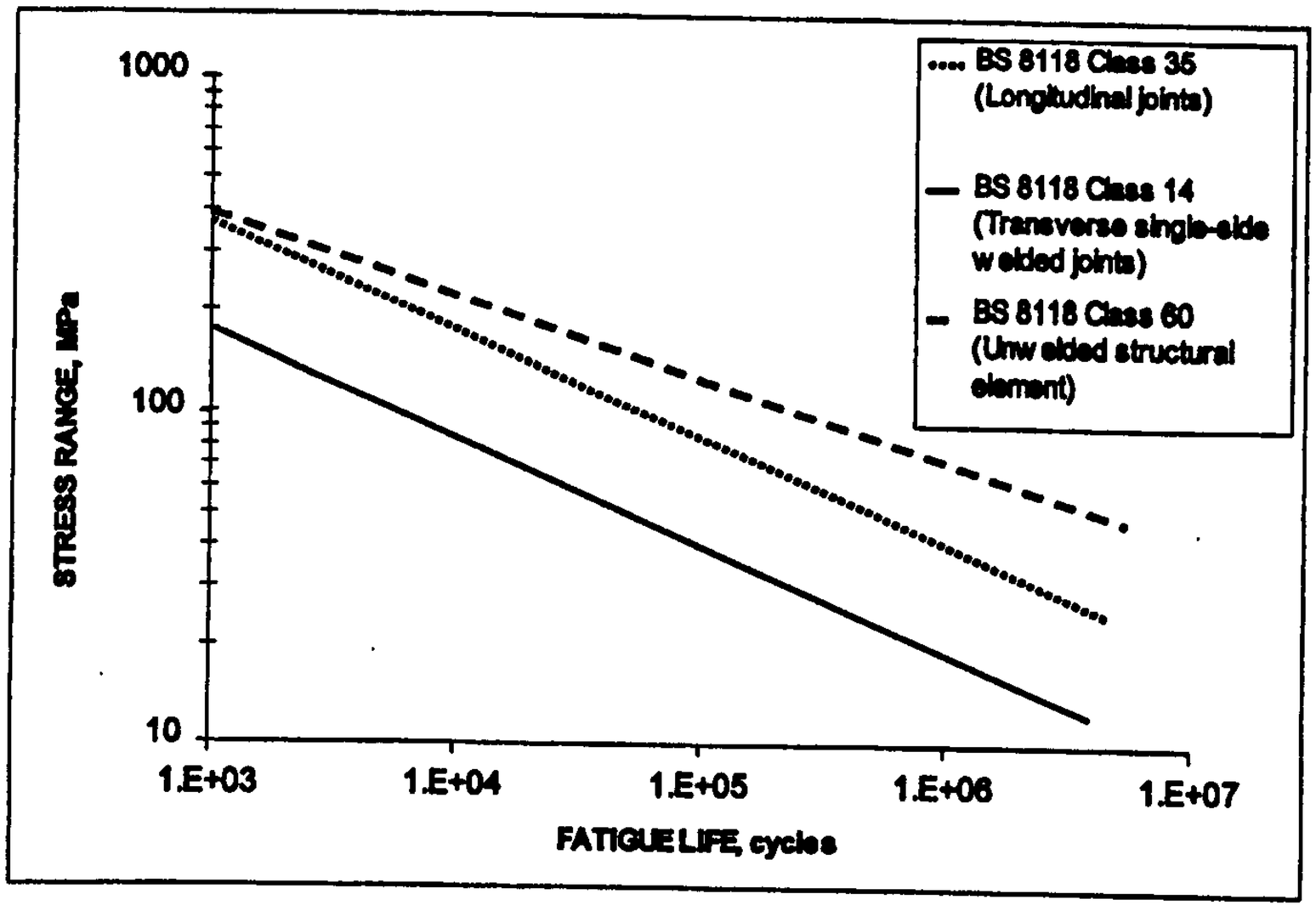

Figure 2.3 Fatigue design curves from BS 8118 for longitudinal and transverse aluminium welded joints compared with that of an un-welded structural element.

In the question how the welding residual stresses affect the fatigue life there is still no conclusive answer. Major difficulties come from two reasons.

- Residual stresses change by the application of repeated loading (fatigue load).
- Stress redistributions around a crack occur as the crack grows due to repeated loading.

Figure 2.4 shows a simple case of longitudinal butt weld under uniform tensile loading in steel weld [5]. Curve 0 shows the lateral distribution of longitudinal residual stress in the as-welded condition. When a uniform stress $\sigma = \sigma_1$ is applied, the stresses increase to those values shown by curve 1. When the load is released, residual stresses change to those shown in curve 1'. Curve 2' shows the distribution of residual-stresses that remain when the tensile stress $\sigma = \sigma_2$, $(\sigma_2 > \sigma_1)$ is released. Curves 1,2 & 3 correspond to applied stress $\sigma_1 < \sigma_2 < \sigma_3$ respectively. Curves 1',2' & 3' present the residual stress distribution when the applied stresses are released.

The important point in Figure 2.4 is that the residual stress distribution after this kind of cyclic loading is more even than the original distribution (curve 0). As the level of loading increases, the residual stress distribution after each cycle becomes more even and decreases. The above is explained with the amount of residual stress reduction that takes place during one cycle of loading and unloading. The stress changes during a number of cycles of repeated loading are more complex, especially if a fatigue crack is formed, causing a stress concentration near the crack tip.

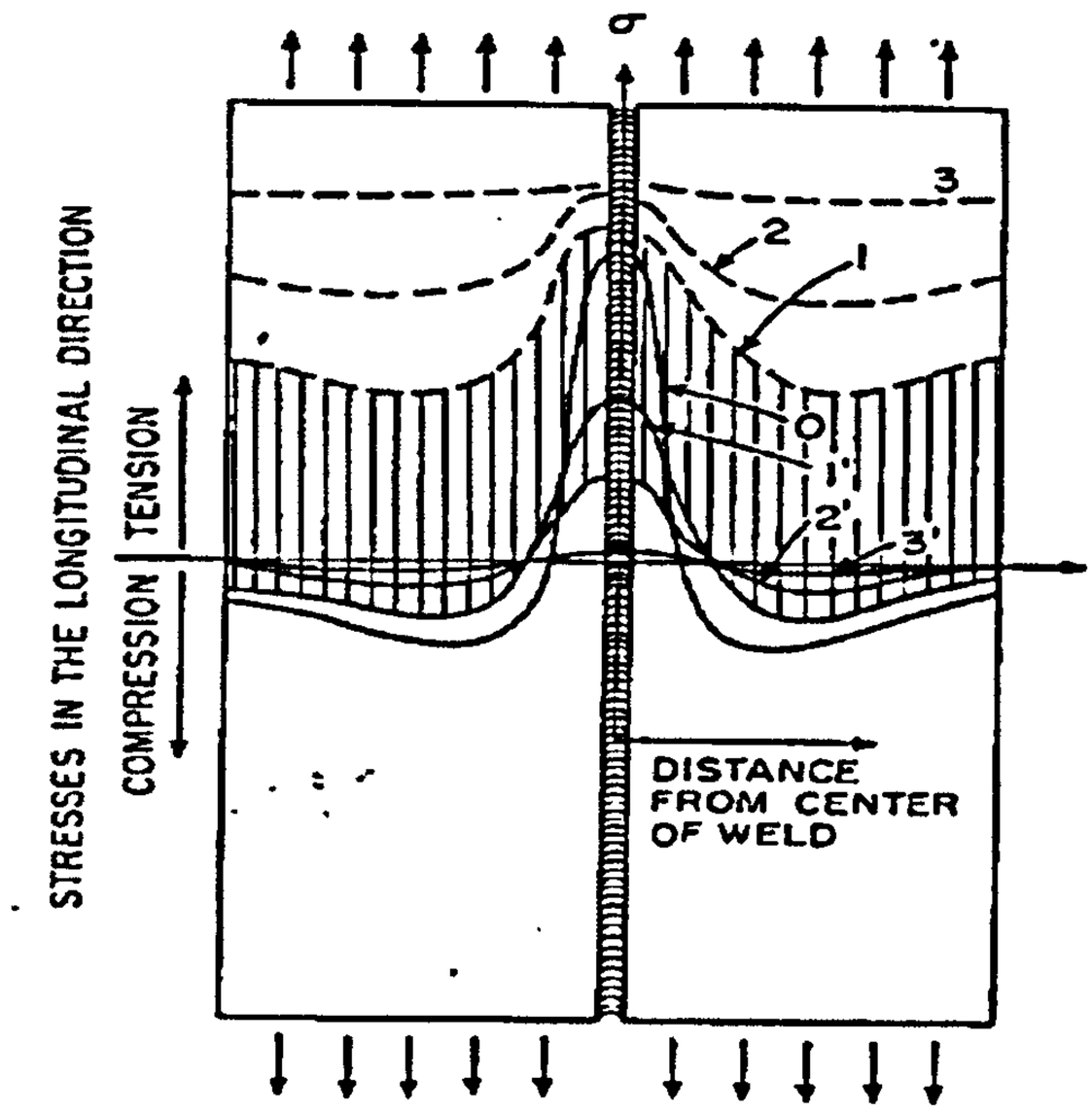

Figure 2.4 Schematic distributions of stresses in a butt weld when uniform tensile loads are applied and of residual stresses after the loads are released.

The application of a nominal tensile stress increases the weld metal stress slightly and all the surrounding elastic stresses increase by an increment equal to the nominal tensile stress (σ_n). Removing the applied stress, unloads the plastically strained weld metal and the surrounding elastic stress field, causing redistribution of the residual stress [9]. Because the weld metal unloads elastically, the magnitude of the drop in the weld metal stress, $\Delta\sigma$ (i.e., the stress range) is equal to the magnitude of the applied stress. Subsequently application and removal of nominal tensile stress results in an elastic cyclic

stress, $\Delta\sigma$, of the weld metal and surrounding elastic stress field equal to the applied nominal stress (σ_n). This behaviour is illustrated in Figure 2.5.

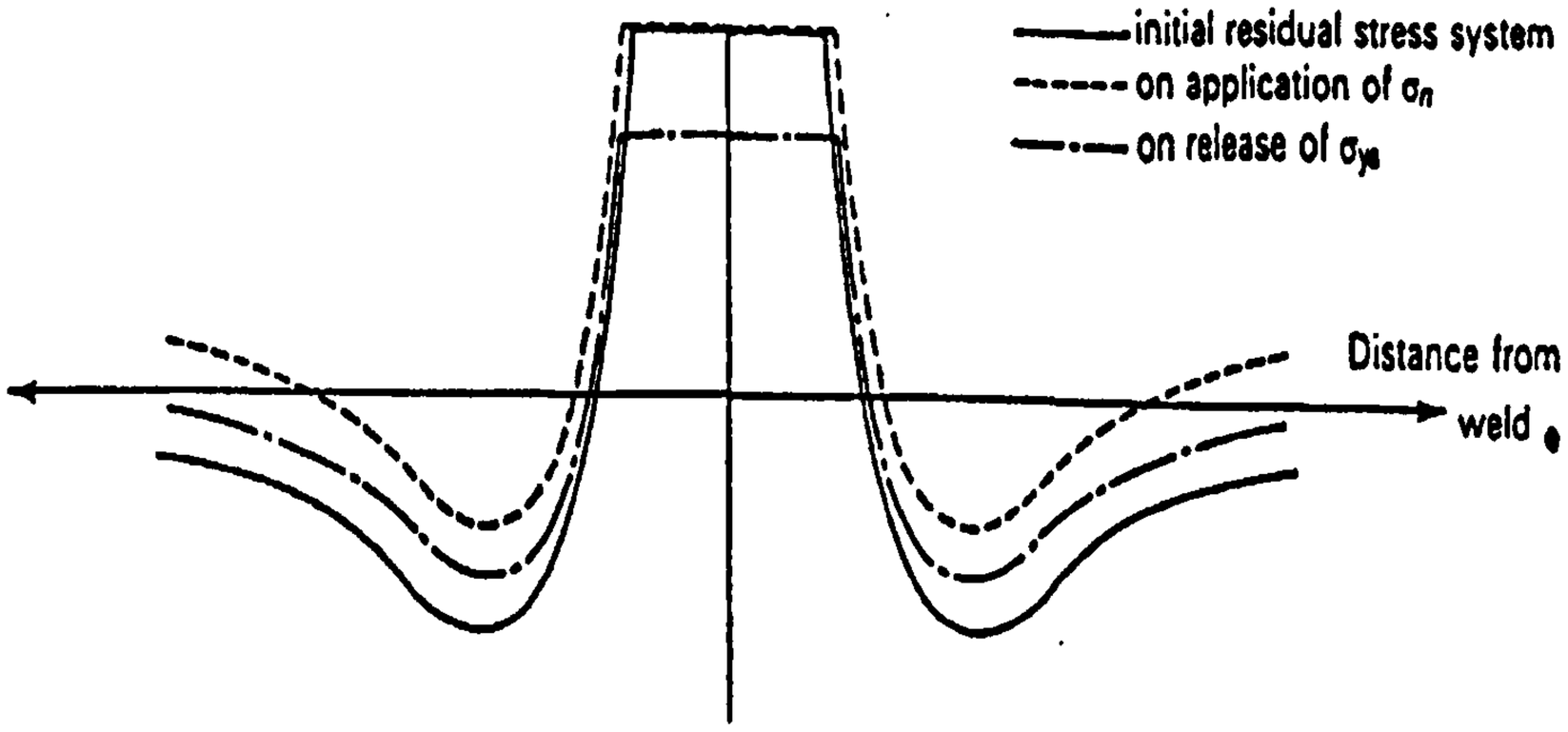

Figure 2.5 Superposition of an applied tensile stress, σ_n, on residual stress, σ_{ys}, of the weld metal.

In most of the experimental programs so far, fatigue tests have been carried out on specimens in the as-welded and stress-relieved conditions, and data were evaluated on the basis of S-N curves. It has been proven very difficult to separate the effect of the various parameters in a welded structure. With the recent development of the use of the fracture mechanics theory to predict fatigue crack growth, it is hoped that more exact information can be obtained on how residual stresses affect the fatigue strength of weldments. This is a major focus point of this thesis and is discussed in chapters 4 and 5.

2.4 Weldability of Aluminium Alloys and Heat Affected Zone Description

Before the discussion of the weldability of aluminium alloys it is necessary to present the different areas of a weld. A typical fusion weld joint consists of fusion zone, heat affected zone (HAZ) and unaffected base/parent material zone. Figure 2.6 illustrates the different zones due to a generic heat source. Figure 2.7 presents these different zones in a cross section of a welded specimen. Fusion zone is the area in which a mixture of filler metal

and parent material melted together homogeneously due to convection as in casting. Heat Affected Zone (HAZ) is the region in which the material is below melting but with substantial microstructural change even though the same chemical composition as base/parent material exists. Usually, degradation in mechanical properties has taken place. The base/parent material area contains high residual stresses especially near the heat affected zone.

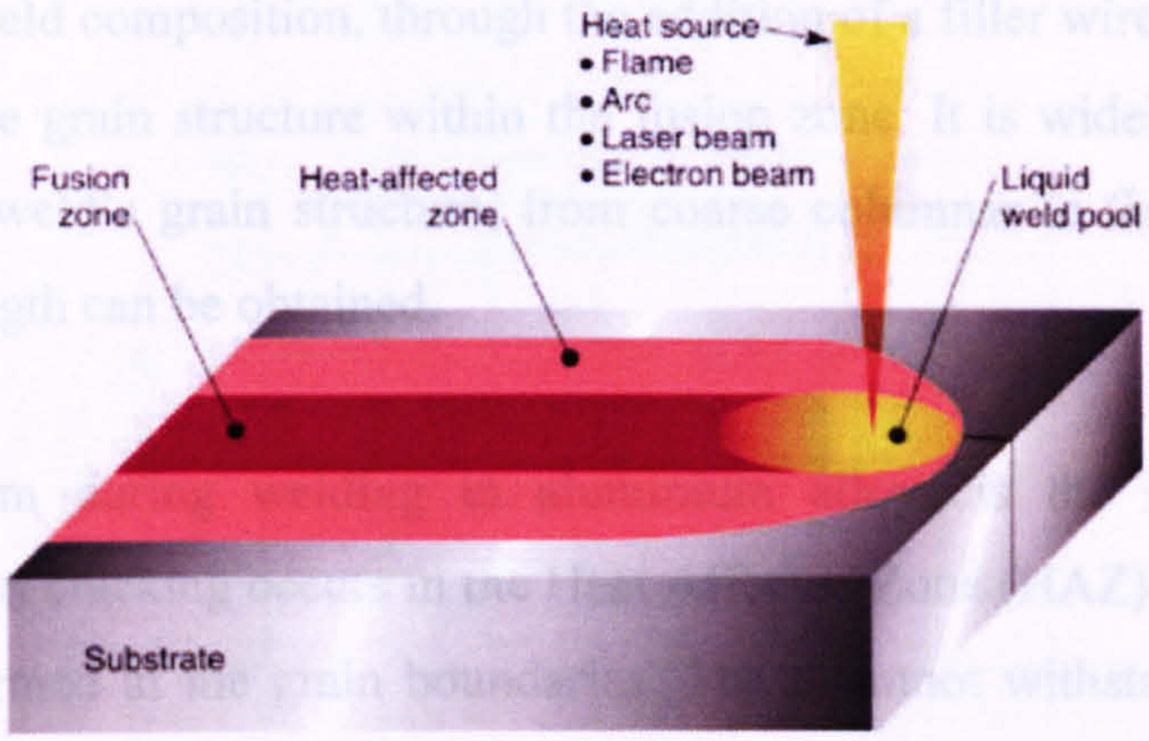

Figure 2.6 A schematic representation of the different zones in a generic weldment.

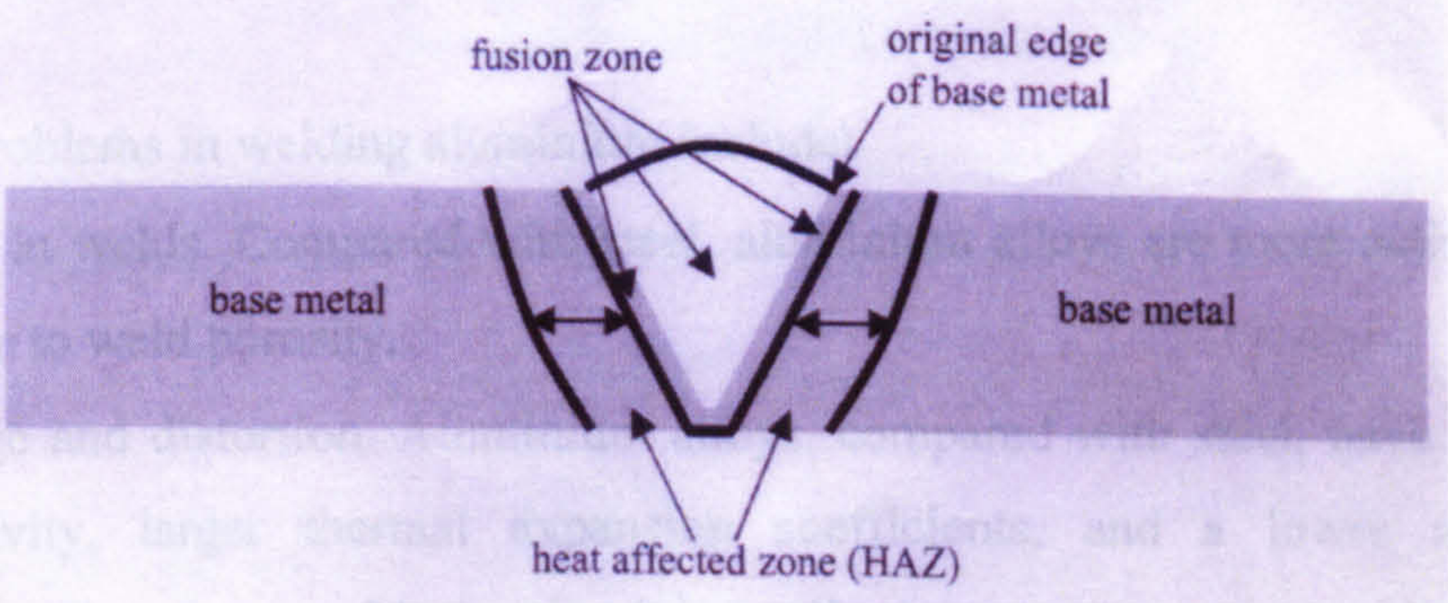

Figure 2.7 The three zones of a weldment in a cross section of a welded specimen.

The advances in welding aluminium greatly affected its use as a construction material. Until suitable welding techniques were developed, the use of aluminium was greatly restricted. New processes allow high-speed welding with manual or automatic equipment. Aluminium alloys are weldable; however, this does not mean aluminium welding is problem free.

One of the main problems of the weld aluminium is the solidification cracking within the weld zone. Cracking occurs in aluminium alloys because of high stresses generated across the weld due to the high thermal expansion (twice that of steel) and the substantial contraction on solidification - typically 5 % more than in equivalent steel welds. Methods that are commonly used to reduce the tendency for solidification cracking include [17]:

- Altering the weld composition, through the addition of a filler wire.
- Controlling the grain structure within the fusion zone. It is widely accepted that by changing the weld's grain structure, from coarse columnar to fine equiaxed, better cohesion strength can be obtained.

One other problem during welding in aluminium alloys is the so-called liquation cracking. Liquation cracking occurs in the Heat Affected Zone (HAZ), when low melting point films are formed at the grain boundaries. These cannot withstand the contraction stresses generated when the weld metal solidifies and cools. The risk can be reduced by using a filler metal with a lower melting temperature than the parent metal.

Additional problems in welding aluminium include:

- Porosity in welds. Compared with steel, aluminium alloys are more active and thus are prone to weld porosity.
- Shrinkage and distortion. Aluminium alloys, compared with steel, have higher heat conductivity, larger thermal expansion coefficients, and a lower modulus of elasticity. Therefore, welds in aluminium alloys are prone to more shrinkage and distortion.
- Loss of strength in the heat-affected zone (HAZ). A reduction in the strength of the heat-affected zone has been experienced in weldments in aluminium alloys, especially heat-treated alloys.

In the fabrication of welded structures must always consider the effects of the welding conditions on the metallurgical characteristics of a weldment. Controlling welding heat input to obtain optimum heat-affected-zone structures for various materials is an

important subject in welding metallurgy. A lot of research has been undertaken in this area [18,19]. Current practice follows two basic guidelines.

- To avoid rapid cooling in order to prevent the occurrence of hard brittle heat-affected zone and possible cracking.
- To avoid too slow cooling in order to prevent the occurrence of less ductile heat-affected structures.

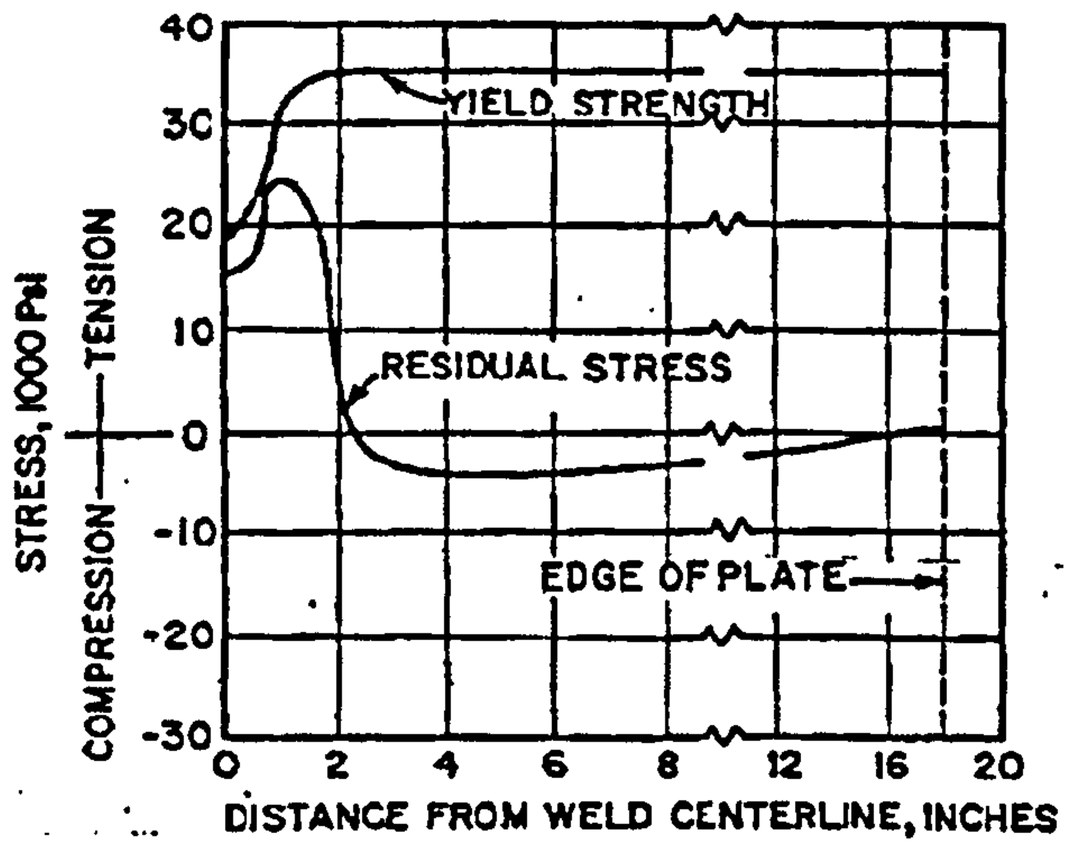

Figure 2.8 Distribution of yield strength and residual stresses in a longitudinally welded 5456-H321 aluminium alloy plate 36 inches wide (914mm) and 0.5 inches (12.7mm) thick.

The heat-affected zone, which is developed due to the welding process in a fabrication, is a major concern mainly for two reasons. First, is the reduction of the mechanic strength. This is caused by the softening of the parent/base material due to the heat input from the welding procedure. Actually the heat source of the welding lowers the yield strength of material. A "different material", which is confined to the region near the weld line, is now present other than the parent/base material due to this change of the material property in this region. Figure 2.8 shows the effect of the welding residual stresses on the yield strength of material [5]. For all welded fabrications testing is a very important part in the evaluation of the mechanic performance especially due to this decrease of the yield strength that the heat source puts into the structure. Last and equally important is the

increase of the possibility of a crack/damage initiation at the heat-affected zone of the structure. Porosity is the main reason for this.

2.5 Fracture Mechanics

In order to study the crack propagation in welded structures the basic fracture mechanics theory is summarised below. The Linear Elastic Fracture Mechanics (LEFM) theory is presented according to [20] and its use and limitations are discussed.

Figure 2.9 illustrates the different crack opening modes. In Irwin's notation, mode I denotes a symmetric opening, the relative displacements between corresponding pairs being normal to the fracture surface, while modes II and III denote anti-symmetric separation through relative tangential displacements, normal and parallel to the crack front, respectively.

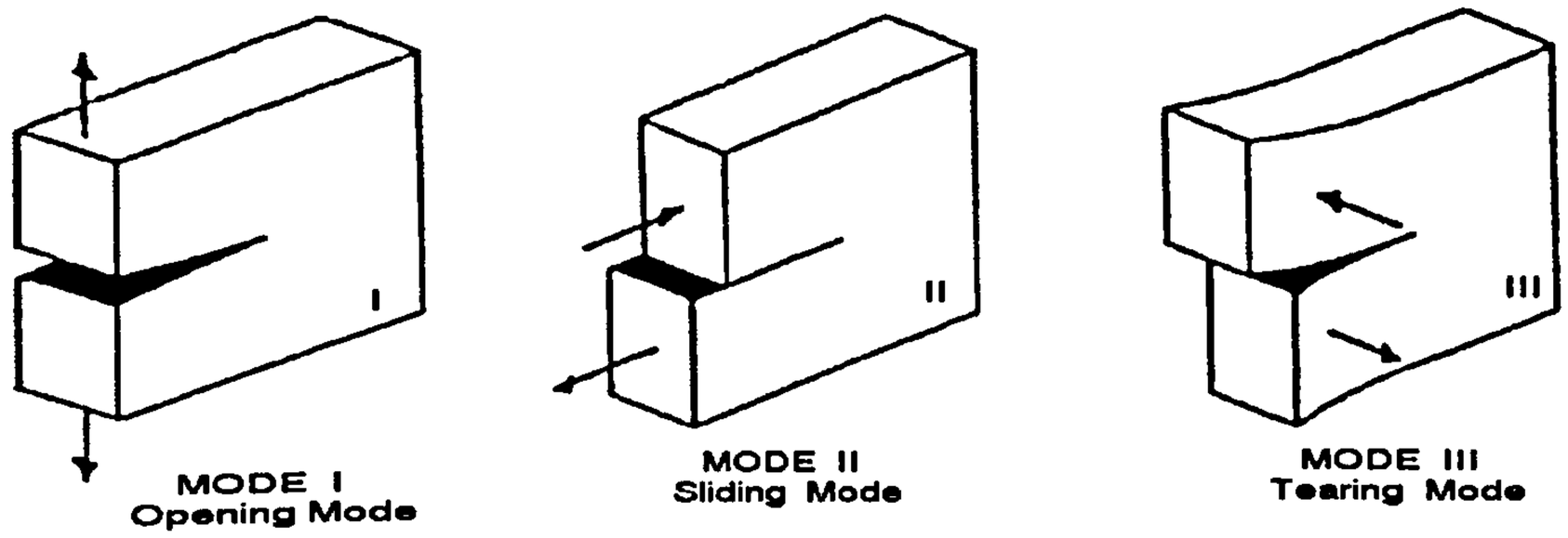

Figure 2.9 The three fracture modes.

In aircraft panels, crack growth usually takes place in mode I or close to it. This is probably also the type of separation, which is easiest to conceive intuitively. Using polar coordinates, r, θ the stresses near the crack tip are:

$$\sigma_{xx} = \frac{K_I}{\sqrt{2\pi r}} \cos\left(\frac{\theta}{2}\right)\left(1 - \sin\left(\frac{\theta}{2}\right)\sin\left(\frac{3\theta}{2}\right)\right)$$

$$\sigma_{yy} = \frac{K_I}{\sqrt{2\pi r}} \cos\left(\frac{\theta}{2}\right)\left(1 + \sin\left(\frac{\theta}{2}\right)\sin\left(\frac{3\theta}{2}\right)\right)$$

$$\sigma_{xy} = \frac{K_I}{\sqrt{2\pi r}} \cos\left(\frac{\theta}{2}\right)\left(\sin\left(\frac{\theta}{2}\right)\sin\left(\frac{3\theta}{2}\right)\right) \qquad (2.1)$$

$$\sigma_{zz} = \nu(\sigma_{xx} + \sigma_{yy}) \qquad \text{(plane strain)}$$

$$\sigma_{zz} = 0 \qquad \text{(plane stress)}$$

$$\sigma_{ij} = \frac{K_I}{\sqrt{2\pi r}} f_{ij}(\theta)$$

Linear elastic stress analysis of sharp cracks predicts infinite stresses at the crack tip. In real materials, however, stresses at the crack tip are finite due to yielding of the material. Inelastic material deformation, such as plasticity in metals and crazing in polymers, leads to further relaxation of crack tip stresses. The elastic stress analysis becomes increasingly inaccurate as the inelastic region at the crack tip grows. Simple corrections to linear elastic fracture mechanics (LEFM) are available when moderate crack tip yielding occurs. For extensive yielding, alternative crack tip parameters must be considered that take into account nonlinear material behaviour. The size of the crack tip-yielding zone is estimated below by the Irwin approach, where the elastic stress analysis is used to estimate the elastic-plastic boundary. Irwin approach leads to simple corrections for the crack tip yielding. The term *plastic zone* usually applies to metals, but will be adopted here to describe inelastic crack tip behaviour in a more general sense.

On the crack plane ($\theta = 0$) the normal stress, σ_{yy}, in a linear elastic material is given by equation (2.2). As a first approximation, it can be assumed that the boundary between elastic and plastic behaviour occurs when the stresses given by equation (2.2) satisfy a yield criterion. For plane stress conditions, yielding occurs when the normal stress is equal to the uniaxial yield strength of the material, ($\sigma_{yy} = \sigma_{YS}$). Substituting the yield strength into the left side of equation (2.2) and solving for r gives a first order estimate of plastic zone equation (2.3)

$$\sigma_{yy} = \frac{K_I}{\sqrt{2\pi r}} \tag{2.2}$$

$$r_y = \frac{1}{2\pi}\left(\frac{K_I}{\sigma_{YS}}\right)^2 \tag{2.3}$$

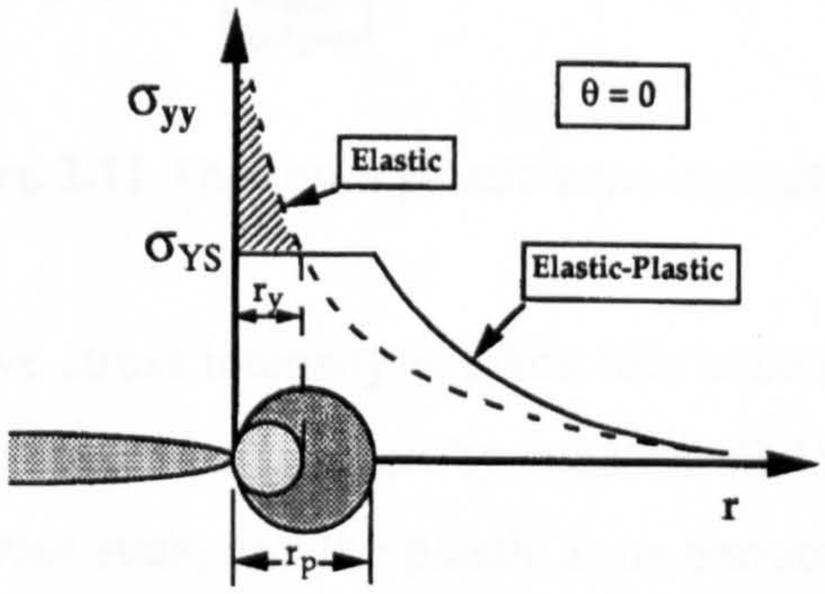

Figure 2.10 First-order and second-order estimates of plastic zone size (r_y and r_p, respectively).

If strain hardening is neglected the stress distribution for $r \le r_y$ can be represented by a horizontal line $\sigma_{yy} = \sigma_{YS}$, as illustrated in Figure 2.10; the stress singularity is reduced by yielding at the crack tip.

Note that the redistributed stress in the elastic region is higher than the prediction in equation (2.2), implying a higher effective stress intensity factor. Irwin [20] accounted for this increase in K by defining an effective crack length that is slightly longer than the actual crack size. He found that a good approximation of K_{eff} can be obtained by placing the tip of the effective crack in the center of the plastic zone, as illustrated Figure 2.11. Thus the effective crack length is defined as the sum of the actual crack size and a plastic zone correction:

$$a_{eff} = a + r_y \tag{2.4}$$

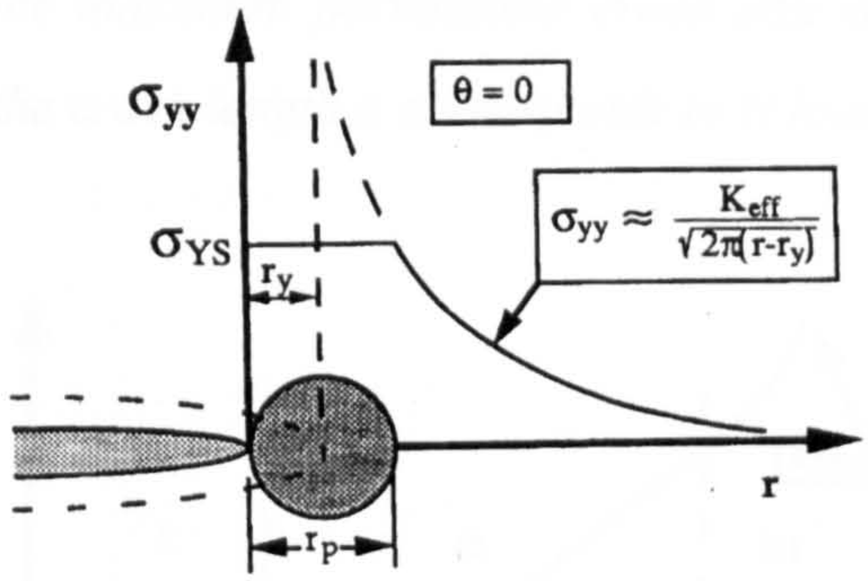

Figure 2.11 The Irwin plastic zone correction.

The increase in the effective stress intensity is taken into account by assuming the crack is longer by r_y. The r_y for plane stress is given by equation (2.4). In plane strain, yielding is suppressed by triaxial stress state, and the plastic zone correction is smaller by a factor of three:

$$r_y = \frac{1}{6\pi}\left(\frac{K_I}{\sigma_{YS}}\right)^2 \tag{2.5}$$

The effective stress intensity factor is obtained by inserting α_{eff} into the K expression for the geometry of interest:

$$K_{eff} = C(a_{eff})\sigma\sqrt{\pi a_{eff}} \tag{2.6}$$

Since the effective crack size is taken into account in the geometry correction factor, C, an iterative solution is usually required to solve for K_{eff}.

2.6 Fundamentals of Fatigue Crack Propagation

Fatigue crack propagation, referred to as stage II in Figure 2.12, represents a large portion of the fatigue life of many materials and engineering structures. Accurate prediction of the fatigue crack propagation stage is of utmost importance for determining the fatigue life. The main objective of the fatigue crack propagation may be presented in this form: "*Determine the number of the cycles N_c required for a crack to grow from a certain*

initial crack size α_o to the maximum permissible crack size α_c , and the form of this increase $\alpha=\alpha(N)$, where the crack length a corresponds to N loading cycles."

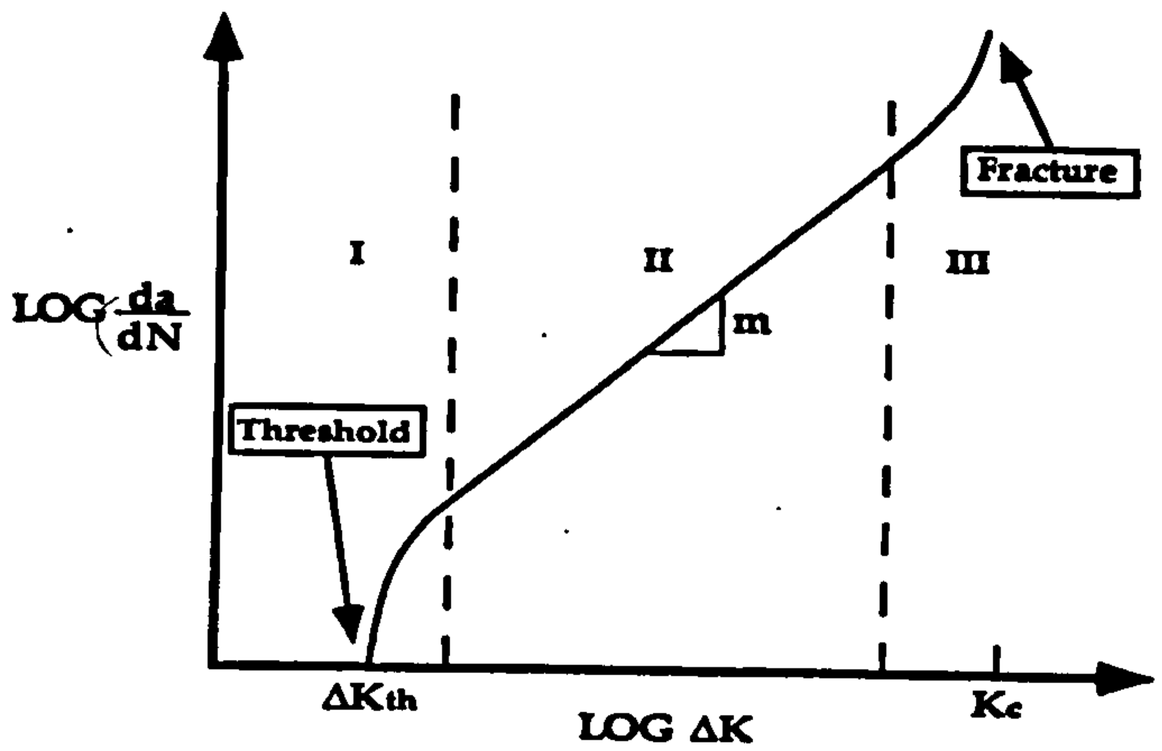

Figure 2.12 Typical fatigue crack growth behaviour in metals.

Fatigue crack propagation data are obtained from pre-cracked specimens subjected to fluctuating loads, and the change in crack length is recorded as a function of loading cycles. The crack length is plotted against the number of the loading cycles for different load amplitudes. The stress intensity factor is used as a correlation parameter in analyzing the fatigue crack propagation results. The experimental results are usually plotted in a log (ΔK) versus log (da/dN) diagram, where ΔK is the range of the stress intensity factor and da/dN is the crack propagation rate. The load is usually sinusoidal with constant amplitude and frequency. Two of the four parameters K_{max}, K_{min}, $\Delta K = K_{max} - K_{min}$ or $R = K_{min}/K_{max}$ are needed to define the stress intensity factor variation during a loading cycle.

A typical plot of the characteristic sigmoidal of a log(ΔK)- log(da/dN) fatigue crack growth rate curve is shown in Figure 2.12. Three regions can be distinguished. In region I, da/dN diminishes rapidly to a very small level, and for some materials there is a threshold value of the stress intensity factor range ΔK_{th} meaning that for $\Delta K < \Delta K_{th}$ no crack propagation takes place. In region II there is a linear log(ΔK) – log(da/dN)

relation. Finally, in region III the crack growth rate curve rises and the critical stress intensity factor K_c, leading to catastrophic failure. Experimental results indicate that the fatigue crack growth rate curve depends on the ratio R, and is shifted toward higher da/dN values as R increases.

Cyclic stresses resulting from constant or variable amplitude loading can be described by two of a number of alternative parameters. Constant amplitude cyclic stresses are defined by three parameters, namely a mean stress, σ_m, a stress amplitude, σ_a, and a frequency ω, ν. The frequency is not needed to describe the magnitude of the stresses. Only two parameters are sufficient to describe the stresses in a constant amplitude loading cycle. It is possible to use other parameters; for example, minimum stress, σ_{min}, and the maximum stress, σ_{max}, to describe the stresses completely. The stress range, $\Delta\sigma = \sigma_{max} - \sigma_{min}$, can also be used in combination with any of the others, except, σ_a. In addition, another parameter is often convenient. This is the so-called stress ratio R, defined as $R=\sigma_{min}/\sigma_{max}$. One of the above parameters can be replaced by the load ratio R to define the cyclic load. Any of the following combinations fully defines the stresses in a constant amplitude loading: $\Delta\sigma$ and R, σ_{min} and R, σ_{max} and R, σ_a and R, and σ_m and R. The case of R=0 defines the condition in which the stress always rises from, and returns to 0. When R=-1, the stress cycles around zero as a mean, which is called fully reversed loading.

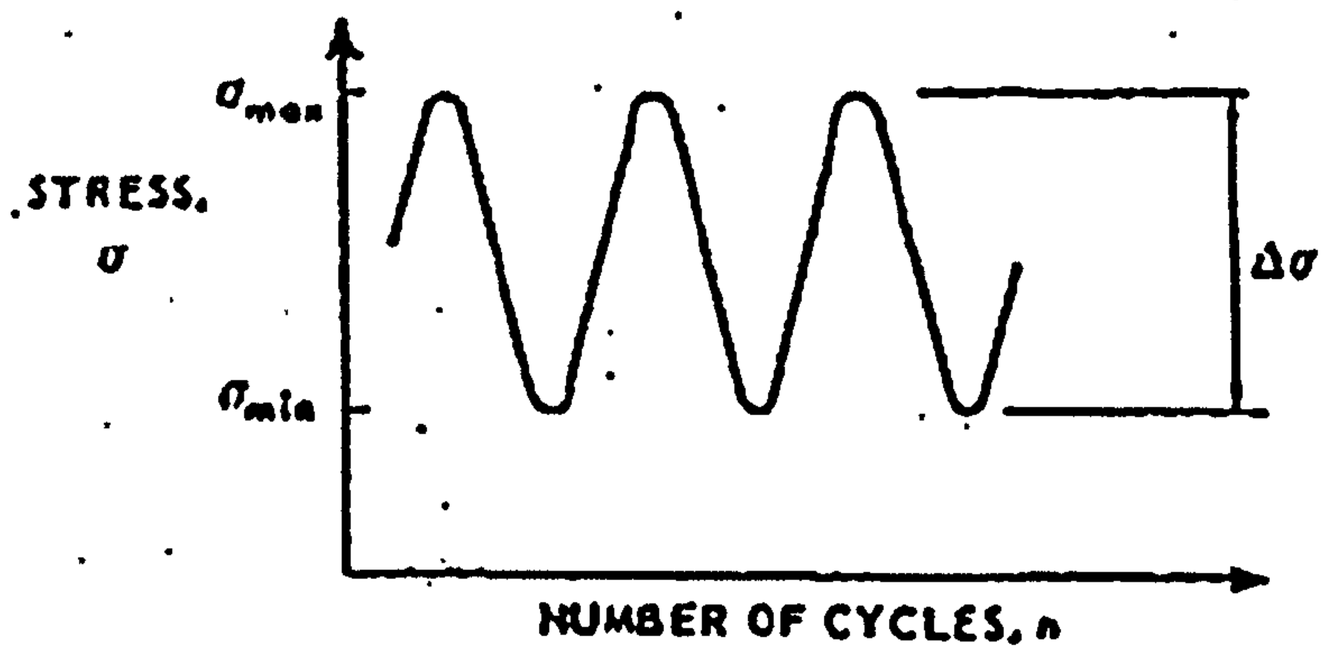

Figure 2.13 Stress-cycle parameters in constant amplitude fatigue.

In order to study the parameters, which affect the fatigue crack growth a through-thickness crack is considered in a wide plate subjected to remote stressing that varies cyclically between constant minimum and maximum values as presented in Figure 2.13. The stress range is defined as $\Delta\sigma = \sigma_{max} - \sigma_{min}$

The fatigue crack propagation rate is defined as the crack extension, $\Delta\alpha$, during a small number of cycles, ΔN, the propagation rate is $\Delta\alpha/\Delta N$, which in the limit can be written as the differential da/dn. It has been found experimentally that provided the stress ratio $R = \sigma_{min}/\sigma_{max}$, is the same then ΔK correlates fatigue crack growth rates in specimens with different stress ranges and crack lengths and also correlates crack growth rates in specimens of different geometry. This correlation is presented in Figure 2.14. The data obtained with a high stress range, $\Delta\sigma_{high}$, commence at relatively high values of da/dN and ΔK. The data for a low stress range, $\Delta\sigma_{low}$, commence at lower values of da/dN and ΔK, but reach the same high values as in high stress range case.

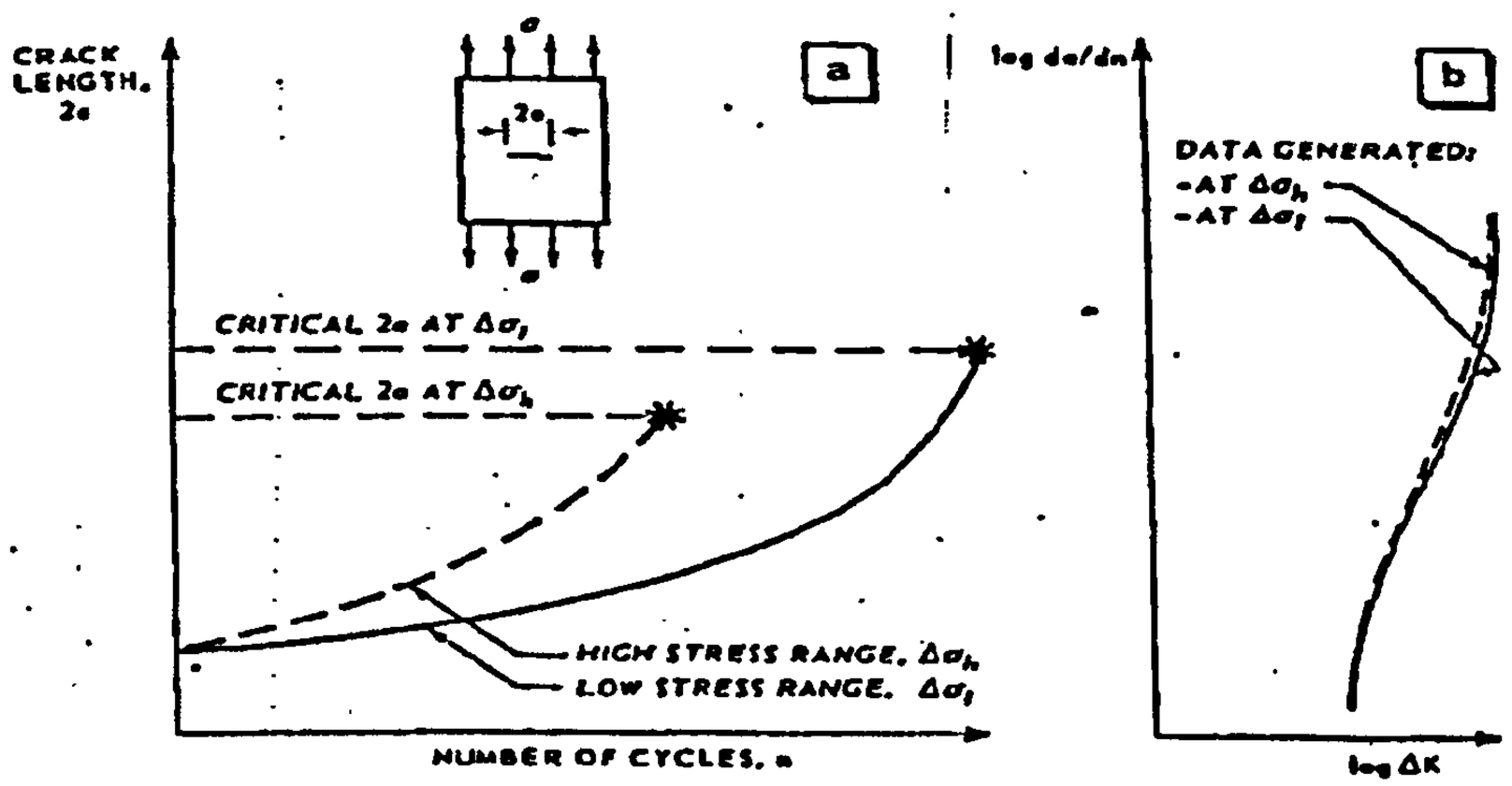

Figure 2.14 Correlation of fatigue crack propagation data by ΔK when the stress ratio R remains the same.

In addition, the stress ratio R can have a significant influence on the crack growth behaviour. In other words, besides the stress intensity factor range, ΔK, there is an influence of the relative values of K_{max} and K_{min}, since $R = \sigma_{min}/\sigma_{max} = K_{max}/K_{min}$. This is presented in Figure 2.15, which shows that crack growth rates at the same stress intensity range ΔK values are generally higher when the load ratio R is increasing. It is important at this point to note that the effect of the load ratio R has proved to be from the bibliography strongly material dependent.

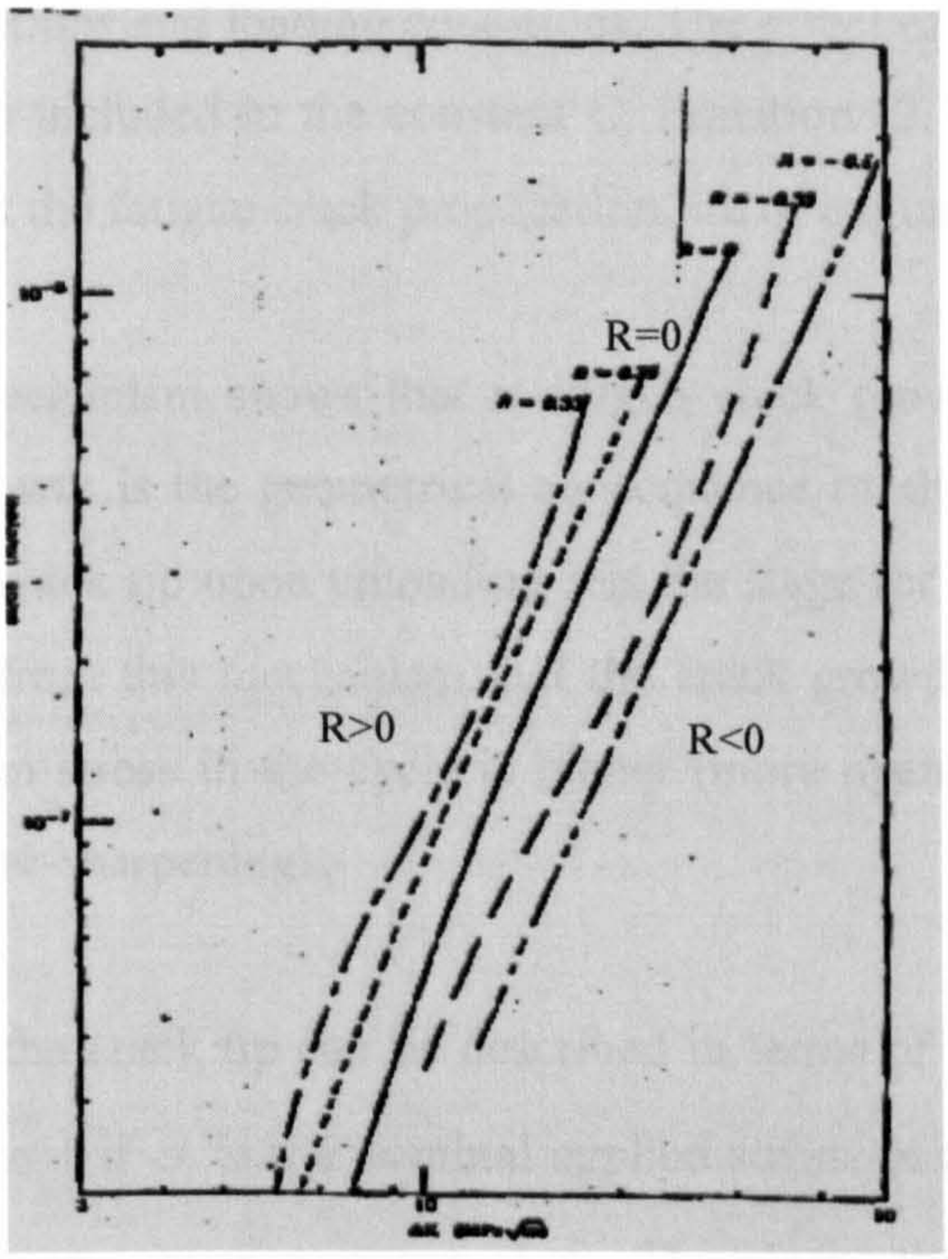

Figure 2.15 Influence of R on fatigue crack growth in aluminium alloy 2024 – T3, [21].

A number of different quantitative continuum mechanics models of fatigue crack propagation have been proposed in the literature. All these models lead to relations based mainly on experimental data correlations. They relate da/dN to such variables as the external load, the crack length, the geometry and the material properties. One of the most widely used fatigue crack propagation laws is that proposed by Paris and Erdogan and is usually referred in the literature as the "Paris law". It has the form:

$$\frac{da}{dN} = C(\Delta K)^m \tag{2.7}$$

where $\Delta K = K_{max} - K_{min}$, with K_{max} and K_{min} referring to the maximum and minimum values of the stress intensity factor in the load cycle. The constant C and m are determined empirically from a $\log(\Delta K)$ – $\log(da/dN)$ plot. The value of m is usually taken equal to 4 for aluminium alloys, resulting in the so-called "4th power law" while the coefficient C is assumed to be a material constant. The equation (2.7) represents a linear relationship between $\log(\Delta K)$ and $\log(da/dN)$ and is used to describe the fatigue crack propagation. Experimental data are well predicted using the equation (2.7) for specific geometrical configurations and loading conditions. The effect of mean stress, loading and specimen geometry is included in the constant C. Equation (2.7) ("Paris law") has been widely used to predict the fatigue crack propagation life of engineering components.

The crack growth mechanism shows that a fatigue crack grows by a small amount in every load cycle. Growth is the geometrical consequence of slip and crack tip blunting. Resharpening of the crack tip upon unloading sets the stage for growth in the next cycle. It can be concluded from this mechanism that the crack growth per cycle, $\Delta\alpha$, will be larger if the maximum stress in the cycle is higher (more opening) and if the minimum stress is lower (more re-sharpening).

The local stresses at the crack tip can be described in terms of the stress intensity factor K, where $K = \beta\sigma\sqrt{\pi\alpha}$, if σ is the nominal applied stress. In a cycle, the applied stress varies from σ_{min} to σ_{max} over a range $\Delta\sigma$. Therefore, the local stresses vary in accordance with:

$$K_{min} = \beta\sigma_{min}\sqrt{\pi\alpha}$$

$$K_{max} = \beta\sigma_{max}\sqrt{\pi\alpha} \qquad (2.8)$$

$$\Delta K = \beta\Delta\sigma\sqrt{\pi\alpha}$$

An amount of crack growth is defined as $\Delta\alpha$ in one cycle, which is expressed in m/cycle. If growth were measured over e.g. ΔN = 10000 cycles, the average growth per

cycle would be $\Delta\alpha/\Delta N$, which is the rate of crack propagation. In the limit where $N \to 1$, this rate can be expressed as the differential da/dN.

When a structural component is subjected to fatigue loading, a dominant crack reaches a critical size under the peak load during the last cycle leading to catastrophic failure. The basic objective of the fatigue crack propagation analysis is the determination of the crack size, α, as a function of the number of the cycles, N. Thus, the fatigue crack propagation life N_p is obtained. When the type of the applied load and the expression of the stress intensity factor are known, application of one of the foregoing fatigue laws enables a realistic calculation of the fatigue crack propagation life of the component. As an example, consider a plane fatigue crack of the length $2\alpha_o$ in a plane subjected to a uniform stress σ perpendicular to the plane of the crack. The stress intensity factor K is given by:

$$K = f(\alpha)\sigma\sqrt{\pi\alpha} \tag{2.9}$$

where $f(\alpha)$ is a geometry dependent function.

Integrating the fatigue crack propagation law expressed by equation (2.7) gives:

$$N - N_0 = \int_{\alpha_o}^{\alpha} \frac{d\alpha}{C(\Delta K)^m} \tag{2.10}$$

where N_0 is the number of load cycles corresponding to the half crack length α_o. Introducing the stress intensity factor range ΔK, where K is given from equation (2.8), into equation (2.7) results in:

$$N - N_0 = \int_{\alpha_o}^{\alpha} \frac{d\alpha}{C\left[f(\alpha)\Delta\sigma\sqrt{\pi\alpha}\right]^m} \tag{2.11}$$

Assuming that the function $f(\alpha)$ is equal to its initial value $f(\alpha_o)$ so that

$$\Delta K = \Delta K_0 \sqrt{\frac{\alpha}{\alpha_o}} \quad , \Delta K_0 = f(\alpha_o)\Delta\sigma\sqrt{\pi\alpha_o} \tag{2.12}$$

equation (2.11) gives:

$$N - N_0 = \frac{2\alpha_o}{(m-2)C(\Delta K_0)^m}\left[1 - \left(\frac{\alpha_o}{\alpha}\right)^{m/2-1}\right] \quad \text{for } m \neq 2. \tag{2.13}$$

Unstable crack propagation occurs when

$$K_{\max} = K_{IC} = f(\alpha)\sigma_{\max}\sqrt{\pi\alpha} \tag{2.14}$$

from which the critical crack length α_o is obtained. Then, the equation 2.11 for $\alpha = \alpha_c$ gives the fatigue crack propagation life $N_p = N_c - N_0$. Usually, however $f(\alpha)$ varies with the crack length α and the integration of equation (2.11) cannot be performed directly, but only through the use of numerical methods.

2.7 Crack Closure Phenomenon in Fatigue Crack Propagation

In the early 1960s, Paris, et al. [22,23] demonstrated that fracture mechanics is a useful tool for characterizing crack growth due to fatigue phenomenon. Since that time, the application of fracture mechanics to fatigue problems has become almost routine. There are, however, a number of controversial issues and unanswered questions in this field. The procedures for analyzing fatigue under constant amplitude loading at small scale yielding conditions are fairly well established, although a number of uncertainties remain.

The concept of similitude, when it applies, provides the theoretical basis for fracture mechanics. Similitude implies that the crack tip conditions are uniquely defined by a single loading parameter such as the stress intensity factor. Consider a growing crack in the presence of a constant amplitude cyclic stress intensity Figure 2.16. A cyclic plastic zone forms at the crack tip, and the growing crack leaves behind a plastic wake. If the plastic zone is sufficiently small that is embedded within an elastic singularity zone, the conditions at the crack tip are uniquely defined by the current K value, and the crack growth rate is characterized by K_{min} and K_{max}. In order for the similitude assumption to be valid the crack tip of the growing crack needs to be sufficiently far from its initial position, and external boundaries should be remote.

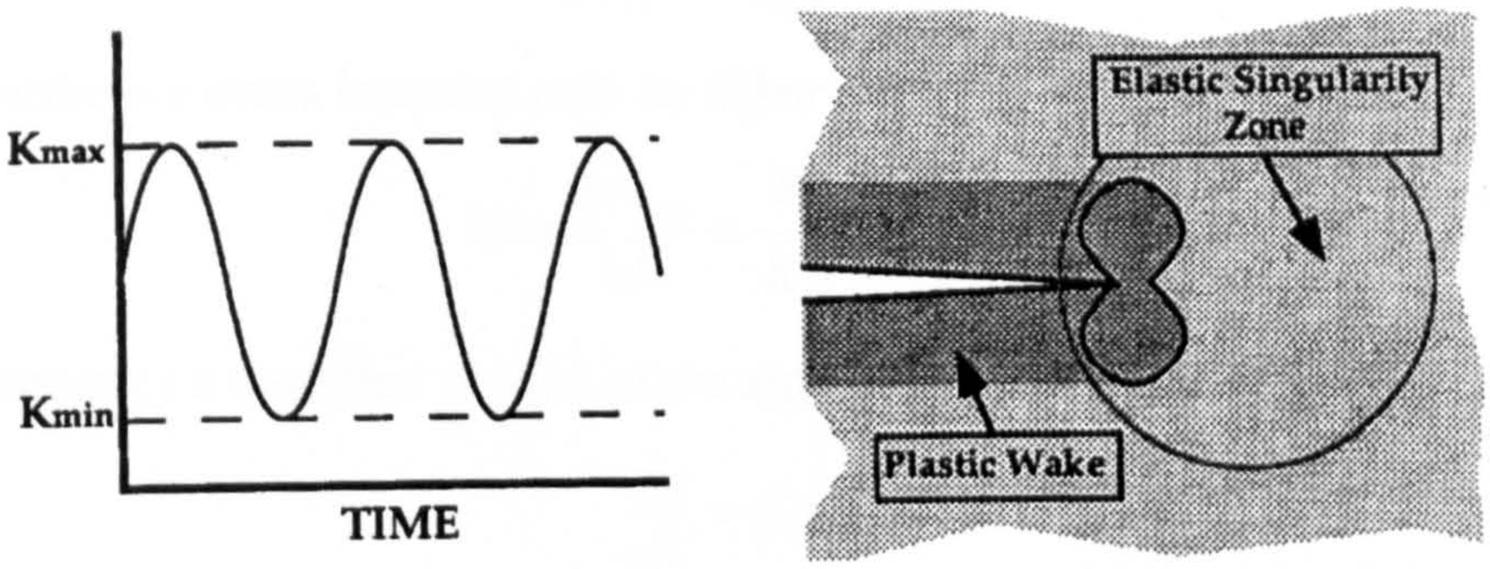

Figure 2.16 Constant amplitude fatigue crack growth under small yielding conditions.

It is convenient to express the functional relationship for crack growth in the following form:

$$\frac{da}{dN} = f_1(\Delta K, R) \tag{2.15}$$

where $\Delta K \equiv (K_{max} - K_{min})$, $R \equiv K_{min}/K_{max}$ and da/dN is the crack growth per cycle. The influence of the plastic zone and the plastic wake on crack growth is implicit in equation 2.15, since the size of the plastic zone depends only on K_{min} and K_{max}. A number of expressions for f_1 function have been proposed, most of which are empirical.

Soon after the Paris law gained wide acceptance as a predictor of fatigue crack growth, many researchers came to the realization that this simple expression was not universally applicable. As Figure 2.12 illustrates, a log-log plot of da/dN versus ΔK is sigmoidal rather than linear when crack growth data are obtained over a sufficiently wide range. Also, the fatigue crack growth rate exhibits a dependence on the R ratio, particularly at both extremes of the crack growth curve. A discovery by Elber [24] provided at least a partial explanation for both the fatigue threshold and R ratio effects.

Elber postulated that crack closure decreased the fatigue crack growth rate by reducing the effective stress intensity range Figure 2.17. When a specimen is cyclically loaded at K_{max} and K_{min}, the crack faces are in contact below K_{op}, the stress intensity at which the crack opens. Elber assumed that the portion of the cycle that is below K_{op} does not contribute to fatigue crack growth. The definition of the effective stress intensity range is:

$$\Delta K_{eff} \equiv K_{\max} - K_{op} \tag{2.16}$$

Also the effective stress intensity ratio by Elber is:

$$U \equiv \frac{\Delta K_{eff}}{\Delta K} = \frac{K_{\max} - K_{op}}{K_{\max} - K_{\min}} \tag{2.17}$$

and consequently a modified version of the equation (2.7) proposed:

$$\frac{da}{dN} = C\Delta K_{eff}{}^{m} \tag{2.18}$$

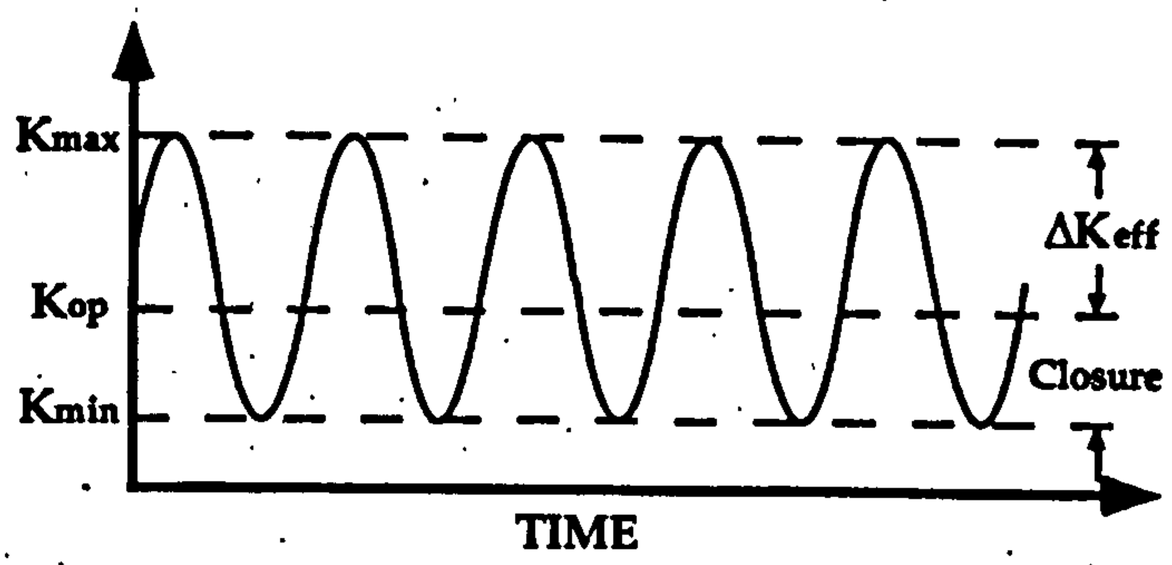

Figure 2.17 Definition of effective stress intensity range.

Crack closure can help to explain the effect of load ratio R on fatigue crack growth rates. Crack closure occurs as a consequence of crack tip plasticity. At the tip of a growing fatigue crack each loading cycle generates a monotonic plastic zone during increased loading and a much smaller reversed plastic zone during unloading. Approximately the reversed plastic zone size is one-quarter of the size of the monotonic plastic zone. Due to this, there is a residual plastic deformation consisting of monotonically stretched material.

As the crack grows the residual plastic deformation forms a wake of monotonically stretched material along the crack edges. Because the residual deformation is the consequence of tensile loading the material in the crack edges is elongated normal to the crack surfaces and has to be accommodated by the surrounding elastically stressed material. This is no problem as long as the crack is open, since then the crack edges will simply show a displacement normal to the crack surfaces. However, as the fatigue load decreases, during unloading, the crack will tend to close and the residual deformation becomes important. The above is illustrated with the help of Figure 2.18.

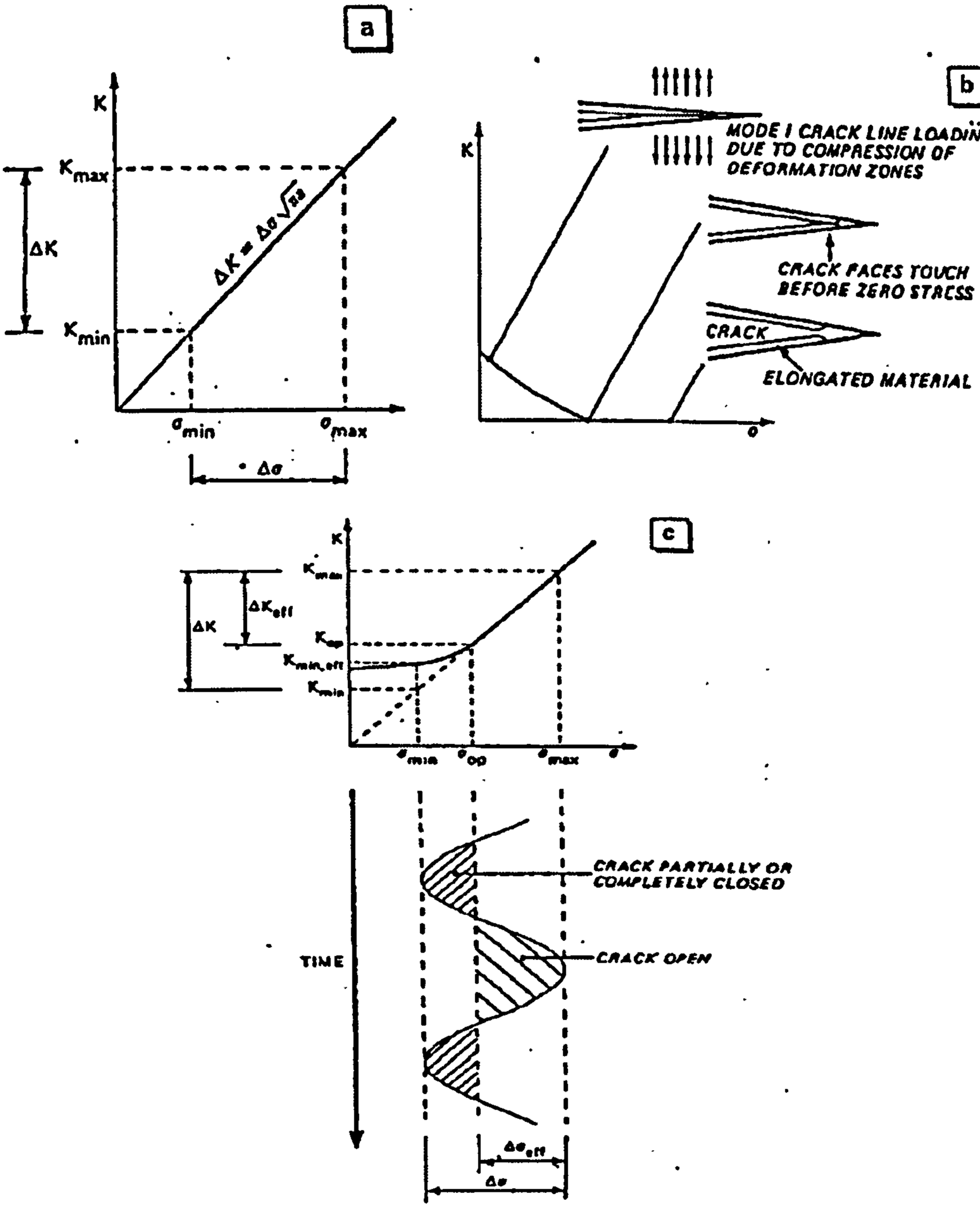

Figure 2.18 Principal of crack closure: (a) Nominal $K-\sigma$ plot, (b) Residual deformation due to crack tip plasticity results in mode I crack line loading K values, (c) Superposition of K values shows the effect of crack closure.

More specific, graph (a) in Figure 2.18 shows the variation in the nominal stress intensity factor K, with the applied stress, σ. Graph (b) in the same figure shows that the applied stresses decreases due to elastic relaxation of the cracked body. However, the crack surfaces are prevented from becoming parallel because the stretched material along the

edges causes closure before zero load is reached. This closure results in reaction forces and a mode I stress intensity, which increases as the applied stress decreases. This mode I stress intensity factor is due to crack line loading.

Graph (c) in Figure 2.18 shows superposition of the stress intensity factors due to the applied stress and the crack closure mechanism and also the important concept of crack opening stress, σ_{op} , which has been defined by Elber as that value of applied stress for which the crack is just fully open. Opening stress σ_{op}, can be determined experimentally from the change in compliance. Crack closure results in an increase of stiffness and a decrease in compliance. Elber further suggested that for fatigue crack growth to occur the crack must be fully open. Thus an effective stress intensity factor range, ΔK_{eff} , can be defined from the stress range $\sigma_{\max} - \sigma_{op}$. ΔK_{eff} is smaller than the nominal range ΔK. At this point it should be noted that Elber's suggestion that fatigue crack growth only occurs when the crack is fully open is not entirely correct. In fact, it would be better to define ΔK_{eff} as $K_{\max} - K_{\min,eff}$. However, $K_{\min,eff}$ cannot be determined experimentally. Based on the above and Figure 2.18 it can be said that higher R values result in less crack closure since ΔK_{eff} becomes more nearly to equal to ΔK. Therefore, Elber proposed that ΔK_{eff} accounts for the effect of the load ratio R on the crack growth rates.

2.8 Effect of Residual Stresses on Crack Propagation

Our knowledge of the relationship between residual stress and fatigue strength is perplexed due to the fact that:

- The fatigue strength depends greatly on the condition of the surface. The effect of residual stress is overshadowed by such major factors as weld geometry and surface irregularities.
- A fatigue crack may initiate in a region containing tensile residual stresses. The rate of crack growth may be increased due to the existence of tensile residual stresses. However, when the crack grows and enters regions containing compressive residual

stresses, the rate of the crack growth may be reduced. As a result, it is questionable whether or not the total effect of the residual stresses on the overall crack growth is significant.

- When residual stresses are altered by a heat treatment such as peening, the metallurgical and mechanical properties of the metal are also changed.

A schematic presentation of the stress field behind and in front of a crack tip under cyclic loading without welding residual stresses is illustrated in Figure 2.19.

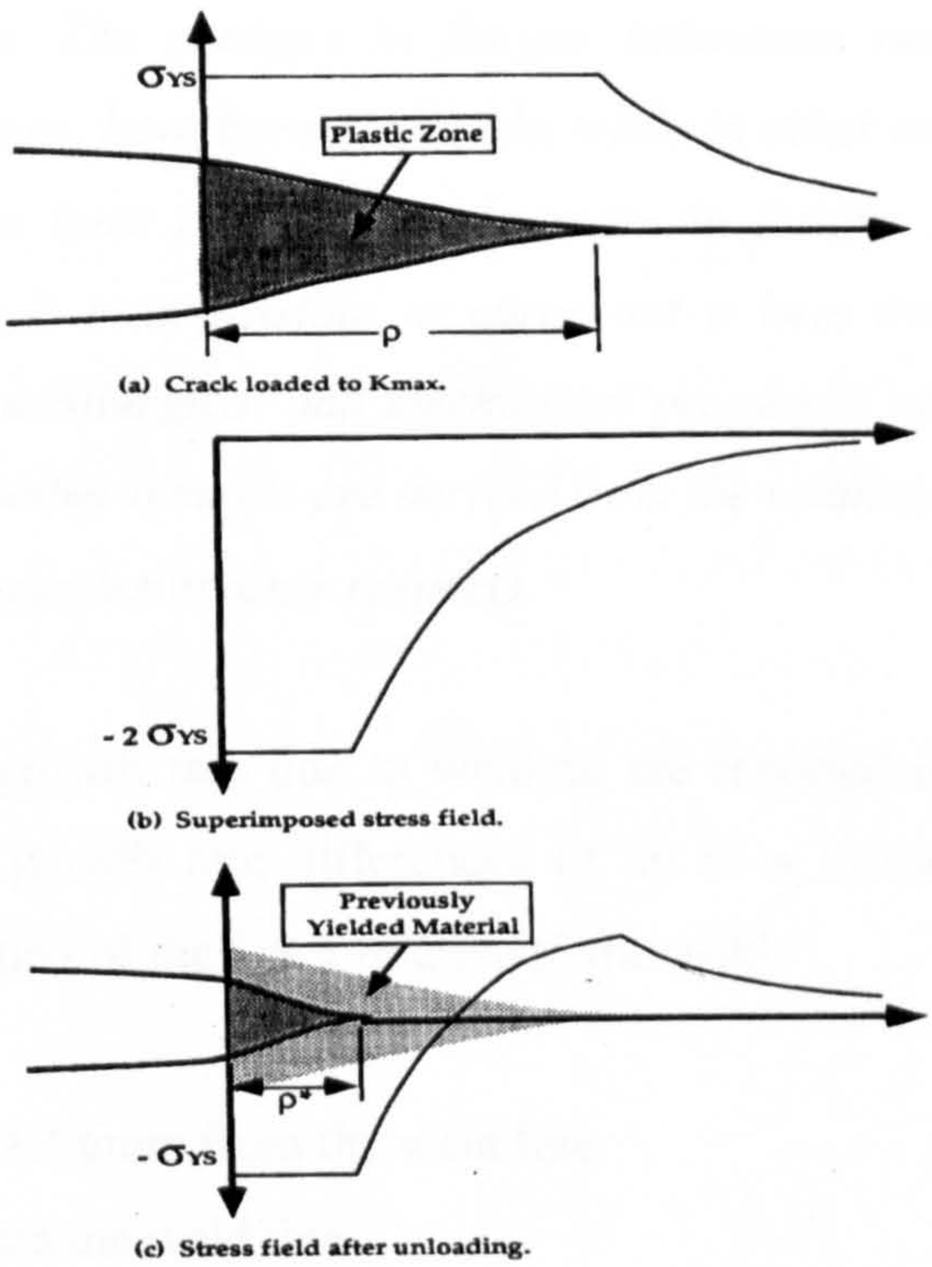

Figure 2.19 Formation of reverse plastic zone during cyclic loading, [20].

How residual stresses actually affect the plastic zone showed in Figure 2.19 and subsequently the fatigue strength of a welded structure is still a matter of debate. Some researchers have reported that the fatigue strength increased when specimens had compressive residual stresses, especially on the specimen surfaces, others believe that residual stresses have only a negligible effect on the fatigue strength of the weldments. It has been suggested that in a good weld residual stresses can be ignored [25]. Also it has been suggested that geometry affects fatigue behaviour much more than residual stresses

[13]. But others researchers [26] feel that there is significant evidence that residual stresses affect the fatigue strength. Munse [27] summarizes as follows:

"On the basis of the available data it is believed that the effects of residual stresses may differ from one instance to another, depending upon the materials and geometry of the members, the state of stress, the magnitude of applied stress, the type of stress cycle and perhaps other factors. Many of the investigations designed to evaluate the effects of residual stress have included tests of members that have been subjected to various stress-relief heat treatments. The changes in fatigue behaviour resulting from these heat treatments, in some cases, have been negligible, while in other investigations, the various stress-relief treatments have produced an increase in fatigue strength of as much as twenty percent. Since it is impossible to carry out a heat treatment for stress relief without altering the metallurgical and mechanical properties of weldment, the question always arises as to whether benefits are derived from the reduction of residual stresses or from the improved properties in other respects."

Differences in crack growth rate due to welding are reported in [28,29]. For the same values of ΔK crack growth rate differences of up to a factor over 100 were found, depending on the position of the crack relative to the weld.

- The weld line
- The softened HAZ 6mm from the weld line
- 28 mm away from the weld line

Bussu and Irving's work shows crack growth rates measured for cracks growing at three areas. All the experimental data of this work are for the friction stir welding procedure (FSW). Crack growth rates were fastest at 28 mm from the weld line and slowest at 6 mm from the weld line in the softest region of the heat affected zone. Parent plate growth rates were intermediate between these two extremes. It has been established that the local level of weld residual stress plays a major role in determining crack growth rate, but microstructure and hardness also change rapidly with distance from the weld, and will influence growth rates.

CHAPTER 3

DESIGN OF 2-STRINGER PANELS FOR FATIGUE EXPERIMENT

3.1 Design Limitations and Guidelines of Wing Panels

This chapter presents the design of the two-stringer panels used for the experimental and numerical study in the WELDES project. Both a lower and upper wing panels were designed. The upper wing panel is designed in compression and the lower panel in tension. As it is well known the main design driving force for the upper stiffened panel is buckling since it is under compression. Damage tolerance is the main design criterion for the lower stiffened panel due to tensile fatigue loading. This chapter also presents the practical design limitations, which had to be considered due to availability in fabrication technology. In the end, the design of the end-fittings for the lower stiffened panel is reported.

The structural elements of a typical aircraft wing are illustrated in Figure 3.1. In general, design wing loads in an aircraft consist of shears, bending moments and torsions, which result from air pressures and inertia loading. Although the skin panels must provide a certain torsional stiffness and resistance to shear, the main criteria in their design is their ability to withstand bending loads. In this study, only the bending moments due to air pressures are considered. The wing bending loads, which cause compression at the upper surface of the wing are generally somewhat higher than those causing compression at the lower surface. This results in a clear separation in terms of the main criterion for the preliminary sizing and design of the upper and lower wing cover.

The first step in the design of the wing skin is to choose the geometry-type of the stiffener [1]. Several stiffener configurations are considered for the stiffener panels of the wing, e.g. Z-, Hat, I-, J-sections. These options are discussed in the current chapter. Other parameters in the wing design include the skin thickness, rib pitch, stringer pitch, stringer height, stringer thickness and flange width.

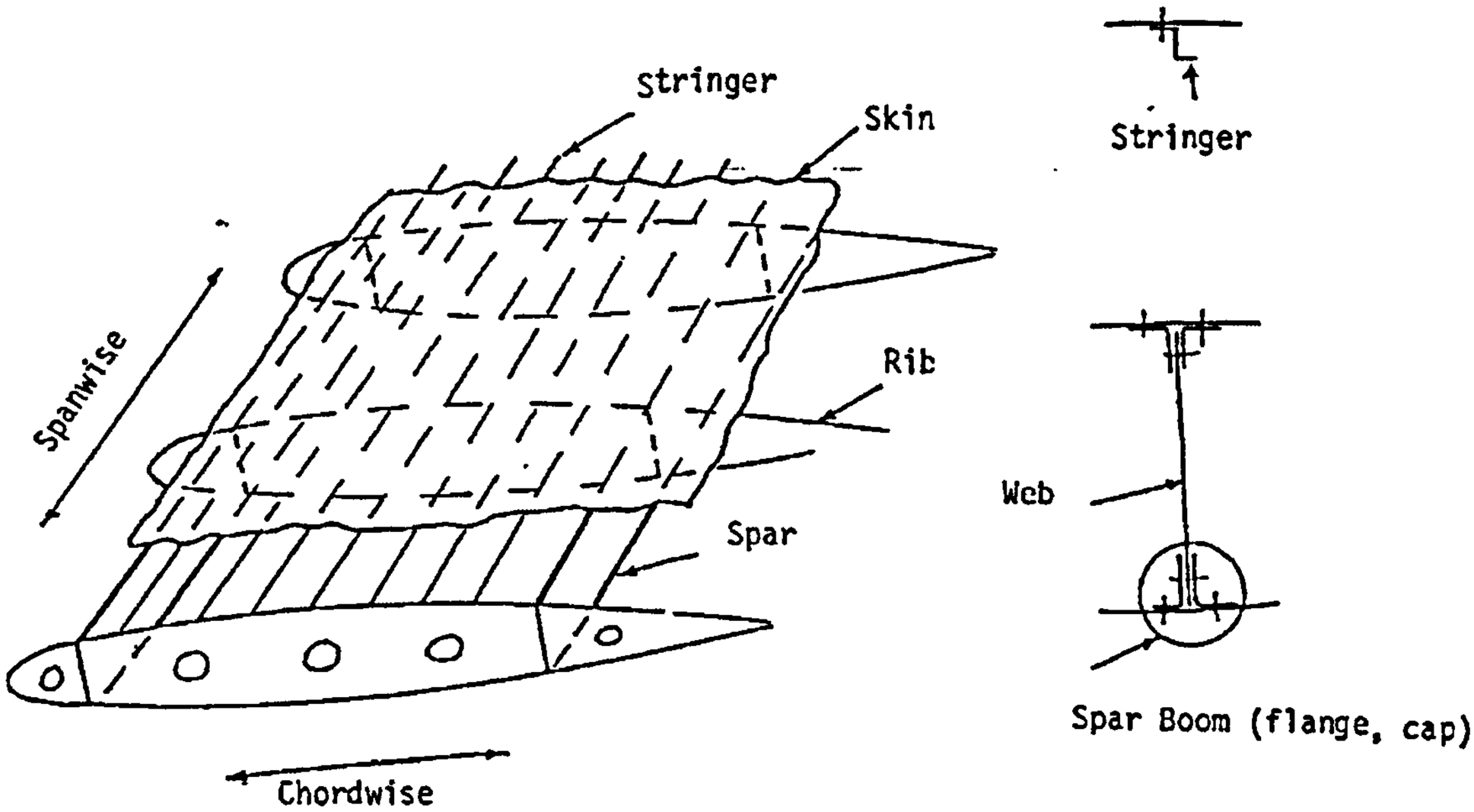

Figure 3.1 Structural elements of a typical aircraft wing.

Practical design guidelines for the preliminary selection of the panel's dimensions are listed in Table 3.1 according to [1]. The symbols used below are illustrated in Figure 3.2. For a stiffened panel of length L and width s: b_f, t_f are the width and thickness of the stringer flange; b_a, t_a are the width and thickness of the skin flange and b_w, t_w are the height and thickness of the stringer respectively. The spacing of the stringers is b and the thickness of the skin is t. The area of the stringer and skin are calculated by equations (3.1). The ratio of the area of the stringer to the skin is called stiffening ratio.

$$A_{skin} = b \times t$$
$$A_{stringer} = b_f \times t_f + b_a \times t_a + (b_w - t_f - t_a) \times t_w \qquad (3.1)$$

Table 3.1 Recommended dimensions for the design of a stringer panel.

PARAMETER	$\frac{b_a}{t_a}$	$\frac{b_w}{t_w}$	$\frac{b_f}{t_f}$	$\frac{A_{stringer}}{A_{skin}}$	t_a	$\frac{b_f}{b_w}$
Design Guidance	≤ 10	18 - 22	6 - 8	≥ 0.5	0.7t	0.4

Additional guidelines for the preliminary sizing [1]:

- Use stiffening ratio $\frac{A_{stringer}}{A_{skin}} \geq 0.5$, a stiffening ratio less than 0.5 should not be used because of the panel damage tolerance considerations.
- $\frac{b_w}{t_a} < 10$
- Set $t_a \geq 0.7t$ (to prevent forced crippling)
- Set $\frac{b_f}{b_w} = 0.4$ to 0.5 (to prevent rolling of the stringer)

According to Airbus design [30], a good starting point for the stiffening ratio is given below for the tension and compression wing skin stiffened panel:

- Wing – tension skin stiffened panel ratio $\frac{A_{stringer}}{A_{skin}} = 0.65$
- Wing – compression skin stiffened panel ratio $\frac{A_{stringer}}{A_{skin}} = 0.8$

Although the two last stiffening ratios do not give the optimum values, it is a good starting point for the preliminary design. Initially, a three-stringer panel was designed as this was considered as good choice for fatigue testing. All the previous general guidelines are applied to both compression and tension stiffened panels. The geometry of the panel is shown in Figure 3.2.

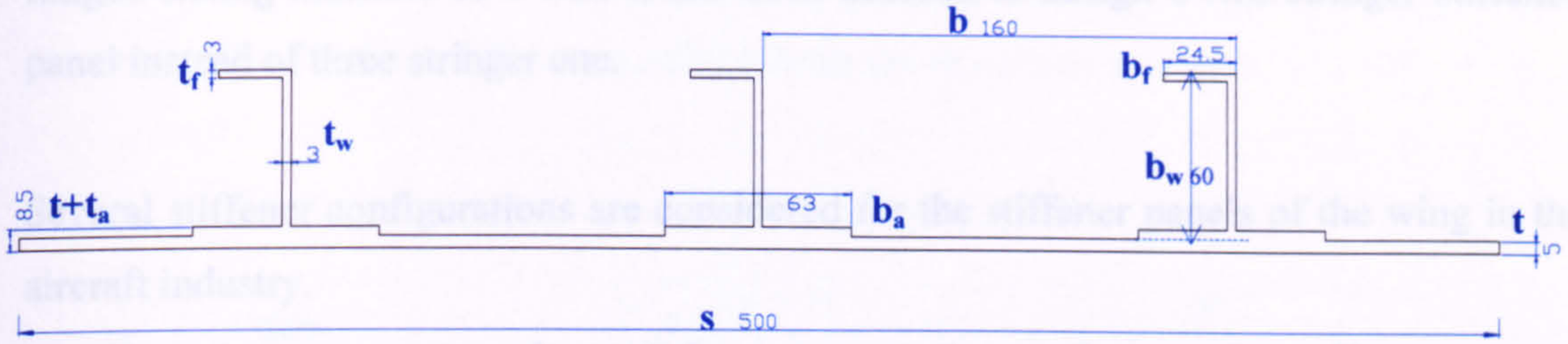

Figure 3.2 The dimensions of cross-section for the initial design.

The following table shows a comparison between the suggested/preliminary design and guidelines [1,30,31].

Table 3.2 Comparison of the initial three-stringer panel design to the guidelines.

	$\frac{b_a}{t_a}$	$\frac{b_w}{t_w}$	$\frac{b_f}{t_f}$	$\frac{A_{stringer}}{A_{skin}}$	t_a (mm)	$\frac{b_f}{b_w}$
Guidelines	≤ 10	18 - 22	6 - 8	0.5	0.7t	0.4
Suggested	9	20	7.67	0.557	3	0.383

One of the most important reasons for having a pad – doubler at the connection of the stringer to the skin is that the centroid of the section should be as close to the skin as possible for maximum centroidal depth of the wing box and minimum panel eccentricity [1]. Another reason is that the pad at the base of the stringer minimizes the possibility of skin cracks in this area.

The position of the neutral axis of the three stringer skin panel is:

$\tilde{y}$ = **11.4mm** **and** $\tilde{x}$ = **250mm**

Within this project some additional limitations were added to the design of the welded stiffened panel. The maximum thickness of the welded web of the stiffener should be 7 mm. This is due to the restrictions from the welding group in Cranfield University that would assemble and weld the wing panels. In addition, due to the load capacity of the

fatigue-testing machine of 1 MN it has been decided to design a two stringer stiffened panel instead of three stringer one.

Several stiffener configurations are considered for the stiffener panels of the wing in the aircraft industry.

- **Z-sections** are commonly used for a compression surface as they offer very good efficiency combined with ease of manufacture. They can be extruded or formed from sheet and they provide good access for attachment to the skin and for cleating to the ribs. The disadvantage of the Z-section is that they are prone to torsional buckling and peeling.
- **Hat-sections** are less efficient than Z-sections but due to their symmetry they are less prone to peeling. They provide a large "bond" area, and are easy to manufacture as they are formed in sheet or extrusions, and they can also serve as fuel vents. The negative aspects of hat sections are that they are prone to corrosion and they reduce the volume of the fuel tank.
- **I-sections** possess better torsional rigidity than Z-sections along with an increased bond area but are more difficult to manufacture and cleat to the ribs.
- **J-sections** although un-symmetric, they offer improved resistance to peeling and torsion over Z-sections, are easier to cleat to ribs than I-sections, and do not result in the fuel loss and corrosion problems caused by hat-sections.

3.2 Welding Design of Stiffened Panels

In conventional fabrication practice, the stringers are extruded from thick plates of the desirable aluminium alloy and then they are machined and heat-treated to achieve the final shape and properties. Replacement of rivets with welding of the upper/lower stringer flanges or stringer web could introduce some advantages. A saving of 65%-75% of the total wing fasteners that are used to join the stringers to the skin could be achieved [4]. The replacement of mechanical fastening with welding could lead to considerable cost saving as well as some weight savings. Three different skin-stringer assemblies were

proposed and studied. These are shown in Figure 3.3. Some considerations in terms of fabrication for the three different configurations are discussed below.

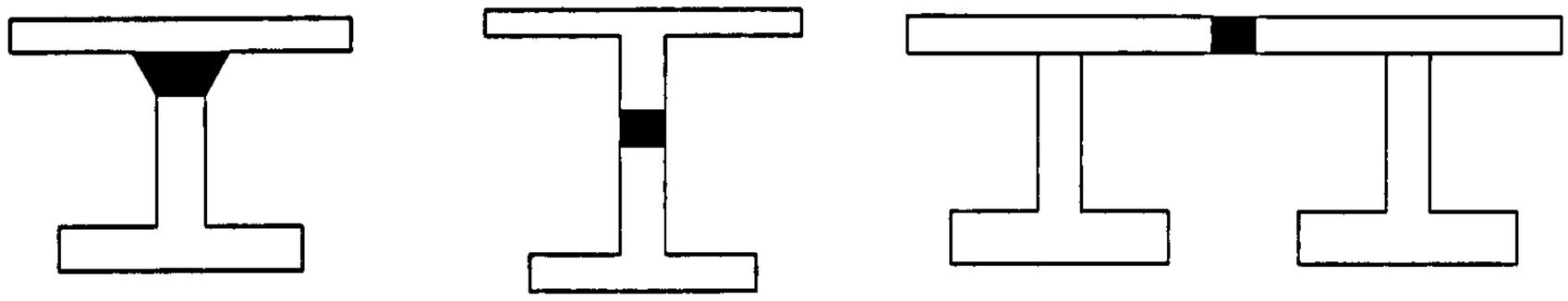

(a) Fillet weld (b) Butt weld (c) Stringer-Skin Assembly

Figure 3.3 Possible skin-stringer and skin-skin welded configurations.

(a) Fillet weld

Using this design, the skin and stringers could be manufactured according to the standard method with no new fabrication method required. A fillet weld is then used to join the two components.

(b) Butt weld

The skin and part of the stringer are either extruded or machined, and the remaining stringer web is extruded. Then the two components are joined with a butt weld. If the skin stringer integral part is machined, extra material will be wasted. Therefore, extrusion might be suitable for this kind of assembly. However, these considerations are strongly dependent on wing location. At the root the thickness and the stringer height might not allow the use of extrusion, since there are fabrication limitations to the geometry of the section, which can be extruded. Also, the stringer cross-section needs to be tapered spanwise in order to match bending moment requirements.

(c) Stringer-Skin assembly weld

Skin-stringer assemblies are extruded, then they are joined with a butt weld and the assembly will be tapered to take into account the spanwise and chordwise change of thickness. Geometry changes might be needed in order to satisfy structural requirements.

This should be accomplished without increasing the wing weight. Then the skin stringer assembly will be joined to the rest of the structure by the conventional fastener method. Taking into account stringer height and section, skin-stringer assemblies cannot be machined without a considerable waste of material. The limitation of the described joining method is the restriction imposed by the extrusion method on the component dimensions. This is due to the maximum volume of material, which is possible to extrude. The maximum allowable extrusion geometry must be assessed, since it affects the wing location and applicability of such a configuration.

Also some considerations in terms of structural behaviour for the three different configurations should be noted.

(a) Fillet weld

The weld is placed in a high stress concentration area, due to the fact that the outer fibres are subjected to the highest bending stress. This may be acceptable for welds with properties similar to those of the parent plate. The outer fibres are located at the maximum distance from the neutral axis of the section where the bending stress reaches the maximum value for a given geometry and load.

(b) Butt weld

This is the best solution, since the weld can be placed closer to the neutral-axis of the wing-box, therefore away from the high stress concentration areas.

(c) Stringer-Skin assembly weld

The weld is placed at the outer fibres, which are subjected to the highest bending stress. However, the skin is mainly designed to resist shear stress and not bending stress, which is also resisted by the stringers. This function of the structure makes the configuration feasible.

In terms of damage tolerance:

(a) Fillet weld

This is prone to early crack initiation since it is located in a high stress concentration zone. Inspection of the weld line would be difficult, but cracks would emerge on the surface before the stringer had failed.

(b) Butt weld

Crack resistance is better than the previous configuration, but inspection is very difficult, and the stringer would have failed by the time the crack emerged on the surface.

(c) Stringer-Skin assembly weld

This design is more damage tolerant than the two previous configurations, due to the easier inspectability and weld location, which is placed in a low stress area. Stringers would be the last items to fail due to cracking from the weld line.

Taking into account the previous statements configuration (b), butt weld, is selected for this study. Configuration (c) Stringer-skin assembly weld is the best in terms of inspectability and requires fewer weld lines compared with the configurations (a) and (b). However, a major drawback in terms of fabrication is the considerable waste of material. Configuration (a) is not selected because it is prone to crack initiation with the weld being located in a stress concentration site.

Overall, it is important to be stated at this point that the final decision of the weld location was taken after extensive discussion and feedback between the partners of the WELDES consortium. Manufacturing restrictions in the welding department at Cranfield University also played an important role for exact location of the weld on the final product. An effort to keep the weld as near as possible to the neutral axis of the section was made in order to avoid any additional stresses on the section due to bending in the welded wing panel of an aircraft.

3.3 Design of the Tension (Lower) Stiffened Panel

Due to the various limitations in fabrication and testing facilities described earlier in section 3.1, a two-stringer panel has been designed. The weld was located on the stringer web. The thickness of the web was selected to be 7 mm. This was the maximum thickness that could be welded with the available equipment in Cranfield University at the time. Taking into account this input the modified stiffened panel geometry of the tension stiffened panel is described in this section and the upper panel design is described in the next section.

I-section stringers were chosen for the tension panel because this is typically used by Airbus and judged to be of a great interest within the consortium. Figure 3.4 illustrates the cross section of the two-stringer lower stiffened panel. Based on the design guidelines in section 3.1 Table 3.3 is produced in order to compare the selected geometry of the wing tension panel. Failure to meet each of the generic design requirements is caused due to the fabrication limitations within this project. In general, based on Table 3.1, can be said that the selected geometry of the tension panel is defined near the suggested ratios.

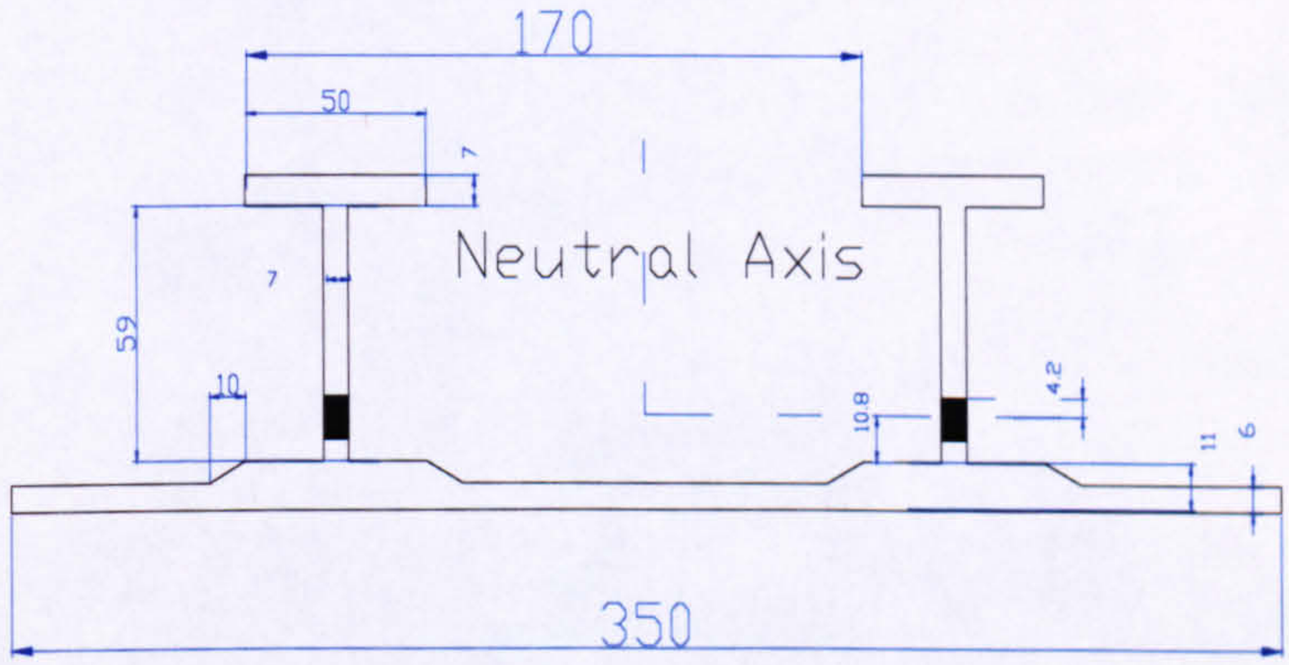

Figure 3.4 Dimensions of the cross-section of the tension panel.

Table 3.3 Final two-stringer wing tension panel and design guidelines.

	$\frac{b_a}{t_a}$	$\frac{b_w}{t_w}$	$\frac{b_f}{t_f}$	$\frac{A_{stringer}}{A_{skin}}$	t_a (mm)	$\frac{b_f}{b_w}$
Guidelines	≤ 10	18 - 22	6 - 8	0.5	0.7t=4.2	0.4
Suggested	10	10	7.1	1.04	5	0.7

3.4 Design of the Compression (Upper) Stiffened Panel

The geometry of the lower wing panel is illustrated in Figure 3.5. Table 3.4 compares the compression panel design with the generic guidelines. Like in the case of the tension panel, the compression panel is defined near the suggested ratios of the generic design guidelines. Two stringer geometries were considered for the compression panel, J-section and Z-section. The buckling analysis for both configurations is given in the next section. The J-stringer was selected due to the advantages described in section 3.1 and the fact that these were commonly used by Airbus, which was strongly involved in this research project.

Table 3.4 Final two-stringer wing compression panel and design guidelines.

	$\frac{b_a}{t_a}$	$\frac{b_w}{t_w}$	$\frac{b_f}{t_f}$	$\frac{A_{stringer}}{A_{skin}}$	t_a (mm)	$\frac{b_f}{b_w}$
Guidelines	≤ 10	18 - 22	6 - 8	0.5	0.7t=4.2	0.4
Suggested	10	4.1	7.1	1.04	5	0.7

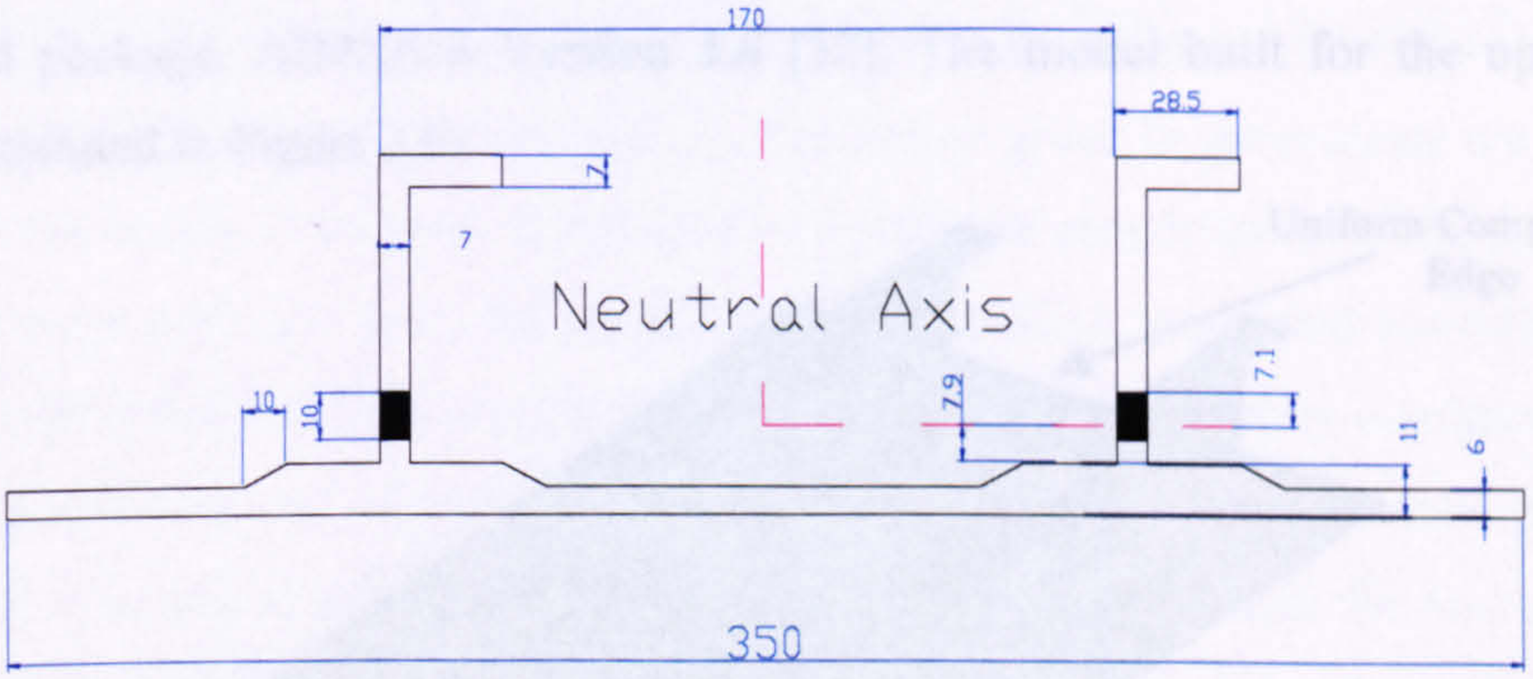

Figure 3.5 Dimensions of the cross-section of the compression skin panel.

3.5 Buckling Analysis of the Compression Stiffened Panel

For the compression stiffened panel the main design criterion is buckling. As stated in section 3.1 no other loading was considered apart from the compression due to bending moments on the wing. In practice, the upper compression panel is also investigated under tension loads due to reverse bending. Reverse bending occurs on the wing during landing or taxi conditions of the aircraft. However, since this is a preliminary design only the main buckling criterion is considered. In addition, within this project the main and only concern for the compression panel was to confirm that it will not buckle under the maximum capacity of the fatigue test machine (1MN).

Two cross-section shapes are considered for the stringers, the J-section and Z-section. The advantages and the limitations have been discussed in section 3.1 as a part of the most popular used geometries of the stiffened wing panels in aircraft industry. The critical buckling load for both configurations was well above the maximum capacity of the fatigue test machine. The J-section stringer panel exhibits a higher critical buckling load and was therefore the safest option.

Buckling analysis was performed by finite element analysis technique using a commercial package, ABAQUS Version 5.8 [32]. The model built for the upper skin panel is illustrated in Figure 3.6.

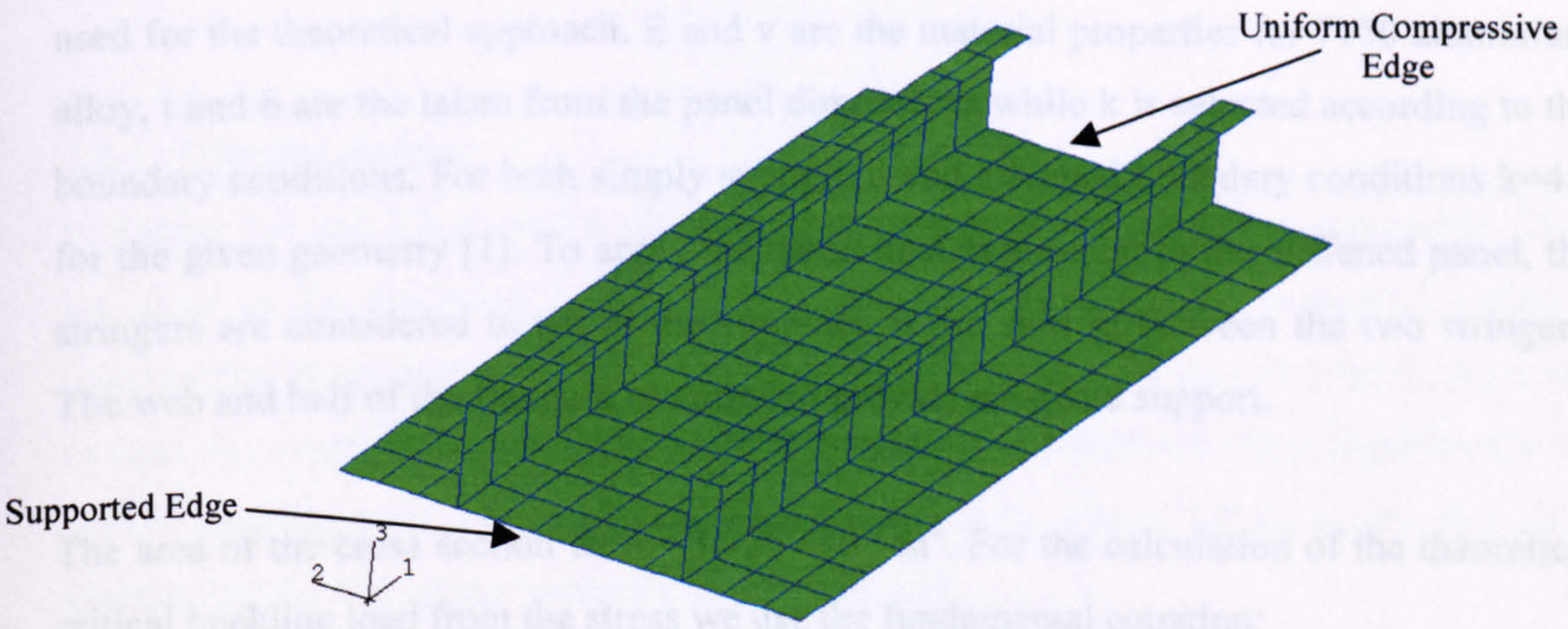

Figure 3.6 Finite element model of the compression skin panel for buckling analysis.

The above FE model comprises of 320 9-node thin shell elements of second order and has a total of 1353 nodes. The choice of elements was based on the bucking analysis of a benchmark test of a simply supported square plate [32] in which the error for first order element and second order element was 2.15 % and 0.15 % respectively. Based on [32], no further converge FE studies are presented in this section. In general, displacements, rotations and other degree of freedoms are calculated only on the nodes of the element. At any other point in the element, displacements are obtained by interpolating from the nodal displacements. Usually, the interpolation order is determined by the number of nodes used in the element. Elements that have only nodes at their corners, such 4-noded shell element use linear interpolation and they called linear or first order elements. Elements with mid-side nodes, such 8-noded shell element use quadratic interpolation and they called quadratic or second order elements.

The theoretical critical buckling load for a simple plate is given by the following equation 3.2:

$$\sigma_{crit} = \frac{k\pi^2 E}{12\left(1-\nu^2\right)} \times \left(\frac{t}{b}\right)^2 \tag{3.2}$$

where, k is the buckling coefficient (k=4.0), E is the young modulus (E=72 GPa), t is the thickness of the skin (t= 6 mm), b is the space between the stringers (b=135 mm) and ν is the Poisson ratio (ν = 0.3) for aluminium. The values given in parenthesis are the ones used for the theoretical approach. E and v are the material properties for 7150 aluminium alloy, t and b are the taken from the panel dimensions while k is selected according to the boundary conditions. For both simply supported and clamped boundary conditions k=4.0 for the given geometry [1]. To apply the theoretical expression to the stiffened panel, the stringers are considered to act as the supports of the skin in between the two stringers. The web and half of the flange is assumed to provide adequate support.

The area of the cross section is: A= 3.925×10^{-3} m^2. For the calculation of the theoretical critical buckling load from the stress we use the fundamental equation:

$$\sigma_{cr} = \frac{P_{cr}}{A} \tag{3.3}$$

It can be seen from equation (3.2) that because of the buckling coefficient k there is a need of numerical calculation of the critical buckling load or stress. The doublers in the stringer panel provide support, which is not clearly simply supported or clamped but something between these two conditions, which affects the value of k. By using the finite element simulation we calculated the buckling critical load since there is no strict analytical solution. This is compared against the theoretical values using the two extreme boundary conditions.

One edge of the panel in the FE model was supported and on the other edge uniform compressive displacement was applied. The sum of the reaction forces of the loaded edge and the first eigenvalue were taken from the FE analysis. These were used to calculate the critical buckling load as described in the following equation:

$$P_{cr} = 1^{th} eigenvalue \times \sum \mathrm{Re}\, actionForces \tag{3.4}$$

Two FE models were built for each stringer geometry. The first had a 700 mm and the second a 1000 mm length. Three different boundary conditions were applied in each model.

3.5.1 J-Section Stringer

In Tables 3.5 and 3.6 it can be observed that the numerical values are acceptable. They are close to the analytical solution where this is known. For the numerical values a convergence study has been performed using a coarse, fine and very fine mesh. As it can be seen the length from 700 mm to 1000 mm of the panel does not affect significantly the critical buckling load. The maximum error is about 4 %. Figure 3.7 shows the first three eigenmodes for one of the boundary conditions used.

Table 3.5 Critical buckling stress results for the J-section.

	Theoretical	FE (700mm)	FE (1000mm)
Simply Supported	514MPa	515 MPa	511 MPa
Clamped	540 MPa	523 MPa	518 MPa
One End Fixed and the other Clamped	-	524 MPa	519 MPa

Table 3.6 Critical buckling load results for the J-section.

	Theoretical	FE (700mm)	FE (1000mm)
Simply Supported	2.02 MN	2.02 MN	2.00 MN
Clamped	2.12 MN	2.05 MN	2.03 MN
One End Fixed and the other Clamped	-	2.05 MN	2.04 MN

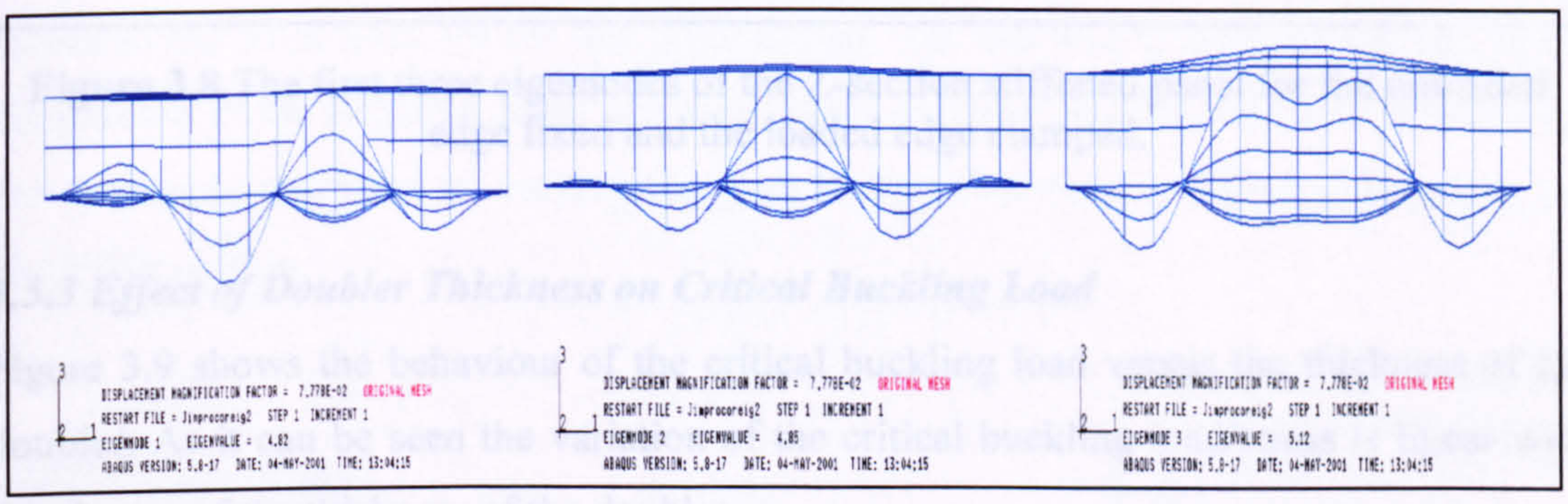

Figure 3.7 The first three eigenmodes of the J-section stiffened panel for the unloaded edge fixed and the loaded edge clamped.

3.5.2 Z-Section Stringer

Following the same procedure like in the J-stringer panel the theoretical and numerical values for the critical buckling stress and load for the Z-section panel were obtained.

Table 3.7 Critical buckling stress results for the Z-section.

	Theoretical	FE (700mm)	FE (1000mm)
Simply Supported	422 MPa	344 MPa	344 MPa
Clamped	443 MPa	360 MPa	353 MPa
One End Fixed and the other Clamped	-	363 MPa	353 MPa

Table 3.8 Critical buckling load results for the Z-section.

	Theoretical	FE (700mm)	FE (1000mm)
Simply Supported	1.54 MN	1.26 MN	1.26 MN
Clamped	1.62 MN	1.32 MN	1.29 MN
One End Fixed and the other Clamped	-	1.33 MN	1.29 MN

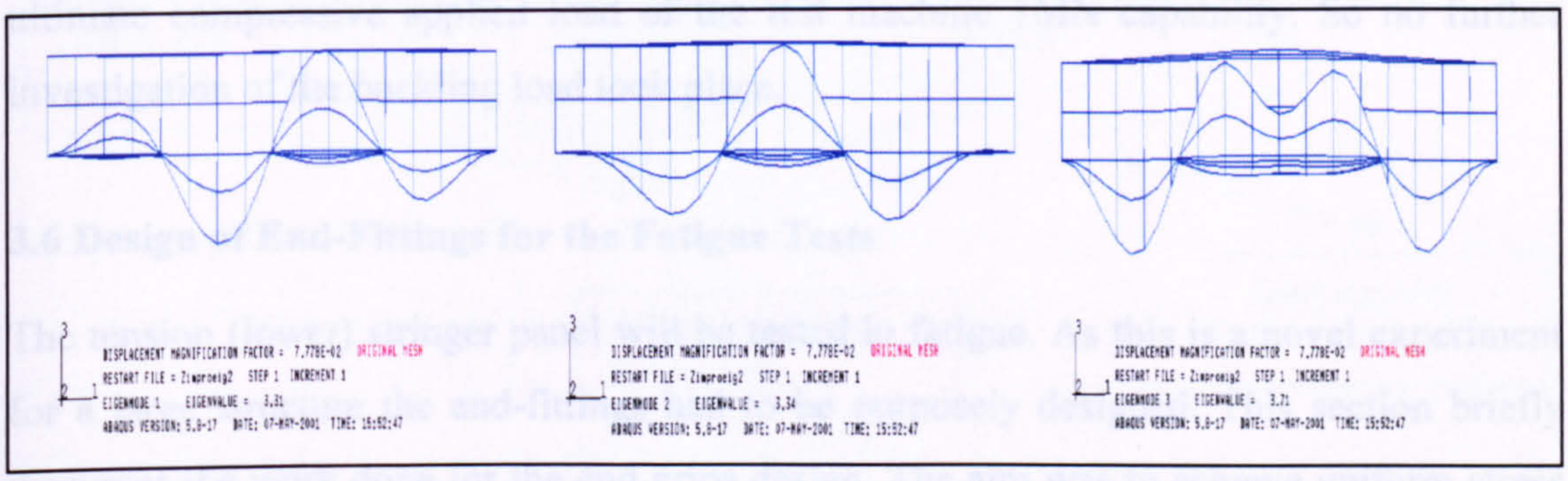

Figure 3.8 The first three eigemodes of the Z-section stiffened panel for the unloaded edge fixed and the loaded edge clamped.

3.5.3 Effect of Doubler Thickness on Critical Buckling Load

Figure 3.9 shows the behaviour of the critical buckling load versus the thickness of the doubler. As it can be seen the variation of the critical buckling load/stress is linear with the change of the thickness of the doubler.

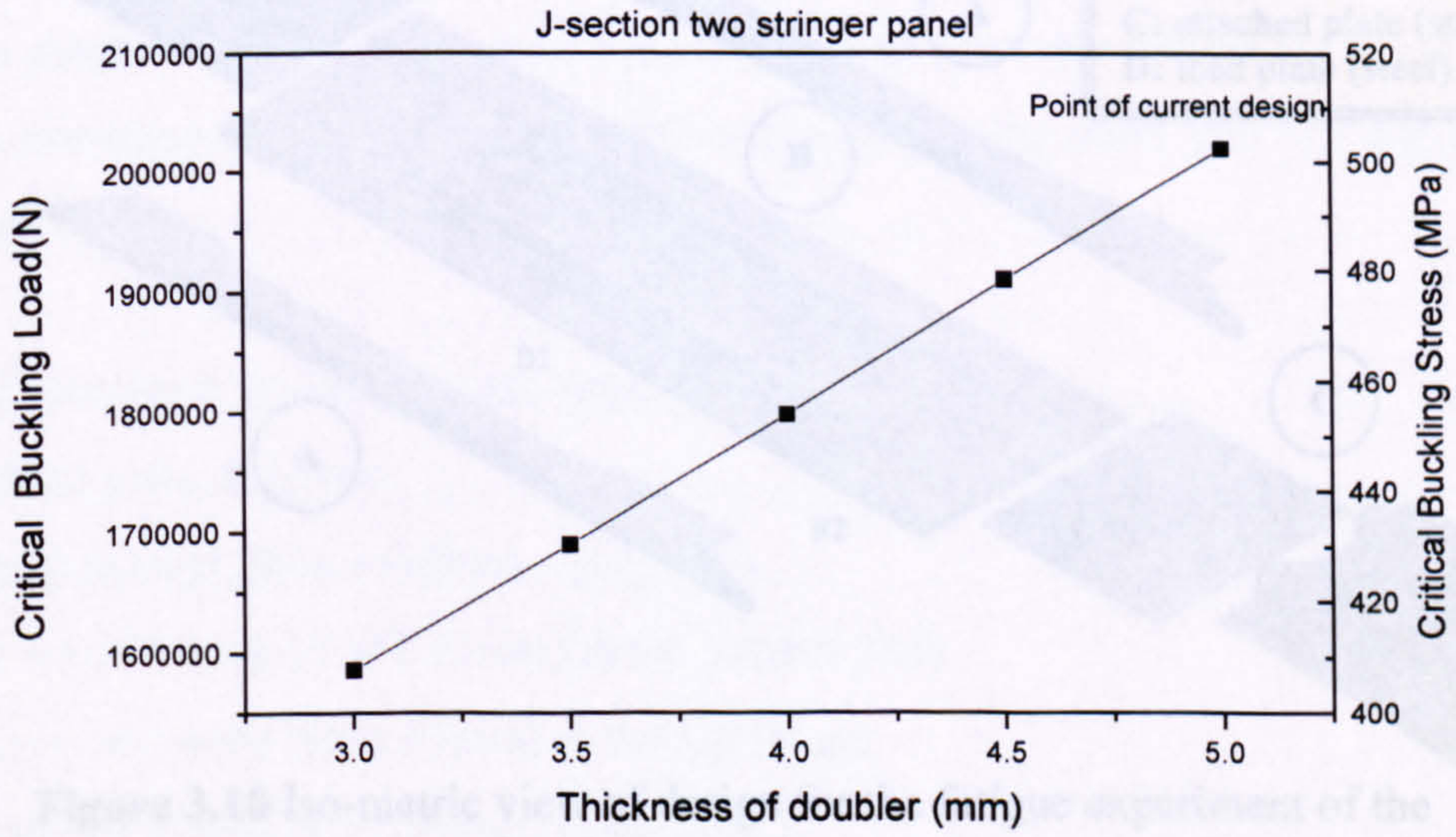

Figure 3.9 Variation of critical buckling load/stress versus the doubler thickness.

This linear relationship between the doubler's thickness and the critical buckling load/stress can not be clearly defined as linear or not and further investigation is required. Nevertheless, the expected behaviour of the increase of the critical buckling load/stress when a thicker doubler is presented has been confirmed.In this study it was enough to prove that the selected final geometry of the stiffened panel will not fail under the ultimate compressive applied load of the test machine 1MN capability. So no further investigation of the buckling load took place.

3.6 Design of End-Fittings for the Fatigue Tests

The tension (lower) stringer panel will be tested in fatigue. As this is a novel experiment for a large structure the end-fittings had to be purposely designed. This section briefly discusses the work done for the end grips design. The aim was to achieve uniform stress distribution in the stiffened panel test area. Finite element analysis was used to calculate the stresses in the panel by varying the grips design. Drawings and final dimensions are given this section.

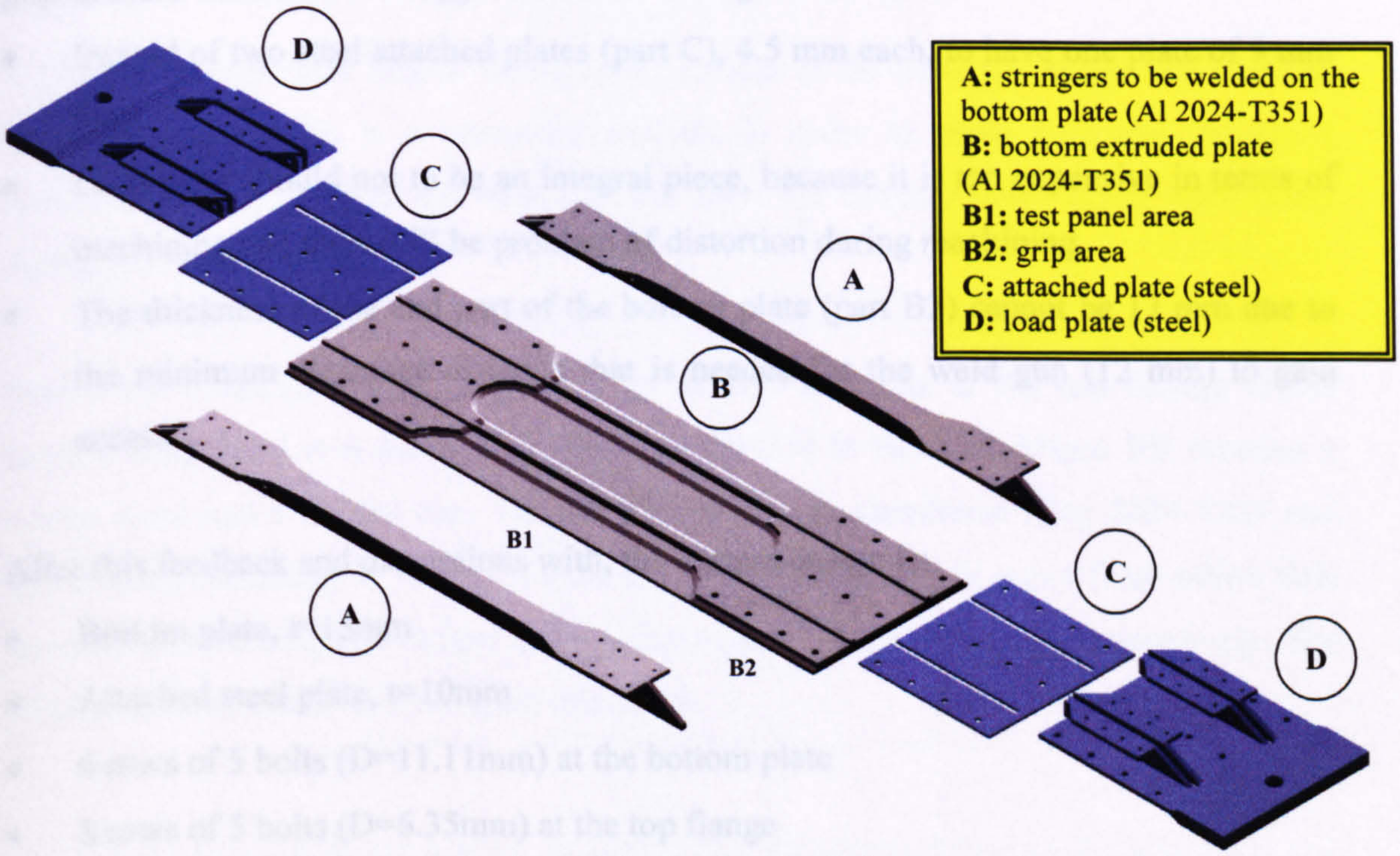

Figure 3.10 Iso-metric view of design for the fatigue experiment of the 2-stringer tension panel.

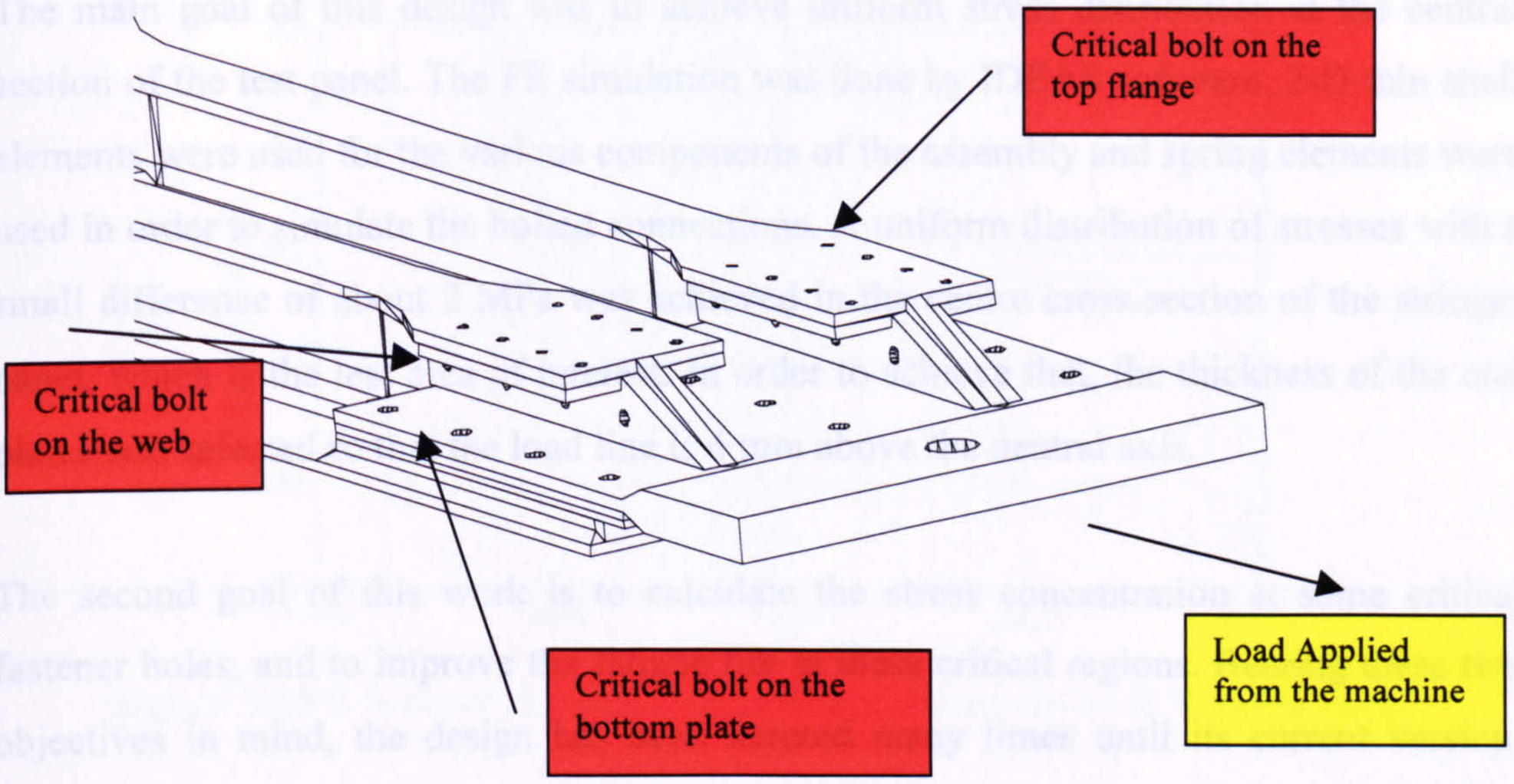

Figure 3.11 3-D View of the end fitting design and detailed bolt description.

The design shown in Figure 3.10 was submitted to Airbus. Figure 3.11 shows the end grip in more detail. Airbus suggested the following modifications.

- Instead of two steel attached plates (part C), 4.5 mm each, to have one plate of 9 mm thick.
- Load plate should not to be an integral piece, because it is too expensive in terms of machining and there will be problem of distortion during machining.
- The thickness of the end part of the bottom plate (part B2) cannot be 17 mm due to the minimum clearance distance that is needed for the weld gun (12 mm) to gain access.

After this feedback and discussions with, the current design is:

- Bottom plate, t=15mm
- Attached steel plate, t=10mm
- 6 rows of 5 bolts (D=11.11mm) at the bottom plate
- 8 rows of 5 bolts (D=6.35mm) at the top flange
- 4 rows of 6 bolts (D=7.94mm) at the web
- 8 rows of 7 bolts (D=7.94mm) at the C-section/load plate (countersunk bolts)

The main goal of this design was to achieve uniform stress distribution at the central section of the test panel. The FE simulation was done by IDEAS software. 2-D thin shell elements were used for the various components of the assembly and spring elements were used in order to simulate the bolted connections. A uniform distribution of stresses with a small difference of about 2 MPa was achieved in the centre cross section of the stringer panel, which is the test area of interest. In order to achieve that, the thickness of the end plates was selected so that the load line is 6 mm above the neutral axis.

The second goal of this work is to calculate the stress concentration at some critical fastener holes, and to improve the fatigue life at these critical regions. Bearing these two objectives in mind, the design has been iterated many times until its current version. Detailed drawings of every component in the basic three engineering standard views for manufacturing are available in appendix A.

3.7 Fatigue Analysis of Joints

A fatigue analysis (safe life) at the various locations of the bolts and at the weld line has been performed. This is a necessary analysis in order to make sure that the crack initiation site comes from the weld line not from the fastener holes at the end-fittings during the fatigue testing.

Before the investigation of fatigue life in various locations at the end-fittings of the tension wing panel it is useful to report a comparison in terms of fatigue life between a parent metal and a welded one. The material used is an aluminium alloy 2024 T351 and the welding technique is VPPA. Figure 3.12 illustrates the S-N curve from which data were obtained during this fatigue analysis for parent and weld material, respectively. The endurance limit can be derived from this graph.

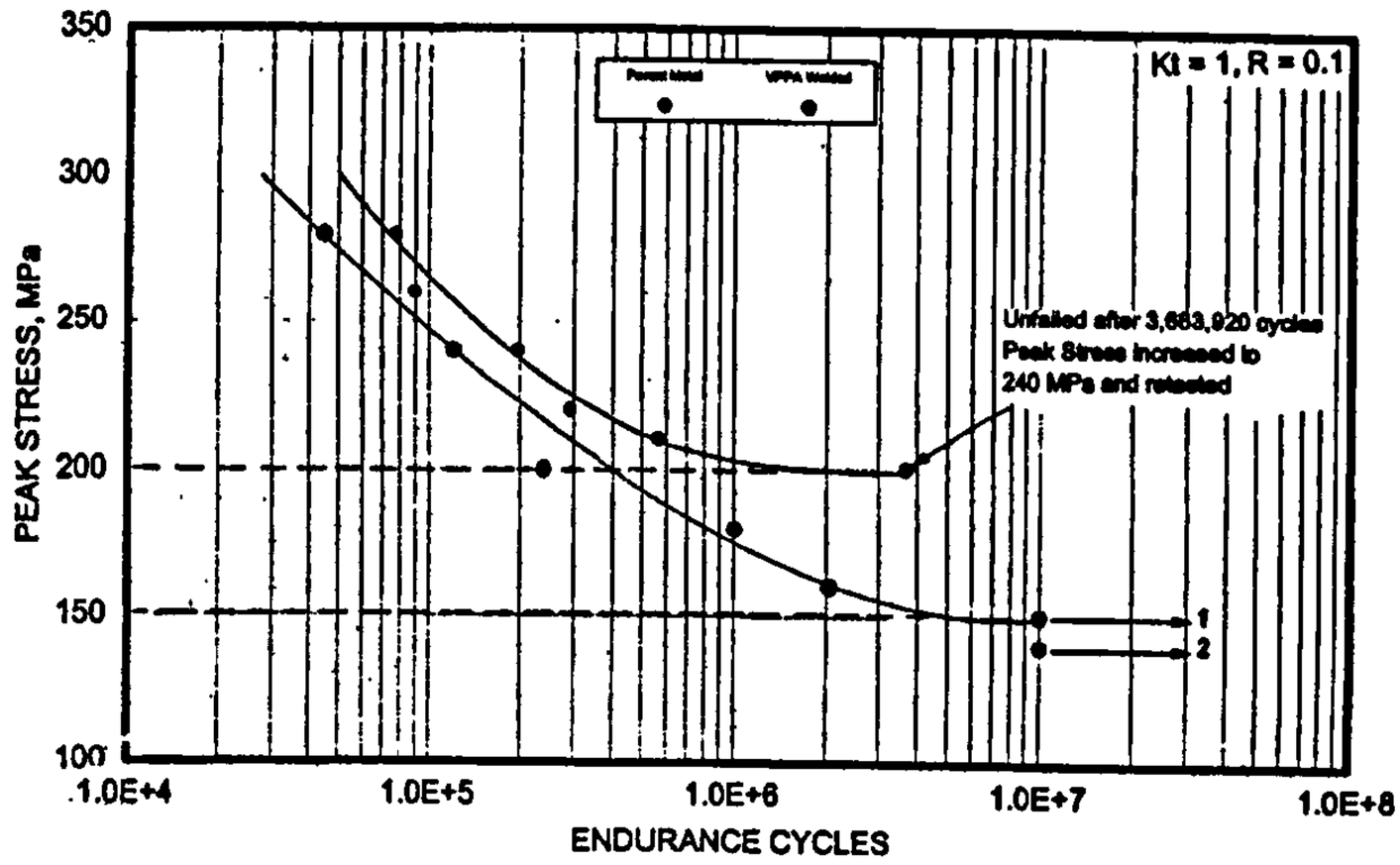

Figure 3.12 S-N curve for 2024-T351, R=0.1. Parent metal & Welded metal.

A very substantial amount of testing is required to obtain an S-N curve for the typical case of fully reversed loading (R=-1 & σ_m=0), and it will usually be impractical to determine whole families of curves for every combination of mean (σ_m) and alternating (σ_{alt}) stress, shown in Figure 3.13. There are a number of available tools in order to overcome this difficult. One common one is the Goodman's equation (3.5).

$$\frac{\sigma_a}{\sigma_{a0}} + \frac{\sigma_m}{\sigma_{ult}} = 1 \tag{3.5}$$

where σ_α, σ_m are the amplitude and mean stress for the general cyclic loading case, σ_{ult} is the static tensile strength and σ_{a0} is the stress amplitude calculated for $\sigma_m = 0$.

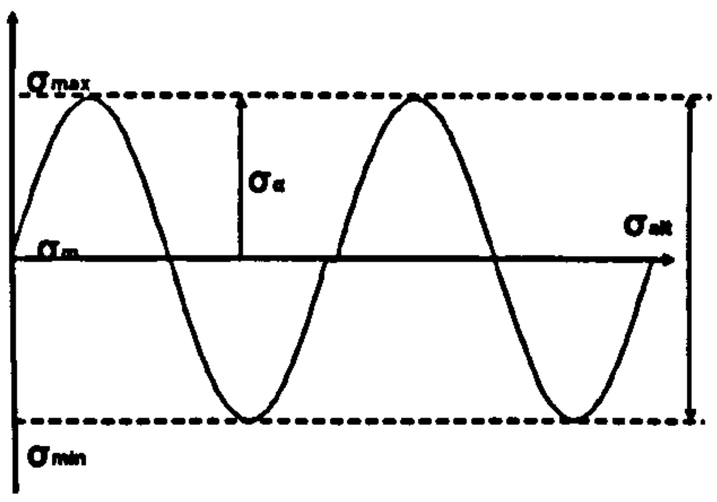

Figure 3.13 General case of cyclic loading.

Goodman's diagram is constructed in Figure 3.14 with mean stress as the horizontal axis and alternating stress as the vertical axis. Then a straight "life-line" is drawn from the

endurance limit (σ_e) on the alternating stress axis (σ_{alt}) to the ultimate tensile stress (σ_{ult}) on the mean stress axis (σ_m). Then for any given mean stress, the endurance limit – the value of alternating stress at which fatigue fracture never occurs – can be read directly as the Y-axis value of the lifeline at that value of mean stress. Alternatively, if the design application dictates a given ratio of (σ_e) to (σ_{alt}), a line is drawn from the origin with a slope equal to that ratio. Its intersection with the "life-line" gives the effective endurance limit for that combination of ultimate tensile stress (σ_{ult}) and mean stress (σ_m).

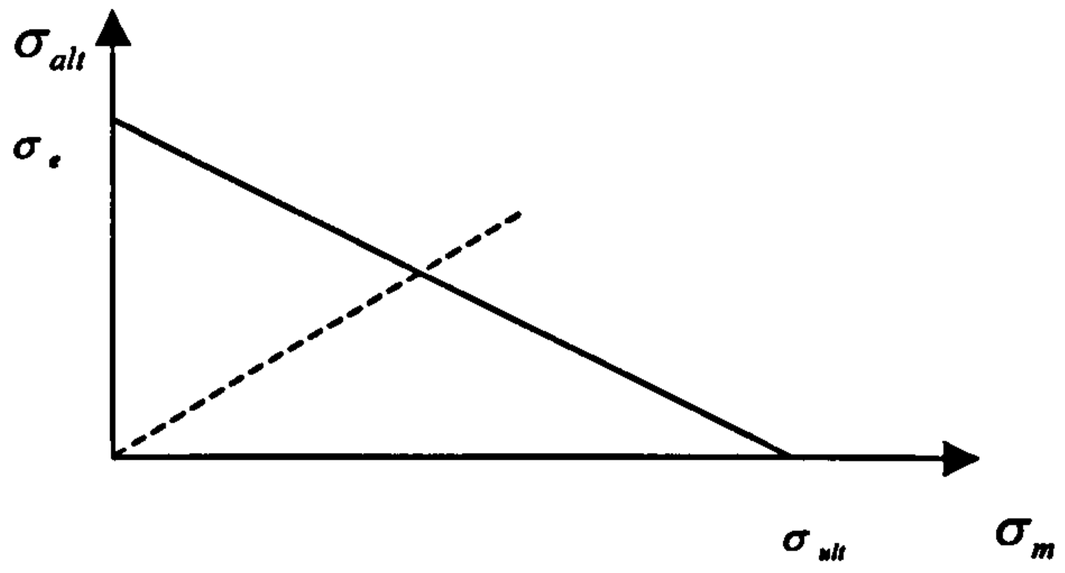

Figure 3.14 The Goodman diagram.

3.7.1 Bolts

Figure 3.15 illustrates the fastener loads on a typical bolted jointed. Local stresses caused by load transfer ΔP and local stresses caused by the bypass load P are presented in Figure 3.16. The maximum local stress is expressed in equation (3.6).

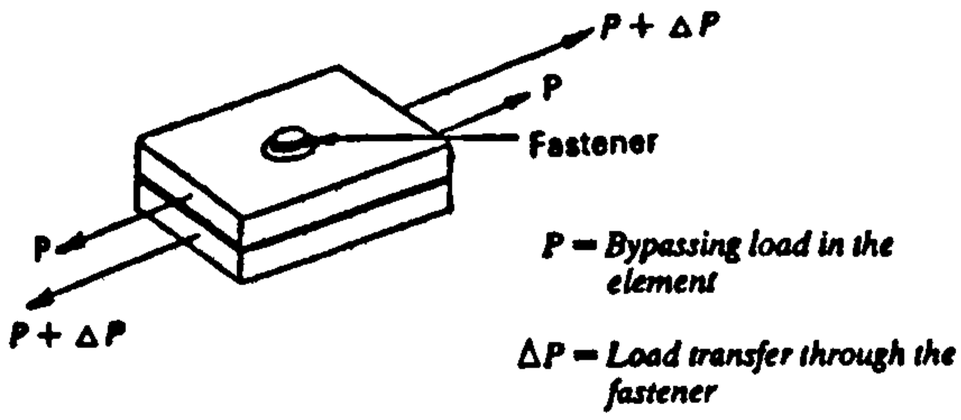

Figure 3.15 Loads in a fastener.

$$S_{max}^{local} = \left(K_{tb} \frac{\Delta P}{dt} \theta + K_{tg} \frac{P}{wt} \right) \alpha\beta \qquad (3.6)$$

where, $\frac{P}{wt}$ is the by-pass stress and $\frac{\Delta P}{dt}$ is the stress of pin load

K_{tb} : Stress concentration factor, bearing stress.

K_{tg} : Stress concentration factor, bypass gross area stress.

θ : Bearing distribution factor.

α : Hole or surface condition factor, (α=0.9 for reamed hole)

β : Hole filling factor, (β=0.75 for Hi-Lok)

For all these factors detailed diagrams [1] can be found in Appendix B.

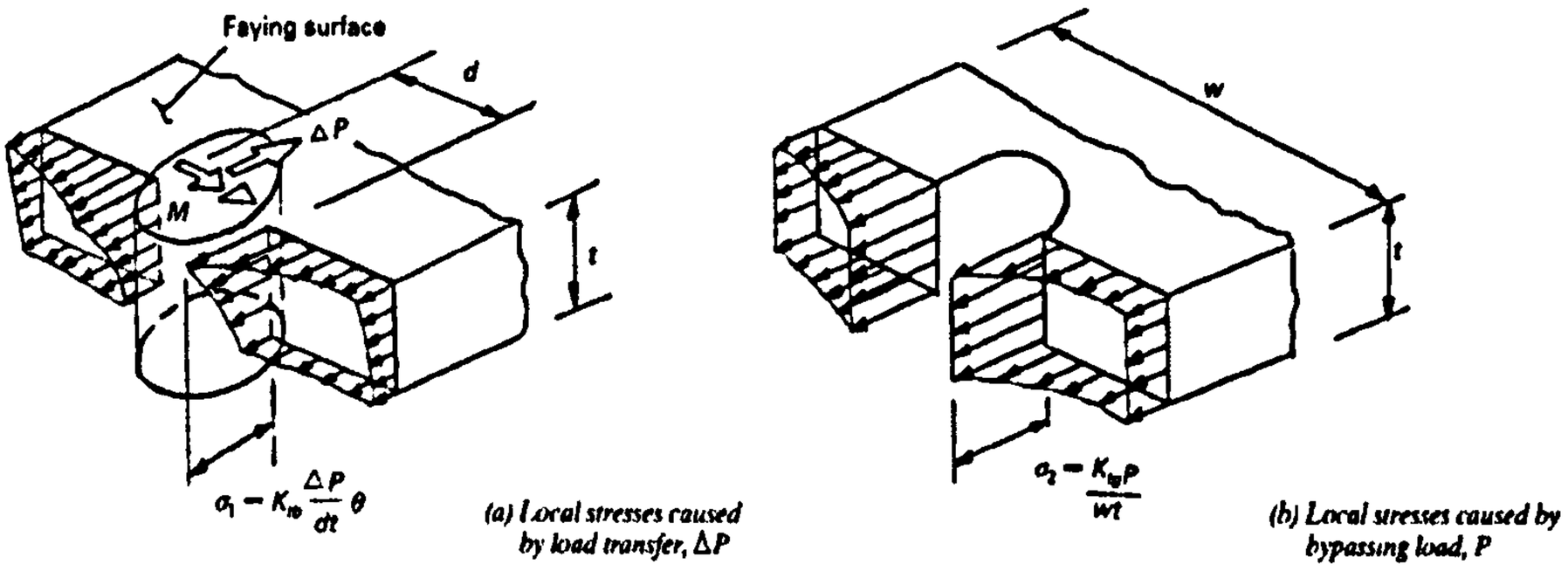

(a) Local stresses caused by load transfer, ΔP

(b) Local stresses caused by bypassing load, P

Figure 3.16 Local peak stresses caused by load transfer and by pass load [1].

The maximum local stresses around a hole are used to calculate the endurance limit of a notched panel, $\overline{\sigma}_{en}$, from the endurance limit of the parent material, σ_{en}. Firstly the stress reduction factors are calculated using the local maximum stress and by pass stress according to the following equations.

Stress intensity factor: $$K_t = \frac{\sigma_{max}}{\sigma_{min}} = \frac{S_{max}^{local}}{\sigma_{bypass}} \quad (3.7)$$

Fatigue stress index: $$K_f = 1 + q(K_t - 1),\ q=0.8 \text{ for Al alloy} \quad (3.8)$$

Endurance limit of notched specimen: $$\overline{\sigma}_{en} = \frac{\sigma_{en}}{K_f} \quad (3.9)$$

The output from the FE model in I-deas is the maximum pin load, as a force on the specific spring element, in every bolted part and the maximum by-pass stress around the same bolt-hole. The applied load in the FE model was selected to give 100 MPa at the test area of the wing panel (central cross-section, Figure 3.10). These values are given in

Table 3.9 for the three different hole locations; at the top-flange, web and bottom plate. The load and stress are used in equation 3.6 to calculate the maximum stress at the bolt hole given in Table 3.10. Then equations 3.7 to 3.9 are used to calculate the endurance limit of the notched panel.

For two cases of load ratios R the fatigue lives of the bolts in these three connections are calculated and presented in Table 3.10. The applied stress at the panel away from the hole is the by pass load. Goodman equations are used to translate the externally general cyclic applied load to amplitude stress at zero mean stress. The safety factors are finally calculated dividing the endurance limit with the applied amplitude stress. The results are presented in Table 3.10. All the values are referring to $N = 10^7$ cycles. An example of these calculations can be found in Appendix B

Comparing the safety factors in Table 3.10 it can be observed that the lowest safety factor is at the web. This indicates that the most possible site for crack initiation and eventually failure is at the bolt-holes on the web.

Table 3.9 Output from the FE analysis in I-deas.

Location	**Top-Flange 1st Hole- Aluminium plate**	**Web 1st Hole- Aluminium plate**	**Bottom Plate 1st Hole- Aluminium plate**
Pin Load (N)	4687	19330	12700
By-pass stress (MPa)	42	65	51

Table 3.10 Fatigue analysis calculations for the bolted parts.

Parameter (Unit)	Top-Flange	Web	Bottom Plate
S_{max}^{local} (MPa)	208	336	227
K_t	4.95	5.16	4.45
K_f	4.16	4.30	3.76
$\overline{\sigma}_{en}$ (MPa)	28.4	27.4	31.4
σ_{a0} (derived from R=0.5)	11.3	18.2	13.9
σ_{a0} (derived from R=0.3)	15.6	25.0	19.2
Safety Factor For R=0.3	**1.8**	**1.1**	**1.6**

3.7.2 Weld Line

The same fatigue analysis is made for the weld line. From Southampton University work within this project the following data are available:

VPPA, R=0.1 $\sigma_{ult} = 350$ MPa

N= $1.5*10^5$cycles, $\Delta\sigma = 270$ MPa, R=0.1, $\sigma_m = 165$ MPa, $\sigma_a = 135$ MPa

using Goodman's equation: $\sigma_{a0} = 255$ MPa

By extending the trend to N=10^7cycles from the curve in Figure 3.12 and with the same procedure as before for N=$1.5*10^5$cycles the values in Table 3.11 have been derived.

Table 3.11 Endurance limit for the weld line.

N (Life-cycles)	Fatigue Strength (MPa) (R=0.1)	Fatigue Strength (MPa) (R=-1.0), $\sigma_m = 0$
$1.5*10^5$	$\sigma_{max} = 300, \sigma_a = 135, \sigma_m = 165$	$\sigma_{max} = \sigma_a = 255, \sigma_m = 0$
10^7	$\sigma_{max} = 189, \sigma_a = 85, \sigma_m = 104$	$\sigma_{max} = \sigma_a = 121, \sigma_m = 0$

The safety factors for two cases of load ratios R and applied maximum load of 100 MPa are calculated.

Case 1, R=0.5: Fatigue loads: $\sigma_{max} = 100$ MPa, $\sigma_{min} = 50$ MPa

$\sigma_m = 75$ MPa, $\sigma_a = 25$ MPa

Goodman's rule predicts $\sigma_{a0} = 32$ MPa, (R=-1)

Case 2, R=0.3: Fatigue loads: $\sigma_{max} = 100$ MPa, $\sigma_{min} = 30$ MPa

$\sigma_m = 65$ MPa , $\sigma_a = 35$ MPa

Goodman's rule predicts $\sigma_{a0} = 43$ MPa, (R=-1)

Table 3.12 Comparison of fatigue strength for the two load ratios at the weld line.

Load Ratio	R=0.5	R=0.3
σ_{a0} (MPa)	32 MPa	43 MPa
Endurance Limit (N=10^7) at the weld line	121 MPa	121 MPa
Safety Factor	**3.8**	**2.8**

It can be seen in Table 3.12 that there is a safety margin of 3 to 4 for the weld and this indicates that crack will be more likely to initiate at the fasteners holes rather than at the weld line where the safety factor is lower (Table 3.10). So it might be necessary to introduce a surface flaw at the weld line in order to study the crack propagation and the behaviour of the welded assembly, which is the main objective of the WELDES project. This has lead to the decision in fatigue testing that an initial flaw should be introduced.

CHAPTER 4

FATIGUE CRACK GROWTH ANALYSIS OF WELDED CENTRE CRACK TENSION (CCT) COUPONS

4.1 Introduction

In this chapter the methodology used to analyse crack propagation in welded coupons is described. The FE model of the CCT coupon is the main tool for the comparison of the fatigue crack behaviour between the parent and the welded coupons. Furthermore, AFGROW software is used together with the output of the FE model to compare the experimental and numerical results in terms of fatigue crack growth lives of welded coupons.

4.2 Finite Element Modelling Techniques used in this Thesis

Finite element methods (FEM) have been successfully used in Fracture Mechanics analyses for several decades. A review of their use to analyse fatigue and fracture related problems can be found in [33]. Both stationary crack and crack growth under monotonic loading problems were reviewed. Numerical and analytical methods for determining the stress intensity factors, for both single and multiple crack problems, have been discussed by Shields et al [34]. The latter covered: (i) direct methods which utilize stress or displacement extrapolation techniques to estimate the stress intensity factor (SIF) at the crack tip, (ii) energy methods such as virtual crack extension and J-integral method, (iii) special singular crack-tip elements, such as the quarter-point element methods, (iv) superposition methods, and (v) boundary integral methods. A review of the existing methods for estimating crack growth direction and crack growth rate under mixed mode I

and II loading was presented by Guo et al [35]. A recent work by Solanki et al [36] demonstrates the concept of the modelling of the crack closure phenomenon induced by cyclic plasticity. In this section a brief summary of the techniques considered for the analysis is presented and their uses and limitations are discussed.

4.2.1 Crack-Tip Singularity Models.

The selection of mesh in the FE model is critical for the SIF calculation. As is shown in Figure 4.1 a fine mesh is concentrated at the crack tip and the area ahead of the crack tip. This is a standard procedure in FE fracture mechanics applications in order to provide sufficient accuracy in the stress concentration factor calculation. Figure 4.1 also illustrates in detail the quarter-point singularity elements employed near the crack tip [37,38].

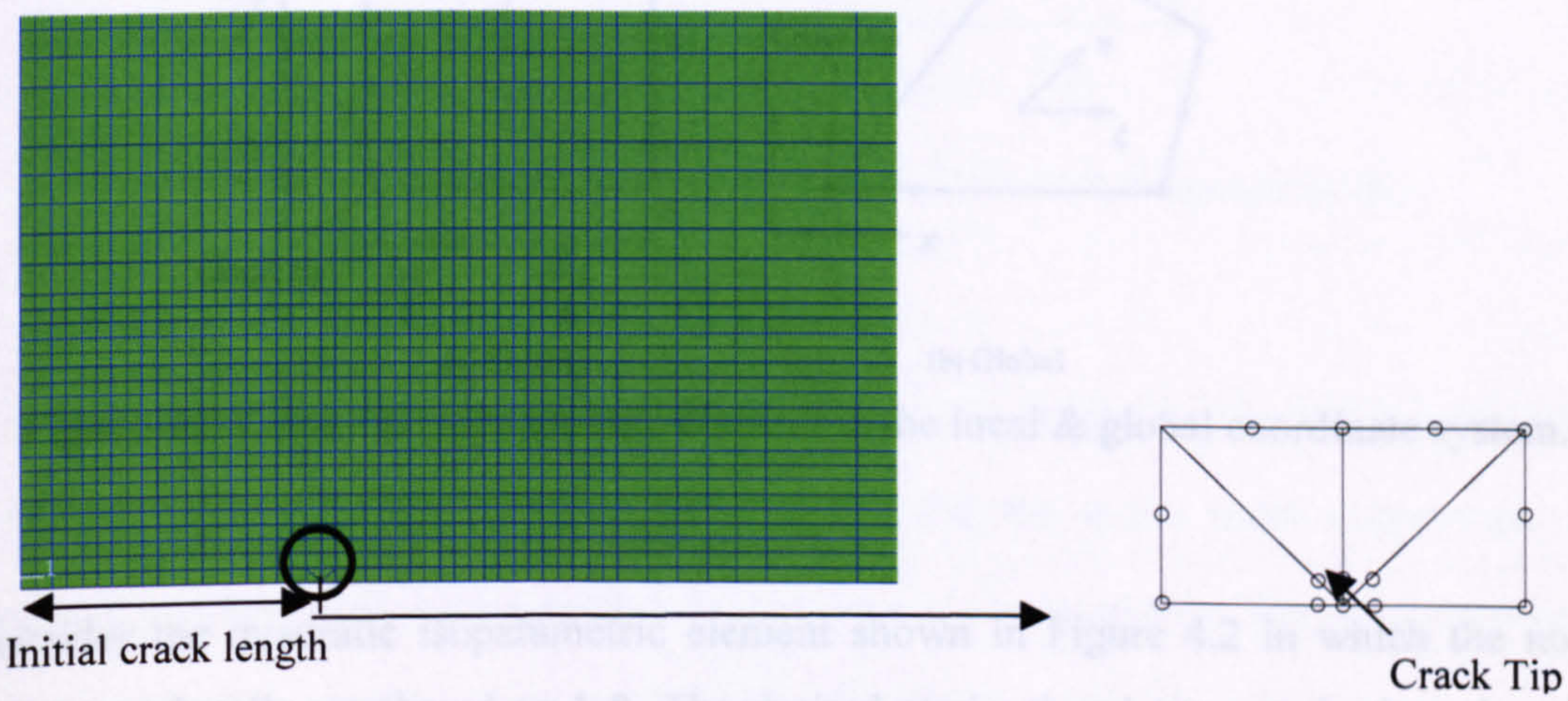

Figure 4.1 Schematic representation of the singular quarter point element.

Evaluation of the stress intensity factor was carried out using special crack tip element as illustrated in Figure 4.1. The need of using these special elements at the crack tip comes from the strain singularity term $1/\sqrt{r}$ near the crack tip. The most convenient way of introducing this strain singularity into a quadratic isoparametric element (conventional

element) is by manipulation of the mid-side node positions. The crack tip element was developed based on this approach by Barsoum [37] and Henshell and Shaw [38]. This approach was very popular in the late 1970s and 1980s when the computer ability was not as powerful as today's computers; hence larger elements would be used.

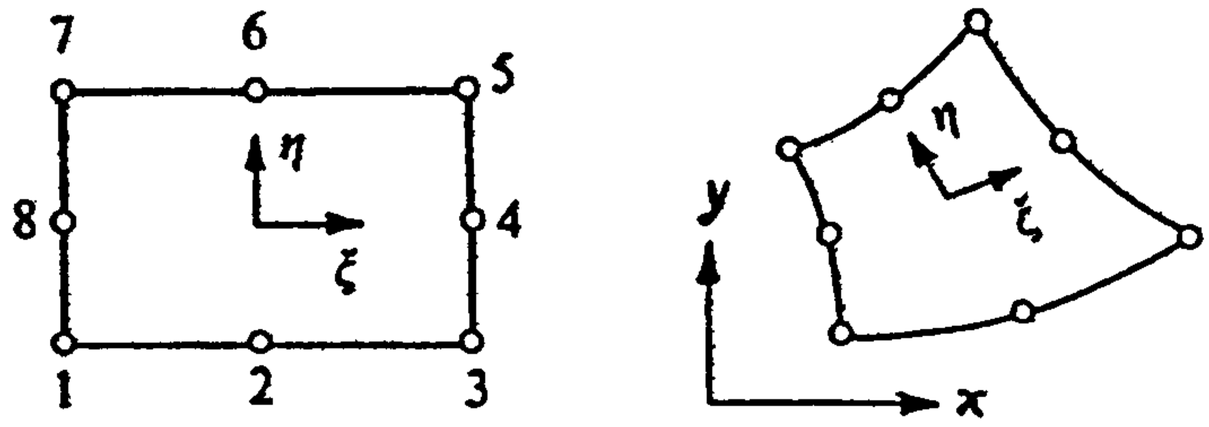

Parent element Global element

Figure 4.2 Quadratic isoparametric element in the local & global coordinate system.

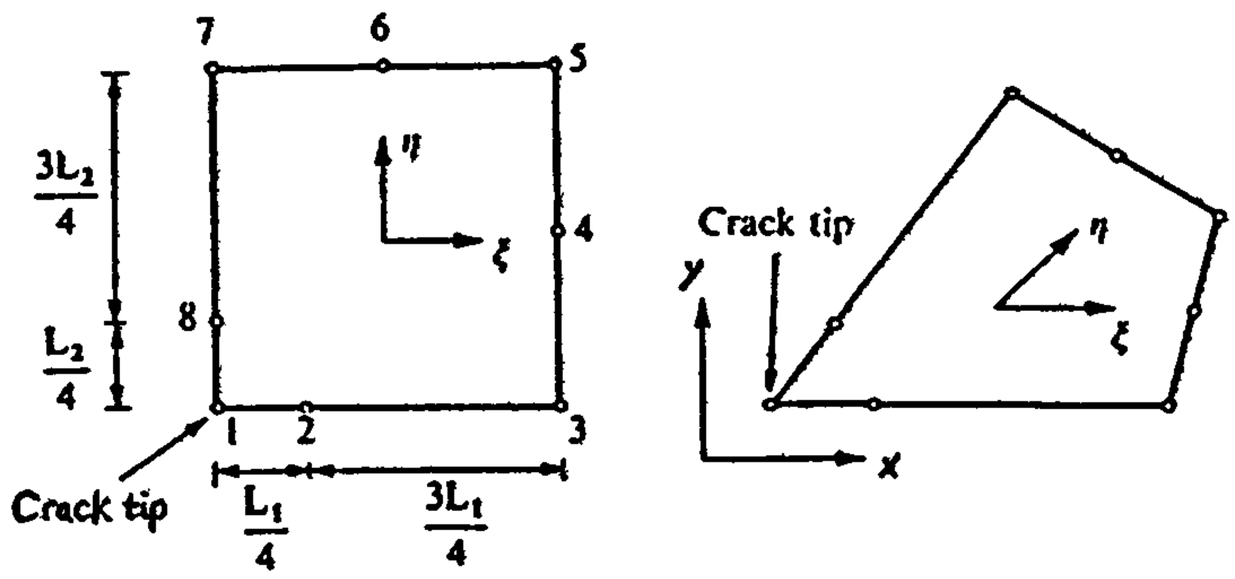

(a) Parent (b) Global

Figure 4.3 Crack-tip isoparametric element in the local & global coordinate system.

Consider the quadratic isoparametric element shown in Figure 4.2 in which the nodal points are locally numbered as 1-8. The desired strain singularity can be introduced at node 1 by moving the mid-point nodes 2 and 8 to the quarter-point positions as shown in Figure 4.3. A summary of the essential expressions employed in isoparametric formulation and the mathematics theory for shape functions of singularity elements can be found in [37,38]. It is proved that the strain singularity along edge 1-3 is of the required order $1/\sqrt{r}$ [37]. The same radial strain variation is also obtained along edge 1-7. However, along the rays within the element originating from node 1 the strain variation

is not of the form $1/\sqrt{r}$. Such a condition can be enforced by forming a triangular element by coalescing nodes 1, 7 and 8 of the quadrilateral element to give the shape shown in Figure 4.4. Once again, the mid-side nodes are moved to the quarter point adjacent to the crack tip node, which is considered to be the coalesced node, 1. The strain distribution is:

$$\varepsilon_x = \frac{1}{L_1}(2u_1 + u_3 + u_5 - 2u_2 - 2u_6) - \frac{1}{2\sqrt{L_1 x}}(3u_1 + u_3 + u_4 + u_5 - 2u_2 - 2u_6) \qquad (4.1)$$

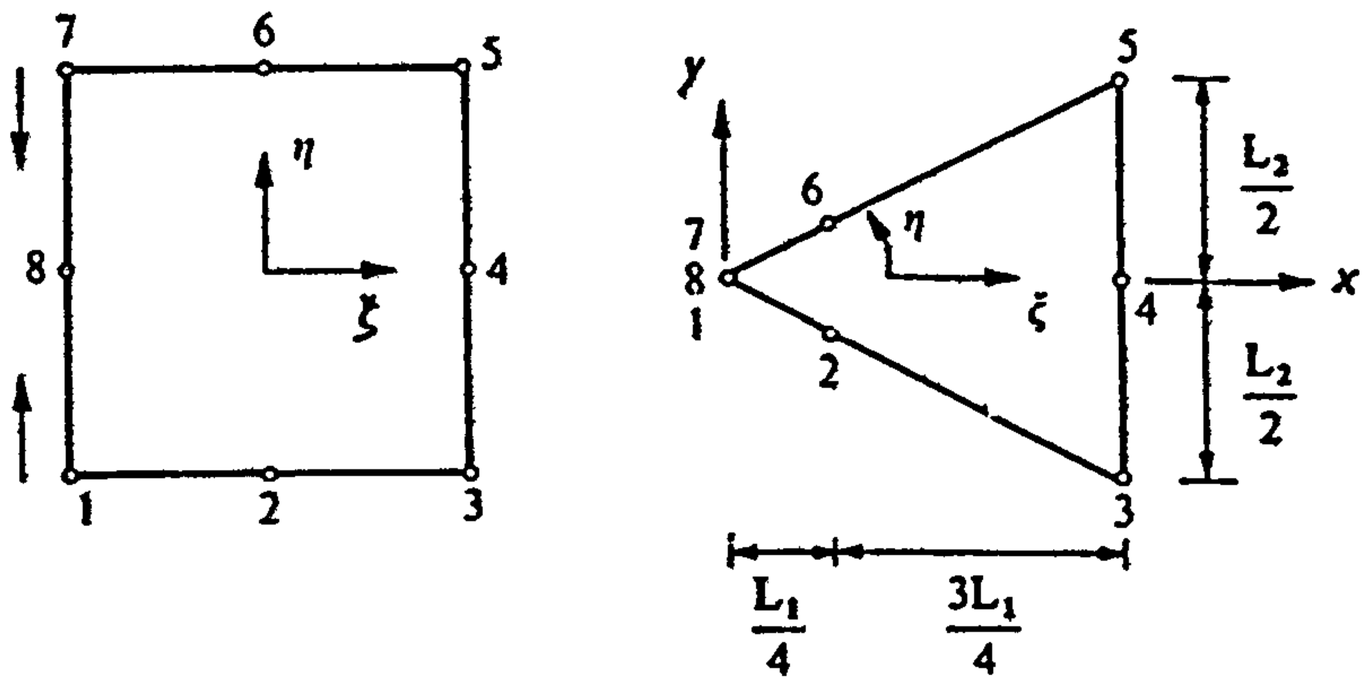

Figure 4.4 Triangular element with mid-side nodes at quarter points.

It is seen again that the strain component ε_x exhibits a $1/\sqrt{r}$ singularity (note when $\theta = 0$, $r = x$). More generally, it can be shown that the radial strain component, ε_r, along all rays originating from node 1, possesses a $1/\sqrt{r}$ singularity. This is in contrast to the quadrilateral version considered earlier in which a $1/\sqrt{r}$ strain singularity was achieved only along the element edges. The application of the above concepts has been developed since 1970s. An example is shown in Figure 4.5, in which the singular elements are at the crack tip (elements A,B,C,D) and that conventional elements (E,F,G,H) surround them.

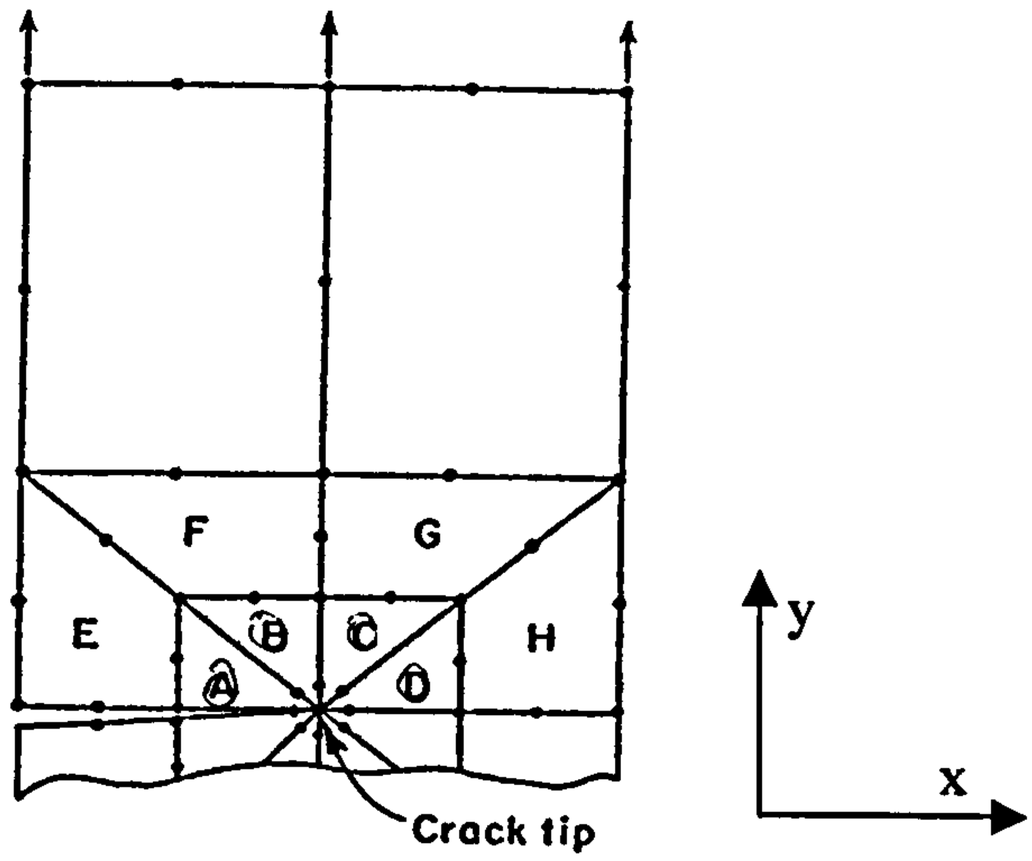

Figure 4.5 Edge-cracked plate finite element modelling with singularity elements.

4.2.2 J – Integral Method

In this study the effect of the welding residual stresses on structures is under investigation. In the case of cracked body in the elastic range the stress intensity factor (SIF) can be employed since the material response is linear and the total value of the SIF due to both the mechanical external applied load and the welding residual stresses can be obtained by superposition [20]. However, outside of linear elastic fracture mechanics (LEFM) the SIF is no longer applicable and another appropriate parameter must be used.

It is generally accepted that a proper description of elastic-plastic fracture behaviour, which usually involves stable crack growth, is not possible by means of straightforward, single parameter. Elastic-Plastic Fracture Mechanics (EPFM) can be employed. So far the only notable success of EPFM for practical applications is the ability to predict crack initiation using one or two parameters.

One of the most accepted concepts is the J-integral approach. The J-integral concept is based on an energy balance approach and it was first introduced by Rice [39]. The basic points of J-integral concept are highlighted in this paragraph.

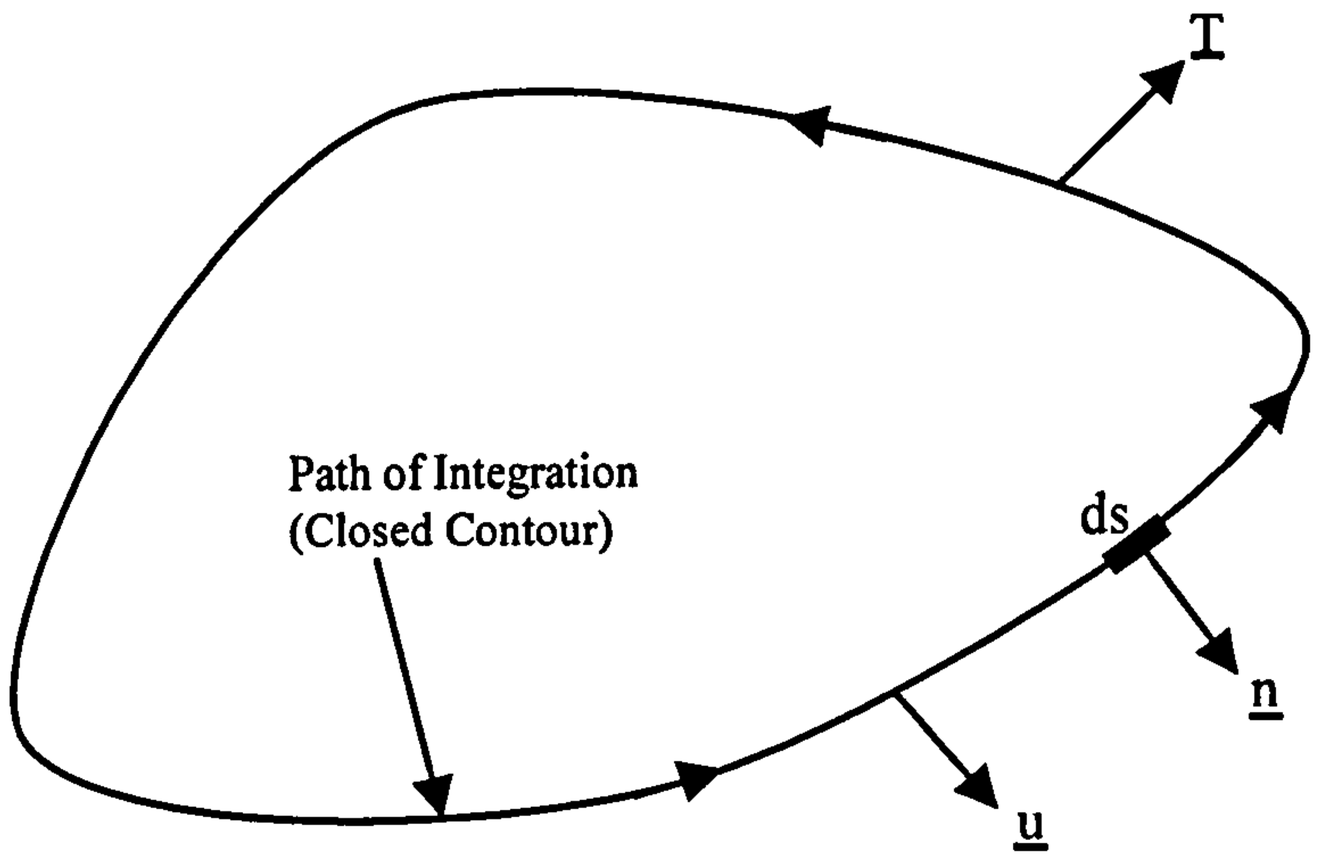

Figure 4.6 A closed contour Γ with parameters used in defining the J-integral.

The definition of the J-integral is:

$$J = \int_{\Gamma} W dy - \int_{\Gamma} T_i \frac{\partial u_i}{\partial x} ds \qquad (4.2)$$

where, W is the strain energy density, T_i and u_i are components of traction and displacement in Cartesian coordinates respectively and J is a closed contour (path of integration). Using Green's theorem it can be proved that for a closed contour as in Figure 4.6 the value of J is zero. Thus J taken along any closed contour Γ is equal to zero.

Figure 4.7 (a) shows a closed contour ABCDEF in a cracked body, which includes two parts of CD and FA of the crack lines and two paths Γ_1 and Γ_2 in opposite directions to each other. Then from the knowledge that the total value of J is zero along the closed contour ABCDEF it follows that:

$$J = J_{\Gamma_1} + J_{CD} + J_{\Gamma_2} + J_{FA} = 0$$

Along the crack lines dy=0 and the traction is zero, so T_i is zero. Thus for CD and FA the open contours J_{CD} and J_{FA} are equal to zero. Then:

$$J = J_{\Gamma_1} + J_{\Gamma_2} = 0 \text{ ; or } J_{\Gamma_1} = -J_{\Gamma_2}$$

Reversing the direction along Γ_2 results I a change of sign. This situation is shown in Figure 4.7 (b). It follows that:

$$J_{\Gamma_1} = J_{\Gamma_2} = J$$

so J integral is path independent when applied around a crack tip from one crack surface to another.

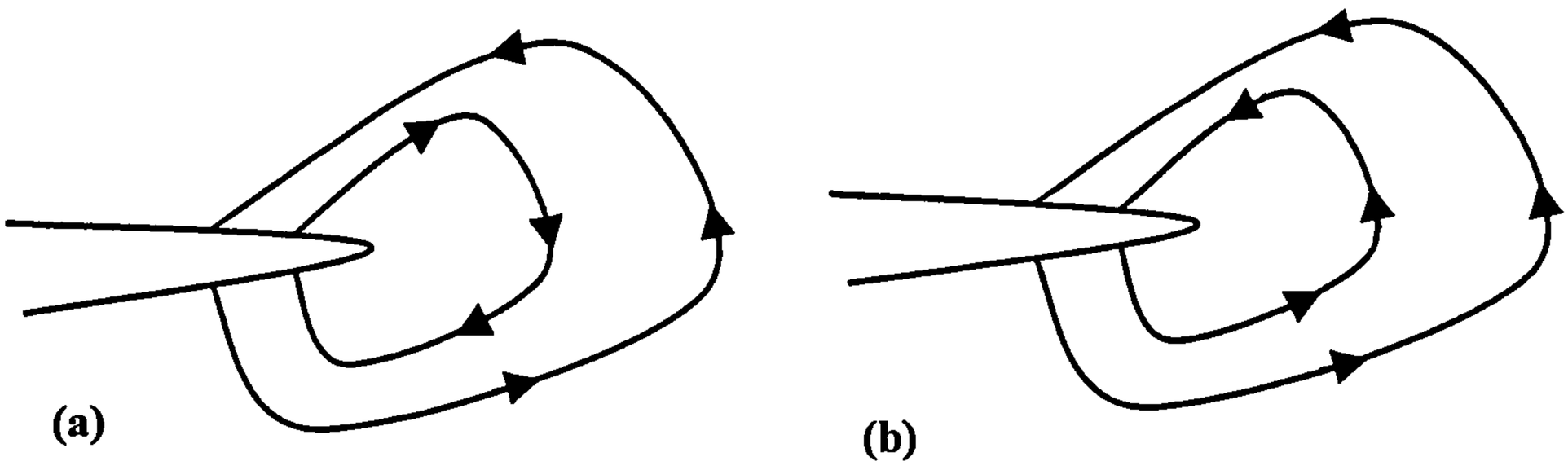

Figure 4.7 (a) A closed contour ABCDEF for a cracked body.
(b) Reversing the direction of open contour Γ_2.

The above standard definition of the J integral method results in path dependence in the case of residual stresses, due to welding in this study, and the external applied mechanical load [40]. Recent work [40,41] has shown that a path independent definition of the J integral can be obtained for the case of combined residual stress and mechanical loading. The modified J integral in small scale yielding conditions is equivalent to the stress intensity factor [40].

An investigation was performed in order to illustrate whether there is path independence or dependence in the present of welding residual stresses in Abaqus 5.8. As a benchmark for this investigation an initial FE study was done to confirm the path independence when no imposed residual stresses are present and only the mechanical external load is applied. Details of the application of the welding residual stresses and the FE model can be found in section 4.3.1 and 4.4.1 respectively.

Figure 4.8 illustrates the path-independence in the J-integral approach. It is clearly demonstrated that both singular crack tip elements and conventional elements are delivering the same accuracy and behaviour in terms of stress intensity factor. It is

important to mention at this point that the J-integral approach provides the same accuracy in terms of stress intensity factor with both singular and conventional elements.

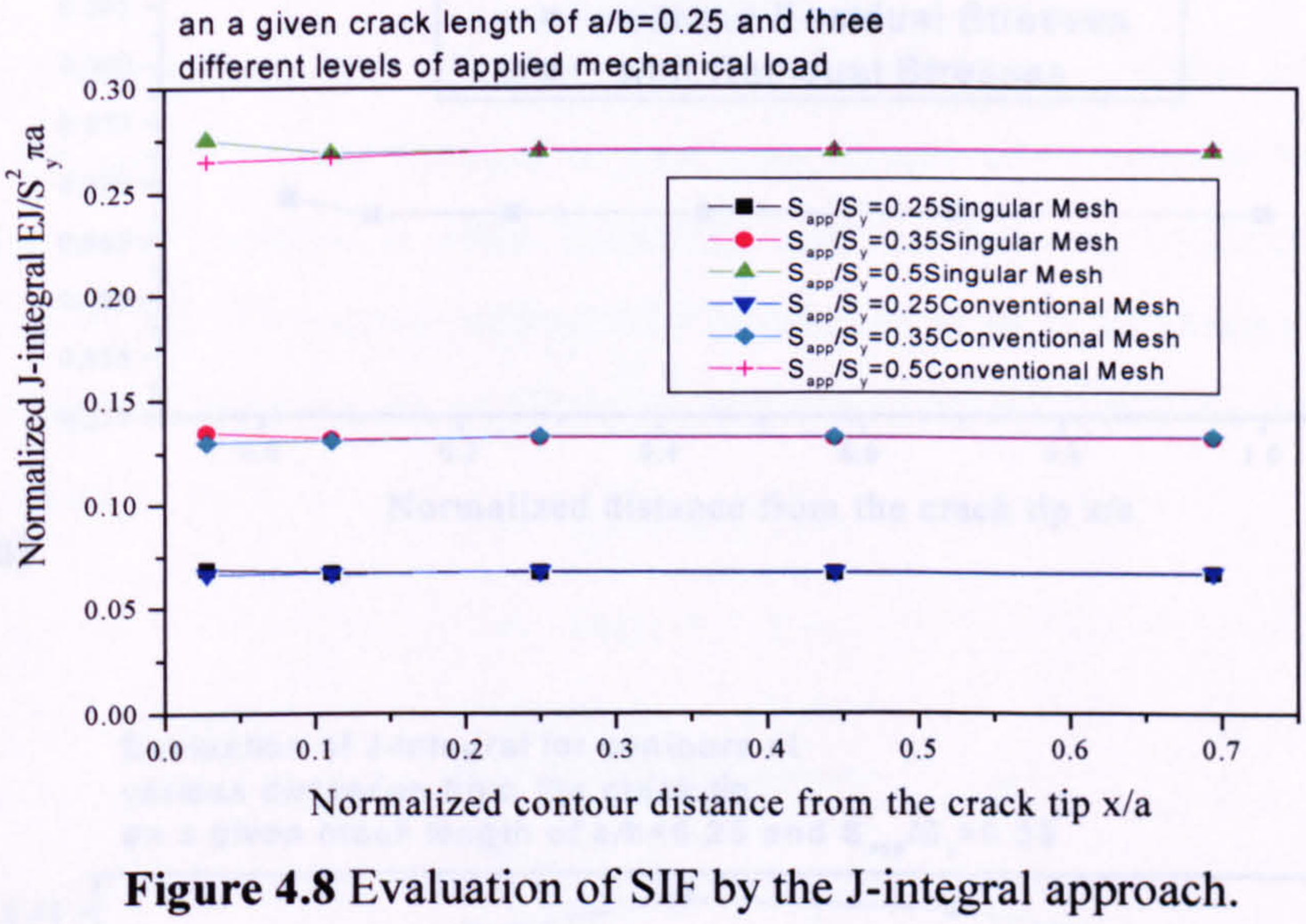

Figure 4.8 Evaluation of SIF by the J-integral approach.

Figures 4.9 (a) and (b) demonstrate a domain dependency of J-integral only within 5% for the case of "with Residual Stresses". Another study [42] has shown a path-dependence in present of compressive residual stress around cold worked holes. No further investigation was performed for the path-dependence or independence of the J-integral in present of residual stress field in this study. No solid conclusion from the findings in Figure 4.9 can be obtained and further investigation is beyond the scope of this thesis.

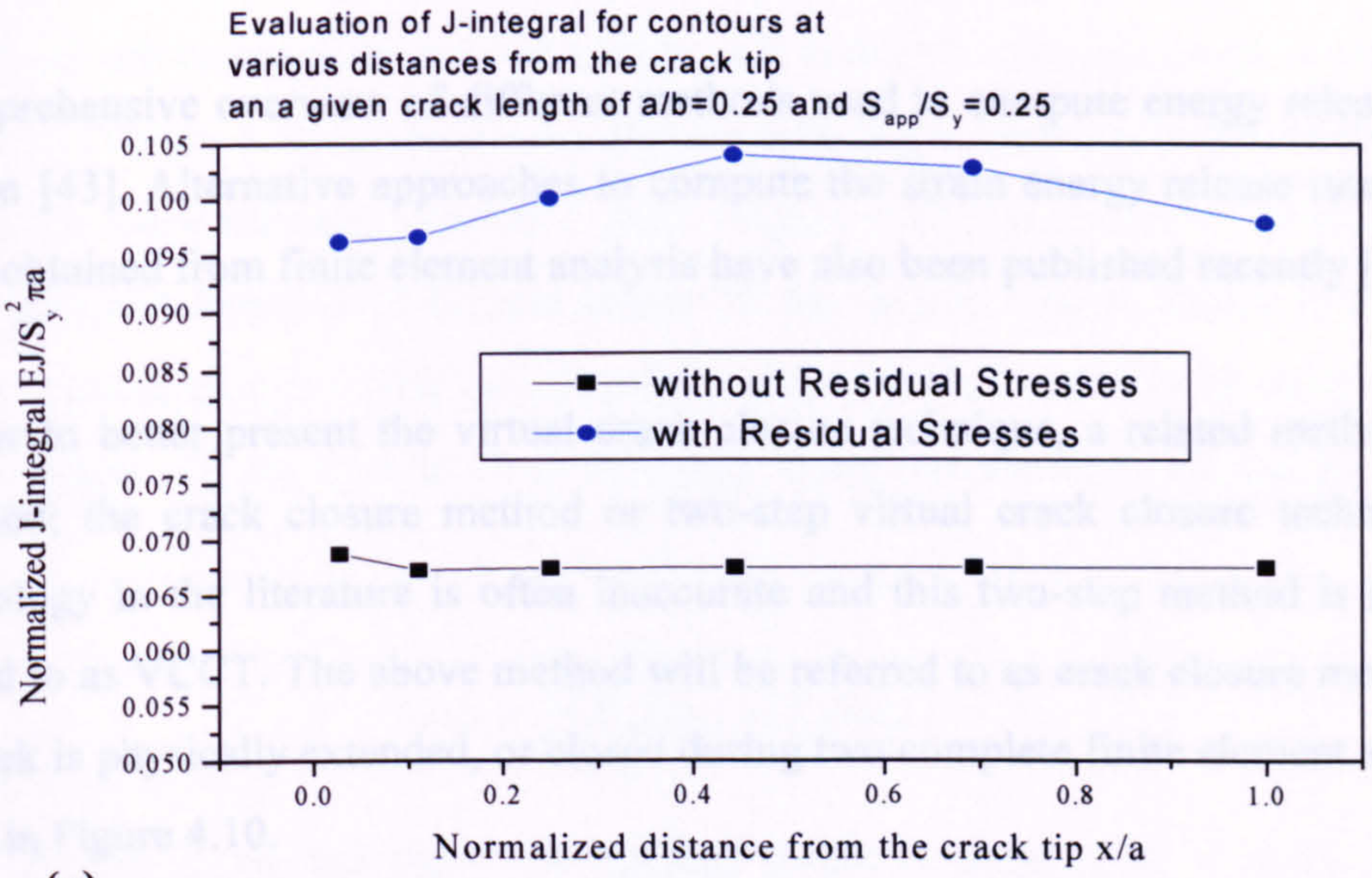

(a)

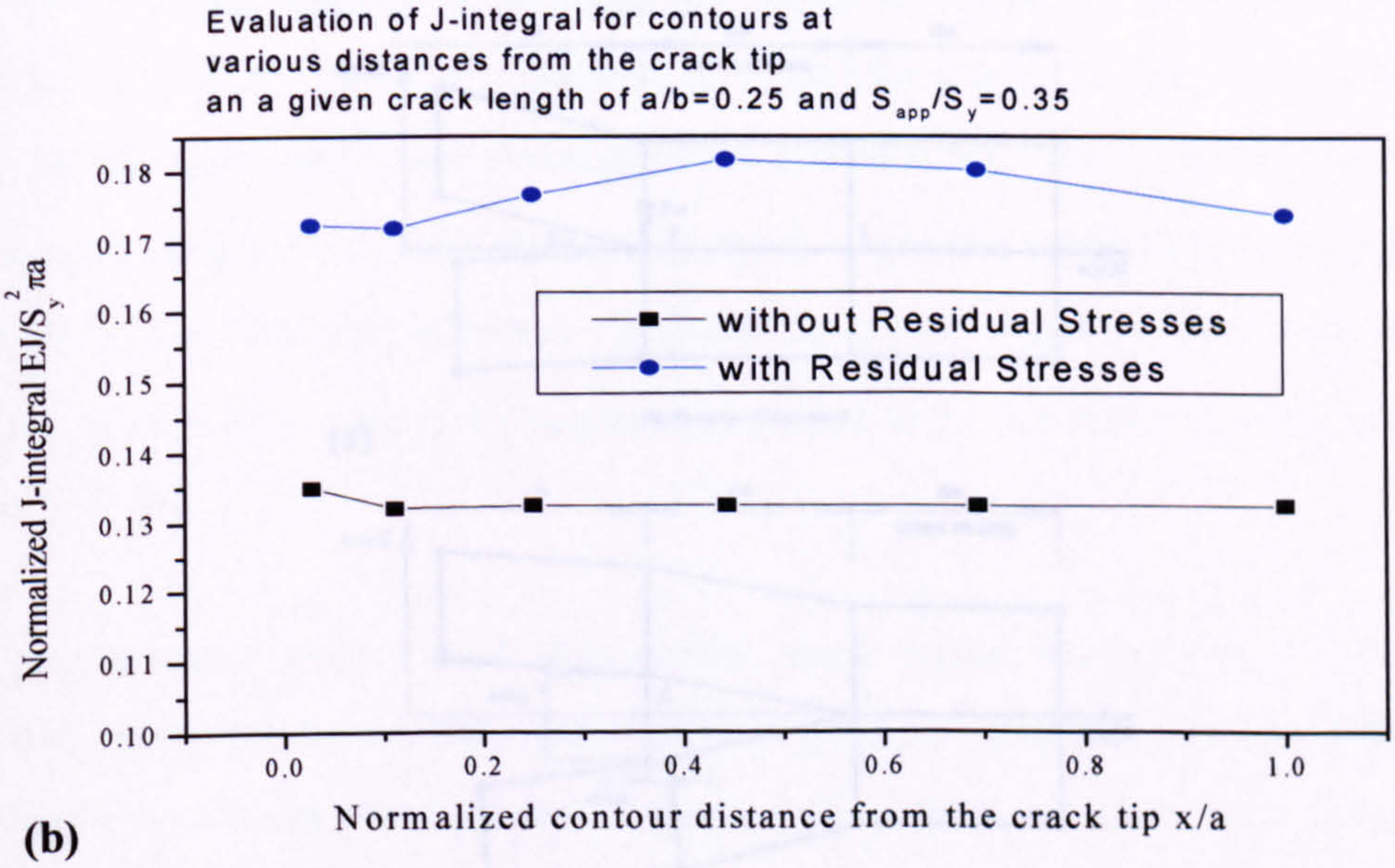

(b)

Figure 4.9 Path-dependence of J-integral in presence of welding residual stresses.

4.2.3 Virtual Crack Closure Technique (VCCT)

A comprehensive overview of different methods used to compute energy release rates is given in [43]. Alternative approaches to compute the strain energy release rate based on results obtained from finite element analysis have also been published recently [44-46].

In order to better present the virtual crack closure technique, a related method will be presented; the crack closure method or two-step virtual crack closure technique. The terminology in the literature is often inaccurate and this two-step method is sometimes referred to as VCCT. The above method will be referred to as crack closure method since the crack is physically extended, or closed during two complete finite element analyses as shown in Figure 4.10.

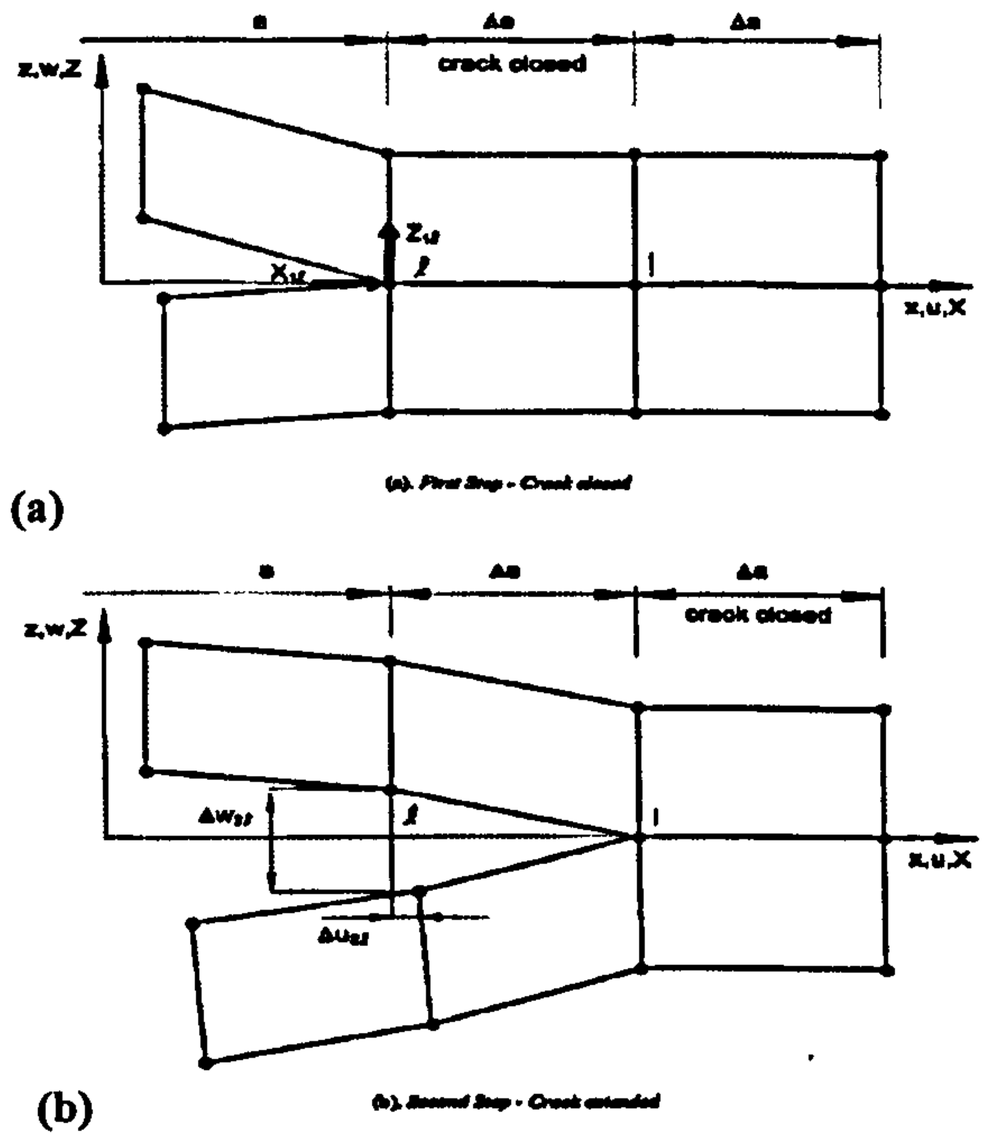

Figure 4.10 Crack Closure Method (Two step VCCT).

The crack closure method is based on Irwin's crack closure integral [20,47]. The method is based on the assumption that the energy ΔE released when the crack is extended by Δa from a (Figure 4.10 (a)) to $a+\Delta a$ (Figure 4.10 (b)) is identical to the energy required to close the crack between location ℓ and i (Figure 4.10 (a)). Index "1" denotes the first step depicted in Figure 4.10 (a) and index "2" the second step as shown in Figure 4.10 (b). For a crack modeled with two-dimensional four-noded elements as shown in Figure 4.10 the work ΔE required to close the crack along one element side can be calculated as:

$$\Delta E = \frac{1}{2}[X_{1\ell}\Delta u_{2\ell} + Z_{1\ell}\Delta w_{2\ell}] \tag{4.3}$$

where $X_{1\ell}$ and $Z_{1\ell}$ are the shear and opening forces at nodal point ℓ to be closed and $\Delta u_{2\ell}$ and $\Delta w_{2\ell}$ are the differences in shear and opening nodal displacements at node ℓ. The crack closure method establishes the original condition before the crack was extended. Therefore the forces required to close the crack are identical to the forces acting on the upper and lower surfaces of the closed crack. The forces $X_{1\ell}$ and $Z_{1\ell}$ may be obtained from a first finite element analysis where the crack is closed as shown in Figure 4.10 (a). The displacement $\Delta u_{2\ell}$ and $\Delta w_{2\ell}$ are obtained from a second finite element analysis where the crack has been extended to its full length $a+\Delta a$ as shown in Figure 4.10 (b).

The modified crack closure method or virtual, crack closure method (VCCT) is based on the same assumptions as the crack closure method described above. Additionally, however, it is assumed that a crack extension of Δa from $a+\Delta a$ (node i) to $a+2\Delta a$ (node k) does not significantly alter the state at the crack tip (Figure 4.11). Therefore, the displacements behind the crack tip at node i are approximately equal to the displacements behind the original crack tip at node ℓ. Further, the energy ΔE released when the crack is extended by Δa from $a+\Delta a$ to $a+2\Delta a$ is identical to the energy required to close the crack between location i and k. For a crack modeled with two-dimensional, four-noded

elements, as shown in Figure 4.11, the work ΔE required to close the crack along one element side therefore can be calculated as:

$$\Delta E = \frac{1}{2}\left[X_i \Delta u_\ell + Z_i \Delta w_\ell\right] \tag{4.4}$$

where X_i and Z_i are the shear and opening forces at nodal point *i* and Δu_ℓ and Δw_ℓ are the shear and opening displacements at node ℓ as shown in Figure 4.11. Thus, forces and displacements required to calculate the energy ΔE to close the crack may be obtained from one single finite element analysis. The details of calculating the energy release rate $G = {}^{\Delta E}/_{\Delta A}$, where ΔA is the crack surface created, and the separation into the individual mode components will be discussed next.

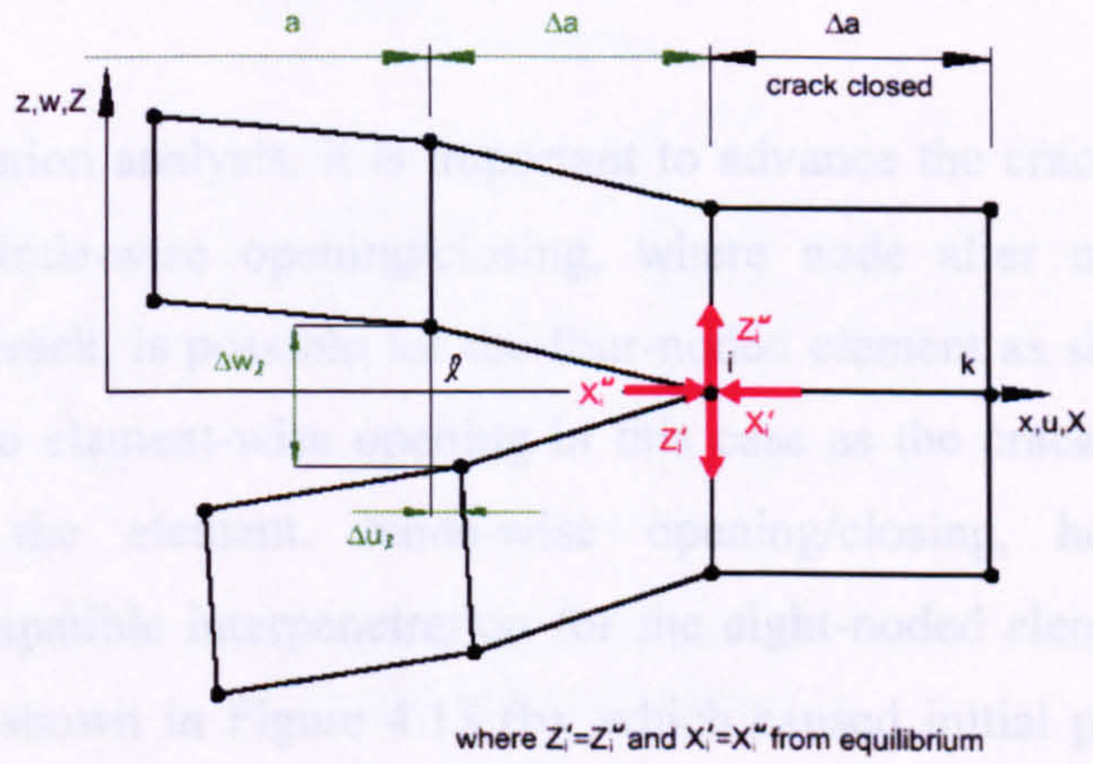

Figure 4.11 Modified Crack Closure Method (One step VCCT)

In a two-dimensional finite element plane stress, or plane strain model, the crack of length *a* is represented as a one-dimensional discontinuity by a line of nodes as shown in Figure 4.12. Nodes at the top surface and the bottom surface of the discontinuity have identical coordinates, however, are not connected with each other as shown in Figure 4.12 (a). This lets the elements connected to the top surface of the crack deform independently from those connected to the bottom surface and allows the crack to open as shown in Figure 4.12 (b). The crack tip and the undamaged section, or the section where the crack is closed and the structure is still intact, is modelled using single nodes.

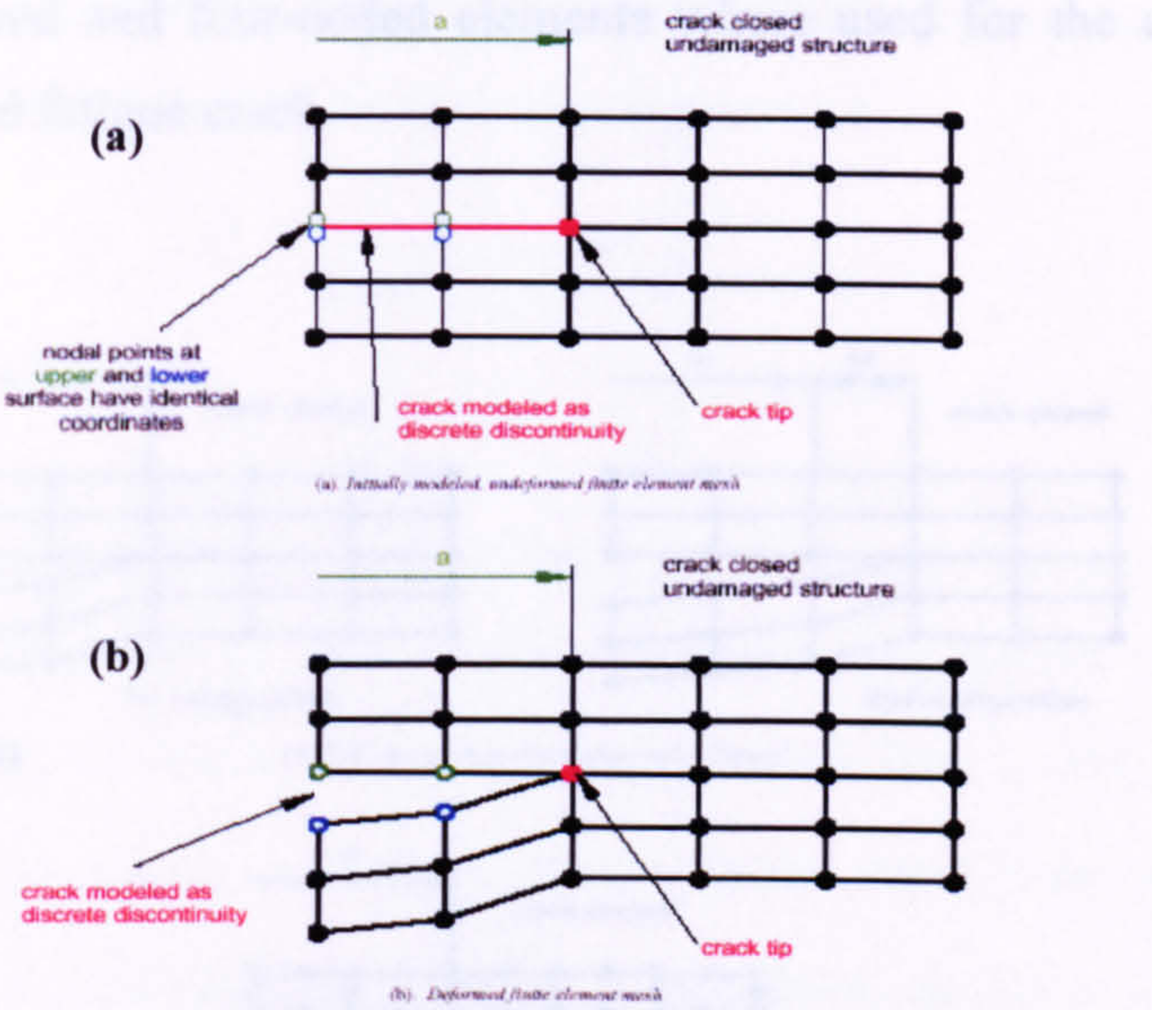

Figure 4.12 Crack modelled as one-dimensional discontinuity.

For a crack propagation analysis, it is important to advance the crack in a kinematically compatible way. Node-wise opening/closing, where node after node is sequentially released along the crack, is possible for the four-noded element as shown in Figure 4.13 (a). It is identical to element-wise opening in this case as the crack is opened over the entire length of the element. Node-wise opening/closing, however, results in kinematically incompatible interpenetration for the eight-noded elements with quadratic shape functions as shown in Figure 4.13 (b), which caused initial problems when eight noded elements were used in connection with the virtual crack closure technique.

In paragraph 4.2.4 only a calculation of the stress intensity factor (SIF) of a given stationary crack without any release of nodes and change of the boundary conditions is presented. Therefore, although the used FE model has 8-noded elements the node-wise concept - applicable in 8-noded element – is not an issue here since no crack propagation analysis is included.

In a crack propagation analysis there is need to establish a specific modelling technique for the release of the nodes along the crack line. This will be discussed in details in paragraph 4.3.2. Also in the crack propagation analysis in this chapter the element-wise

concept was followed and four-noded elements where used for the calculation of the (SIF) in a propagated fatigue crack.

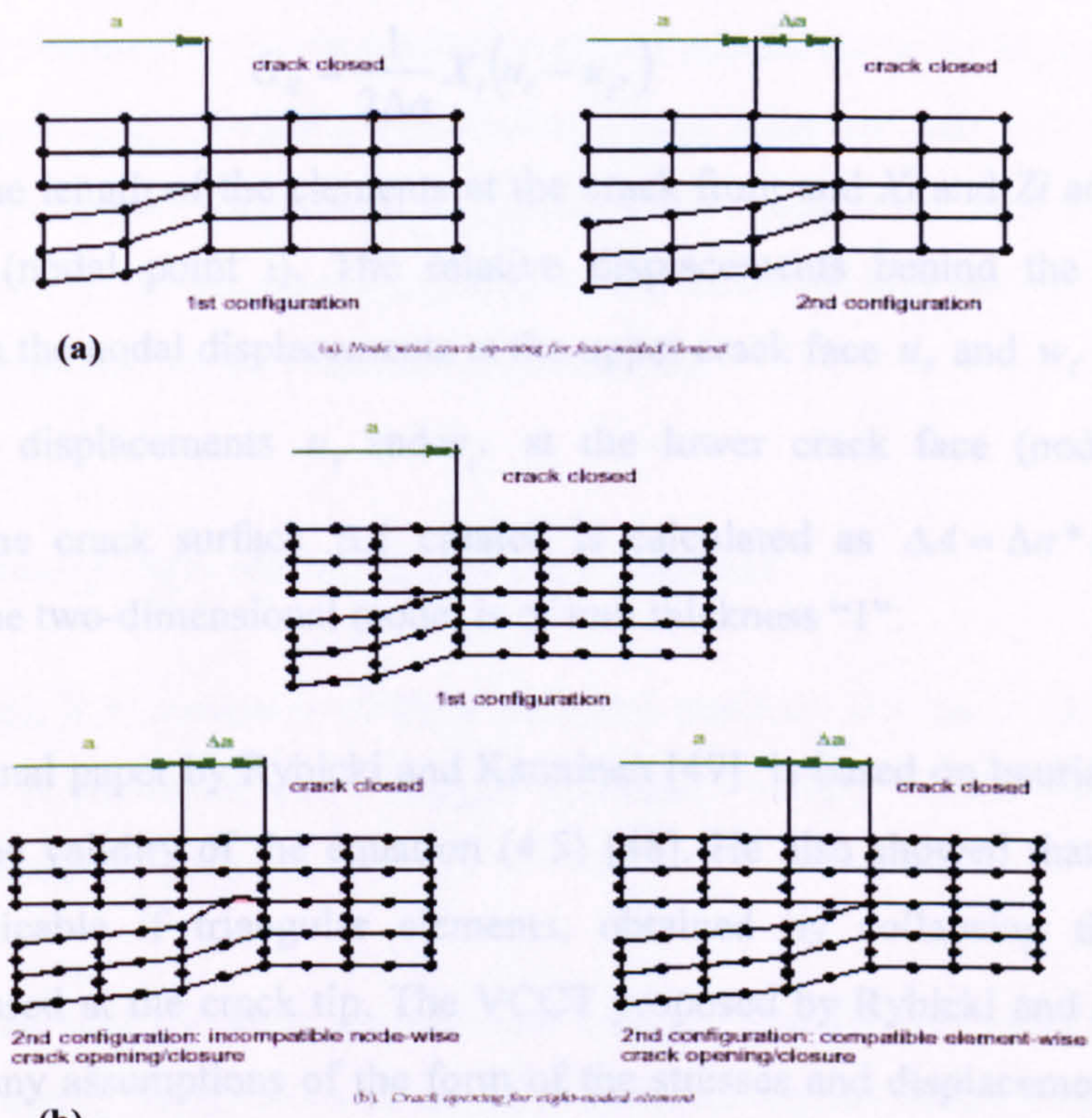

Figure 4.13 Virtual Crack Closure Technique for two-dimensional four nodded solid elements.

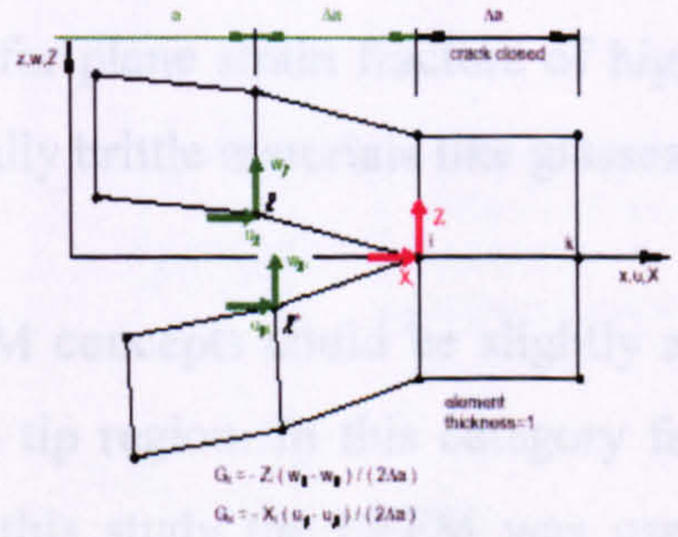

Figure 4.14 VCCT for two-dimensional four-noded solid elements.

The mode I, and mode II components of the strain energy release rate, *GI* and *GII* are calculated for four-noded elements as shown in Figure 4.14.

$$G_I = \frac{1}{2\Delta a} Z_i \left(w_\ell - w_{\ell^*} \right)$$
$$G_{II} = \frac{1}{2\Delta a} X_i \left(u_\ell - u_{\ell^*} \right) \qquad (4.5)$$

where Δa is the length of the elements at the crack front and *Xi* and *Zi* are the forces at the crack tip (nodal point i). The relative displacements behind the crack tip are calculated from the nodal displacements at the upper crack face u_ℓ and w_ℓ (nodal point i) and the nodal displacements u_{ℓ^*} and w_{ℓ^*} at the lower crack face (nodal point ℓ^*) respecively. The crack surface ΔA created is calculated as $\Delta A = \Delta a * 1$, where it is assumed that the two-dimensional model is of unit thickness "1".

While the original paper by Rybicki and Kanninen [49] is based on heuristic arguments, Raju proved the validity of the equation (4.5) [48]. He also showed that the equations (4.5) are applicable if triangular elements, obtained by collapsing the rectangular elements, are used at the crack tip. The VCCT proposed by Rybicki and Kanninen [49] did not make any assumptions of the form of the stresses and displacements. Therefore, singularity elements like the ones in Figure 4.4 are not required at the crack tip.

Linear Elastic Fracture Mechanics (LEFM) was originally developed to describe crack growth and fracture under essentially elastic conditions, as the name implies. However, such conditions are met only for plane strain fracture of high strength metallic materials and for fracture of fundamentally brittle materials like glasses, ceramics, rocks and ice.

Later it was shown that LEFM concepts could be slightly altered in order to cope with limited plasticity in the crack tip region. In this category falls the treatment of fracture problems in plane stress. In this study the LEFM was used since limited plasticity is present only around the crack tip region and the rest of the structure is in the linear elastic region. Nevertheless, there are many important classes of material that are too ductile to

permit description of their behaviour by LEFM because the plastic zone at the crack tip is too large. For these materials the EPFM is applicable.

In practice, most contributions to the development of EPFM have come from power generating and chemical industries where most of cracks occur in high pressure parts, which are apparently thick-walled vessels and pipes. Also, the offshore industry has to cope with cracks in very large thick sectioned welded structures. In contrast, LEFM is principally applied in the aerospace industry, where weigh savings are the main focus and high strength, relatively brittle materials must be used.

4.2.4 Comparison of Different SIF Calculation Methods

In this paragraph a comparison of three different methods for the evaluation of stress intensity factor is presented; the J-integral approach, Virtual Crack Closure Technique and Displacement Extrapolation.

Figures 4.15 and 4.16 illustrate the physical coupon used for this comparison together with all the necessary information about the reference analytical solution used to compare the accuracy of the different methods.

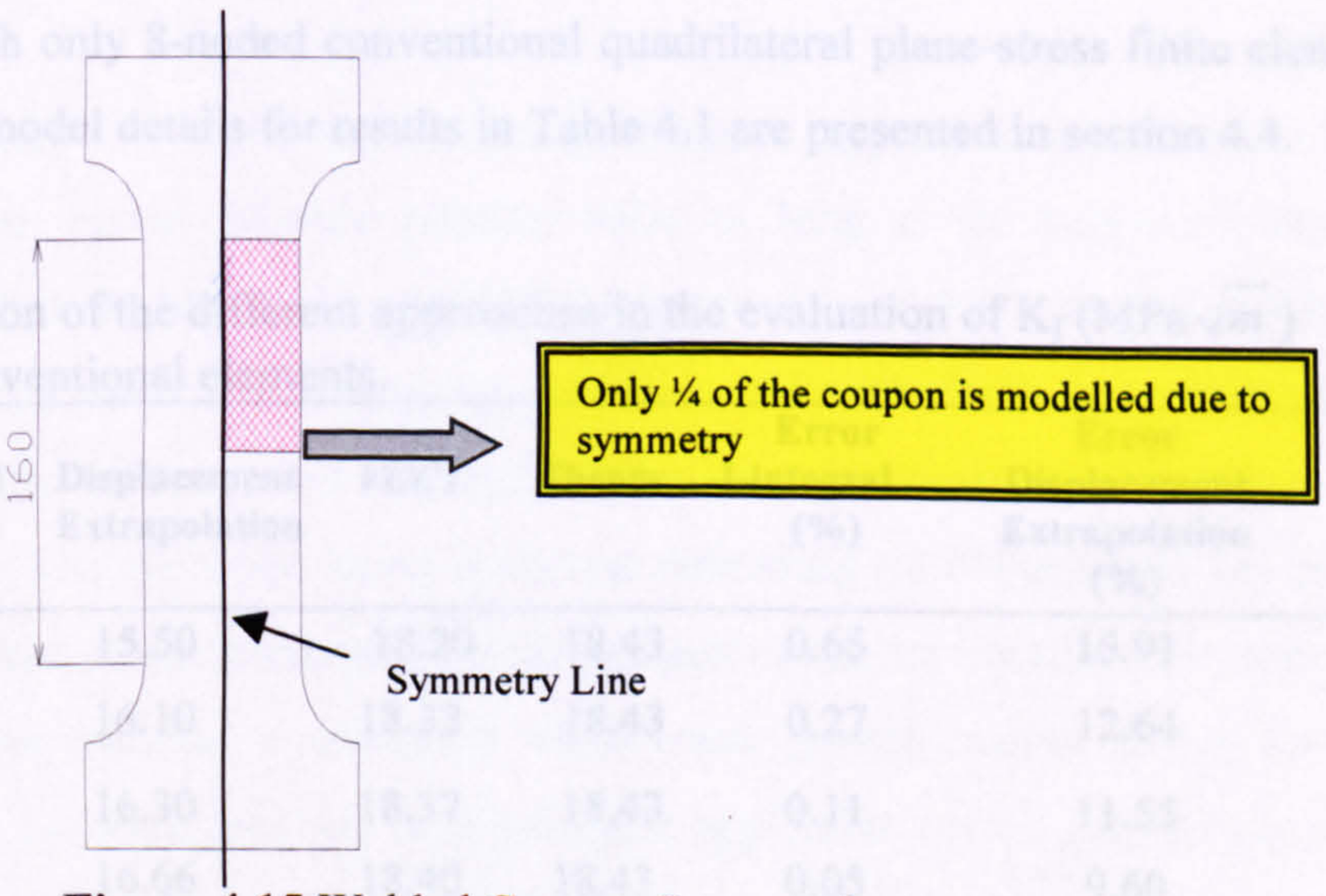

Figure 4.15 Welded Coupon Presentation.

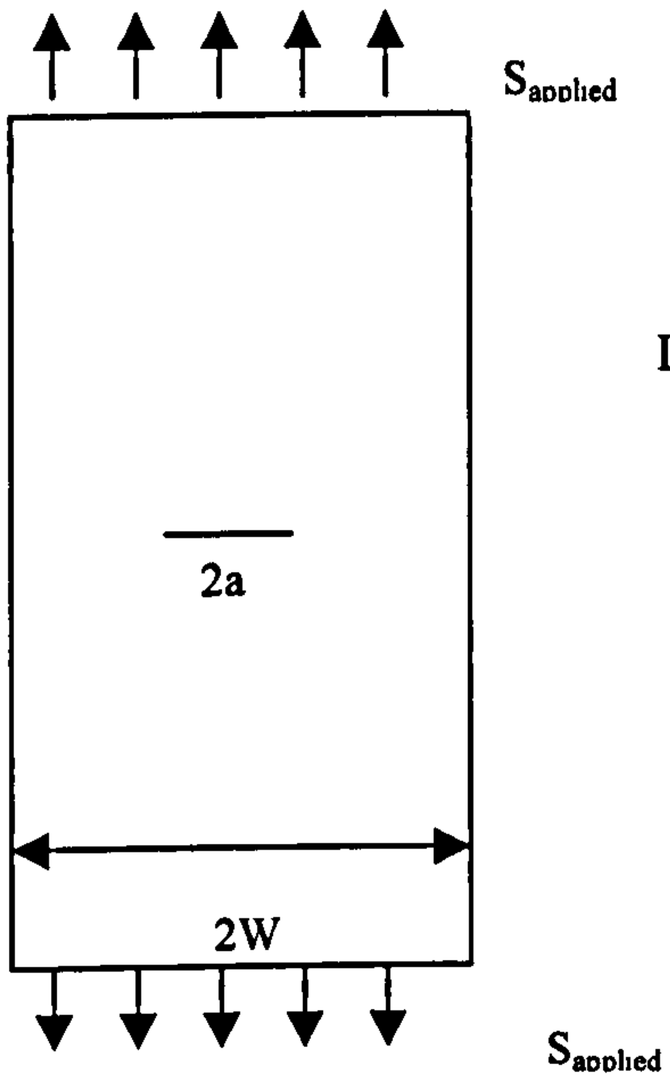

$S_{applied}$ = 100 MPa
$2a$ = 20 mm , 2W= 80 mm
E = 72 GPa
Linear Elastic Fracture Mechanics solution:

$$K_I = \beta S_{applied}\sqrt{\pi a}$$

$$\beta = \sqrt{\sec\left(\frac{\pi a}{W}\right)}$$

$\mathbf{K_I = 18.43}\ MPa\sqrt{m}$ (Theory)

Figure 4.16 Centre Crack Tension Plate Benchmark (CCT).

The theoretical solution is $K = \beta\sigma\sqrt{\pi a}$, $\beta = \sqrt{\sec\left(\frac{\pi a}{2W}\right)}$ (4.6)

Before analysing a welded plate, FE benchmark tests were conducted using ABAQUS. Table 4.1 shows calculated values of stress intensity factor K_I by using different approaches, in which only 8-noded conventional quadrilateral plane-stress finite element were used. The FE model details for results in Table 4.1 are presented in section 4.4.

Table 4.1 Comparison of the different approaches in the evaluation of K_I (MPa$\sqrt{m}$) using conventional elements.

Crack-tip Element Size (mm)	J-Integral Approach	Displacement Extrapolation	*VCCT*	Theory	Error J-integral (%)	Error Displacement Extrapolation (%)	Error VCCT (%)
2	18.31	15.50	18.20	18.43	0.65	15.91	1.28
1	18.38	16.10	18.32	18.43	0.27	12.64	0.60
0.5	18.41	16.30	18.37	18.43	0.11	11.55	0.32
0.25	18.42	16.66	18.40	18.43	0.05	9.60	0.16

It is clearly presented in Table 4.1 that both the J-integral and Virtual Crack Closure Technique (VCCT) approaches are sufficiently accurate by giving an error from 0.65% to 0.05% and 1.28% to 0.16% respectively in calculating the stress intensity factor even for larger element size of 2 mm. On the other hand, the displacement-extrapolation approach is proved to be the least accurate with a range of error 16% to 9.6% depending on the crack tip element length, which is used to model the area near the crack tip.

Table 4.2 Comparison of the different approaches in the evaluation of K_I (MPa$\sqrt{m}$) using singularity elements.

Crack-tip Element Size (mm)	J-Integral Approach	Displacement Extrapolation	*VCCT*	Theory	Error J-integral (%)	Error Displacement Extrapolation (%)	Error VCCT (%)
2	18.30	17.92	18.22	18.43	0.70	2.77	1.14
1	18.36	18.11	18.34	18.43	0.38	1.74	0.49
0.5	18.35	18.36	18.38	18.43	0.43	0.38	0.27
0.25	18.42	18.32	18.41	18.43	0.05	0.60	0.11

By employing the crack-tip singularity elements (i.e. quarter-node element, Figure 4.5) it was proved (Table 4.2) that the error in calculating the stress intensity factor by displacement extrapolation was reduced to the same level like the J-integral and VCCT approach.

The J-integral concept is based on an energy balance approach in a linear elastic behaviour. However, energy balance remains valid as long as the behaviour remains elastic but not necessarily linear. An important consequence of this extended validity of energy balance is that under certain restrictions this nonlinear elastic behaviour can be used to model plastic behaviour of a material. The latter is known as the deformation theory of plasticity. The main restriction is that no unloading should occur in any part of a body since for actual plastic behaviour the plastic part of the deformation is irreversible. At the crack tip the material is unloaded when crack growth occurs due to the free surface. Therefore, J-integral method is in principle applicable only up to the beginning of crack extension and not for crack growth [21].

In this study the main focus is the crack propagation under fatigue load in welded structures in order to evaluate the effect of the welding residual stresses on the crack growth of the structure. Therefore, the VCCT approach was used from this point onwards.

4.3 Description of the FE Model

4.3.1 Modelling of Welding Residual Stresses

Figure 4.17 shows the basic geometry of a welded centre crack tension specimen for this study. Also a typical welding residual stress distribution in the longitudinal loading direction across the width of the coupon is illustrated.

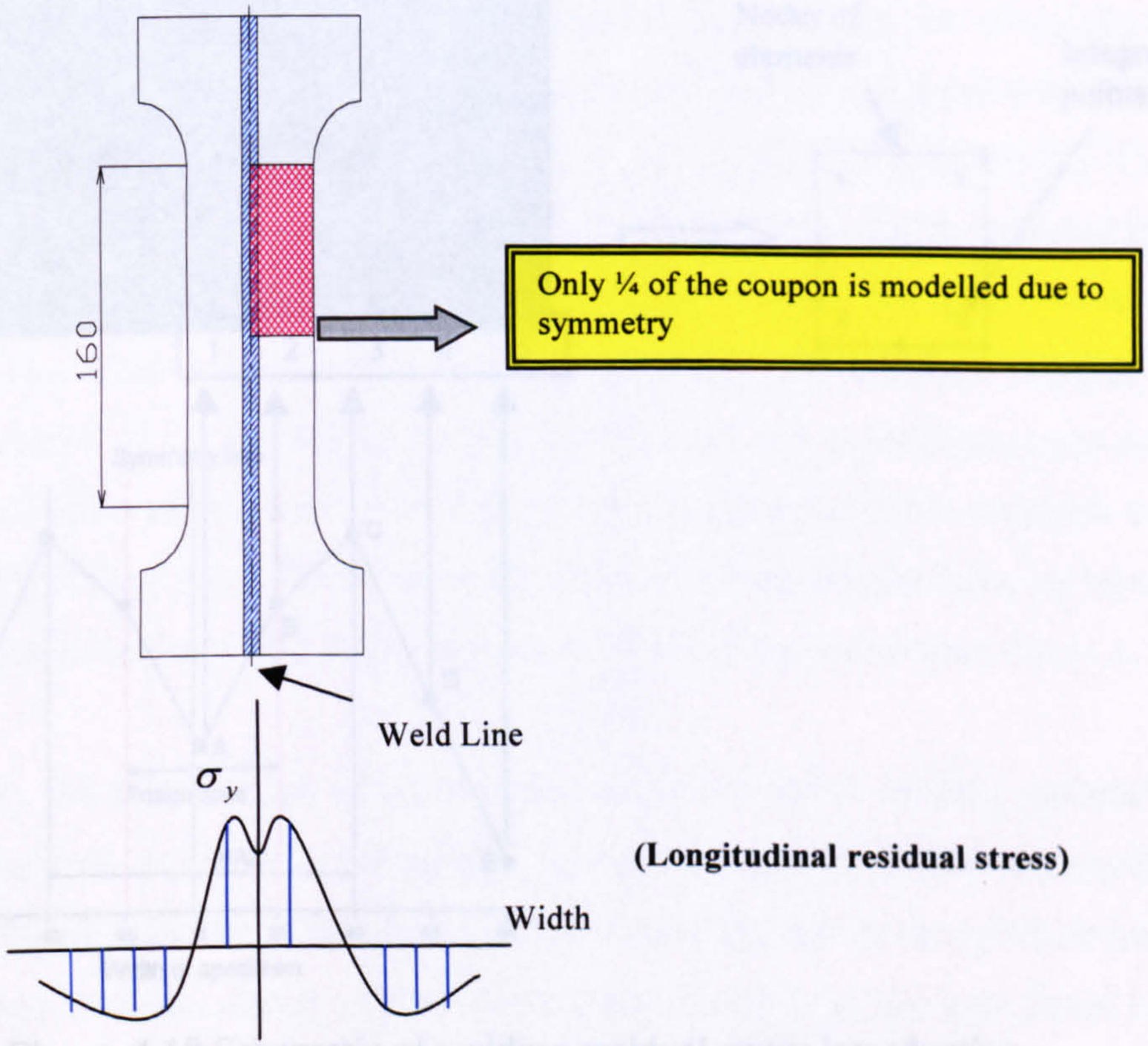

Figure 4.17 Welded coupon and generic shape of longitudinal residual stress distribution due to welding.

Figure 4.18 shows the technique, which is used to model the residual stresses in the ABAQUS model. First, the mesh of finite elements in the model is divided into 5; columns 1 to 5 as shown in Figure 4.18). Then through the use of a subroutine in ABAQUS the values of the residual stresses at these positions are applied at the integration points (Gauss points) of each element. In Figure 4.18 the values on Y-axis of the residual stresses are only for illustration purpose. The actual measured welding residual stresses are listed later on in the chapter.

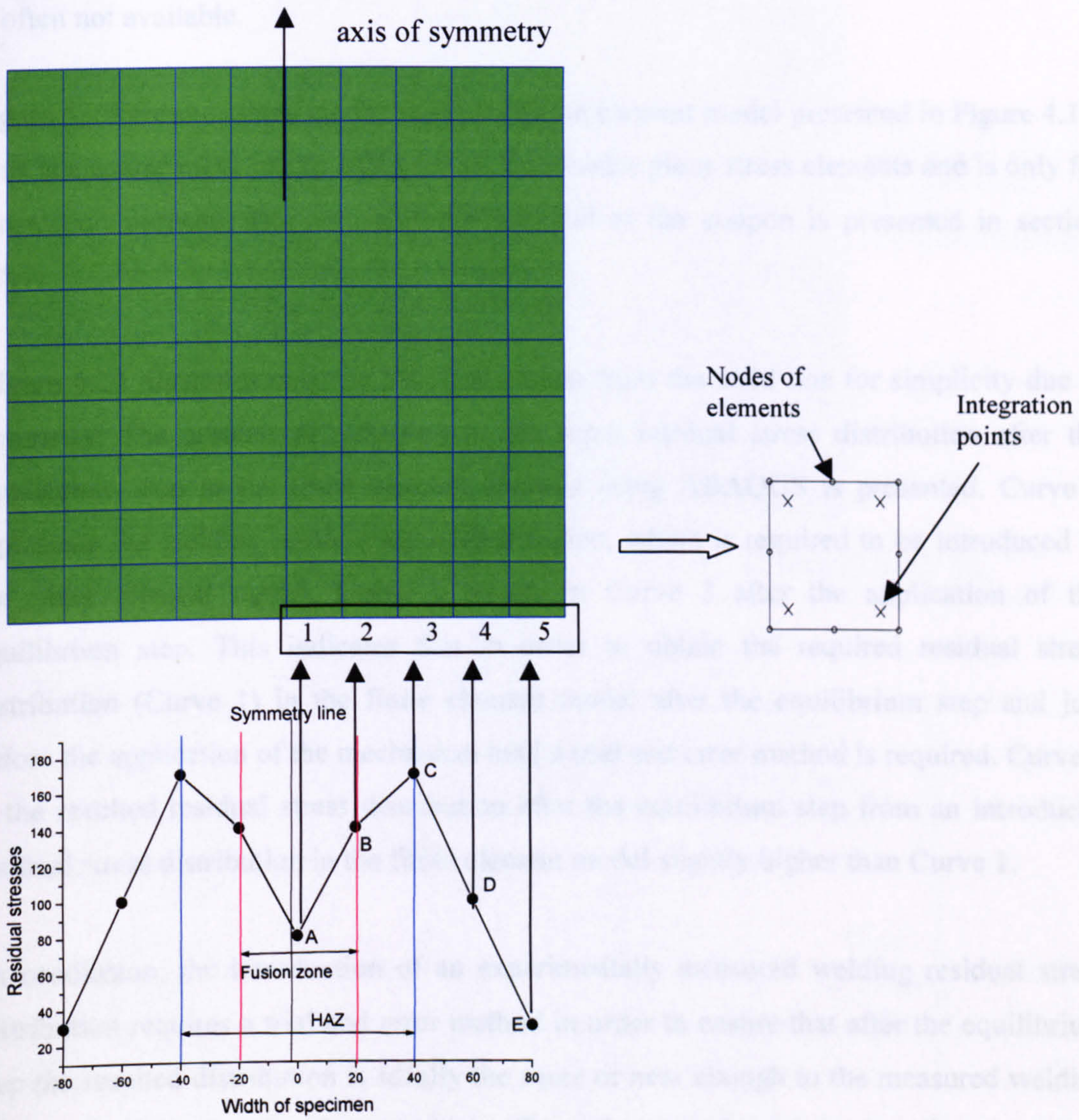

Figure 4.18 Schematic of welding residual stress introduction.
into the ABAQUS model.

After the application of the values of the welding residual stresses an equilibrium step is required. During this step these stresses are smoothed out to satisfy equilibrium for the structure. Because in this application the residual stresses have been applied in the whole area of the finite element model the obtained-desired residual stress distribution, after the equilibrium step, is very near to the applied residual stress distribution, before the equilibrium step. It should also mentioned that in practice, residual stress distributions are measured only at selected positions and therefore a full distribution of the residual stress is often not available.

Figure 4.20 presents three curves using the finite element model presented in Figure 4.19. This is a coarse mesh model using simple four-nodes plane stress elements and is only for illustration purpose. The actual used FE model of the coupon is presented in section 4.4.1.

Figure 4.20 illustrates only the half distribution from the weld line for simplicity due to symmetry. The amount of reduction of the input residual stress distribution after the equilibrium step in the finite element analysis using ABAQUS is presented. Curve 1 represents the welding residual stress distribution, which is required to be introduced in the finite element model. Curve 1 results in Curve 3 after the application of the equilibrium step. This indicates that in order to obtain the required residual stress distribution (Curve 1) in the finite element model after the equilibrium step and just before the application of the mechanical load a trial and error method is required. Curve 2 is the resulted residual stress distribution after the equilibrium step from an introduced residual stress distribution in the finite element model slightly higher than Curve 1.

In conclusion, the introduction of an experimentally measured welding residual stress distribution requires a trial and error method in order to ensure that after the equilibrium step the resulted distribution is ideally the same or near enough to the measured welding residual stresses. Another factor, which affects the reduction of the introduced residual stress distribution is the mesh density of the finite element model. The more fine mesh the more accurate the representation of the measured residual stress distribution in the

finite element model. But the more fine the mesh the more calculation load is present and clearly a compromise and judgement should be used in order to accept a solution within an acceptable error margin.

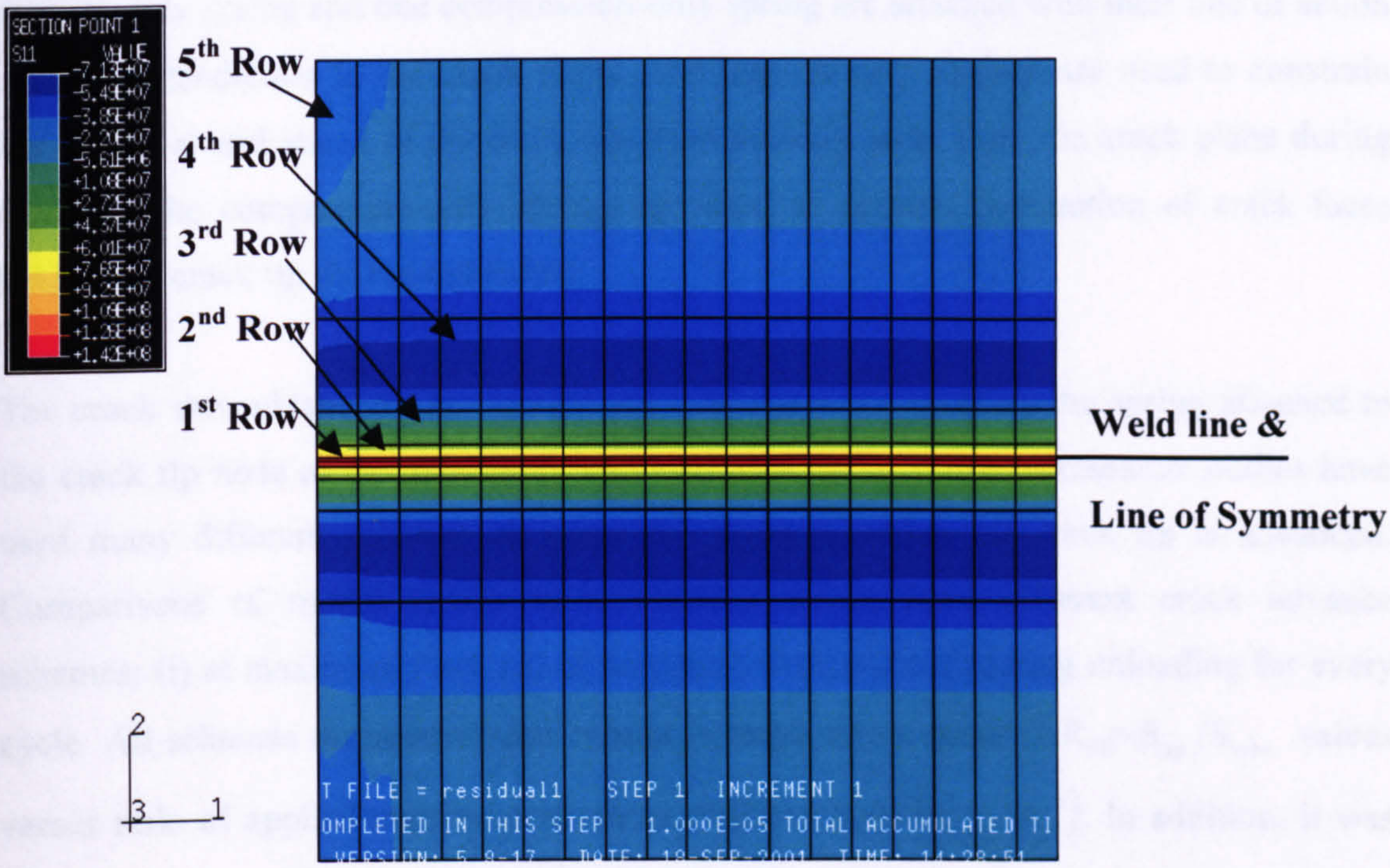

Figure 4.19 Contour of Curve 3 after equilibrium of uniaxial stress S_{xx}.

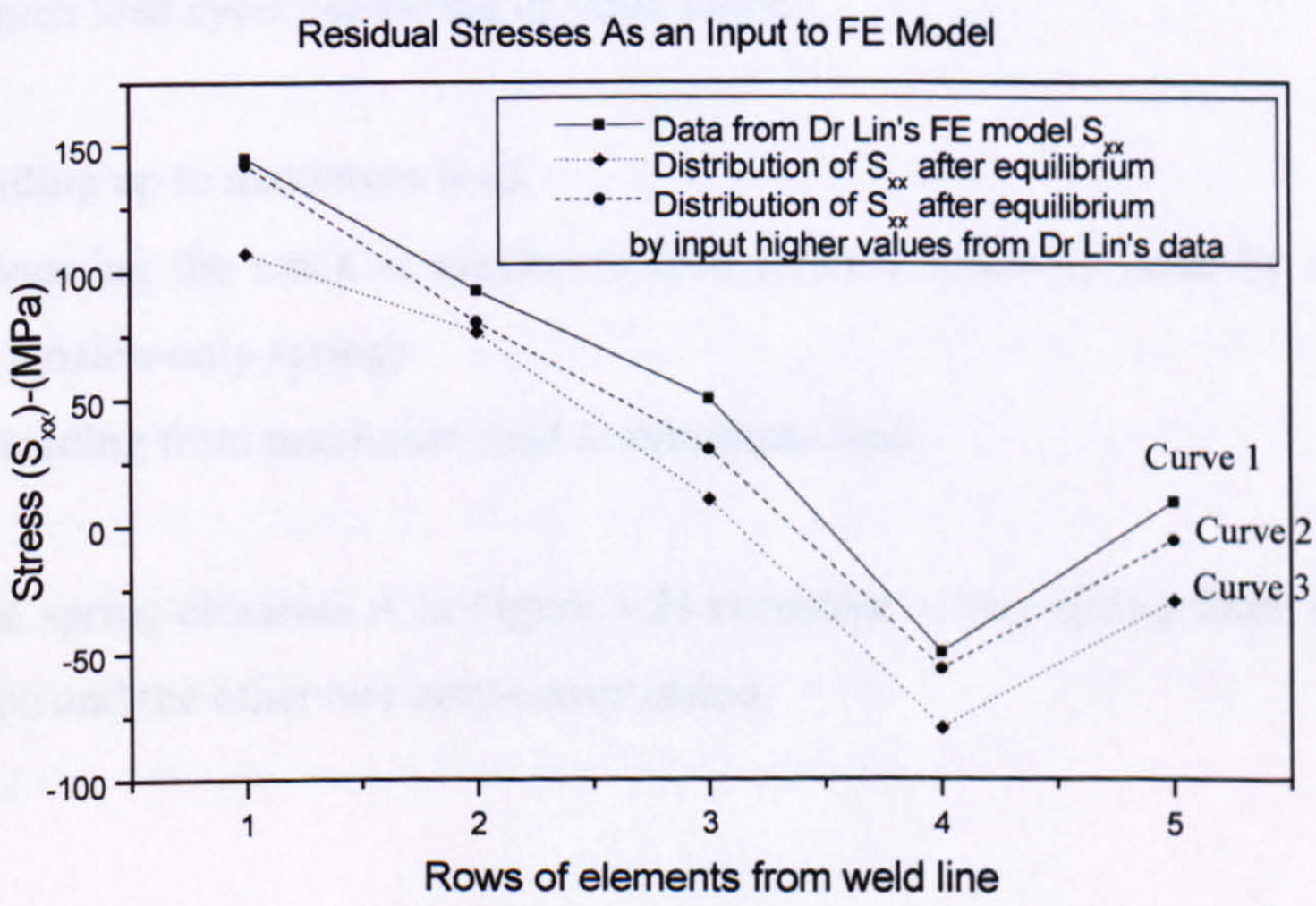

Figure 4.20 Reduction of the input residual stress distribution after the equilibrium step.

4.3.2 Fatigue Crack Growth Modelling

This study is focused on the elastic-plastic analysis. A spring finite element approach is being used, based on the work of Newman [50]. For each node along the crack plane, one tension-only spring and one compression-only spring are attached with their line of action acting perpendicular to the crack plane. The tension–only springs are used to constrain the nodes, at and ahead of the crack tip, from moving away from the crack plane during loading. The compression-only springs are used to prevent penetration of crack faces behind the crack tip during unloading.

The crack was advanced one element per load cycle by releasing the spring attached to the crack tip node at the maximum load of a load cycle. Previous research studies have used many different schemes to select the point at which the crack tip is advanced. Comparisons of model results were obtained using three different crack advance schemes: (i) at maximum load, (ii) at minimum load and (iii) during unloading for every cycle. All schemes revealed similar results in terms of the trend in $R_{op}=S_{op}/S_{max}$ values versus ratio of applied maximum stress to yield strength $(\sigma_{max}/\sigma_{ys})$. In addition, it was found that crack advancement at maximum loading yielded a closer representation of the actual crack growth phenomenon. Therefore, utilizing the first crack advance scheme results in each load cycle consisting of three steps:

- Loading up to maximum load.
- Advancing the crack at maximum load (release crack-tip node by disconnecting the tension-only spring)
- Unloading from maximum load to minimum load

Each of the spring elements A in Figure 4.21 comprise of two spring finite elements, one only-tension and the other one only-compression.

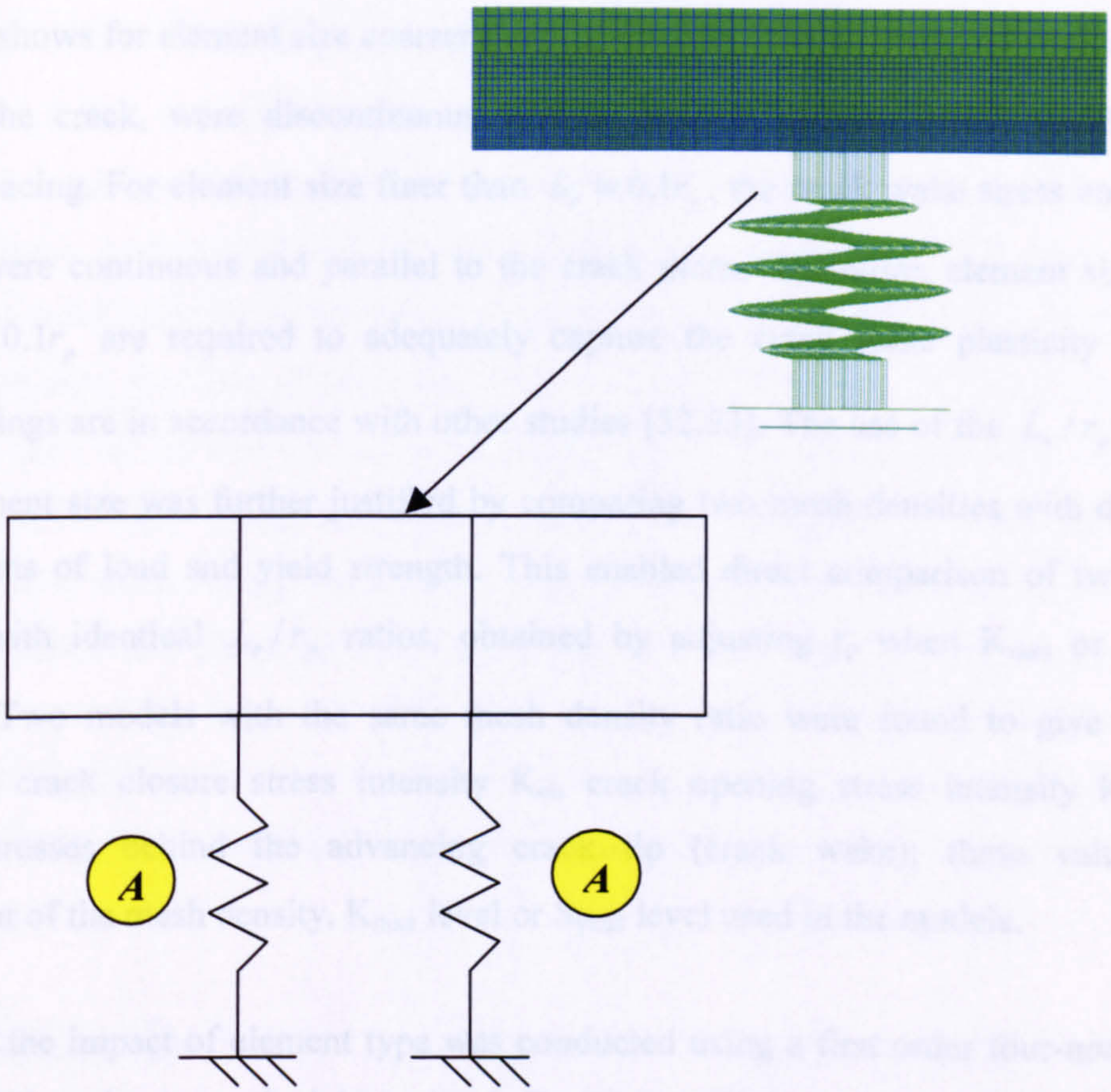

Figure 4.21 FE model with spring element concept.

The refinement of the mesh along the crack line is important for at least two reasons. Firstly, the mesh must be fine enough to capture the severe stress singularity at the crack tip. Secondly, the element size defines the crack growth increment, which should be as small as possible in order to simulate "real" crack growth. In opposition to these arguments for abundance of tiny finite elements, however, are considerations of computing time and cost. A balance between these two factors is required which does not seriously degrade the reliability of the results. A mesh refinement study was conducted by Dougherty to determine the size of the element length (L_e) along the crack plane [51]. The parameter selected for rating mesh density was the ratio of the element length to the forward plastic zone size (r_p), which is given by equation 4.7.

$$r_p = \frac{1}{2\pi} \times \left(K_{\max}/\sigma_{ys}\right)^2 \tag{4.7}$$

The study shows for element size coarser than $L_e = 0.15r_p$, the stresses and strains, in the wake of the crack, were discontinuous with a periodic pattern, which matched the element spacing. For element size finer than $L_e = 0.1r_p$, the crack wake stress and strain contours were continuous and parallel to the crack plane. Therefore, element sizes less than $L_e = 0.1r_p$ are required to adequately capture the crack wake plasticity effects. These findings are in accordance with other studies [52,53]. The use of the L_e / r_p ratio in rating element size was further justified by comparing two mesh densities with different combinations of load and yield strength. This enabled direct comparison of two mesh densities with identical L_e / r_p ratios, obtained by adjusting r_p when K_{max} or σ_{ys} is changing. Two models with the same mesh density ratio were found to give similar results for crack closure stress intensity K_{cl}, crack opening stress intensity K_{op} and residual stresses behind the advancing crack tip (crack wake); these values are independent of the mesh density, K_{max} level or S_{yield} level used in the models.

A study of the impact of element type was conducted using a first order four-node shell element (Q4) and a second eight-node shell element (Q8). A comparison of residual stresses at the wake of the advancing crack was conducted [51]. For (Q8) elements, a sinusoidal pattern of residual stresses was revealed. These residual stresses behind the propagating crack tip or in other words at the crack wake are present due to the cyclic plasticity and crack growth. These residual stresses are present in all the structures whether they are parent or welded structures. The pattern of the residual stress behind the crack tip is expected to be compressive. This is due to the reaction of the "elastic-part" of the structure towards the "plastic-part" of the structure, which is the area of the plastic zone. During unloading, the elastic-part" pushes the "plastic-part" in order to return to zero strain. For the squeeze of the "plastic-part" to its original size reverse yielding is required. Also this compressive residual stress must be internally equilibrated by tension further away. The residual stresses at the corner nodes were compressive, while those at the mid-side nodes were tensile.

Use of a finer mesh (lower L_e / r_p ratio than 0.10) reduced the amplitude of the sinusoidal pattern, but failed to eliminate the compression-tension-compression pattern of the residual stress behind the crack. The above pattern resulted whether a constant element edge stiffness or a constant nodal stiffness approach was used for the crack plane springs. This demonstrates that the pattern of the residual stresses behind the crack is independent from the selected approach of the spring stiffness in the FE model. The same result was also found for a model without the compression-only springs along the crack plane, thus allowing over-closure along the crack wake. This behaviour is attributed to the displacement functions (shape functions) used for the Q8 element, which results in the element stiffness not being uniform along the element edge. For Q4 elements, the residual stresses along the crack plane have a saw-tooth pattern. Use of a finer mesh, reduces the amplitude of the saw-tooth pattern to an acceptably low magnitude. Based on the study of Dougherty [51], Q4 elements were selected for the FE model in this study.

4.4 Numerical Results

4.4.1 FE Results of Crack Closure in Parent Coupons

A FE model was created in order to investigate the cyclic plasticity phenomenon. The input file of the model can be found in Appendix C. Figures 4.22 and 4.23 present the geometry and the mesh pattern of the FE model. In Figure 4.22 the five different zones (A,B,C,D,E) are presented in the used mesh. The group of spring elements used are based on the same concept of Figure 4.21. In this model the used finite elements are two-dimensional plane stress with four-nodes each. Each node has two degree of freedom. The applied fatigue load is constant with load ratio of R=0.1 and S_{max}= 100 MPa. As it can be seen from Figure 4.23 the transition from one mesh zone to the other was done with the use of multipoint constrain concept (MPC). That was realised in order to avoid an unnecessary fine mesh in areas away from the crack plane. Also due to symmetry in Figure 4.24 (b) only the quarter of the coupon was modelled. The boundary conditions in Figure 4.22 follow the symmetry. Therefore BC1 constrains the degree of freedom (DOF)

in 1-direction and BC2 constrains the (DOF) in 2-direction (see coordinate system in Figure 4.22).

In order to create an initial crack of 10mm, a number of spring elements at the crack tip were deleted to represent the crack length. A fatigue crack propagation simulation took place from initial crack of 10mm to 13mm. To realise the fatigue crack propagation the proposed method from Newman, described in paragraph 4.3.1, was employed.

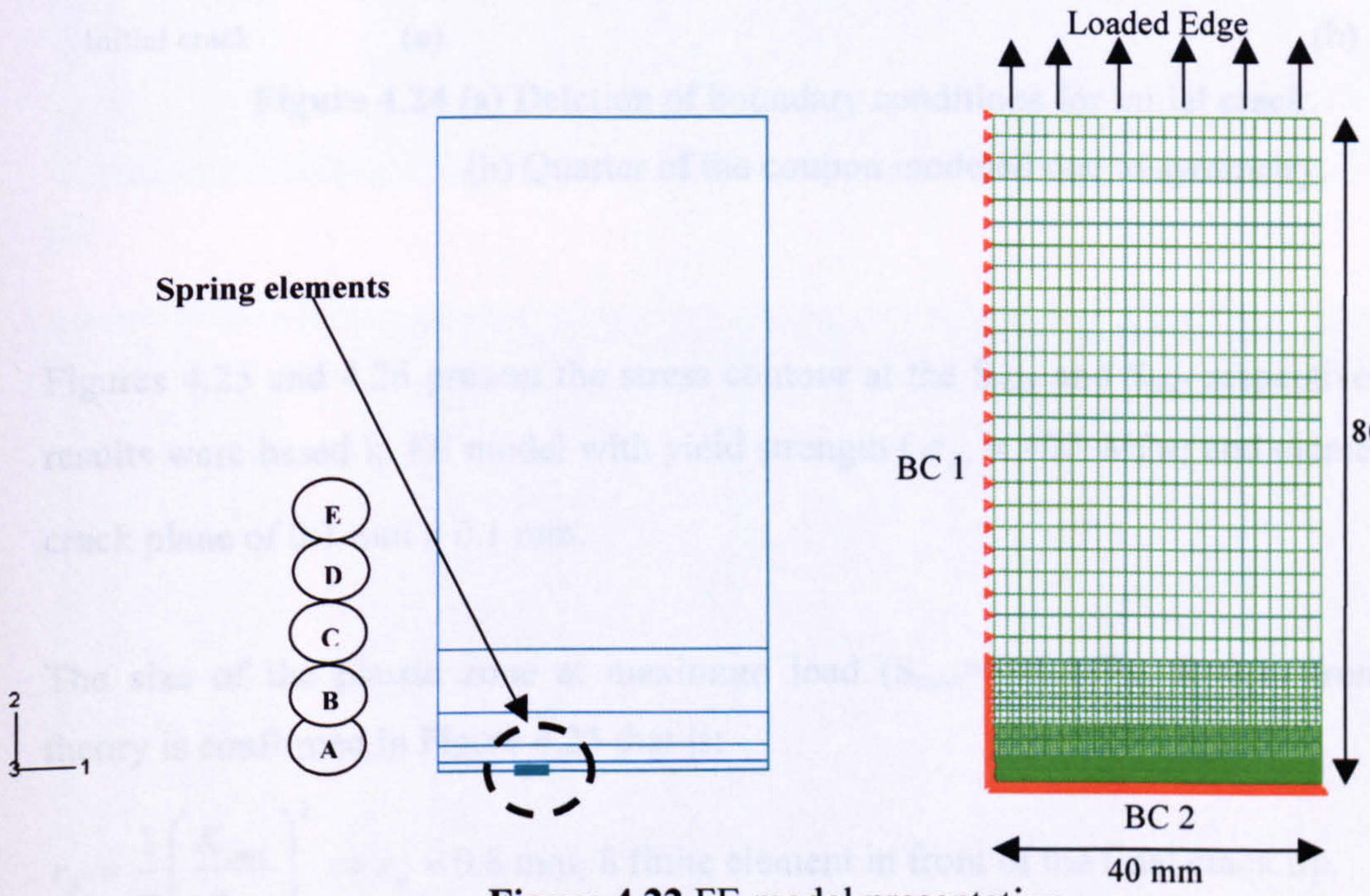

Figure 4.22 FE model presentation.

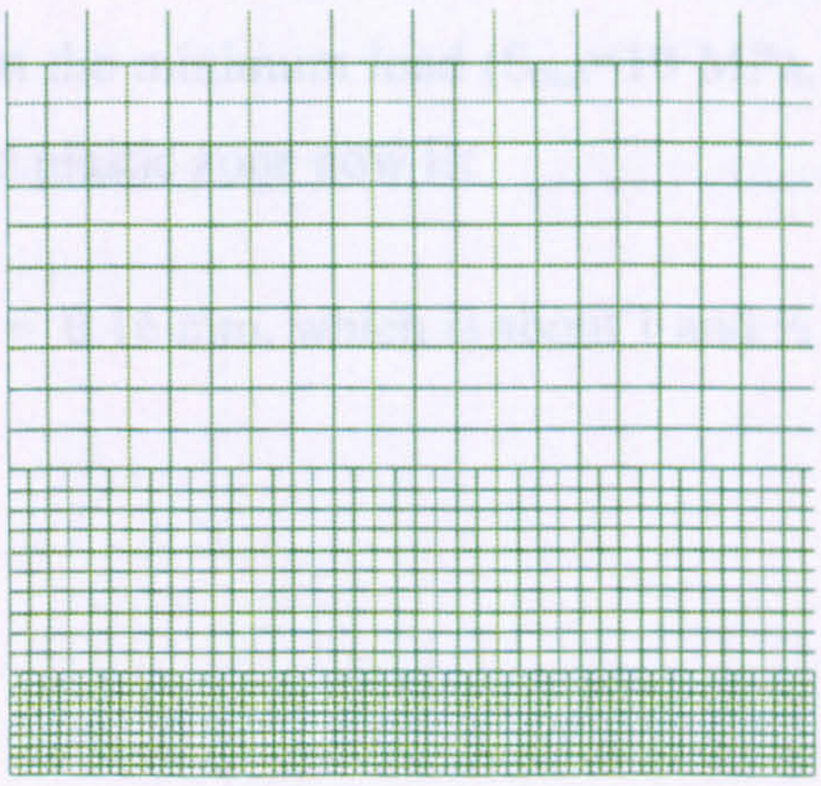

Figure 4.23 Multipoint constraints (MPC) concept.

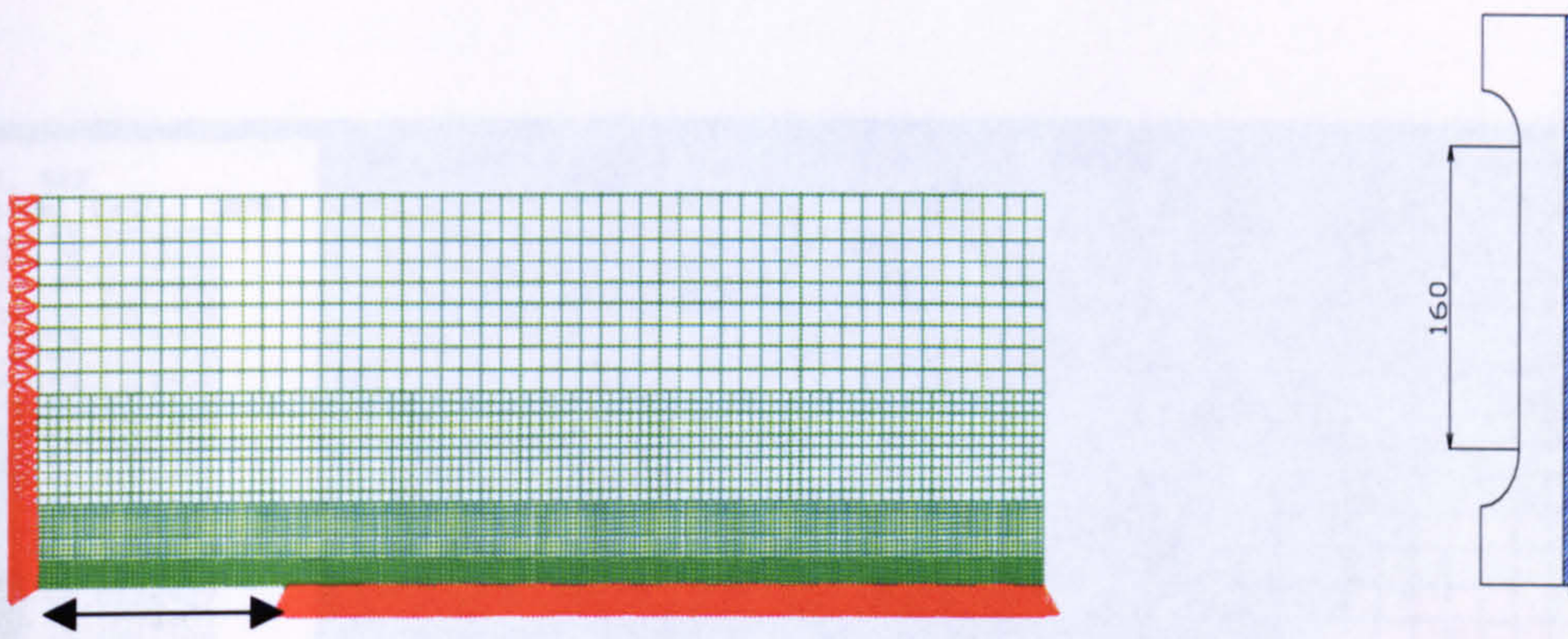

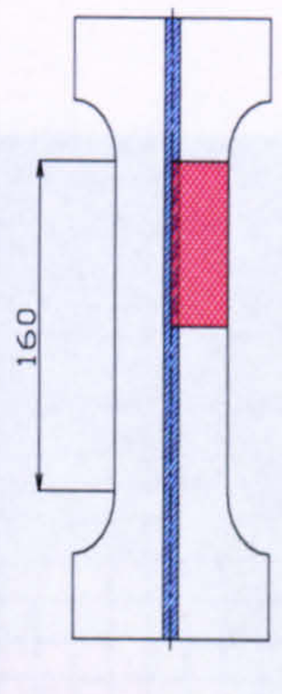

Figure 4.24 (a) Deletion of boundary conditions for initial crack.
(b) Quarter of the coupon modeled due to symmetry.

Figures 4.25 and 4.26 present the stress contour at the S_{max} and S_{min} respectively. These results were based in FE model with yield strength ($\sigma_{ys} = 400$ MPa) and element size in crack plane of 0.1 mm x 0.1 mm.

The size of the plastic zone at maximum load (S_{max}=100 MPa, R=0.1) from Irwin's theory is confirmed in Figure 4.25 that is:

$$r_p = \frac{1}{\pi}\left(\frac{K_{\max}}{\sigma_{ys}}\right)^2 \Rightarrow r_p = 0.8 \text{ mm, 8 finite element in front of the final crack tip.}$$

In the case of unloading, at the minimum load (S_{min}=10 MPa, R=0.1) Figure 4.26 shows that the size of the reversed plastic zone now is:

$$\Delta r_p = \frac{1}{\pi}\left(\frac{K_{\max}}{2\sigma_{ys}}\right)^2 \Rightarrow \Delta r_p = 0.16 \text{ mm, which is about 1 and ½ finite element size.}$$

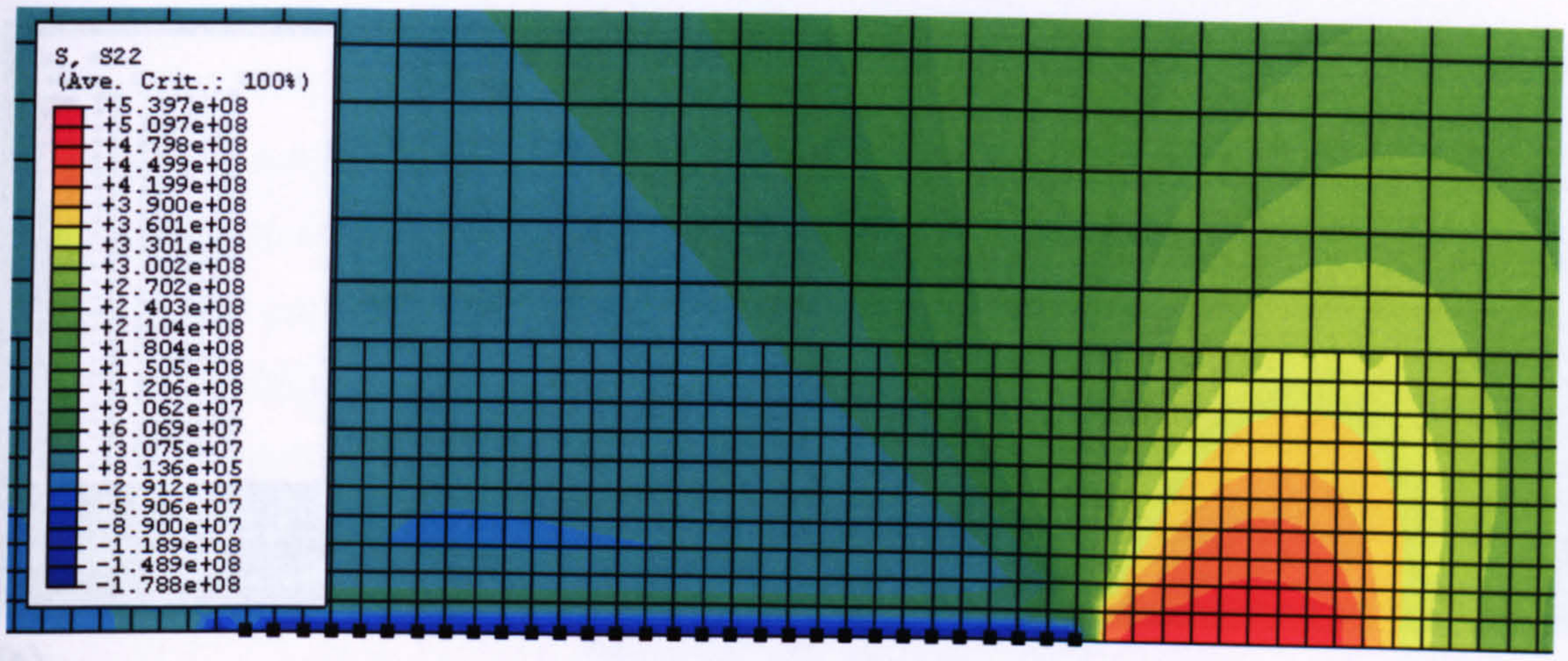

(a)

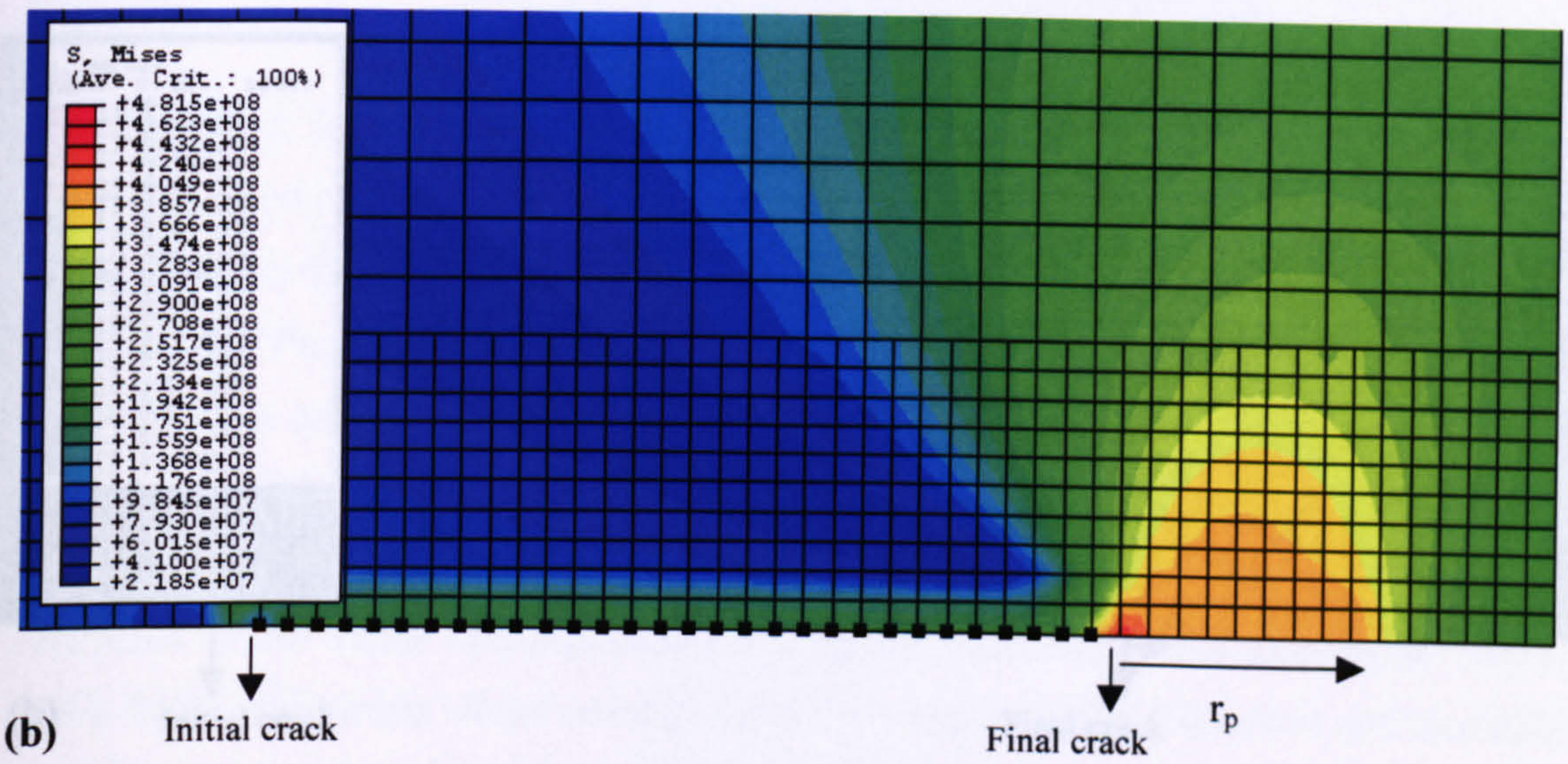

(b)

Figure 4.25 (a) Uniaxial stress contour & (b) Von-Mises stress contour at maximum fatigueload (100 MPa).

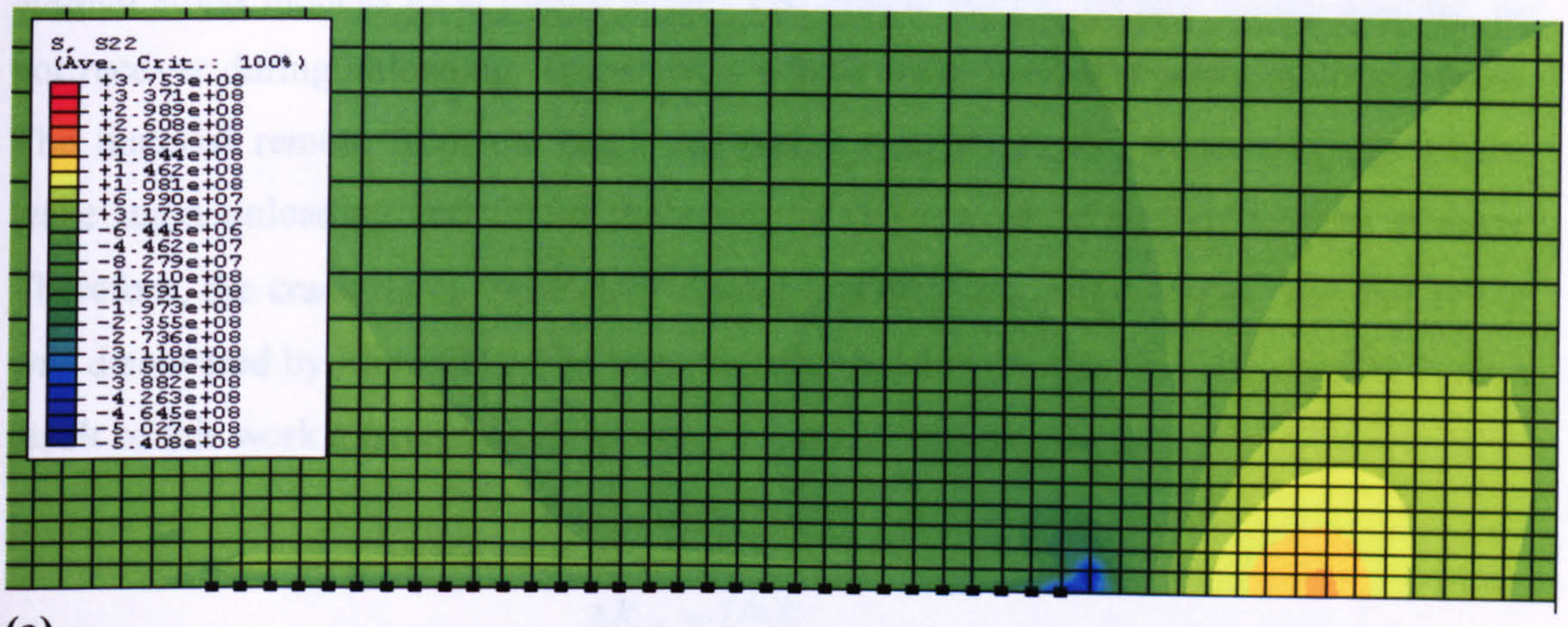

(a)

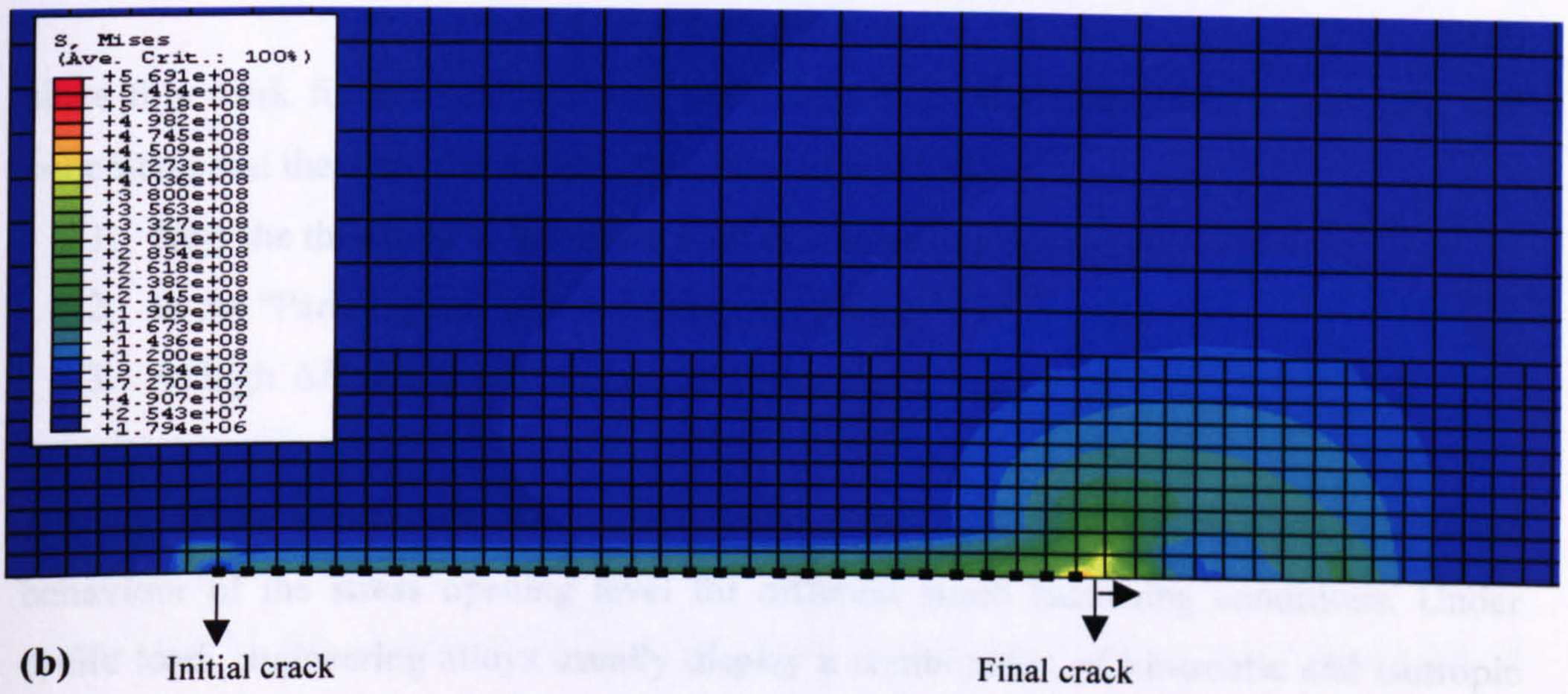

(b) Initial crack Final crack

Figure 4.26 (a) Uniaxial stress contour & (b) Von-Mises stress contour at minimum fatigue load (10 MPa).

At the crack tip local region the significantly higher level of stress compared with the applied stress induces local plastic strain. The plastic strains, created during loading, do not recover during unloading. Therefore, a plastic wake is created along the crack faces. The material remote from the crack tip, which remains elastic, constrains this plastic wake upon unloading and forces the crack to close, even at positive remote stresses. Therefore, the crack tip is "protected" during a part of the fatigue cycle. This behaviour was discovered by Elber [24]. The later was discussed in paragraph 2.7 in chapter 2. As a result of this work a fatigue crack growth rate model was established.

$$da/dN = C(U\Delta K)^m$$
$$\Delta K_{eff} = U\Delta K \tag{4.8}$$

where U is the stress intensity ratio. Elber's assumed that U depends only on R- ratio:

$$U = 0.5 + 0.4 \times R \tag{4.9}$$

since this work further developments have been made from other researchers [54] and concluded that there are three distinct regimes of crack closure:

1. Near the threshold U decreases with the increasing K_{max}.
2. In the "Paris region" U is independent of K_{max}.
3. At high ΔK values U decreases with increasing K_{max}.

A study for the effect of the strain hardening is presented next in an effort to evaluate the behaviour of the stress opening level for different strain hardening conditions. Under cyclic load, engineering alloys usually display a combination of kinematic and isotropic hardening, the so-called Bauschinger effect. This effect is observed by the decrease in material yield stress under unloading following a pre-strain in reverse direction. The Bauschinger effect can have a strong influence on the level of plasticity-induced crack closure and as consequence to the crack opening level. Therefore the crack tip plastic zone may undergo large reverse plastic strain during unloading. The above reduces the compressive residual stresses at the crack wake, which serve to clamp the crack closed [55]. Therefore, the crack tip is "protected" during a much lower part of the subsequent fatigue cycle. Finally, the Bauschinger effect should be taken into account in the

comparison of the resistance to crack propagation of various materials for two reasons [56]:

- The crack opening level $\frac{K_{op}}{K_{max}}$ or $\frac{S_{op}}{S_{max}}$ is diminished.
- The cyclic strain amplitude within the crack tip plastic zone is increased, therefore increasing the amount of damage.

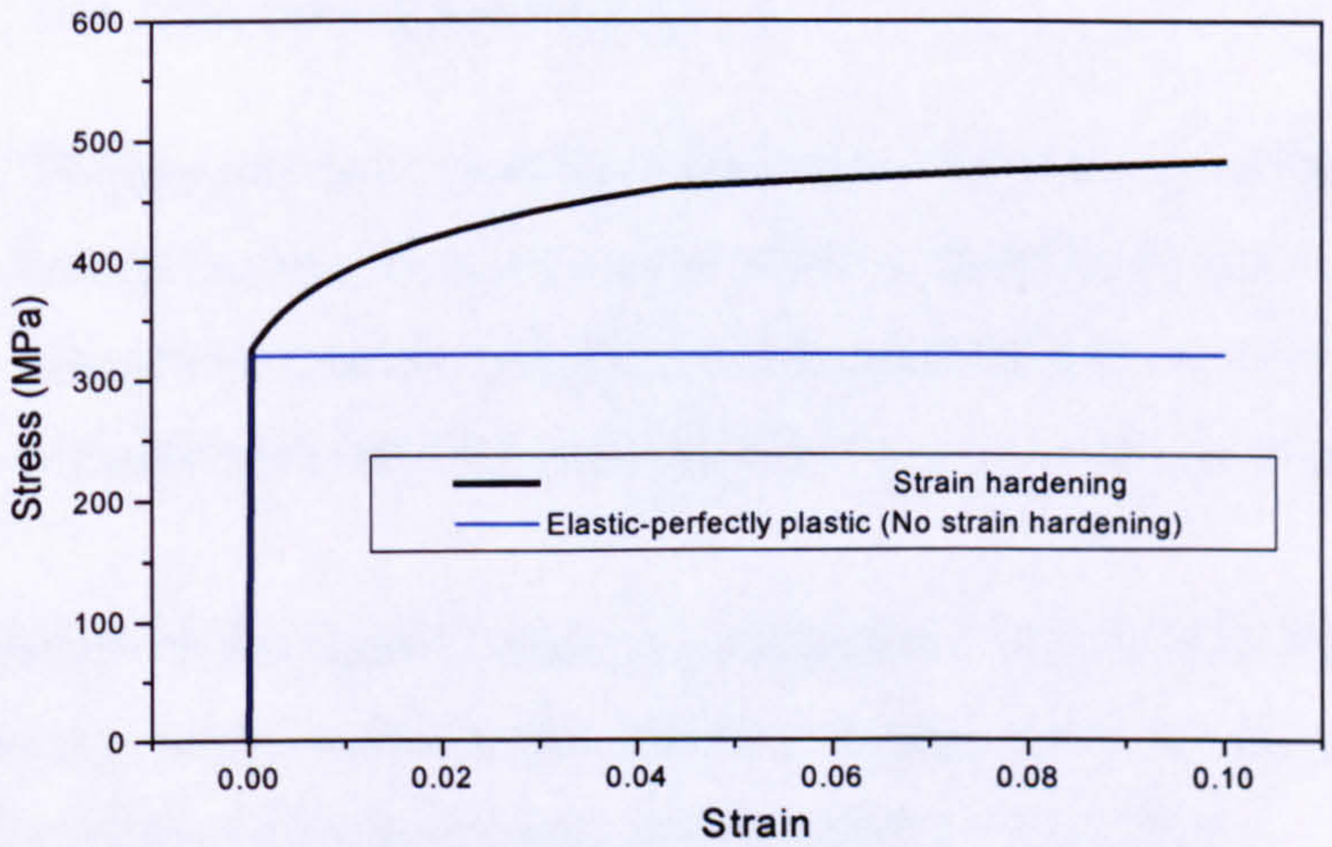

Figure 4.27 Stress strain behaviour in the two plasticity models.

In Figure 4.27 one curve describes the behaviour when strain hardening is present; on the other hand if the elastic-perfectly plastic model is being used no strain hardening is present. In the case of elastic-perfectly plastic behaviour the only information, which needs to be entered into the FE model, is the yield strength value of the material. In the case of strain hardening it is necessary to input a table of values. For every value of stress a suitable value of strain needs to be entered. This information comes from experimental data under cyclic load for the appropriate material, which in this study is the aluminium alloy 2024 T351, (see Appendix C).

In practice, there are difficulties in measuring the crack opening load since K_{op} depends on measurement location and techniques. Also, K_{op} changes with heat treatment since this

will effect the plastic zone size at the crack tip. Finally, geometry of crack, specimen thickness and initial crack length affect the level of K_{op}.

There are two definitions from the literature for calculating the S_{op} and subsequently the K_{op}.

Definition 1 : The traditional finite element definition of crack opening stress considers it as that stress corresponding to separation of the fracture surfaces at the first node behind the crack tip.

Definition 2 : Shifting the focus from the node behind the crack tip to the crack tip. During loading the compressive stress perpendicular to the crack tip changes to a tensile one, the crack is considered to be fully open and the corresponding applied stress is referred to as crack opening stress S_{op}.

For the calculation of the opening stress S_{op} definition 2 was used in this thesis to obtain the crack opening stress, which is the effective driving force for the crack propagation study. The level of the opening stress S_{op} is presented in Figure 4.28.

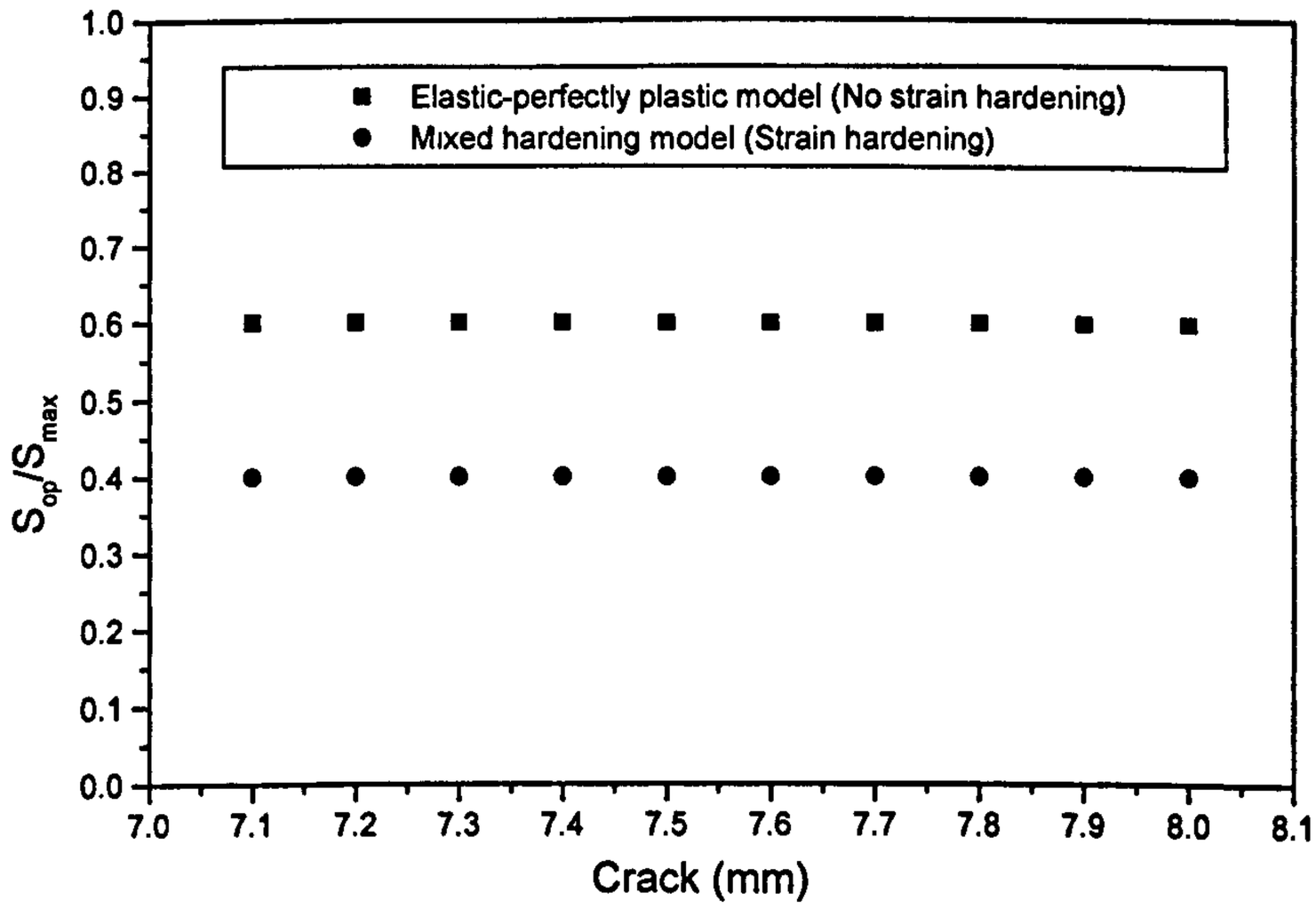

Figure 4.28 Level opening stress S_{op} for the two plasticity model.

Figure 4.28 was obtained from the FE model of a coupon with a centre crack like in Figure 4.16, under constant amplitude stress cycles S_{max}=100 MPa, R=0.1 Both no strain hardening and strain hardening were investigated. The FE model used is a typical CCT coupon with 80 mm width and 160 mm length on which the symmetry boundary conditions have been applied and so only the quarter of the coupon is modelled such as illustrated in Figure 4.15. Also the crack propagation length is only 1 mm, 7 mm to 8 mm from the initial crack tip.

From Figure 4.28 it can be said that strain hardening produces lower level of S_{op}. This is because the strain hardening produces less plastic deformation at the plastic wake of the crack. So, less compressive residual stresses due to plasticity. This means that the crack opens earlier than the case of elastic-perfectly plastic model (without strain hardening) as found in [55]. Therefore, the crack propagation rate is expected to be faster in the case of strain hardening when is compared with the elastic-perfectly plastic model (without strain hardening). The latter is in agreement with the findings in [56].

4.4.2 FE Results of Crack Closure in Welded Coupons

The following conditions were applied in this study in terms of fatigue load and input of welding residual stress distribution in the longitudinal direction. Residual stress distribution 1 and 2 in Figure 4.29 are shown only at the half part of the welded specimen due to symmetry. Residual stress distribution 1 represents an upper limit for the values of the measured welding residual stresses. Residual stress distribution 2 represents a lower bound. This is due to the variation of the experimentally measured residual stress values. The results sensitivity from residual stress distribution 1 to residual stress distribution 2 proved to be insignificant for these two welding residual stress distribution. So only the results based on the residual distribution 1 are presented in this study.

The following loading cases and crack length ranges were modelled. These cases will help the study of the relationship of crack opening stress with applied maximum stress and crack length, if any.

(1) $Smax = 110\ MPa,\ R=0.1,\ a = 4 - 7\ mm$, Residual stress distribution 1

(2) $Smax = 60\ MPa,\ R=0.1,\ a = 10 - 14\ mm$, Residual stress distribution 1

(3) $Smax = 100\ MPa,\ R=0.1,\ a = 2 - 14\ mm$, Residual stress distribution 1

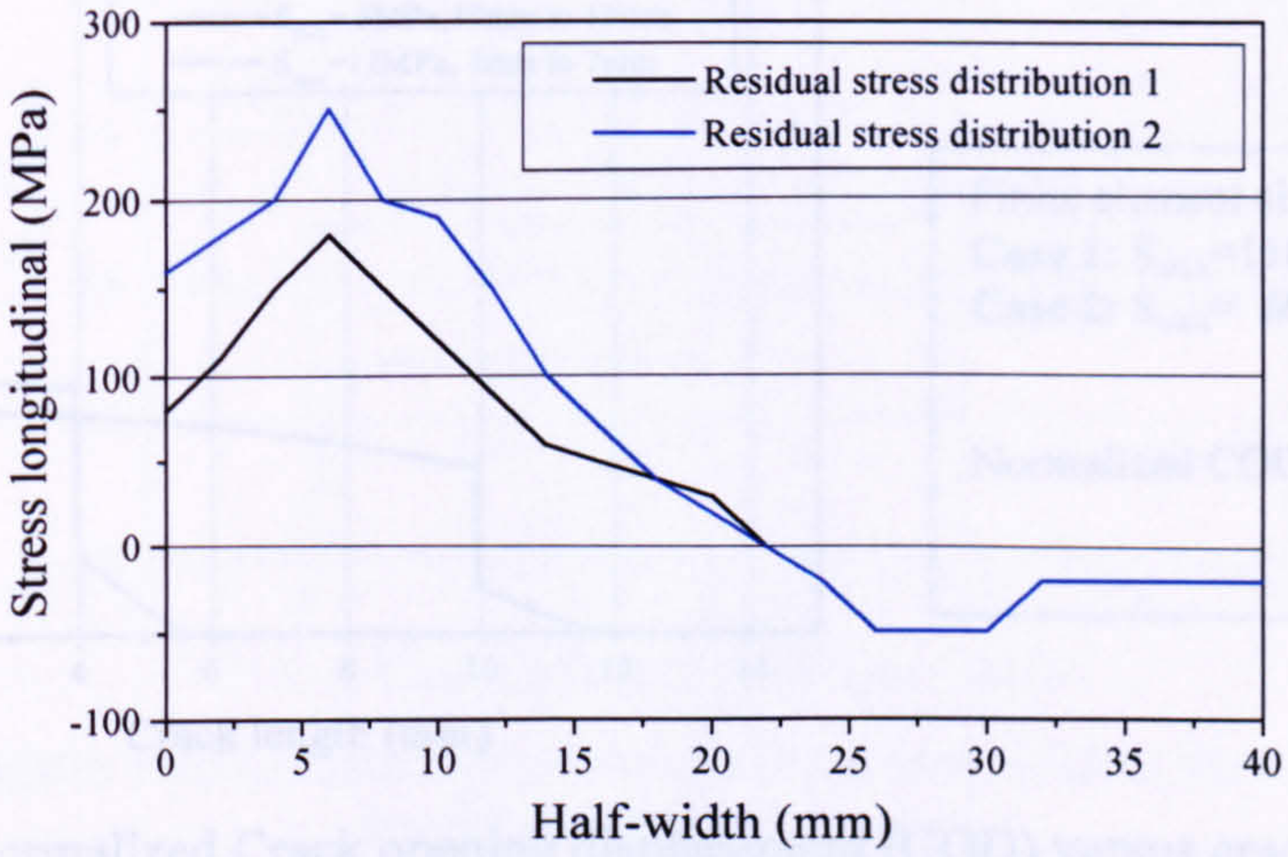

Figure 4.29 Longitudinal welding residual stress distributions.

Firstly, an investigation is carried out to establish whether or not there is a strong dependency of crack closure behaviour on the S_{max} and initial crack length. Figures 4.30 and 4.31 are both without any welding residual stresses and only illustrate the effect of the initial crack length and the S_{max} on the crack opening displacement (COD) and the opening stress level S_{op} respectively. Especially, for the crack opening displacement the presentation in Figure 4.30 is at the S_{min} level of the fatigue load, which is the $S_{min}=0.1S_{max}$ for a load ratio of R=0.1. The crack opening displacement (COD) is presented in Figure 4.30 to demonstrate the crack closure phenomenon during unloading. In addition, the opening stress level S_{op} is strongly related with the COD. The bigger the crack closure, which is illustrated with the COD profile being almost close the higher the opening stress level S_{op}.

The main conclusion based on the findings from Figure 4.30 is that the crack closure is independent of S_{max} and initial crack length. Furthermore, from Figure 4.31 it can be observed that the dependence of S_{open} on S_{max} and initial crack length is not strong, only 7%, and supports the finding on Figure 4.30, that over a 3 mm crack propagation the

crack opening displacement (COD) at the S_{min} level demonstrates about 2 mm of crack closure for both cases.

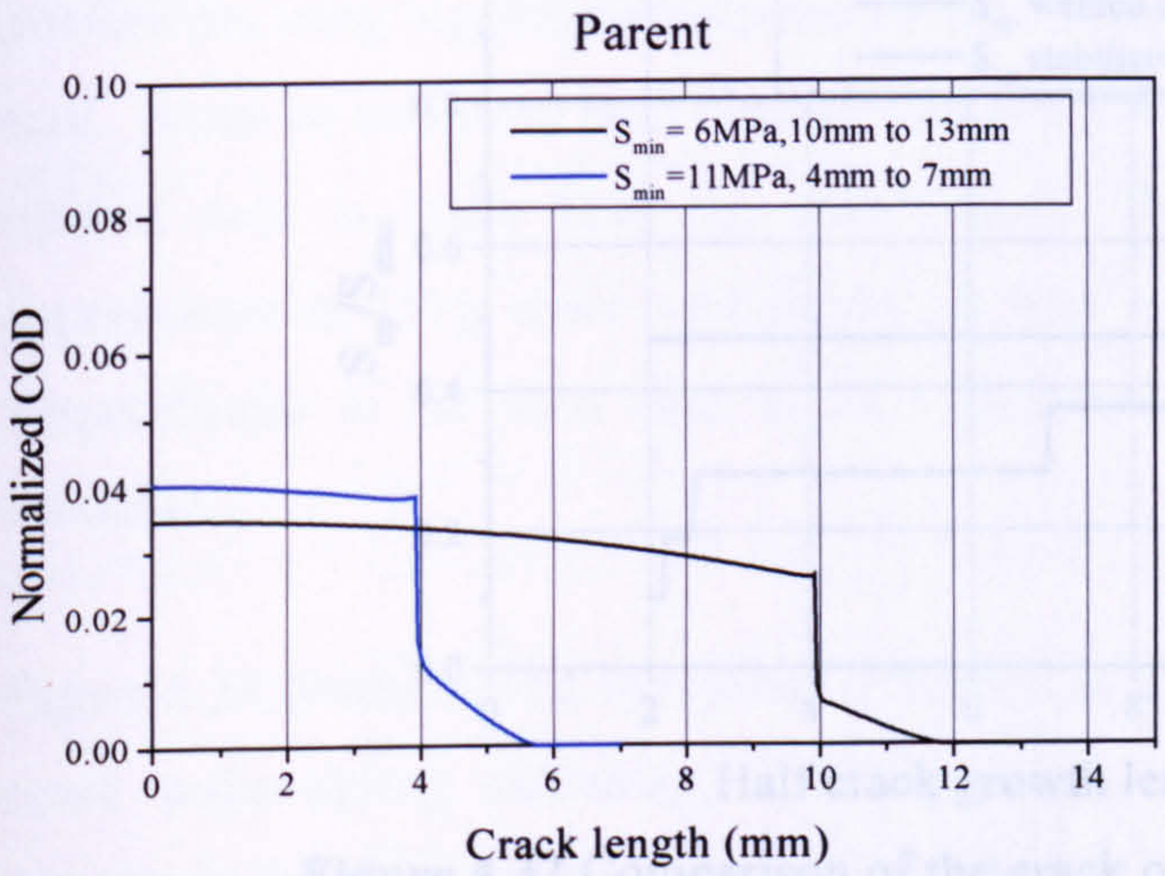

Finite element size = 0.04mm (10% r_p)
Case 1: S_{max}=110 MPa and a_o = 4mm
Case 2: S_{max}= 60 MPa and a_o = 10mm

Normalized COD: $\dfrac{E \times 0.5COD}{\sigma_{yield} \times a}$

Figure 4.30 Normalized Crack opening displacement (COD) versus crack length for two cases at S_{min}. No welding residual stress influence.

In Figure 4.31 the empirical Elber's level of stress opening is also presented. This demonstrates that the results are in the expected region in terms of the S_{op}/S_{max} as equation 4.10 states:

$$U = 0.5 + 0.4 \times R = 0.5 + 0.4 \times 0.1 \Rightarrow \text{U= } 0.54 \qquad (4.10)$$

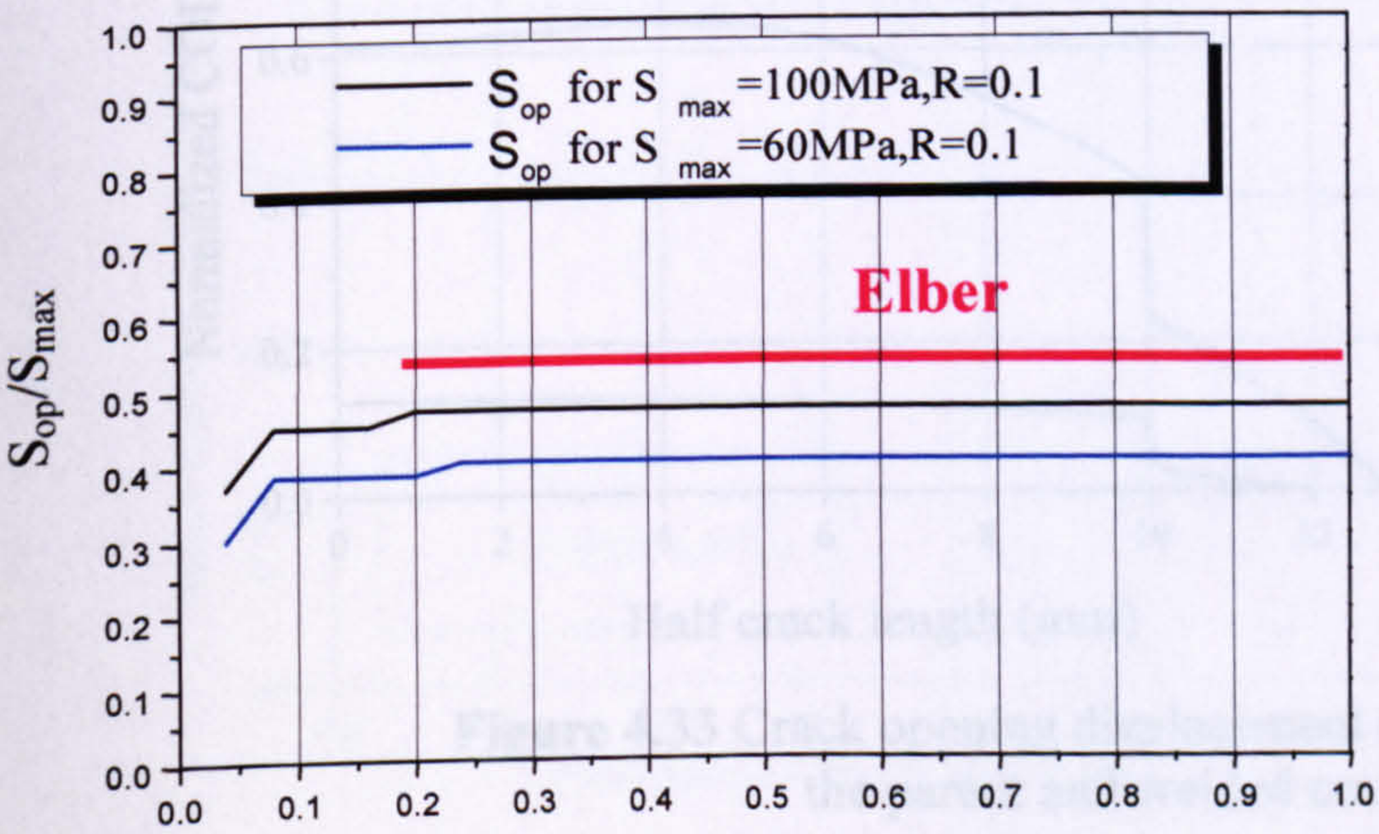

Finite element size = 0.04mm (10% r_p)
Case 1: S_{max}=110 MPa and a_o = 4mm
Case 2: S_{max}= 60 MPa and a_o = 10mm

Difference in S_{open} = 7%

(Empirical Elber's rule)

Figure 4.31 Level of crack opening stress ratio versus crack length for two study cases. No welding residual stress influence.

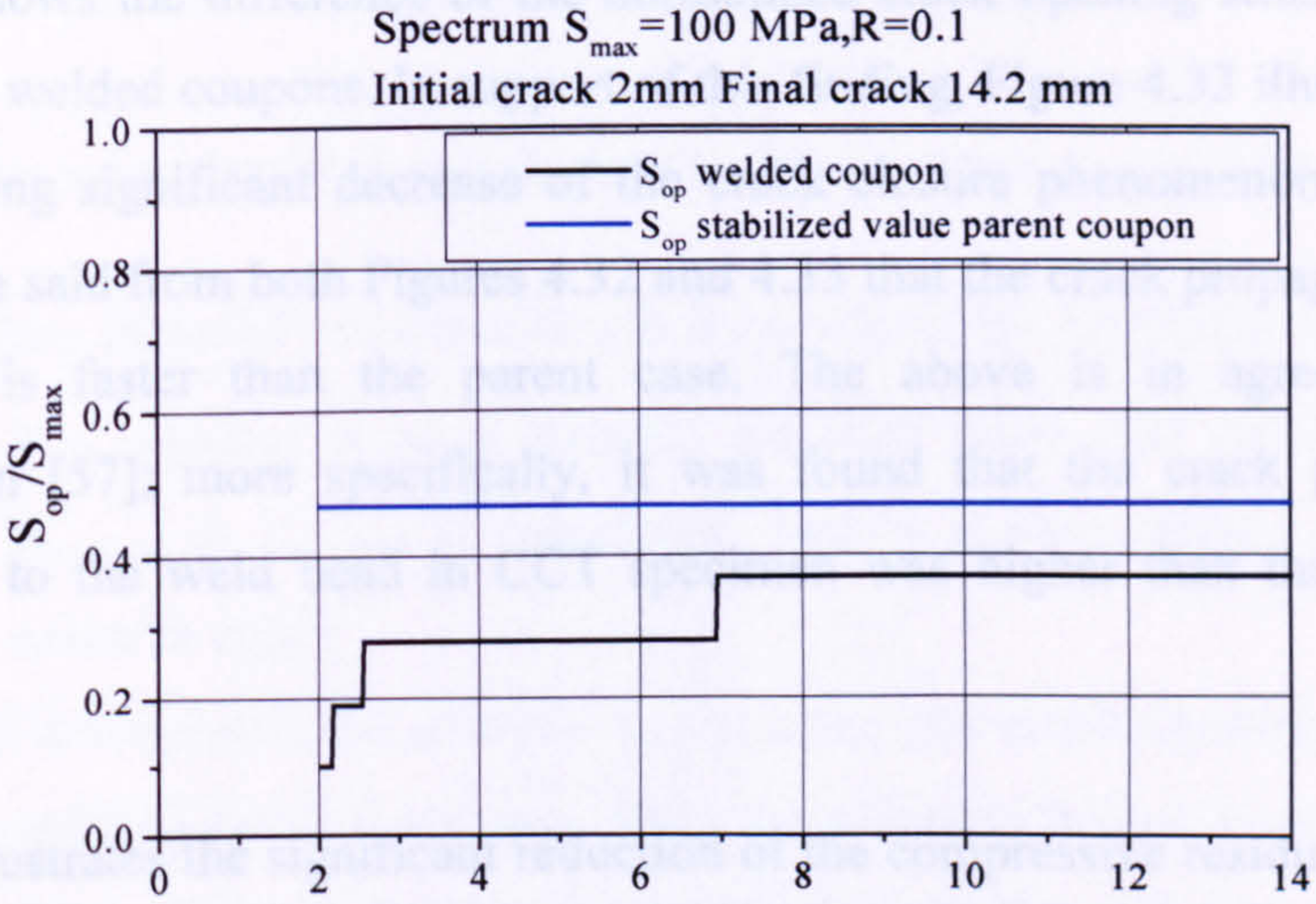

Figure 4.32 Comparison of the crack opening ratio between the Parent and Welded coupon.

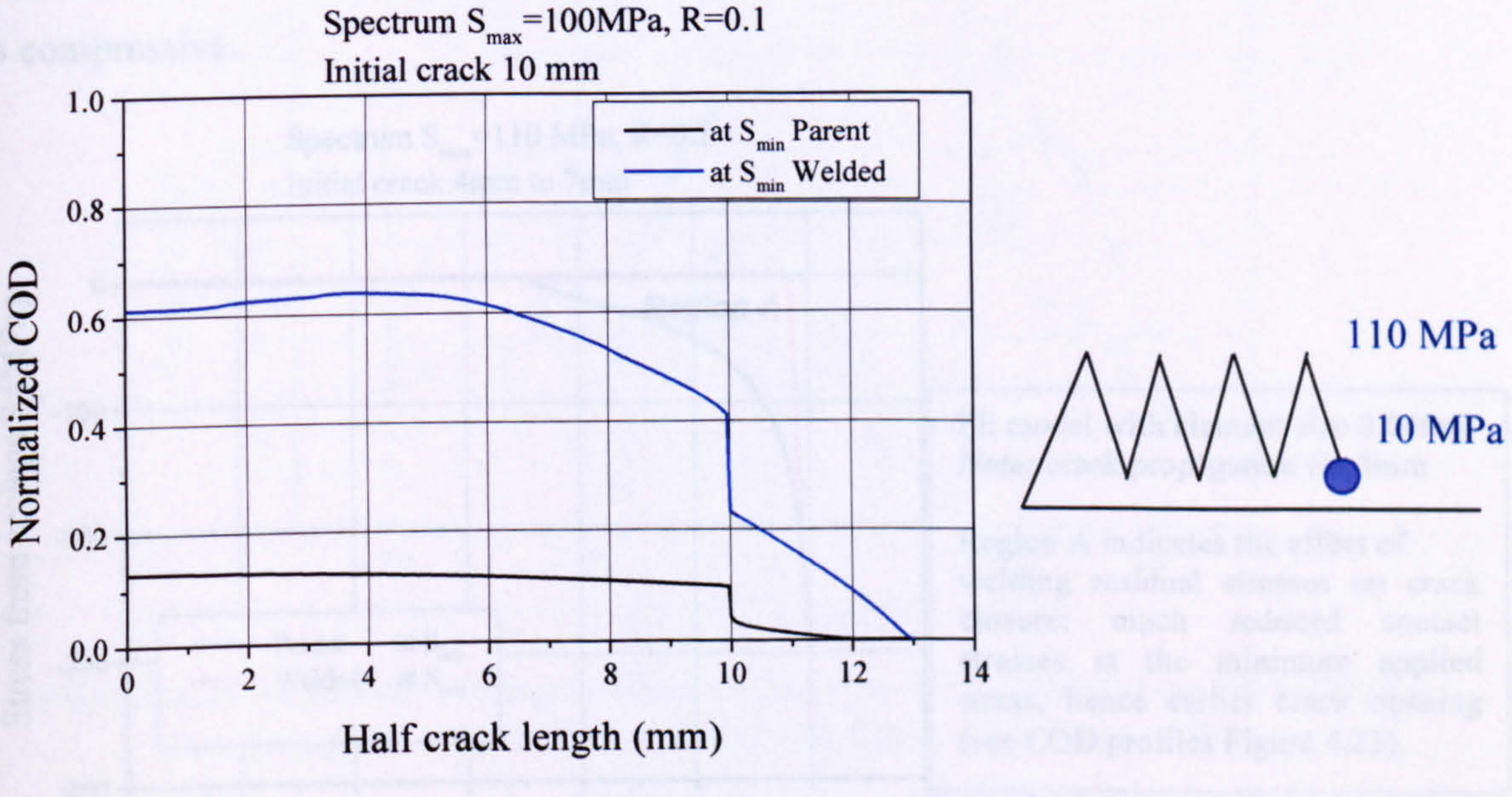

Figure 4.33 Crack opening displacement comparison between the parent and welded coupon.

Figure 4.32 shows the difference of the normalized crack opening stresses between the parent and the welded coupons. In support of this finding, Figure 4.33 illustrates the COD profiles showing significant decrease of the crack closure phenomenon for the welded case. It can be said from both Figures 4.32 and 4.33 that the crack propagation rate in the welded case is faster than the parent case. The above is in agreement with the experiments in [57]; more specifically, it was found that the crack propagation rate perpendicular to the weld bead in CCT specimen was higher than the CT un-welded specimen .

Figure 4.34 illustrates the significant reduction of the compressive residual stresses in the crack wake during unloading. That significant effect on these compressive residual stresses in the crack wake is due to the welding tensile residual stresses. Especially, at the early stage of the crack propagation and near the weld line where the welding residual stresses are highly tensile this phenomenon is more intense. Further away this effect is reduced since the welding residual stresses away from the weld line change from tensile to compressive.

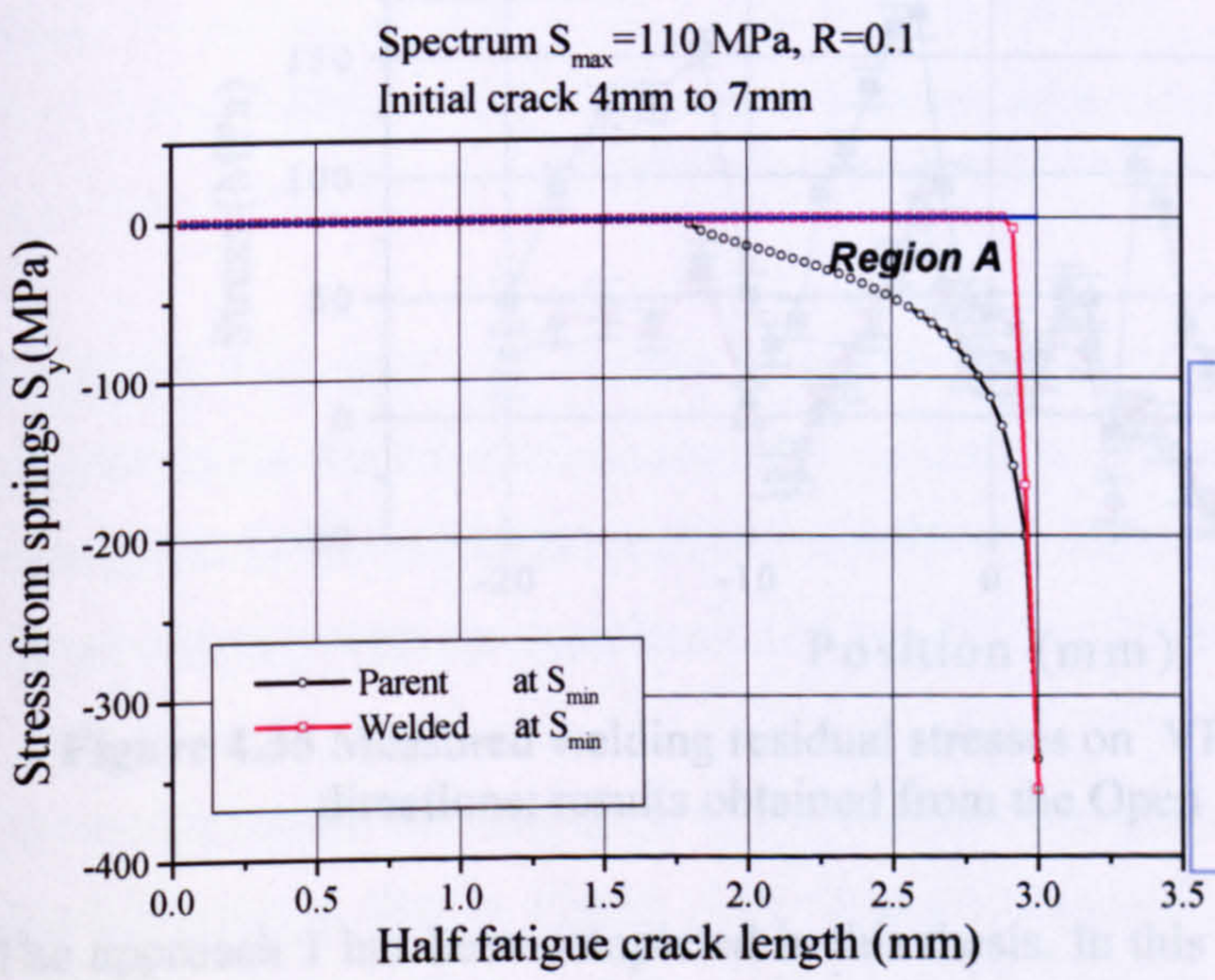

FE model with element size 0.04mm
Note: crack propagation for 3mm

Region A indicates the effect of welding residual stresses on crack closure: much reduced contact stresses at the minimum applied stress, hence earlier crack opening (see COD profiles Figure 4.33).

Figure 4.34 Local stresses at region A at the crack wake of the advanced crack tip.

4.5 Prediction of Crack Propagation Life of Welded Coupons

Two approaches were identified and planned to predict crack growth life.

Approach 1: Beta factor (β) vs crack length is calculated by ABAQUS for plain samples. The welding residual stresses are then input into AFGROW code and $K_{residual}$ & $K_{applied}$ is calculated. This is a linear-elastic approach and is easier to apply.

Approach 2: Elastic-plastic FE analysis to calculate the crack opening level including welding residual stresses. Then the effective fatigue cycle load versus the crack length is known. So a definition of the effective part of the cycle load can be established. Unfortunately, in this thesis *approach 2* was not demonstrated.

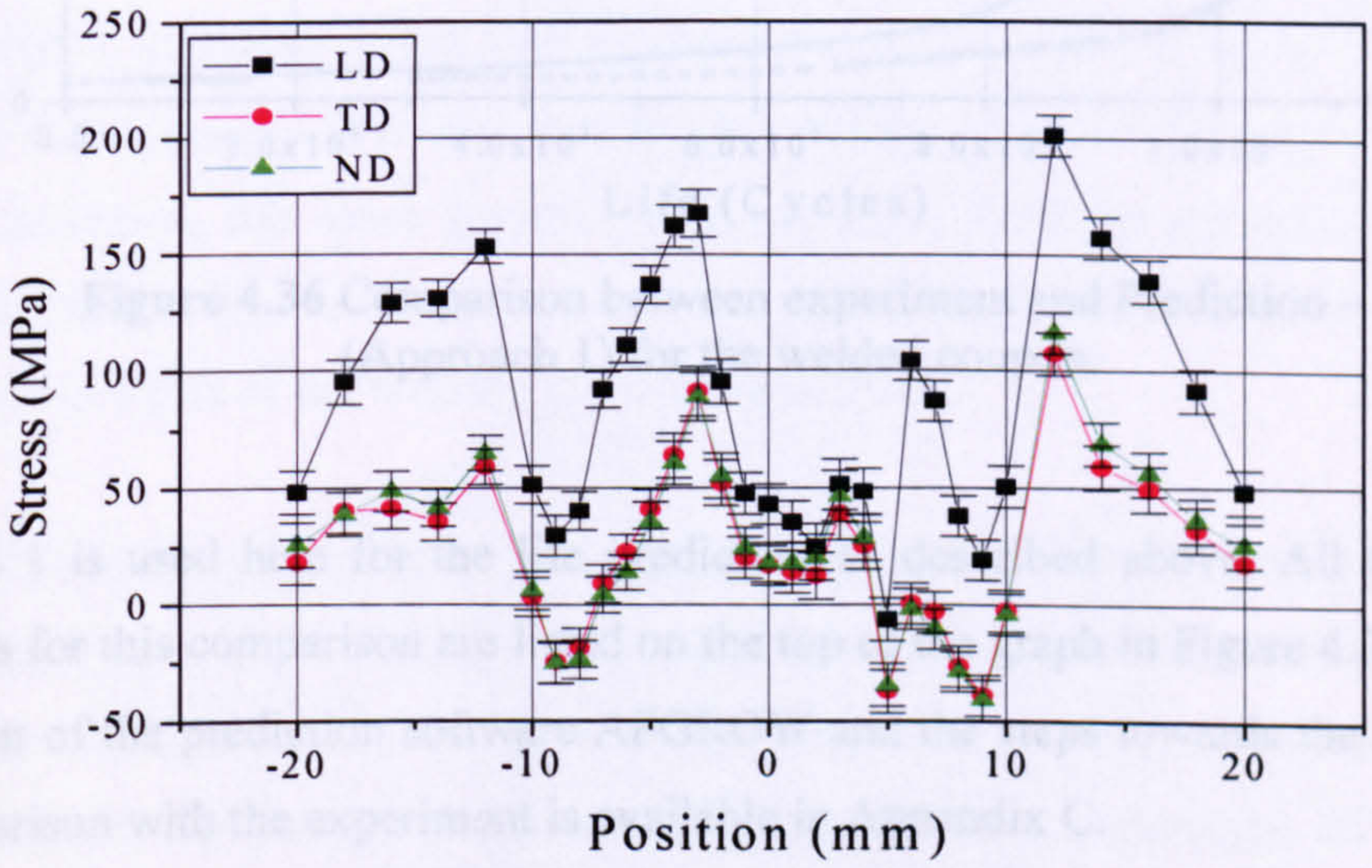

Figure 4.35 Measured welding residual stresses on VPPA welded coupons at three directions; results obtained from the Open University [58].

The approach 1 has been completed in this thesis. In this application, the latest and more accurate measurements on the CCT coupons in terms of welding residual stresses distributions are presented in Figure 4.35 [58]. Only the longitudinal (LD) and transverse (TD) distributions were used in the 2-D FE model of this study since no modelling into the three dimensions was done.

AFGROW software [59] was used in this paragraph in order to predict the crack propagation of the welded dog-bone coupon. This prediction was compared with the available experimental crack propagation curve. The method used for the acquisition of this experimental curve (crack length versus life) is Direct Current Potential Drop (DCPD). This method was used from Dr. Lin in SIMS department in Cranfield University [60].

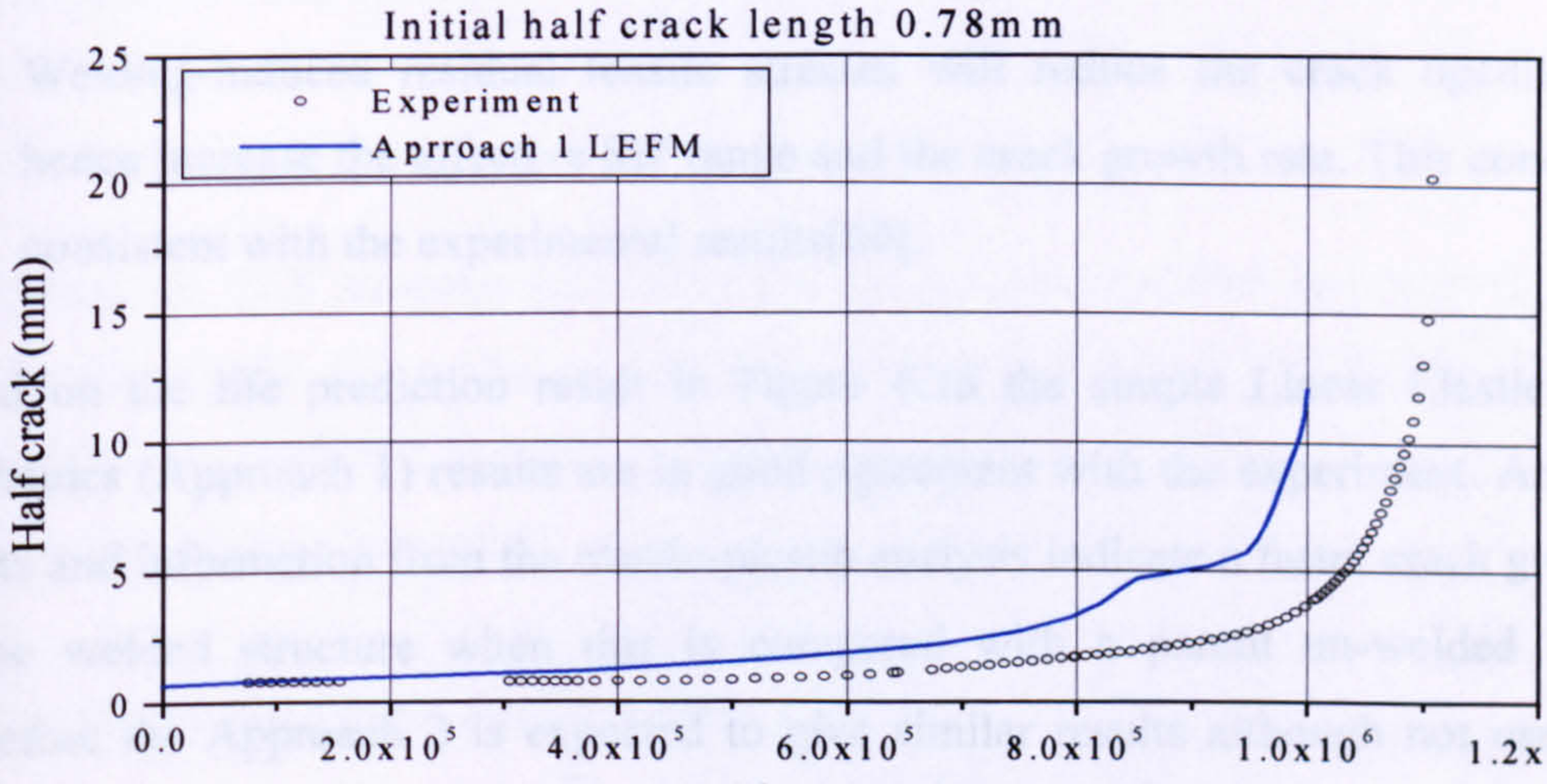

Figure 4.36 Comparison between experiment and Prediction – (Approach 1) for the welded coupon.

Approach 1 is used here for the life prediction as described above. All the necessary conditions for this comparison are listed on the top of the graph in Figure 4.36. A detailed description of the prediction software AFGROW and the steps towards the realisation of the comparison with the experiment is available in Appendix C.

The experimental data in Figure 4.36 are from experiment on through crack CCT coupon dog-bone shape like in Figure 4.15. The welding method, which was used for these welded coupon is VPPA and the material aluminium alloy 2024-T351 [60]. From Figure 4.36 it can be observed that a good agreement was achieved between the prediction and the experiment.

4.6 Concluding remarks

Following the report of these FE results in the coupon level two main conclusions can be drawn.

- Crack opening stress is mainly affected by the R-ratio of cyclic stresses, and is relatively independent of the maximum applied stress and initial crack length. This is advantageous for structural fatigue analysis under various amplitude analysis.

- Welding-induced residual tensile stresses will reduce the crack opening stress, hence increase the effective SIF range and the crack growth rate. This conclusion is consistent with the experimental results[60].

Based on the life prediction result in Figure 4.36 the simple Linear Elastic Fracture Mechanics (Approach 1) results are in good agreement with the experiment. Also all the results and information from the elastic-plastic analysis indicate a faster crack growth rate of the welded structure when this is compared with a parent un-welded structure. Therefore the Approach 2 is expected to give similar results although not used in this study. In addiction, this crack growth rate slows down since the advancing crack leaves the intense tensile residual stress part near the weld line and HAZ and moves forward to the compressive part of the welding residual stress field.

Furthermore, it can be said that the welding procedure tends to diminish the plasticity induced crack closure phenomenon near the weld line, where tensile residual stresses are present like was concluded in Figure 4.34. On the contrary, in regions where compressive residual stresses are present due to welding there is an enhancement of the plasticity induced crack closure phenomenon since the compressive part of the welding residual stress distribution contributes at the compressive residual stresses at the crack wake.

CHAPTER 5

CRACK PROPAGATION ANALYSIS IN STIFFENED WELDED PANELS

Following the CCT coupons modelling, the analysis is expanded in larger structures. A description of the FE model of the two-stringer panel is given first. Fatigue crack propagation is predicted in both the parent and welded structure and comparison with experimental data is presented.

5.1 FE Model Description and Modelling Strategy

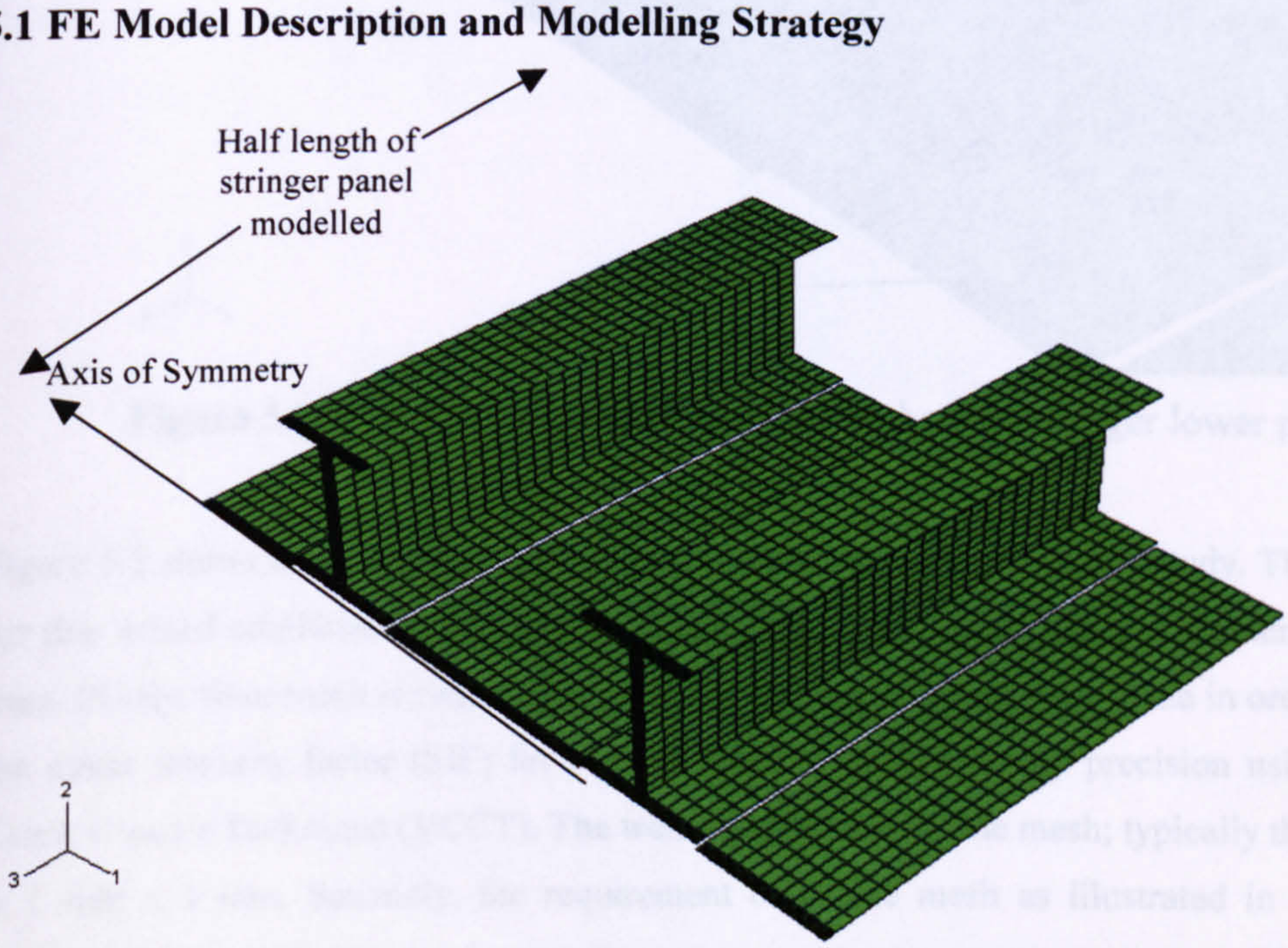

Figure 5.1 Iso-metric view of the FE model of the two-stringer tension panel.

Figure 5.1 illustrates the FE model of the two-stringer tension panel. This is a 2-D FE model using thin shell elements of eight nodes. Only the half modeled due to symmetry. The locations of damage initiation were assumed at:

- The web of the stiffener.
- The mid-bay skin of the stiffened panel.

The load is applied on the nodes of the thin shell elements. Due to the second order of the used thin shell elements the ratio of 1:4:1 between the three nodes of the element edge must be considered in order to result in a uniform applied load.

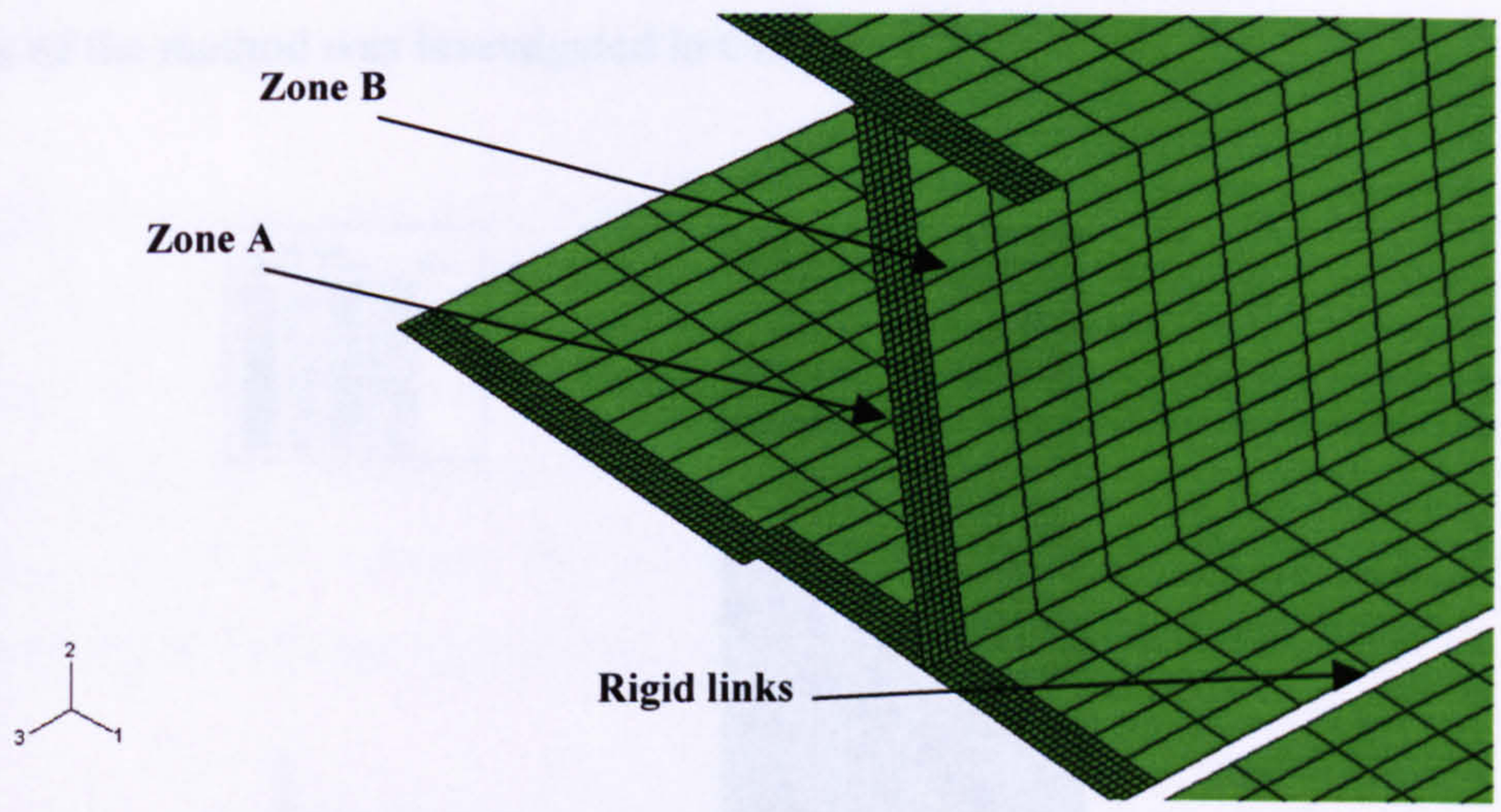

Figure 5.2 A close view of the FE model of the two-stringer lower panel.

Figure 5.2 shows the two-zones mesh concept, which was applied in this study. The main reason for this mixed combination of coarse and fine mesh is to satisfy two requirements at the same time. Firstly, finer mesh is required in zone A in region near the crack plane in order to calculate the stress intensity factor (SIF) for a given crack with satisfactory precision using the Virtual Crack Closure Technique (VCCT). The technique requires a fine mesh; typically the element size is 1 mm x 1 mm. Secondly, the requirement of coarse mesh as illustrated in Zone B is for efficient FE model with low calculation time on the personal computer. The connection between the two zones is achieved by utilizing the multipoint constraint (MPC) in

ABAQUS. This enables the FE model to behave as one part under the application of external load.

In addition, due to the different level of the thin shell finite elements plane, which represents the skin area and the doublers area, there is need for use of rigid link elements along these two edges, which are in different height. Rigid link elements provide a bond between these nodes and as a result the whole FE model functions as one part under the applied load (Figure 5.2). Using the VCCT concept and having already validated the accuracy in a simple plate model for the same mesh pattern the SIF can be calculated and therefore the geometry factor beta is derived. The FE model length is 500 mm due to the symmetry axis. Like in the coupon-level analysis the VCCT methods was used here. The accuracy of the method was investigated in Chapter 4.

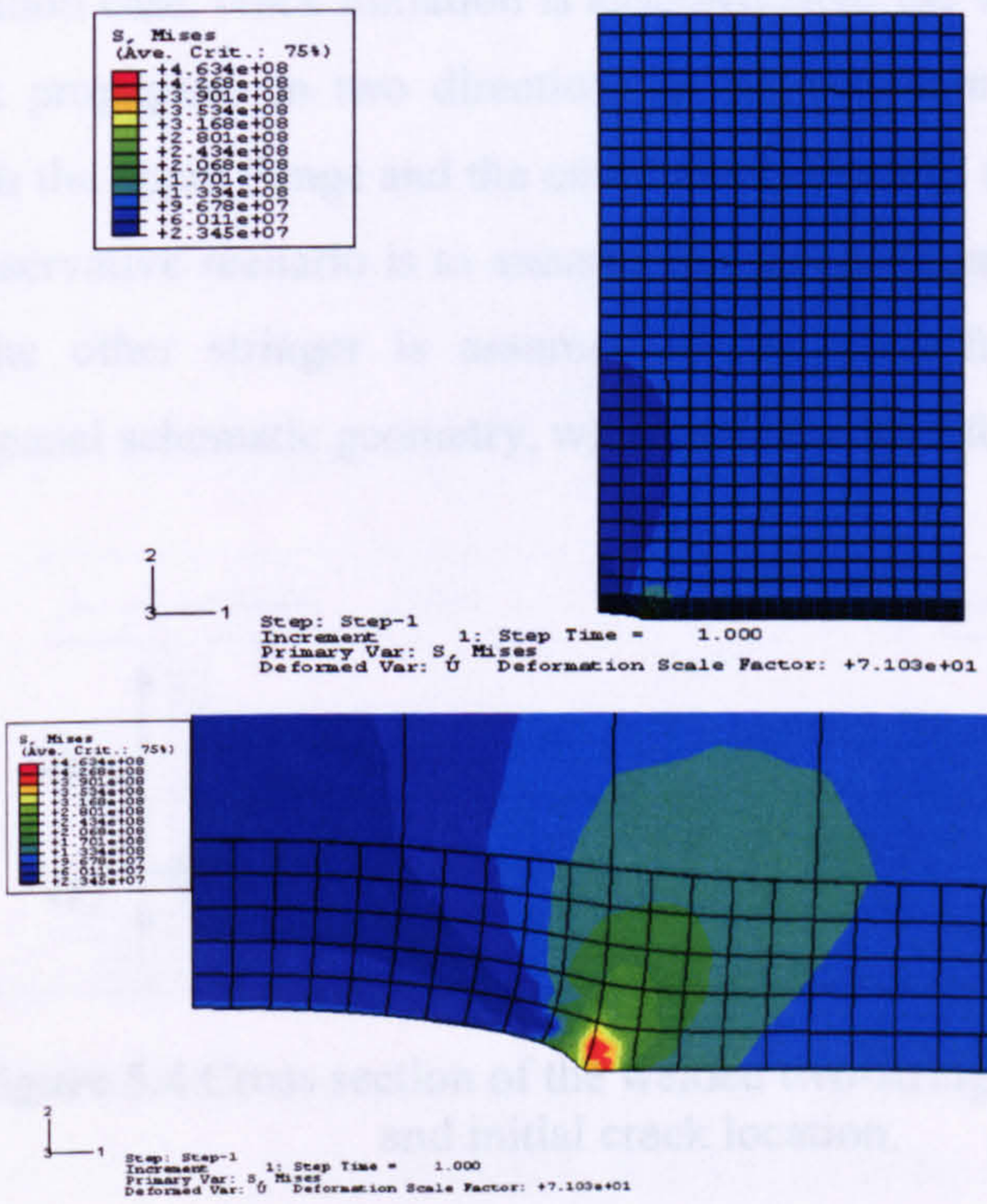

Figure 5.3 Presentation of Von Mises stress contour at the area of MPC.

Figure 5.3 illustrates the Von mises stress distribution around the crack tip but more importantly around the transition area from the zone of the fine mesh (Zone A) to the coarse mesh (Zone B). Generally, it is not good practice to connect one finite element to 4 sub-elements using the multipoint constrain tool available in ABAQUS. The above is not considered to be a smooth transition from one region to the other and maybe more zones should be used between the existing ones in order to ensure a more smooth transition like in was done in chapter 4. Nevertheless, a simple finite element plate model with the MPC scheme used in the stiffened panel model is presented in Figure 5.3 that illustrates an adequately smooth stress contour.

5.2 Results of Simple LEFM Approach – (Crack Starts on the Web)

In this calculation case, crack initiation is assumed from the weld line at the stringer web and the crack propagates in two directions as illustrated in Figure 5.4. One crack tip moves towards the upper flange and the other moves towards the doubler of the stiffener. The most conservative scenario is to assume that the crack grows simultaneously in both directions. The other stringer is assumed to be crack free. Figure 5.4 shows the experimental panel schematic geometry, which was the base for the FE model

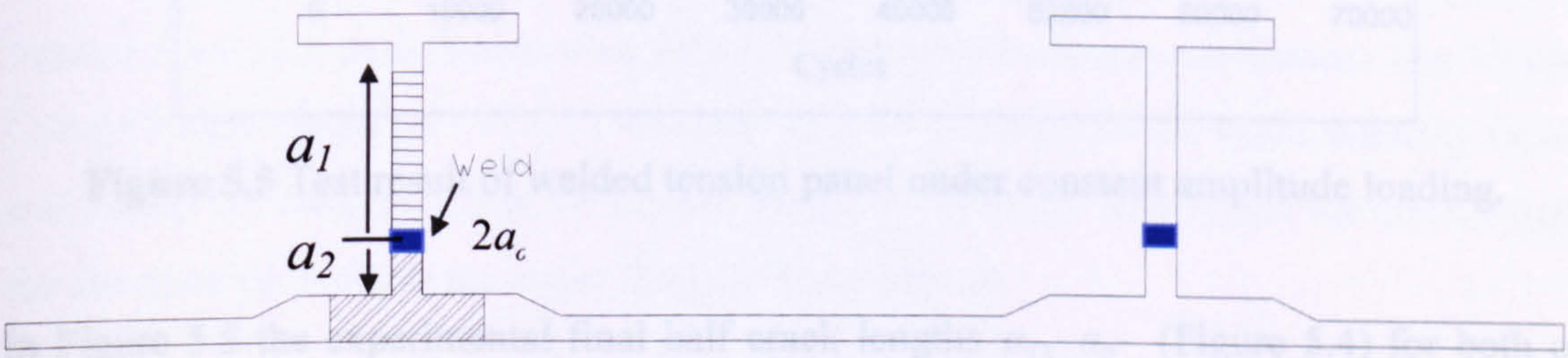

Figure 5.4 Cross section of the welded two-stringer tension panel and initial crack location.

Before a comparison is achieved between the experimental results and the simple linear elastic fracture mechanics approach in terms of crack length versus life-cycles the results from the experiment are shown in Figure 5.5. The initial crack is a through-thickness

crack having an initial crack length $2a_o = 5.62$ mm. Due to the dual crack propagation direction the initial crack length for each path was taken as the half crack length α_o.

The experimental method used in order to produce the measurements in Figure 5.5 is called Direct Current Potential Drop Technique (DCPD). The principal purpose of DCPD technique is measurement of crack length during a fatigue test on a structure [61]. The latter enables further manipulation of the experimental data in order to build an experimental curve like in Figure 5.5. The experiments presented here were carried out in SIMS department of Cranfield University. Dr. Lin was in charge at the time. Further details and more of Dr. Lin's experimental work within this project can be found in [60].

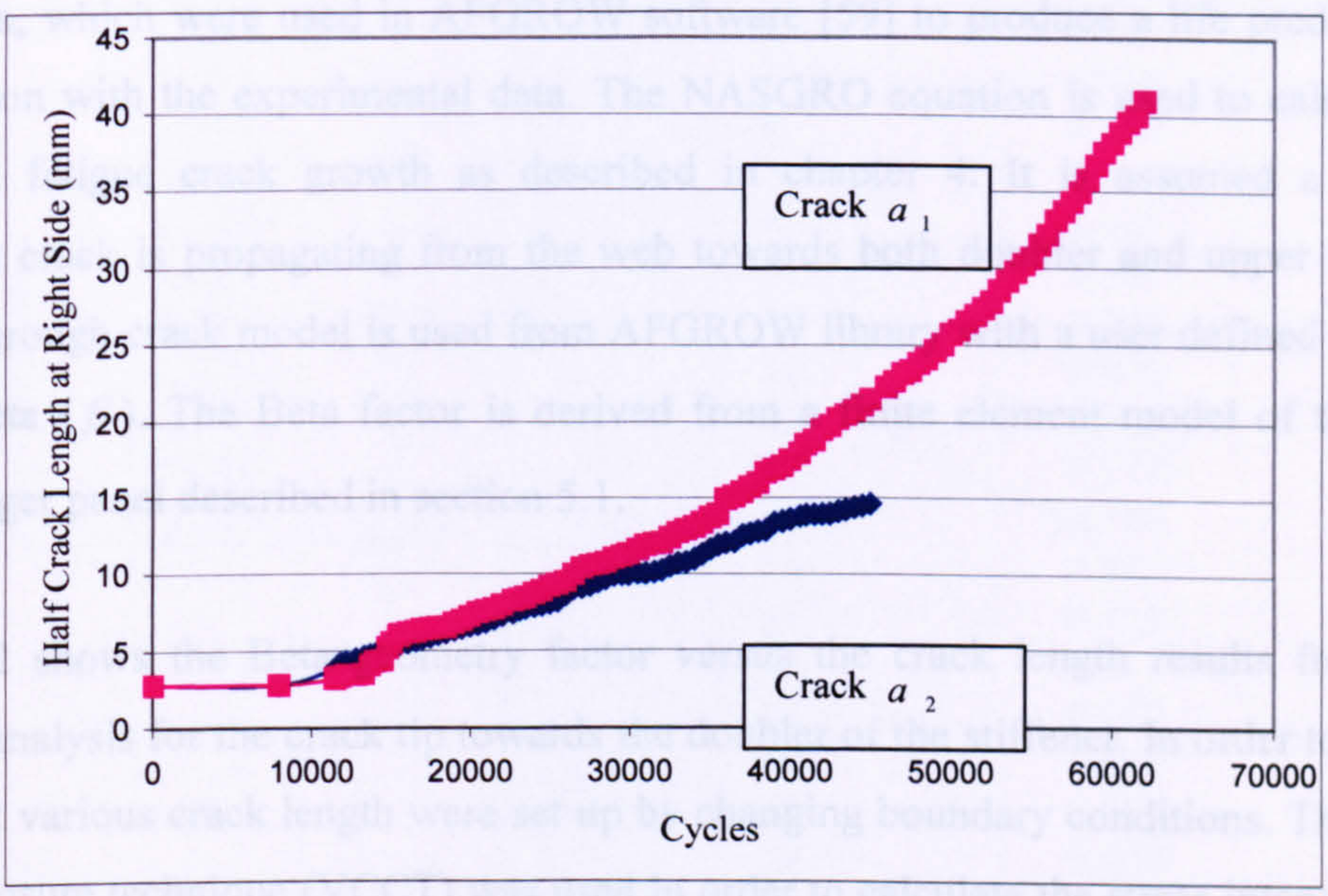

Figure 5.5 Test result of welded tension panel under constant amplitude loading.

In Figure 5.5 the experimental final half crack lengths α_1, α_2 (Figure 5.4) for both of the crack tips of the crack are illustrated there. The weld line in the FE modeling is assumed to be 15 mm away from the doubler in order to be compatible with the experiment. Therefore the final half crack length for the crack tip which moves towards the doubler is 15 mm as it can be seen from Figure 5.5. Experimental data up to 42 mm final crack length towards the upper flange were available.

Table 5.1 Material properties and required parameters for NASGRO equation.

Properties (Unit)	Value
Young's Modulus (GPa)	73
Poisson Ratio	0.33
Yield Strength (MPa)	372
Plane Strain, K_{IC} (MPa$\sqrt{m}$)	37
Plane Stress K_C (MPa$\sqrt{m}$)	75
Paris Constant, C	0.7073E-10
Paris Constant, n, in NASGRO	3.353
NASGRO parameter, p	0.5
NASGRO parameter, q	1

The material of the stiffened panel is 2024-T351. Table 5.1 illustrates the full material properties, which were used in AFGROW software [59] to produce a life prediction for comparison with the experimental data. The NASGRO equation is used to calculate the predicted fatigue crack growth as described in chapter 4. It is assumed a through-thickness crack is propagating from the web towards both doubler and upper flange. A central through crack model is used from AFGROW library with a user defined geometry factor Beta (β). The Beta factor is derived from a finite element model of the parent two-stringer panel described in section 5.1.

Table 5.2 shows the Beta geometry factor versus the crack length results from finite element analysis for the crack tip towards the doubler of the stiffener. In order to produce Table 5.2 various crack length were set up by changing boundary conditions. The Virtual Crack Closure technique (VCCT) was used in order to calculate the stress intensity factor and finally the factor β. Table 5.3 reports the geometry factor beta versus the crack length for the crack tip towards the upper flange of the stiffener.

The whole range of crack length for each case is required from AFGROW in terms of crack length for a valid comparison between the prediction of the model and the experimental data. In case of insufficient data of the geometry factor for the range of the crack length indicated from the experimental data, AFGROW uses the last available value of the geometry factor in order to continue the life prediction. This function of AFGROW indicates the importance of sufficient data of geometry factor in order to

obtain a valid comparison with the experiment. Based on the experimental data in Figure 5.5 the measured crack length before failure for the crack tip towards the flange is 41 mm. The final measured crack length for crack tip towards the doubler is 14.6 mm. Tables 5.2 and 5.3 provide sufficient data of the geometry factor beta from the finite element analysis in order to ensure the valid comparison of the life prediction and the experiment.

Table 5.2 Beta versus crack length for crack tip towards doubler.

Crack length (mm)	Beta factor (β)
3	0.899
4	0.909
5	0.911
6	0.907
7	0.899
8	0.890
9	0.876
10	0.857
11	0.830
12	0.695
13	0.644
14	0.56

Table 5.3 Beta versus crack length for crack tip towards stiffener upper flange.

Crack length (mm)	Beta factor (β)
3	0.901
4	0.909
5	0.914
6	0.916
7	0.915
8	0.912
9	0.907
10	0.903
11	0.899
12	0.785
13	0.778
14	0.770
16	0.748
18	0.728
20	0.713
22	0.703
24	0.689
26	0.682
28	0.675
30	0.669
32	0.665
34	0.661
36	0.657
38	0.652
40	0.648

The next step for the prediction of crack growth in the welded panel is to input the measured welding residual stresses in AFGROW. Due to the one dimension crack propagation problem only the longitudinal distribution of the welding residual stresses is used here. The longitudinal welding residual stresses have been proved to be the dominant direction for this study. The effect from the transverse direction is insignificant

in terms of crack growth rate. Figure 5.6 illustrates the measured longitudinal welding residual stress distribution on the web of the stiffened panel [58].

The numerical calculation is based on the following data on initial crack length and load spectrum.

- Initial half crack : 2.81 mm (at experiment)
- Initial crack : 3 mm (at modeling)
- Constant amplitude Fatigue load : S_{max}=88 MPa , R=0.1

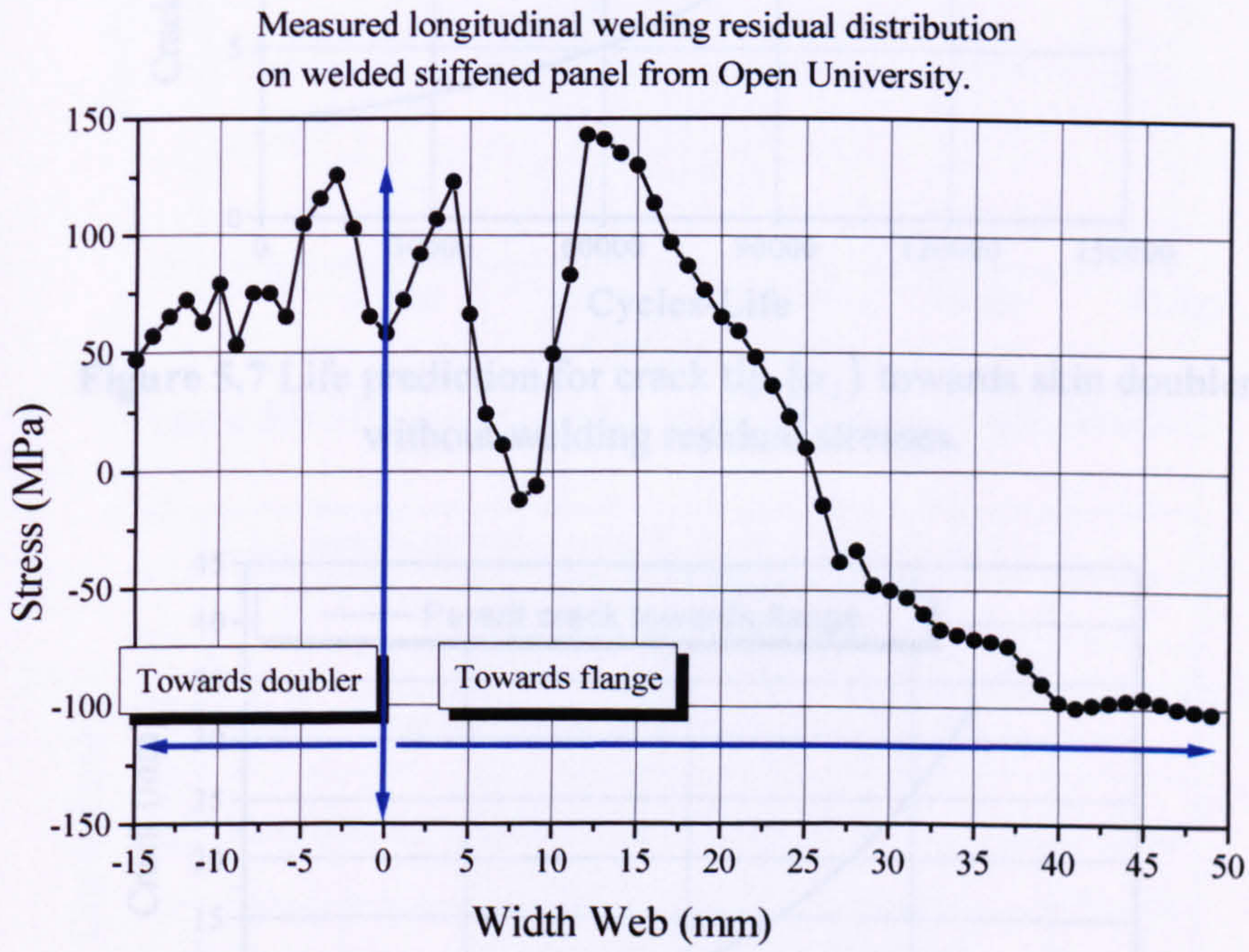

Figure 5.6 Measured longitudinal welding residual stress distribution.

Figures 5.7 and 5.8 present the life prediction for both crack tips going towards skin doubler and upper flange in the parent structure, respectively. In Figures 5.9 and 5.10 the solid lines illustrate the crack growth prediction for the welded case. It can be observed that the presence of welding residual stresses accelerates the crack growth in both directions significantly. For the same crack length the number of cycles for the crack towards the skin doubler is 110,000 and 30,000 for the parent and welded panels respectively. While for the other direction towards the upper flange, the rate reduces from 165,000 cycles to 60,000 cycles approximately. In Figure 5.10 as the crack approached

the upper flange boundary retardation of crack growth is evident. This is due to the boundary and the compressive stress zone in the welding residual stress distribution (α_1=25-40, Figure 5.6).

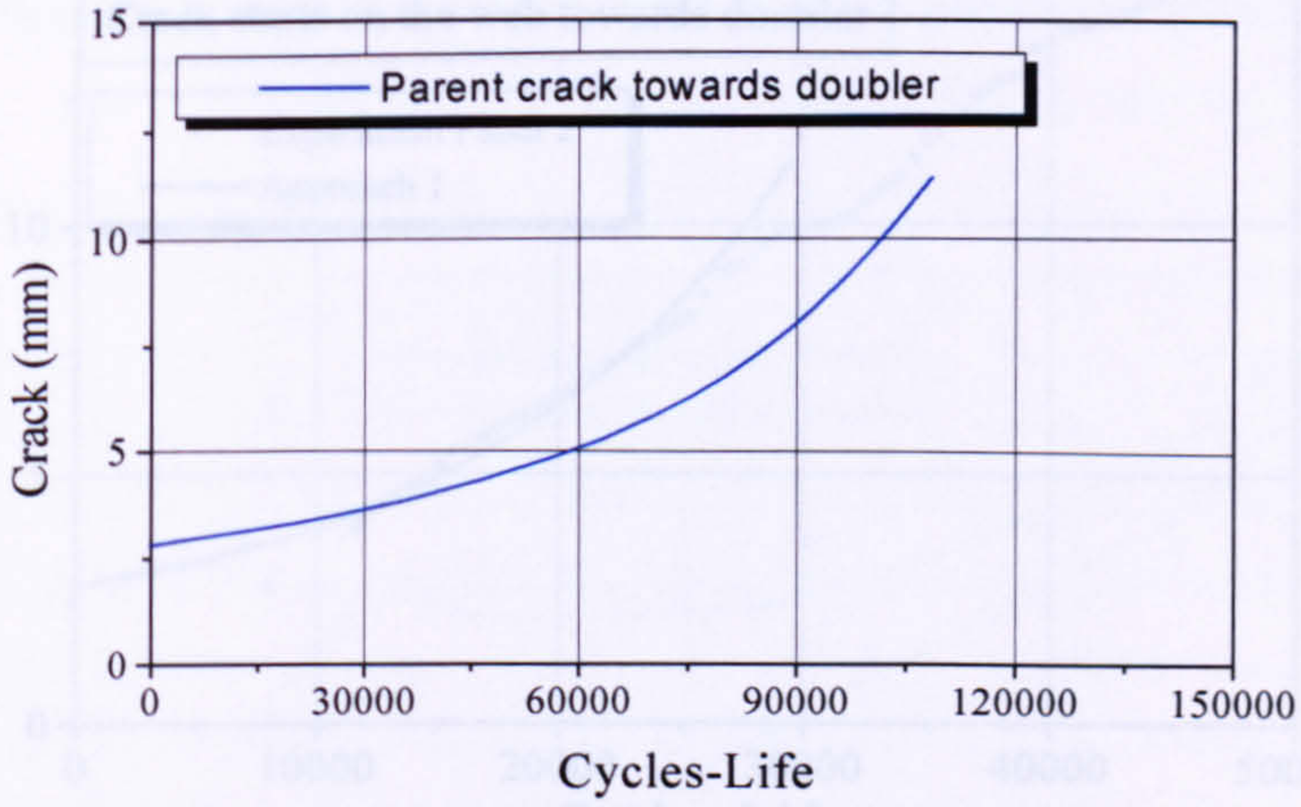

Figure 5.7 Life prediction for crack tip (α_2) towards skin doubler without welding residual stresses.

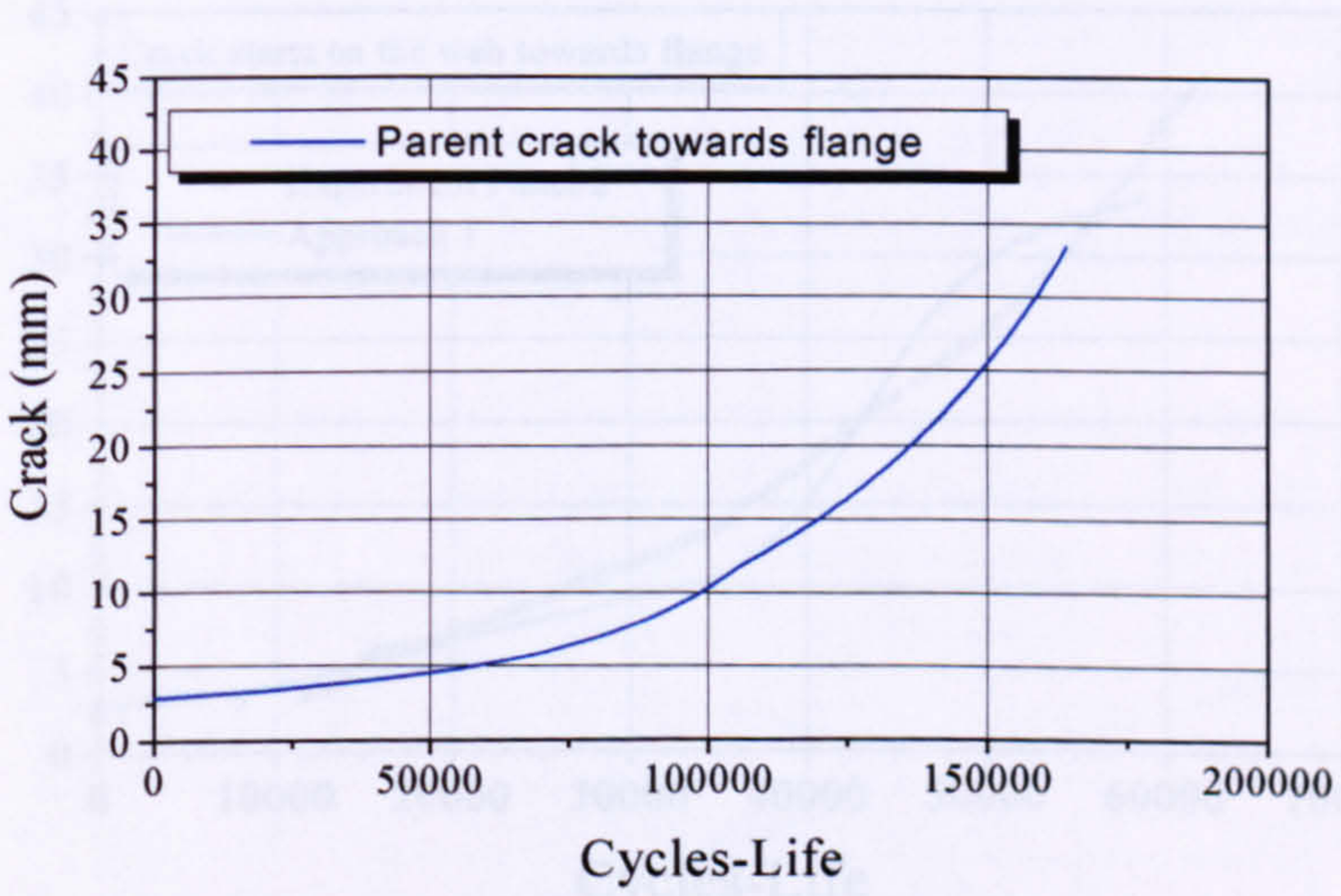

Figure 5.8 Life prediction for crack tip (α_1) towards upper flange without welding residual stresses.

Figures 5.9 and 5.10 present the comparison between the experiment and the numerical prediction for the crack tips towards skin doubler and upper flange, respectively, with the influence of welding residual stresses. A good comparison between the experiment and the numerical prediction is presented. Unfortunately no additional experimental curves

under the same conditions were available. Thus, the comparison between the numerical prediction and the experiment in Figures 5.9 and 5.10 do not present any experimental scatter range.

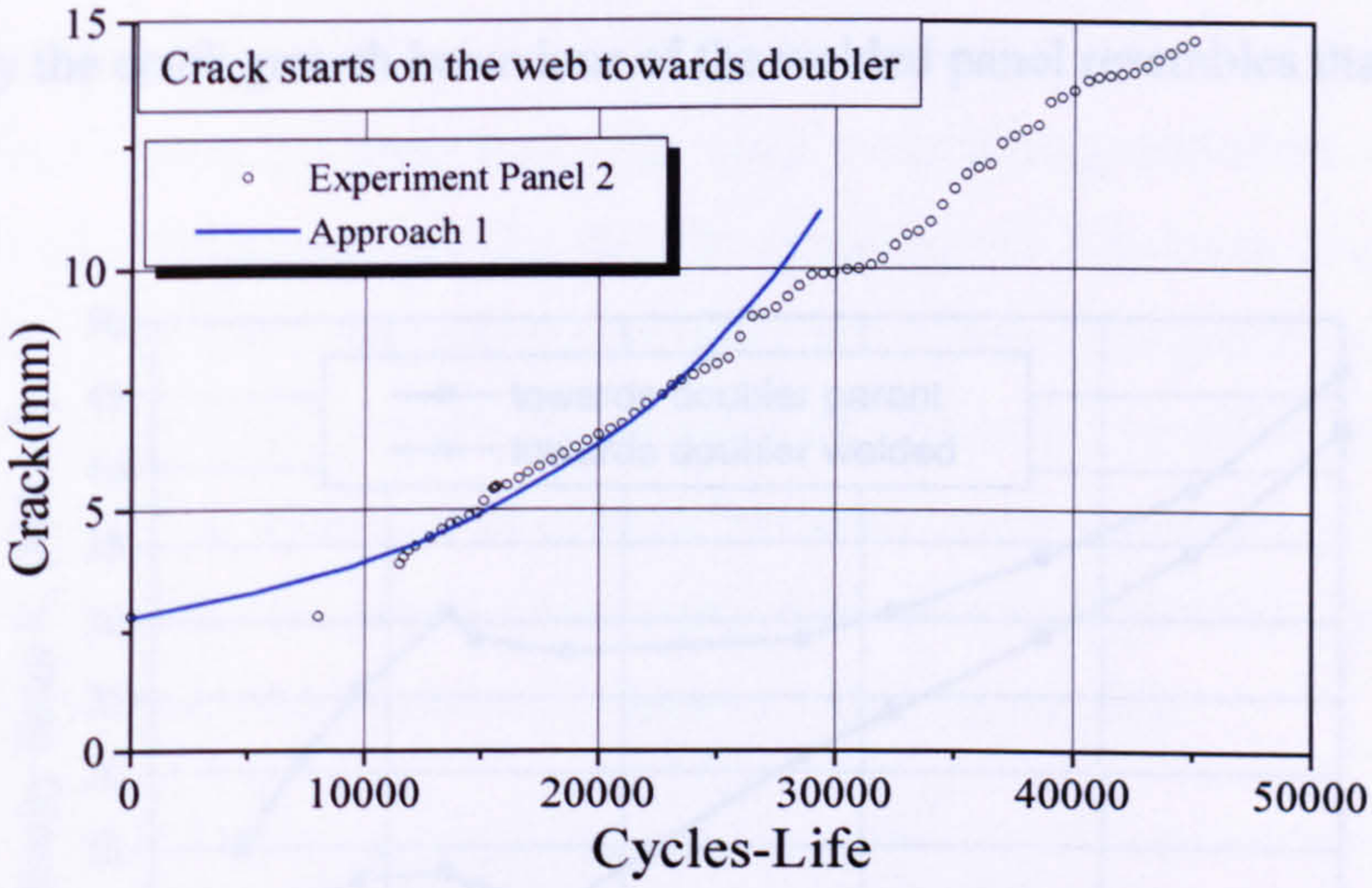

Figure 5.9 Life prediction for crack tip towards skin doubler.

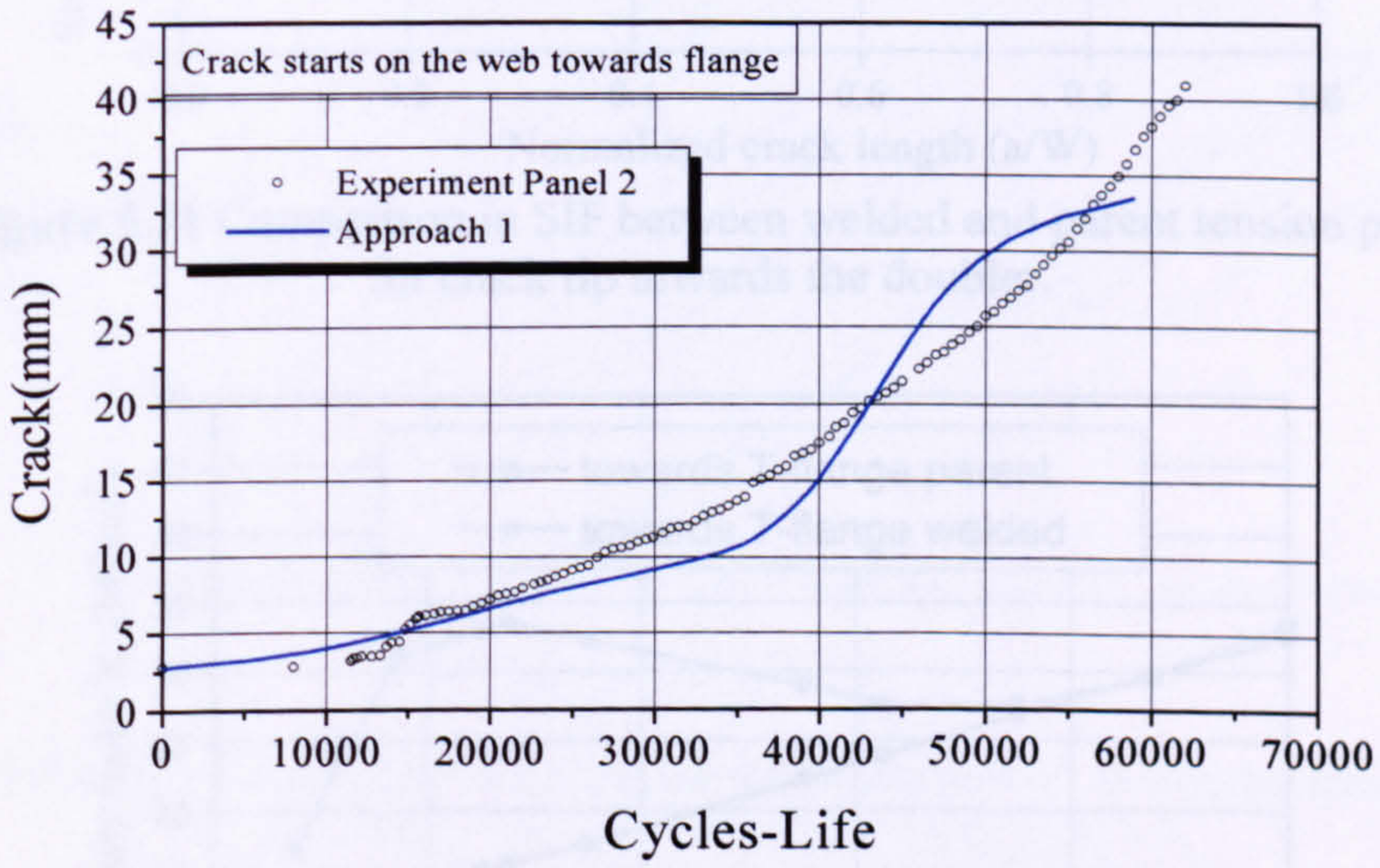

Figure 5.10 Life prediction for crack tip towards upper flange.

The effect of welding residual stresses on the stress intensity factor (SIF) is studied next using FE analysis for the parent and welded stiffened panels. Figures 5.11 and 5.12 illustrate the SIF versus the normalized crack length for the crack towards and the upper flange the doubler respectively. It can be observed that in the initial crack propagation stage the SIF of the welded panel is higher compared to the parent. This phenomenon is

due to the high tensile residual stresses in the area near the weld line. As the crack moves away from the welded area and into the compressive residual stress zone the SIF of the welded structure reduces. At that point the crack length is large enough so that the crack propagation is not slown down by the compressive region. Therefore the SIF and consequently the crack growth behaviour of the welded panel resembles that of the parent panel.

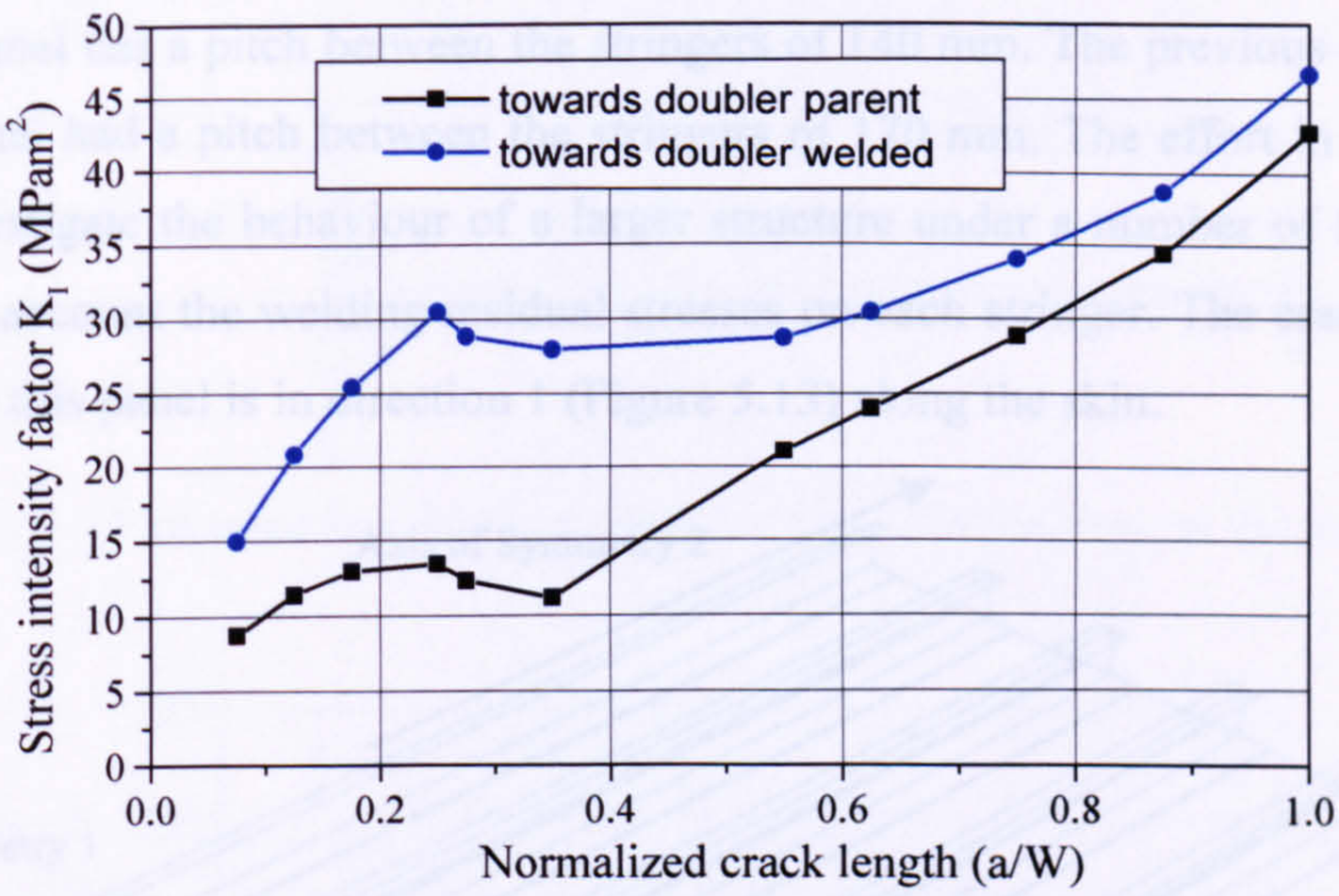

Figure 5.11 Comparison in SIF between welded and parent tension panel for crack tip towards the doubler.

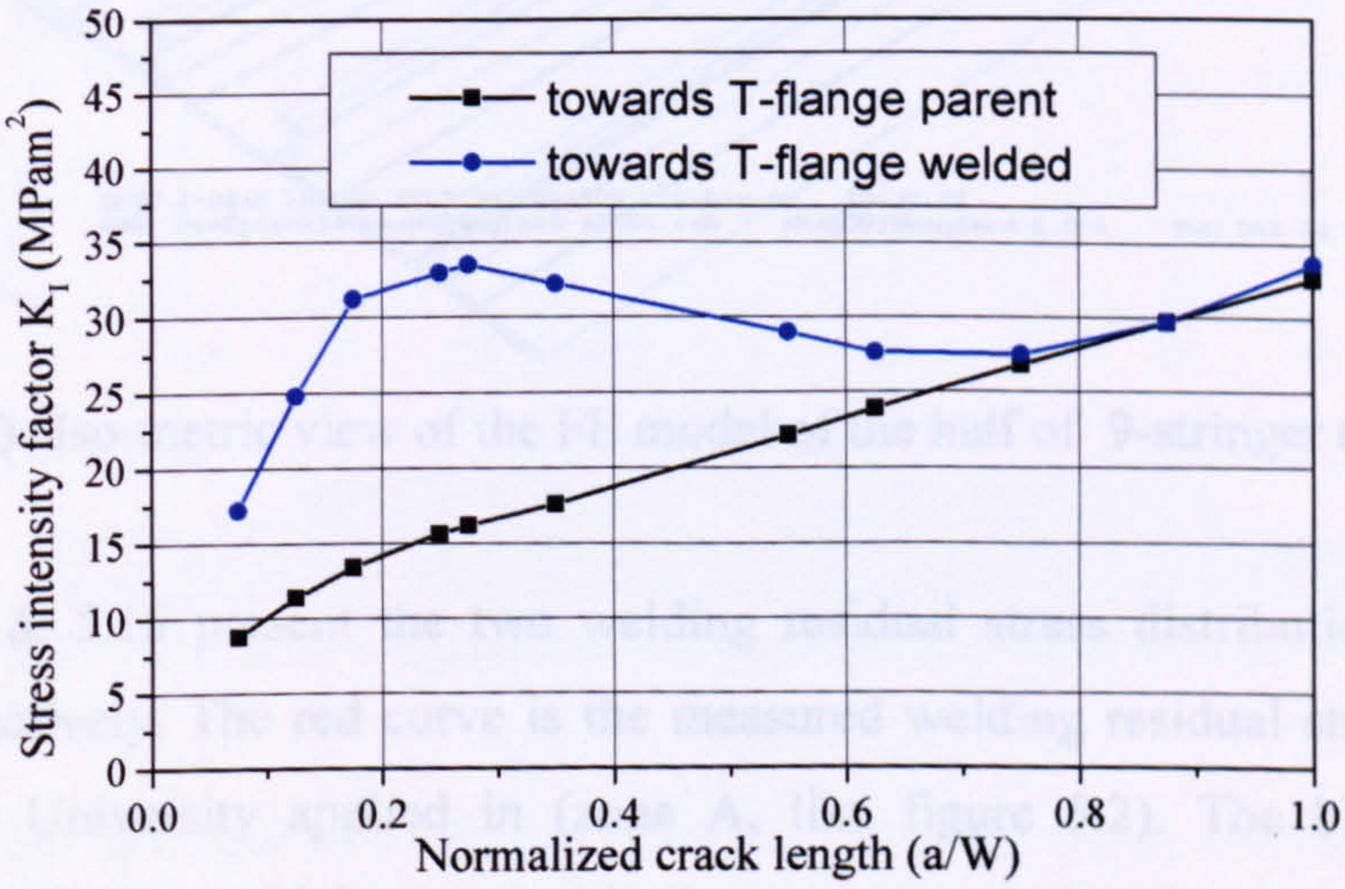

Figure 5.12 Comparison in SIF between welded and parent tension panel for crack tip towards the upper flange.

5.3 Large Scale Stringer Panel Study – (Crack Starts on the Skin)

The study is extended for larger stiffened panels were the crack assumed to start on the skin. Figure 5.13 presents the FE model of half of a nine-stringer stiffened panel. Due to the two axis of symmetry only one quarter of the panel, i.e. the four and a half stringers are modeled as shown in Figure 5.13. The same methodology and mesh were used here like as described in section 5.1 for the FE modeling of 2-stringer panel. This larger stiffened panel has a pitch between the stringers of 140 mm. The previous described two-stringer panel had a pitch between the stringers of 170 mm. The effort in this paragraph was to investigate the behaviour of a larger structure under a number of failed stringers taking into account the welding residual stresses on each stringer. The crack propagation direction in this panel is in direction 1 (Figure 5.13) along the skin.

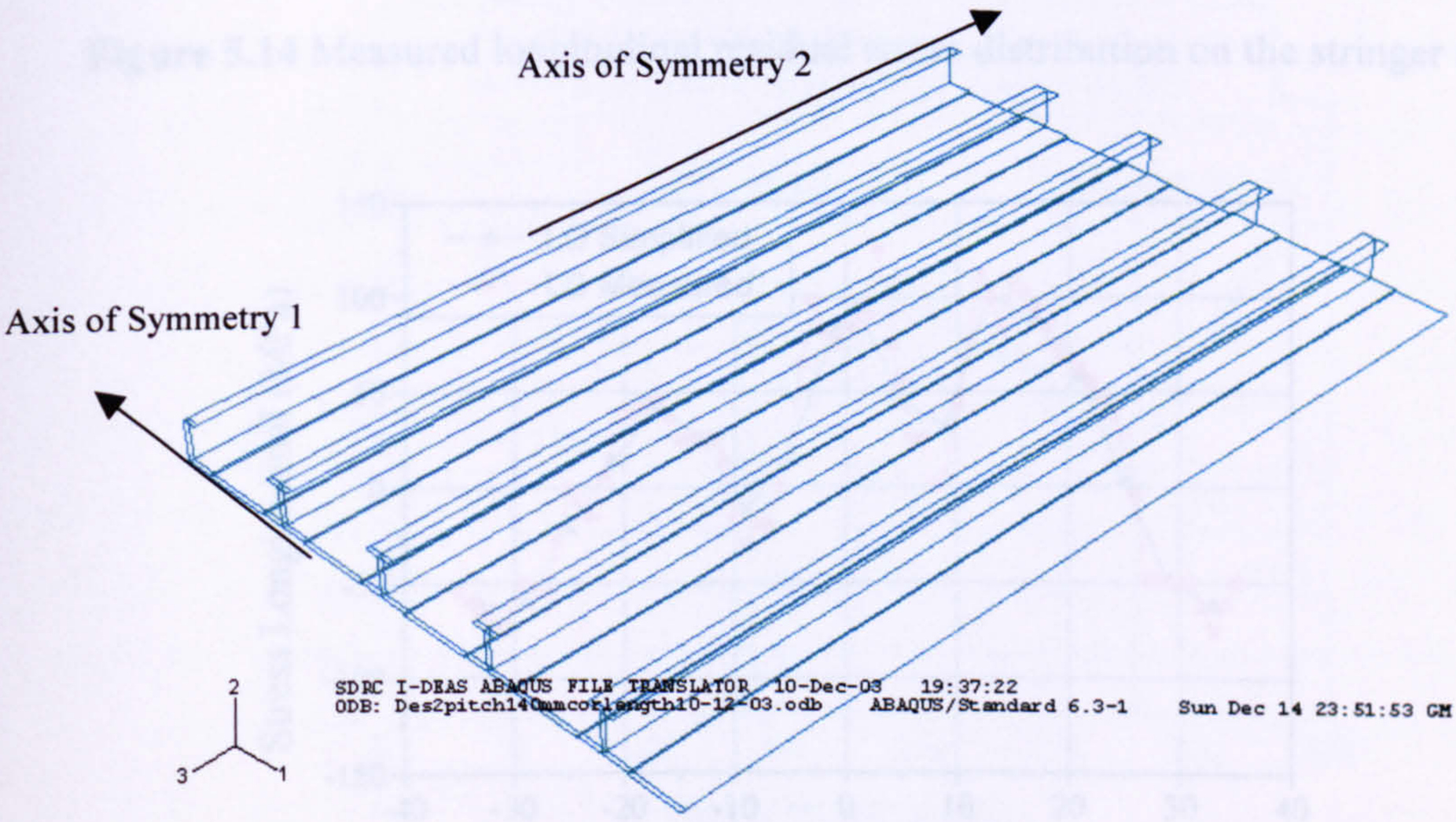

Figure 5.13: Iso-metric view of the FE model of the half of 9-stringer tension panel.

Figures 5.14 & 5.15 present the two welding residual stress distribution for web and doubler respectively. The red curve is the measured welding residual stress distribution by the Open University applied in (zone A, like figure 5.2). The black curve is a simplified distribution, which was used in the coarse mesh area (zone B, like figure 5.2) corresponding to the fewer number of elements.

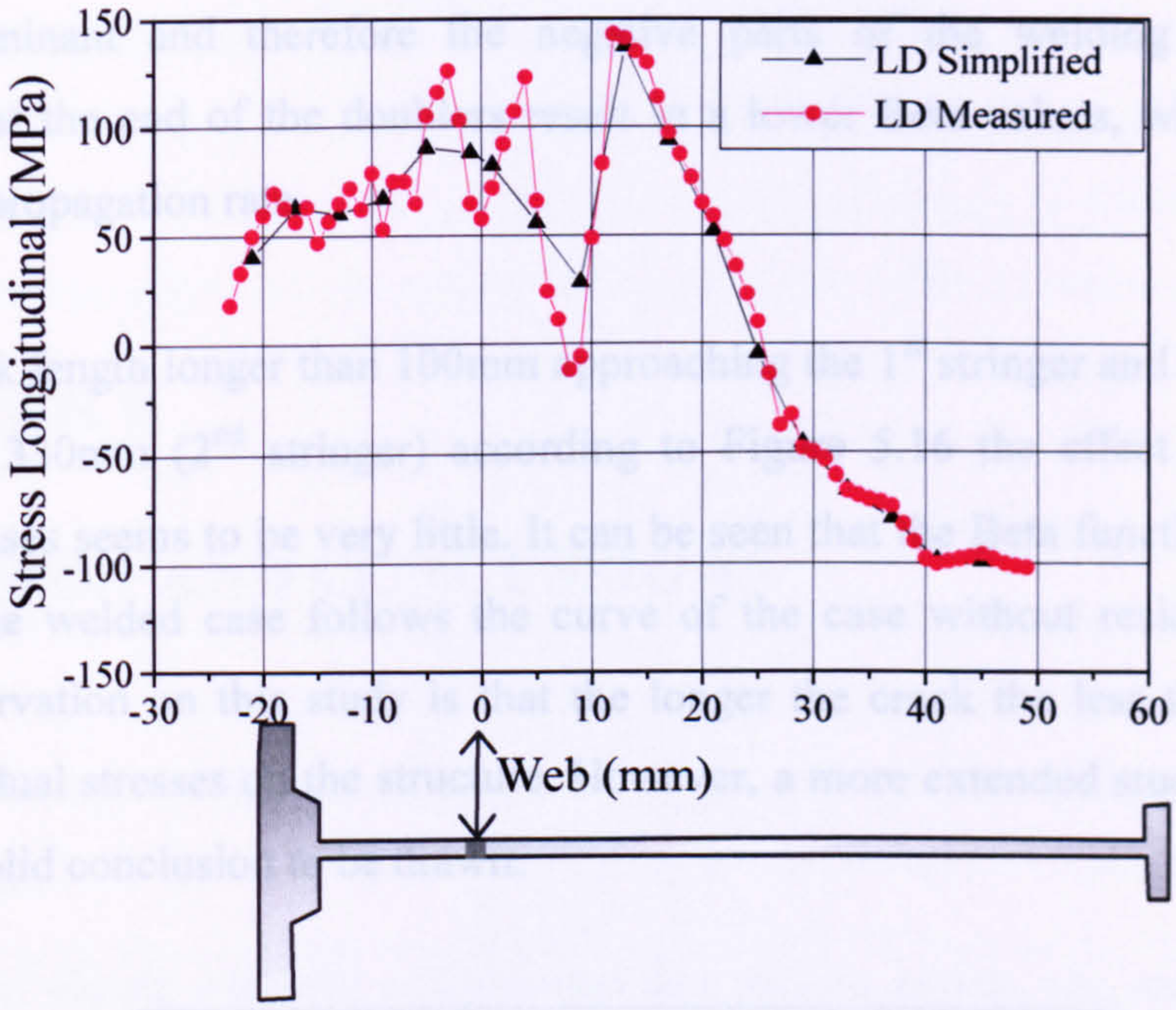

Figure 5.14 Measured longitudinal residual stress distribution on the stringer web.

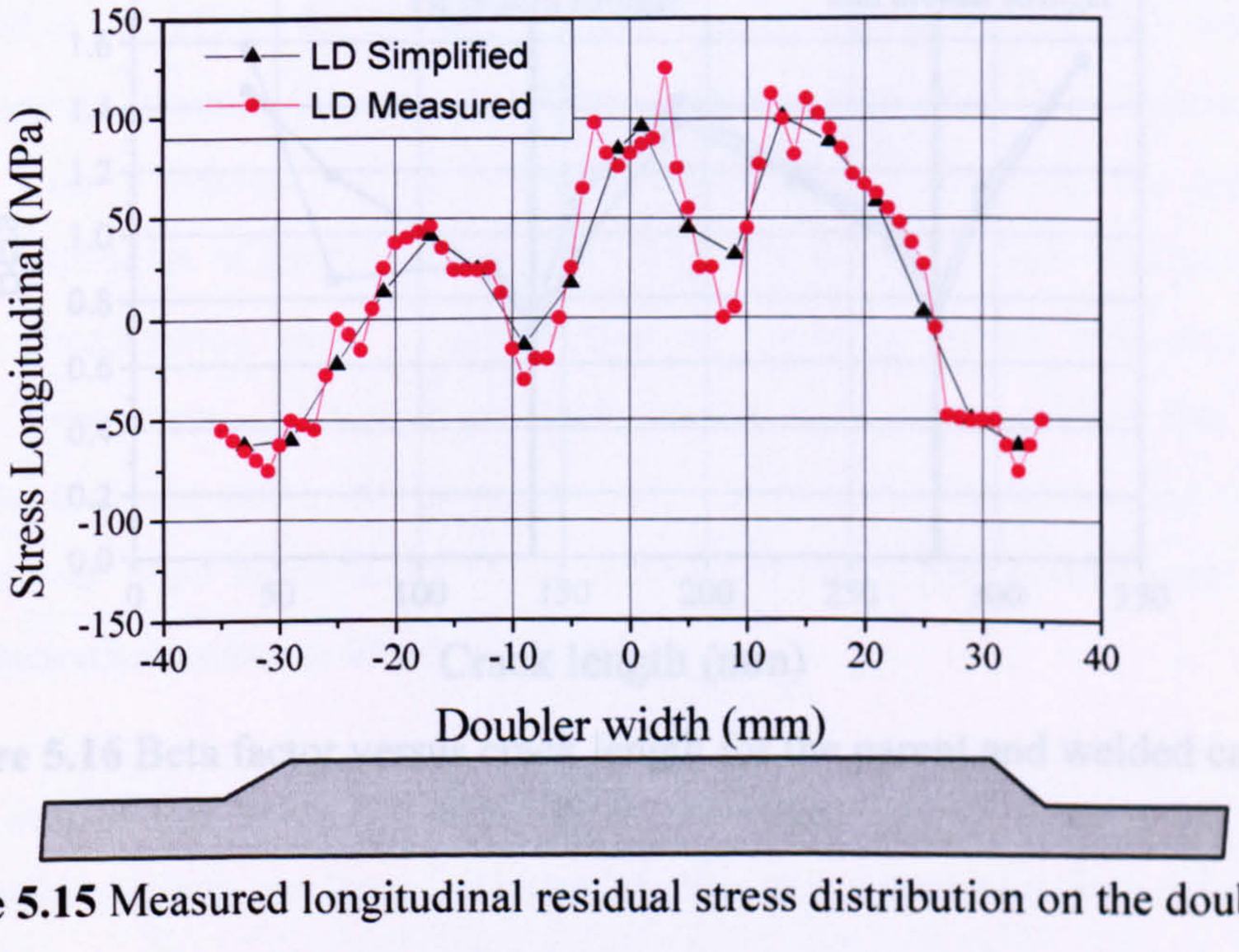

Figure 5.15 Measured longitudinal residual stress distribution on the doubler.

For crack length less than 100 mm in Figure 5.16 the beta factor is lower in the welded panel. This suggests that the crack propagation is slower for this case. This could be true due to the fact that residual stresses on the first bay (symmetric FE model/two bay crack)

is more dominant and therefore the negative parts of the welding residual stress distribution at the end of the doublers result in a lower Beta values, which indicates a lower crack propagation rate.

For half crack length longer than 100mm approaching the 1st stringer and up to the region further than 330mm (2nd stringer) according to Figure 5.16 the effect of the welding residual stresses seems to be very little. It can be seen that the Beta function versus crack length for the welded case follows the curve of the case without residual stresses. A general observation on this study is that the longer the crack the less the effect of the welding residual stresses on the structure. However, a more extended study is required in order for a solid conclusion to be drawn.

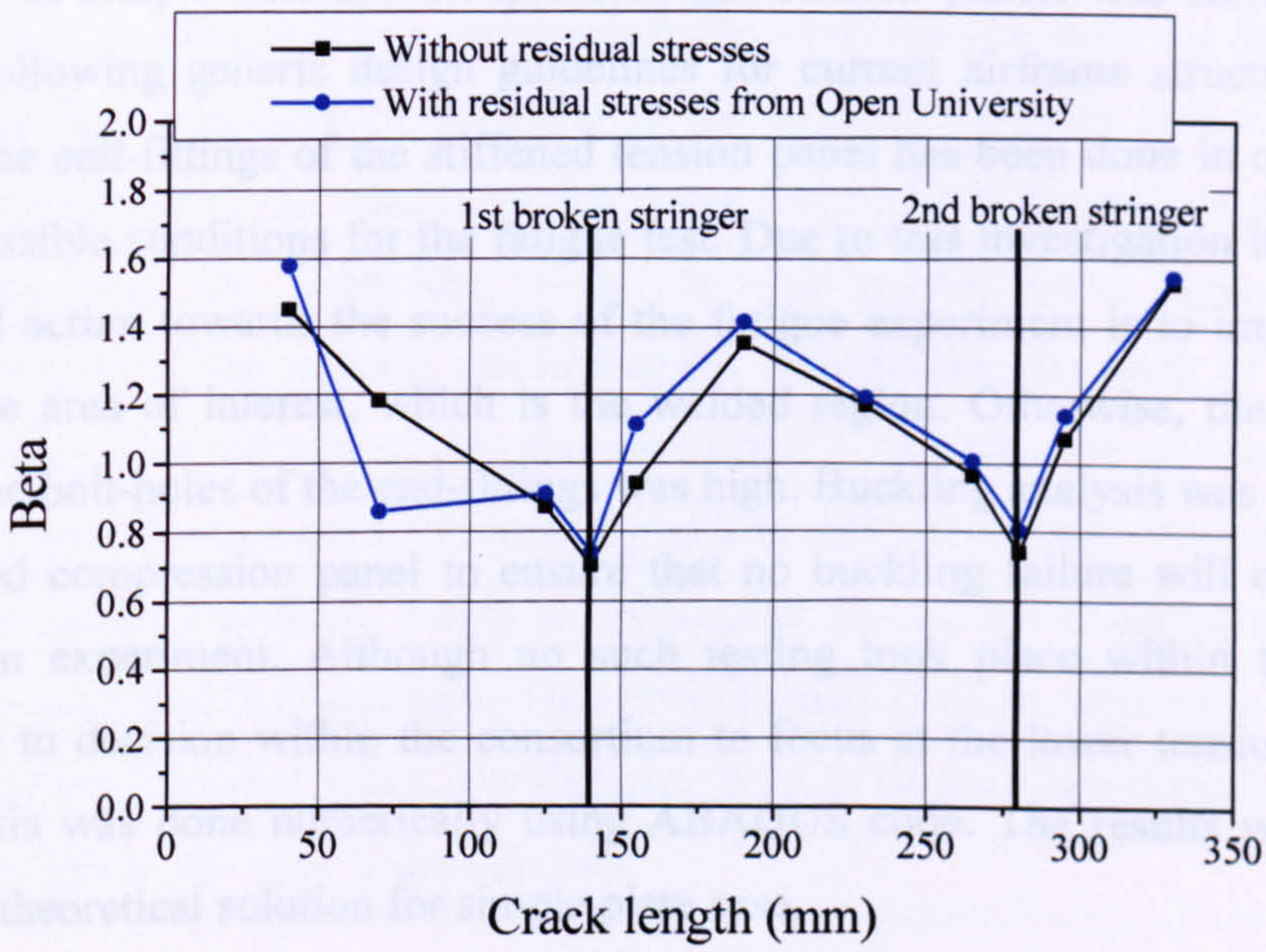

Figure 5.16 Beta factor versus crack length for the parent and welded case.

CHAPTER 6

DISCUSSION AND CONCUSSIONS

6.1 Discussion

The design of simple stiffened compression and tension panels was carried out in this study by following generic design guidelines for current airframe structures. Also the design of the end-fittings of the stiffened tension panel has been done in order to ensure the best possible conditions for the fatigue test. Due to this investigation it became clear that a good action towards the success of the fatigue experiment is to impose an initial crack in the area of interest, which is the welded region. Otherwise, the possibility of failure at the bolt-holes of the end-fittings was high. Buckling analysis was carried out for the stiffened compression panel to ensure that no buckling failure will occur during a compression experiment. Although no such testing took place within this WELDES project due to decision within the consortium to focus at the lower tension wing panel. This analysis was done numerically using ABAQUS code. The results were compared against the theoretical solution for simple plate case.

In the main part of this study the effect of the welding residual stresses on the fatigue crack propagation growth has been investigated. The above was done in two levels. In the coupon-level a more extensive investigation has been performed in order to understand the mechanisms behind the fatigue crack growth. Apart from the comparison in terms of crack length versus cycle loads between the parent and welded structures, studies of the local stress field in the fatigue crack have been presented. In the structural-level, the results are not so extended. Nevertheless, a good agreement of life prediction with the

experimental data has been achieved. An investigation of the strain hardening effect was also carried out showing that the strain hardening causes earlier opening of the fatigue crack profile when this is compared with ideal non-hardening material. This causes a faster crack propagation rate compared with a structure with no strain hardening under the cyclic load.

At the second part of coupon-level analysis, the significant effect of the welding residual stresses on the fatigue crack propagation has been demonstrated. Results in chapter 4 in terms of the crack opening displacement and the stress field around the crack tip at various points during the crack propagation suggest that in welded structures the crack propagation is faster than the crack propagation at non welded structures. This finding is in agreement with the available experiments on welded CCT coupons. It is believed that the high tensile welding residual stresses near the weld line are reducing the crack closure phenomenon that is induced by plasticity so the crack growth rate is faster. In addition, from the calculation of the crack opening stress levels it was found that as the crack tip moves away from the weld line, from the high tensile stress region towards the compressive part of the welding residual stress distribution, the level of crack opening stress increases. The increase of the opening stress S_{op} indicates the decrease of the crack propagation growth since the compressive welding residual stresses intensify the existing compressive residual stresses, due to the unloading part of the fatigue load, at the crack wake of the advanced fatigue crack. This phenomenon is more noticeable in larger scale structures where the crack is not a significant portion of the characteristic dimension of the structure like in the case of the coupons.

In structural-level analysis presented in chapter 5 the investigation of larger structures is presented. Good agreement with the experiment, in terms of fatigue crack growth life, for the two-stringer welded tension panel has been achieved. The crack starts at the stringer web at the weld joint due to an initial crack of 3 mm. In order to achieve this prediction in terms of crack length versus load cycles the Beta factor (β) needed to be calculated over a sufficient crack length in a finite element analysis for a case of non-welded structure. Next, the function of β versus crack length was used as input in a life prediction

software package called AFGROW. In addition, the measured residual stresses were also introduced in this package. So by applying the same fatigue load conditions the life prediction was performed. As a last part of this structural-scale study an investigation in a larger stiffened panel with nine stringers was carried out. In this case the crack has been assumed to initiate from the panel skin and as it propagates the stringers are failing. From the calculation of geometry factor beta for a crack length shorter than the distance from the first stringer a conclusion may be drawn. Due to the negative part of the welding residual stress distribution on the doubler of the stringer the geometry factor (β) is lower than the value for the case of without weld. But the latter has not been well established in this study and further investigation is required in terms of residual strength of the structure.

6.2 Main Conclusions

- Two stringer panels have been designed using the welding joining technique, a tension panel and a compression panel. The compression panel was designed to satisfy the buckling criterion.

- End-fittings for the tension panel were designed and finite element analysis has been performed. The key design criteria are smooth load transfer from the machine's grips to the tension panel and good fatigue strength of the fastener holes. Following this analysis an initial crack had to be introduced at the weld joint. This was essential in order to avoid any possible premature failure from the fastener holes in the end-fittings.

- In the coupon-level analysis of crack growth the first part was dedicated to study the stress intensity factor in the presence of welding residual stresses. Both VCCT technique and J-integral approach are proved to provide very accurate results in terms of stress intensity factor for non-welded structures. J-integral method is in principle applicable only up to the beginning of crack extension and not for crack growth. Therefore, the VCCT approach was selected.

- It has been demonstrated that strain hardening affects the opening stress level. Subsequently, the crack growth rate is affected from the change of the yield strength. This point is very important since it indicates the need for further investigation of the effect of hardening or softening of the material due to welding process on the crack growth rate.

- In chapter 5 good agreement with experimental data was achieved for larger structures for the crack started on the web of the welded panel although more testing data needed to establish the experimental scatter range.

6.3 Recommended future work

The elastic-plastic FE analysis needs to be expanded in an effort to use the crack opening level findings in a prediction life procedure, which was not presented in this study up to a sufficient point. Additional investigation needs to be done in the area of the change in hardness of the material due to the welding procedure. The effect of the change in hardness of the material should be taken into account for a detailed research on the crack propagation in welded structures.

In the large structures such as the 9-stringer stiffened panel presented at the end of chapter 5 another aspect needs to be covered in the fracture analysis apart from the geometry factor (β). This is a residual strength analysis, which combined with the geometry factor (β) provides a more complete investigation.

The welded structures are considered to be similar with the integral structures in terms of damage tolerance. In both structures, there is no crack stopper function. A step forward should be the research of the effect of local reinforcements on the crack propagation growth. These local reinforcements could be titanium or composite patches bonded on the welded structures with the use of very efficient adhesives, which nowadays are

available in the industry. The aim should be to demonstrate crack arrest against the welded structures without the local reinforcement.

References

[1] Niu, M.C.Y., *Airframe Stress Analysis and Sizing*, Hong Kong Conmilit Press Ltd, 1997.

[2] Polmear, I.J., *Light Alloys: Metallurgy of Light Metals*, Arnold, 1995.

[3] Bussu, G., *Damage Tolerance in Welded Aluminium Aircraft Structures, PhD Thesis*, Cranfield University, Cranfield, UK, 2000.

[4] Meo, G., *Design Stress Analysis and Cost Studies of Welded Aircraft Structures, PhD Thesis*, Cranfield University, Cranfield, UK, 2000.

[5] Masubuchi, K., *Analysis of Welded Structures*, International Series on Materials and Technology, Vol. 33, Pergamon Press.

[6] Mendez, P.F., *New Trends in Welding in the Aeronautic Industry*, New Trends for the Manufacturing in the Aeronautic Industry, Hegan/Inasmet, San Sebastian, Spain, 24 May 2000-25 May 2000, 21-38.

[7] Shah, R.C. and Lin, F.T., *Stress-Intensity Factors of Stiffened Panels with Partially Cracked Stiffeners*, Fracture Mechanics: Fourteenth Symposium, Theory and Analysis, ASTM STP 791, Vol. I, 1983, 157-171.

[8] Maddox, S.J., *Fatigue Strength of Welded Structures, 2nd Edition*, Abington Publishing, UK, 1994.

[9] Barson, J.M. and Stanley, T.R., *Fracture and Fatigue Control in Structures, 3rd Edition*, ASTM, 1999.

[10] Ochi, Y., Masaki, K., Matsumura, T. and Sekino, T., *Effect of Shot-Peening Treatment on High Cycle Fatigue Property of Ductile Cast Iron,* Int. J. of Fatigue, 23(5), 2001, 441-448.

[11] Masubuchi, K., *Investigation of Methods of Controlling and Reducing Weld Distortion in Aluminium Structures,* Welding Research Council Bulletin, No 237, May 1978.

[12] Maddox, S.J., *Review of Fatigue Assessment Procedures for Welded Aluminium Structures,* Int. J. of Fatigue, 25(12), 2003, 1359-1378.

[13] Hebrant, F., Louis, H., Soete, W. and Vinckier, A., *The Relaxation of Residual Welding Stresses by Static and Fatigue Loading,* Welding Research Abroad, Sept. 1957, 58-63.

[14] Tanala, E., Bourse, G., Fremiot, M. and De Belleval, J.F., *Determination of Near Surface Residual Stresses on Welded Joints Ultrasonic Methods,* NDT&E International, 28(2), 1995, 83-88.

[15] Albertini, G., Bruno, G., Dunn, B.D., Fiori, F., Riemers, W. and Wright, J.S., *Comparative Neutron and X-ray Residual Stress Measurements on Al-2219 Welded Plate,* Materials Science & Engineering, A224, 1997, 157-165.

[16] Sanders, W.W.J. and Day, R.H., *Fatigue Behaviour of Aluminium Alloy Weldments,* Welding Research Council Bulletin, No. 286, Aug. 1983.

[17] Norman, A.F., Hyde, K., Costello, F., Thompson, S., Birley, S. and Prangnell, P.B., *Examination of the Effect of Sc on 2000 and 7000 Series Aluminium Alloy Castings: for Improvements in Fusion Welding,* Materials Science & Engineering, A354, 2003, 188-198.

[18] Linnert, G.E., *Welding Metallurgy: Carbon and Alloy Steels*, American Welding Society, 1965.

[19] Sekiguchi, H., *Fundamental Research on the Welding Heat-affected Zone of Steel*, The Nikkan Kogyo Shimbun Ltd, Tokyo-Japan, 1976.

[20] Anderson, T.L., *Fracture Mechanics Fundamentals and Applications*, CRC Press, 1991.

[21] Ewalds, H.L. and Wanhill, R.J.H., *Fracture Mechanics*, Edward Arnold, USA, 1989.

[22] Paris, P.C., Gomez, M.P. and Anderson, W.P., *A Rational Analytic Theory of Fatigue,* The Trend in Engineering, 13, 1961, 9-14.

[23] Paris, P.C. and Ergogan, F., *A Critical Analysis of Crack Propagation Laws,* J. of Basic Engineering, 85, 1960, 528-534.

[24] Elber, W., *Fatigue Crack Closure Under Cyclic Tension,* Eng. Fracture Mechanics, 2(1), July 1970, 37-44.

[25] Ross, M., *Experiments for the Determination of the Influence of Residual Stresses on the Fatigue Strength of Structures,* Welding Research BWRA, 4(5), Oct. 1950, 83-93.

[26] Dugdale, D.S., *Effect of Residual Stress on Fatigue Strength,* Welding Journal, Research Supplement, 38(1), 1959, 45-48.

[27] Munse, W.H., *Fatigue of Welded Steel Structures*, Welding Research Counci, 1964.

[28] Bussu, G. and Irving, P.E., *The Role of Residual Stress and Heat Affected Zone Properites on Fatigue Crack Propagation in Friction Stir Welded 2024-T351 Aluminium Joints,* Int. J. of Fatigue, 25(1), Jan. 2003, 77-88.

[29] Irving, P.E. and Bussu, G., *Lessons Learned: Damage /tolerance of Welded Aircraft Structures,* Research Findings of the Cranfield Damage Tolerance Group, Number 026, Apr. 2000.

[30] Hunt, E., *Fatigue and Damage Tolerance of Large Airbus Wing Structures*, Sept. 1970.

[31] Catchpole, E.J., *The Optimum Design of Compression Surfaces Having Un-flanged Integral Stiffeners* , J. of Royal Aeronautical Society, 58, 1954, 765-768.

[32] *ABAQUS Standard User's Manual, Version 5.8*, Hibbitt Karlsson & Sorensen, U.S.A.

[33] Liebowitz, H. and Moyer, E.T.J., *Finite Element Methods in Fracture Mechanics,* Computers & Structures, 31(1), 1989, 1-9.

[34] Shields, E.B., Srivatsan, T.S. and Padovan, J., *Analytical Methods for Evaluation of Stress Intensity Factors and Fatigue Crack Growth,* Eng. Fracture Mechanics, 42(1), May 1992, 1-26.

[35] Guo, Y.H., Srivatsan, T.S. and Padovan, J., *Influence of Mixed-Mode Loading on Fatigue Crack Propagation Analysis,* Eng. Fracture Mechanics, 47(6), Apr. 1994, 843-866.

[36] Solanki, K. and Daniewicz, S.R.N.J.C.J., *Finite Element Modeling of Plasticity-Induced Crack Closure with Emphasis on Geometry and Mesh Refiniment,* Eng. Fracture Mechanics, 70(12), Aug. 2003, 1475-1489.

[37] Barsoum, R.S., *On the Use of Isoparametric Finite Elements in Linear Fracture Mechanics,* J. Num. Meth. Engineering, 10, 1976, 25-37.

[38] Henshell, R.D. and Shaw, K.G., *Crack Tip Elements are Unnecessary,* Int. J. Num. Meth. Engineering, 9, 1975, 495-509.

[39] Rice, J.R., *A Path Independent Integral and the Approximate Analysis of Strain Concentration by Notches and Cracks,* J. of Applied Mechanics, 35, 1968, 379-386.

[40] Lei, Y., O'Dowd, N.P. and Webster, G.A., *Fracture Mechanics Analysis of a Crack in a Residual Stress Field,* Int. J. of Fracture, 106, 2000, 195-216.

[41] Meith, W.A. and Hill, M.R., *Domain-Independent Values of the J-Integral for Cracks in Three-Dimensional Residual Stress Bearing Bodies,* Eng. Fracture Mechanics, 69, 2002, 1301-1314.

[42] Pavier, M.J., Poussard, C.G.C. and Smith, D.J., *Effect of Residual Stress Around Cold Worked Holes on Fracture under Superimposed Mechanical Load,* Eng. Fracture Mechanics, 63(6), 1999, 751-773.

[43] Banks-Sills, L., *Application of the Finite Element Method to Linear Elastic Fracture Mechanics,* Applied Mechanics Reviews, 44, 1991, 447-461.

[44] Chow, W.T. and Atluri, S.N., *Stress Intensity Factors as the Fracture Parameters for Delamination Crack Growth in Composite Laminates,* Composites, Part B, 28(4), 1997, 375-384.

[45] Gosz, M. and Moran, B., *An Interaction Energy Integral Method for Computation of Mixed-Mode Stress Intensity Factors Along Non-Planar Crack Fronts in Three Dimensions,* Eng. Fracture Mechanics, 69(3), Feb. 2002, 299-319.

[46] Park, O. and Sankar, B.V., *Crack-Tip Force Method for Computing Energy Release Rate in Delaminated Plates,* Composite Structures, 55(4), Mar. 2002, 429-434.

[47] Broek, D., *Elementary Engineering Fracture Mechanics, 4th edition*, Kluwer Academic

Publishers, 1991.

[48] Raju, I.S., *Calculation of Strain-Energy Release Rates With Higher Order and Singular Finite Elements,* Eng. Fracture Mechanics, 28(3), 1987, 251-274.

[49] Rybicki, E.F. and Kanninen, F., *A Finite Element Calculation of Stress Intensity Factors by Modified Crack Closure Integral,* Eng. Fracture Mechanics, 9(4), 1977, 931-938.

[50] Newman , J.C.J., *A Finite Element Analysis of Fatigue Crack Propagation Including the Effects of the Crack Closure, PhD thesis*, 1974.

[51] Dougherty, J.D., *Combined Experimental and Finite Element Study of Fatigue Crack Closure in 1070M Steel, PhD thesis*, The University of Akron, 1994.

[52] McClung, R.C. and Sehitoglu, H., *On the Finite Element Analysis of the Fatigue Crack Closure -1. Basic Modeling Issues,* Eng. Fracture Mechanics, 33(2), 1989, 237-252.

[53] McClung, R.C. and Sehitoglu, H., *On the Finite Element Analysis of the Fatigue Crack Closure -2. Numerical Results,* Eng. Fracture Mechanics, 33(2), 1989, 253-272.

[54] McClung, R.C. and Davidson, D.L., *High Resolution Numerical and Experimental Studies of Fatigue Cracks,* Eng. Fracture Mechanics, 39(1), 1991, 113-130.

[55] Pommier, S., *Plane Strain Crack Closure and Cyclic Hardening,* Eng. Fracture Mechanics, 69(1), 2002, 25-44.

[56] Pommier, S. and Bompard, Ph., *Bauschinger Effect of Alloys and Plasticity-Induced Crack Closure: a Finite Element Analysis,* Fatigue Fract. Engng. Mater. Struct., 23, 2000, 129-139.

[57] Galatolo, R. and Lanciotti, A., *Fatigue Crack Propagation in Residual Stress Fields of Welded Plates,* Int. J. of Fatigue, 19(1), 1997, 43-49.

[58] Edwards, L., Stelmukh, V., Santisteban, J.R., Ganguly, S. and Fitzpatrick, M.E., *Measurement of Residual Stresses in MIG &VPPA welded 2024,* Weldes Research Project Reports, Material Engineering, The Open University, 2000.

[59] *AFGROW Version 4.0008.12.11, Copyright 1996-2003 AFRL/VASM.*

[60] Lin, J. and Irving, P.E., *Fatigue Crack Propagation in Weld Joints,* Weldes Research Project Reports, Damage Tolerance Group, SIMS, Cranfield University, 2000.

[61] Evans, W.J. and Spence, S.H., *Characterisation of Crack Tip and Geometry Induced Closure,* Int. J. of Fatigue, 19, Supp. No. 1, 1997, S205-S210.

APPENDIX A

ENGINEERING DRAWINGS OF TENSION PANEL & END-FITTINGS

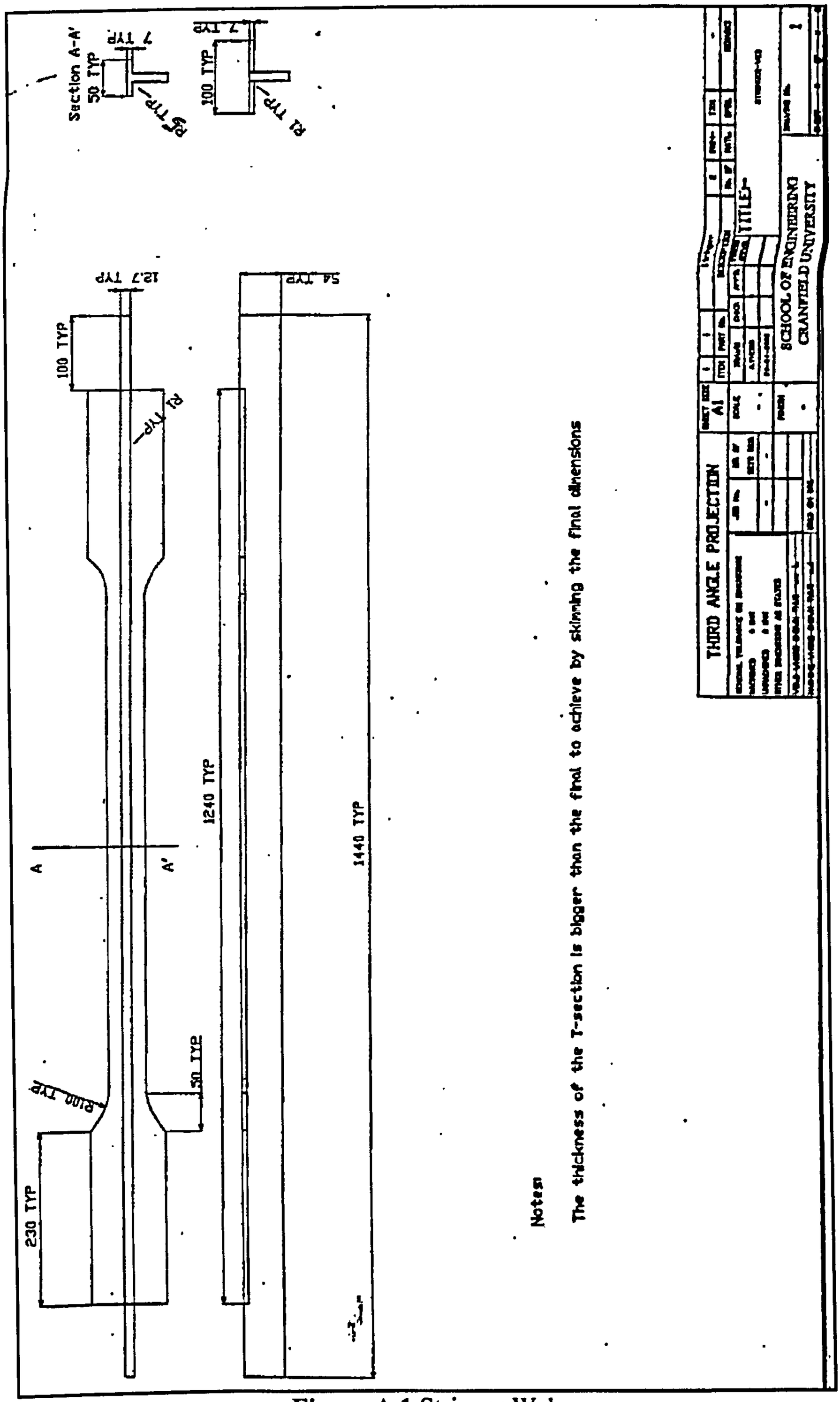

Figure A.1 Stringer Web

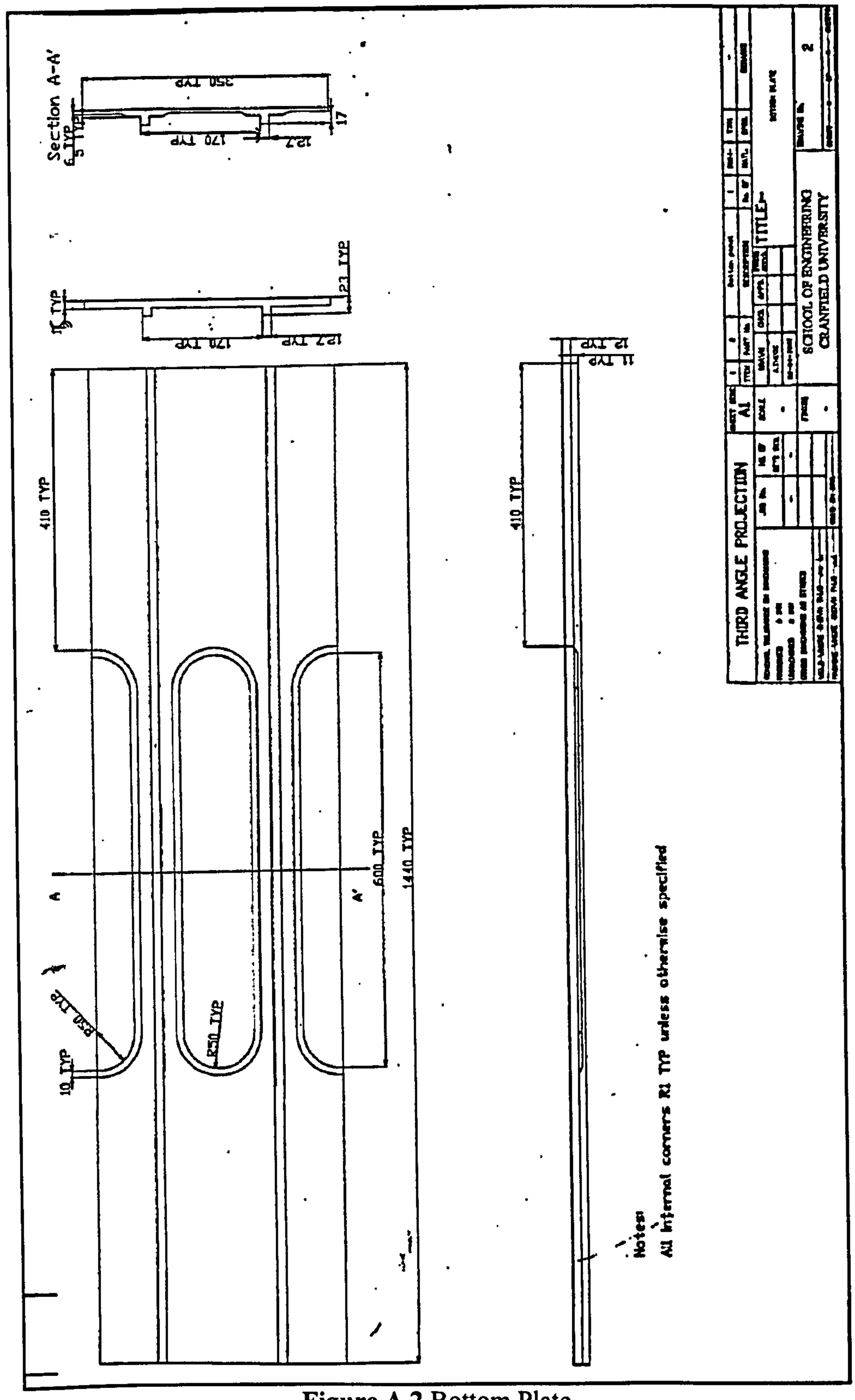

Figure A.2 Bottom Plate

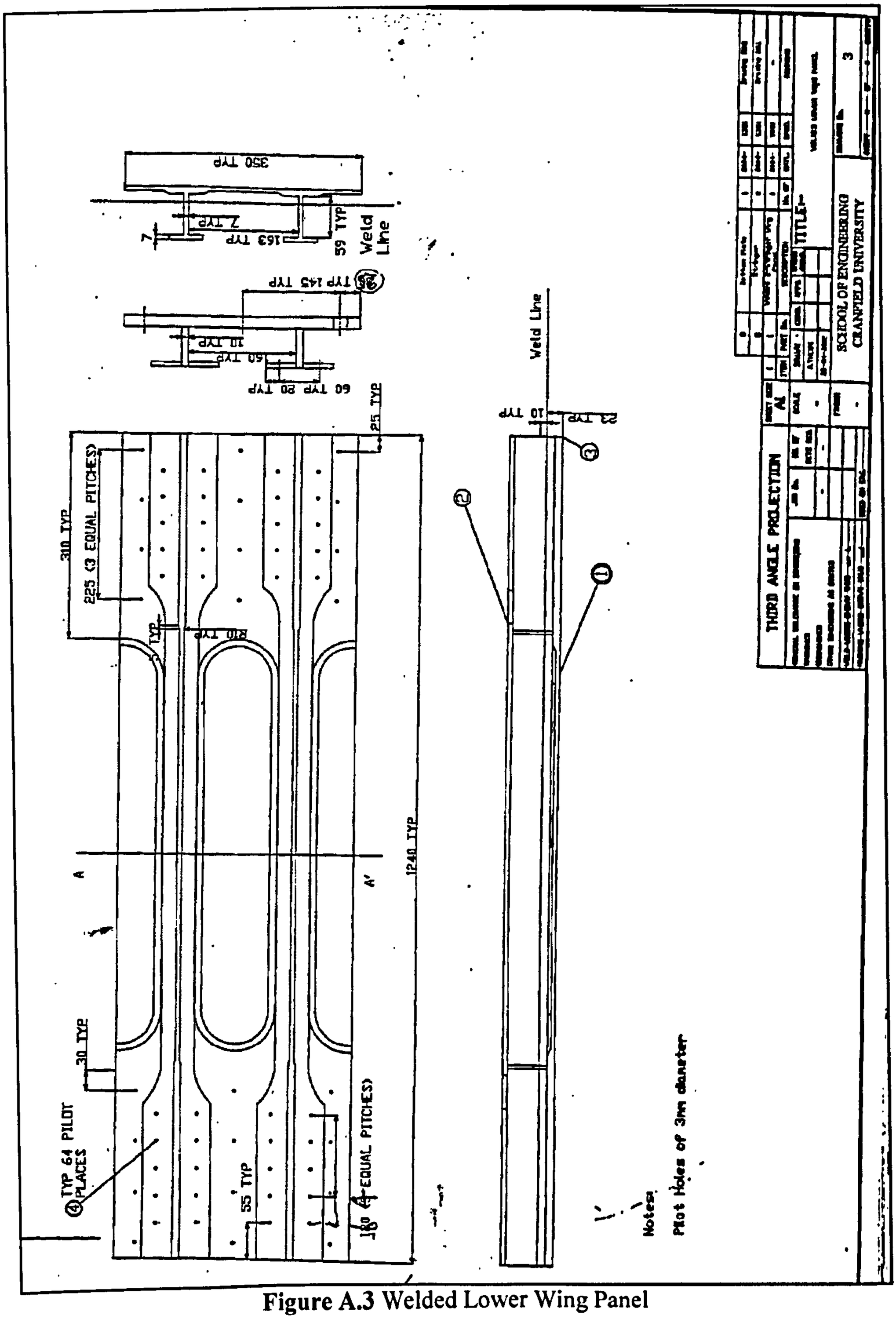

Figure A.3 Welded Lower Wing Panel

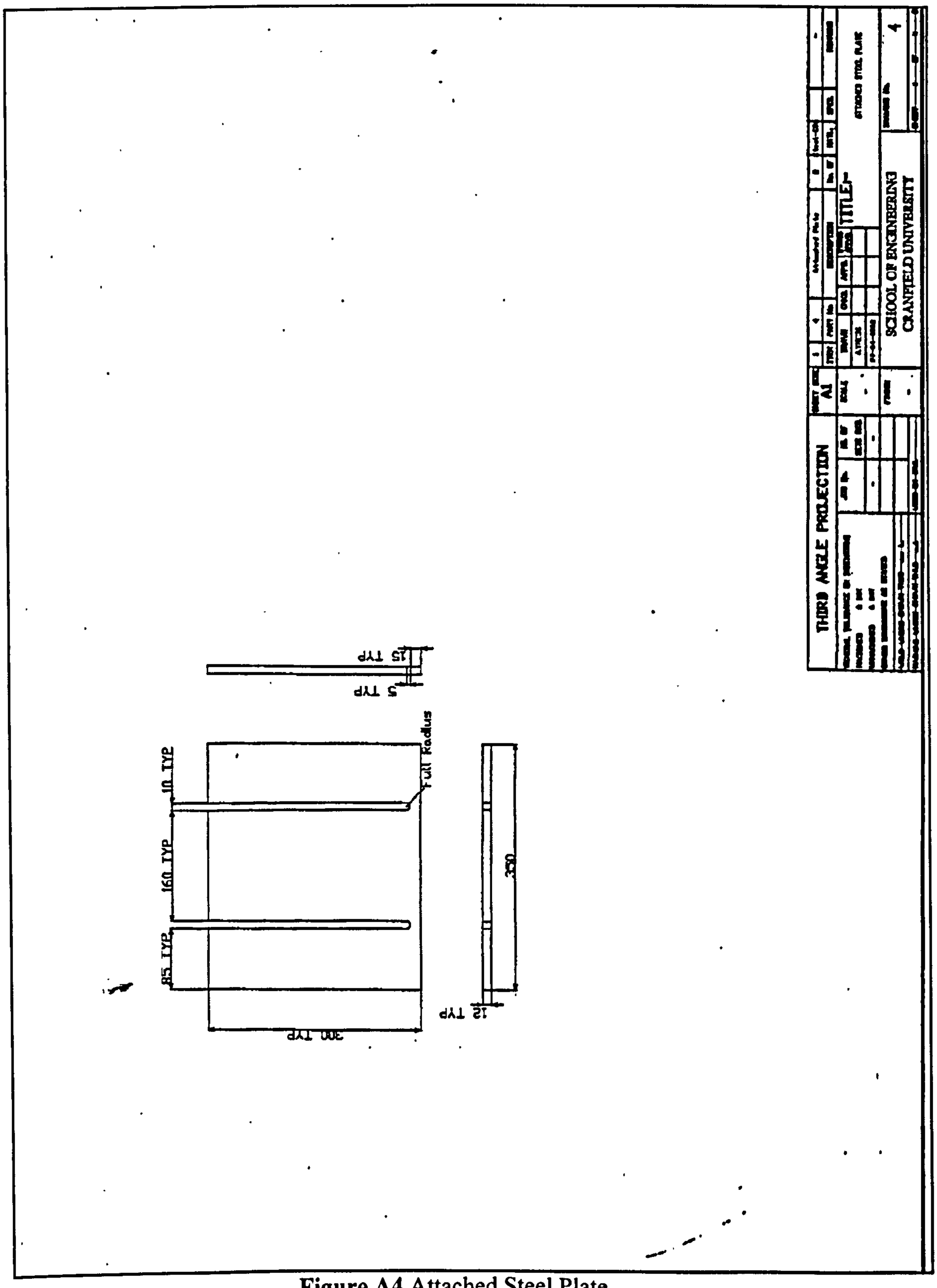

Figure A4 Attached Steel Plate

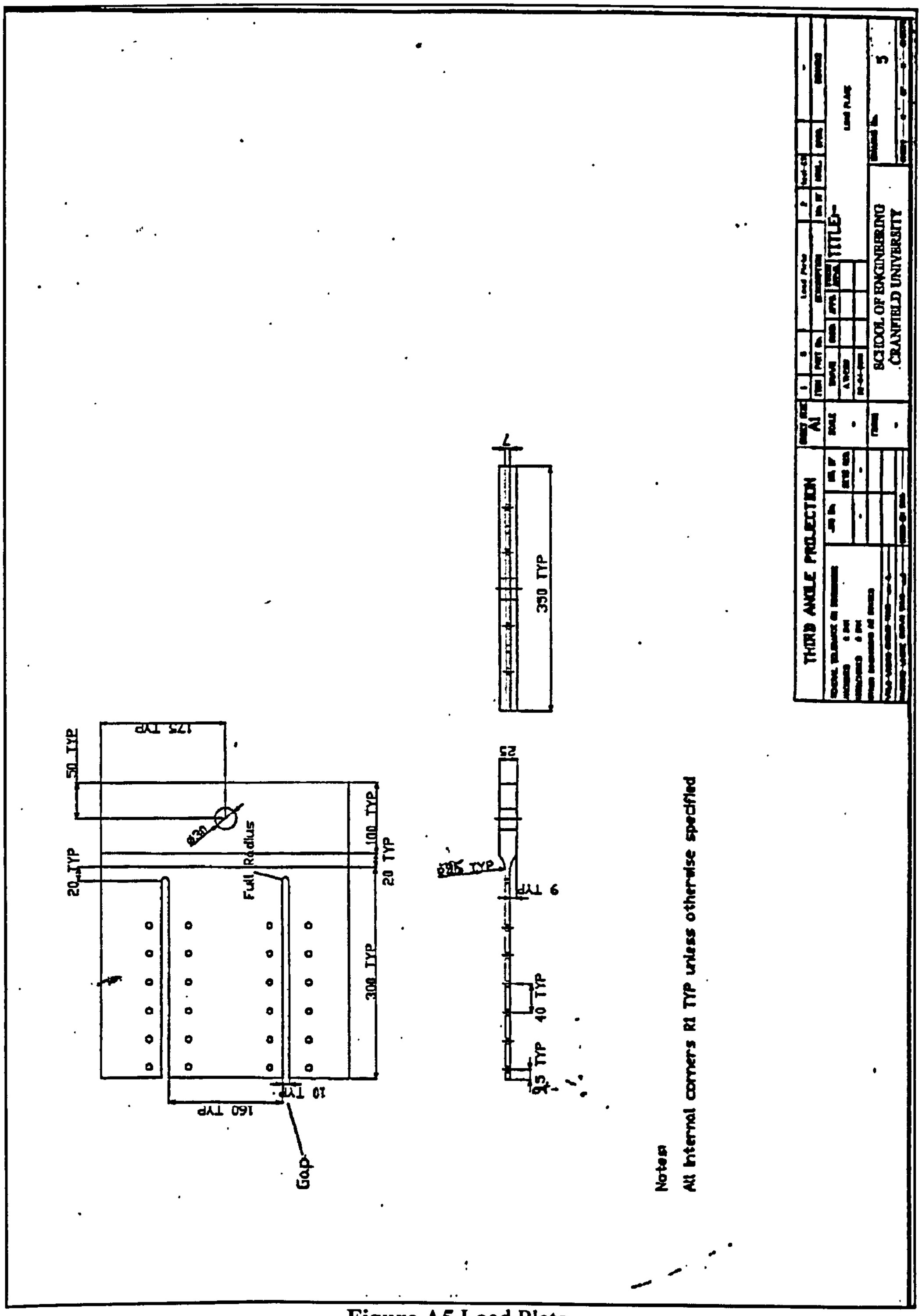

Figure A5 Load Plate

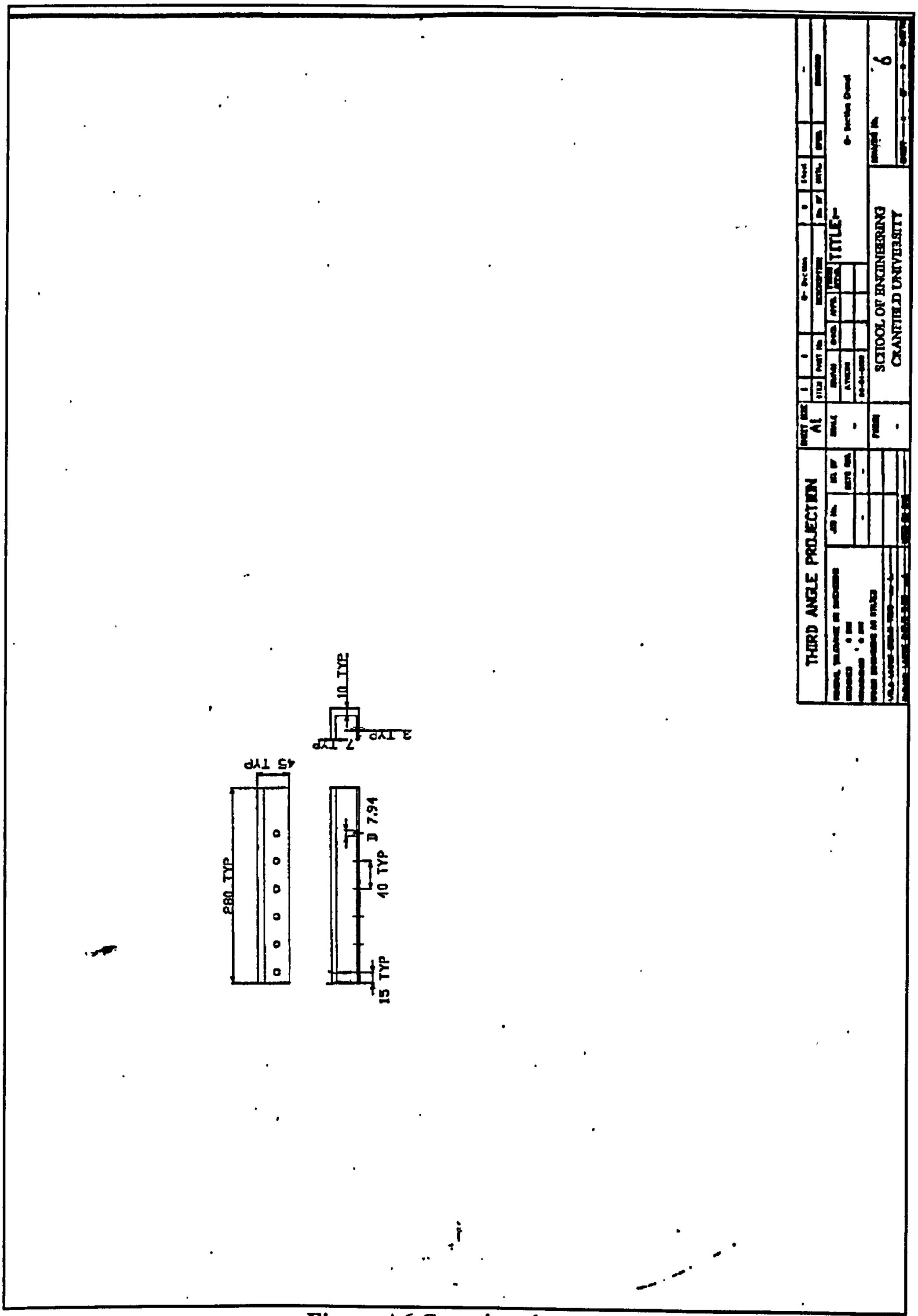

Figure A6 C-section channel

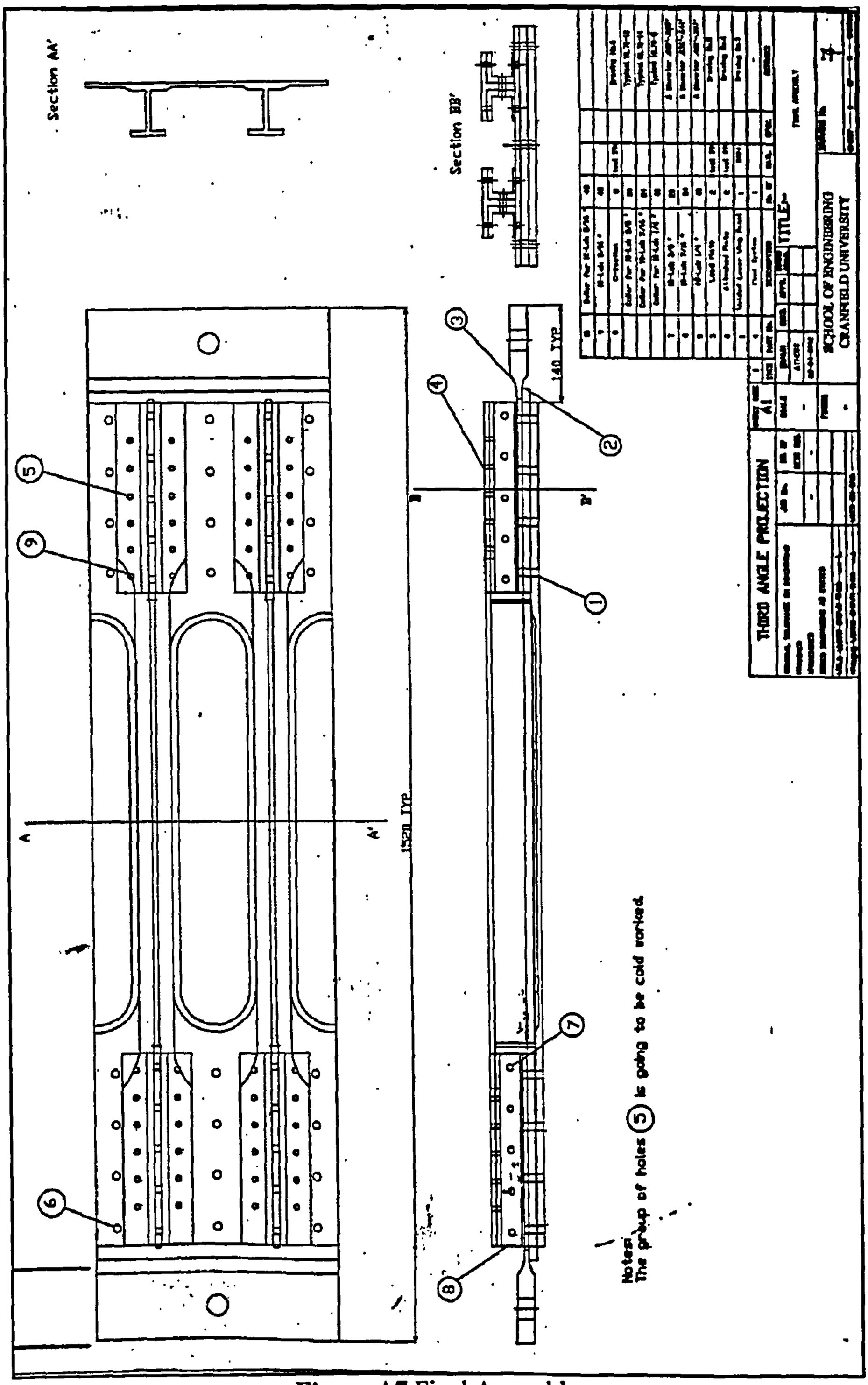

Figure A7 Final Assembly

APPENDIX B

EXAMPLE OF FATIGUE LIFE CALCULATION AT THE END-FITTINGS

Appendix B presents an example of calculation for the values in Tables 3.9 and 3.10 in the main body of the Thesis. The calculations concerning the top flange are given here. This is a representative location and all other locations follow the same methodology.

STEP 1: Input Data from FE analysis & Maximum Stress Calculation

$$S_{max}^{local} = \alpha\beta\left(K_{tb}\frac{\Delta P}{dt}\theta + K_{tg}\frac{P}{wt}\right)$$

$\alpha = 0.9$ (for reamed hole)

$\beta = 0.75$ (for Hi-Lok fastener)

$K_{tb} = 1.12$ (See figure B.1)

$K_{tg} = 3.13$ (See figure B.2)

$\theta = 1.5$ (See figure B.3 – Assumption of joint between single and double shear)

$d = 6.35mm$

$t = 7mm$

$w = 59\ mm$

$\sigma_{bypass} = 42MPa$ (from FE analysis)

$P = 4687\ N$ (from FE analysis)

so the above result in $\boxed{S_{max}^{local} = 208MPa}$

STEP 2: Fatigue Strength Reduction & Material Property

$$K_f = 1 + q(K_t - 1)$$

$$K_t = \frac{S_{max}^{local}}{\sigma_{bypass}} = \frac{208}{42} \Rightarrow K_t = 4.95$$

$q = 0.8$ (for aluminium)

The fatigue strength reduction is: $\boxed{K_f = 4.16}$

Material (Aluminium 2024 – T351)

$\sigma_{ult} = 460\text{MPa}$

For life of $N = 10^7$ cycles the endurance limit is : $\sigma_e = 118\text{MPa}$ (for smooth specimen & $R=-1$, $\sigma_m = 0$).

Due to the notched area of investigation (fastener hole) the endurance limit for this location is factored according to the fatigue strength reduction factor K_f calculated above.

$$\bar{\sigma}_e = \frac{\sigma_e}{K_f} = \frac{118}{4.16} \Rightarrow \bar{\sigma}_e = 28.4\text{MPa}$$ (for the fastener location-notched & $R=-1$, $\sigma_m = 0$)

STEP 3: Equivalent Stress Amplitude (Goodman equation)

1) Load ratio R=0.5:

The bypass stress is $\sigma_{max} = 42\text{MPa}$ and $\sigma_{min} = 21\text{MPa}$

So the mean stress is : $\sigma_m = \frac{\sigma_{max} + \sigma_{min}}{2} = \frac{42+21}{2} \Rightarrow \sigma_m = 31.5\text{MPa}$

the stress amplitude is : $\sigma_a = \frac{\sigma_{max} - \sigma_{min}}{2} = \frac{42-21}{2} \Rightarrow \sigma_a = 10.5\text{MPa}$

Using the Goodman equation :

$$\frac{\sigma_a}{\sigma_{a0}} + \frac{\sigma_m}{\sigma_{ult}} = 1 \Rightarrow \frac{10.5}{\sigma_{a0}} + \frac{31.5}{460} = 1 \Rightarrow \sigma_{a0} = 11.27\text{MPa}$$, for $\sigma_m = 0$

2) Load ratio R=0.3:

The bypass stress is $\sigma_{max} = 42MPa$ and $\sigma_{min} = 12.6MPa$

So the mean stress is : $\sigma_m = \frac{\sigma_{max} + \sigma_{min}}{2} = \frac{42+12.6}{2} \Rightarrow \sigma_m = 27.3MPa$

the stress amplitude is : $\sigma_a = \frac{\sigma_{max} - \sigma_{min}}{2} = \frac{42-12.6}{2} \Rightarrow \sigma_a = 14.7\text{MPa}$

Using the Goodman equation :

$$\frac{\sigma_a}{\sigma_{a0}} + \frac{\sigma_m}{\sigma_{ult}} = 1 \Rightarrow \frac{14.7}{\sigma_{a0}} + \frac{27.3}{460} = 1 \Rightarrow \sigma_{a0} = 15.63 MPa, \text{ for } \sigma_m = 0$$

STEP 4: Calculation of Safety Factor.

For Load ratio R = 0.5: $SF = \frac{\bar{\sigma}_{en}}{\sigma_{a0}} = \frac{28.4}{15.63} \Rightarrow \mathbf{SF = 1.8}$

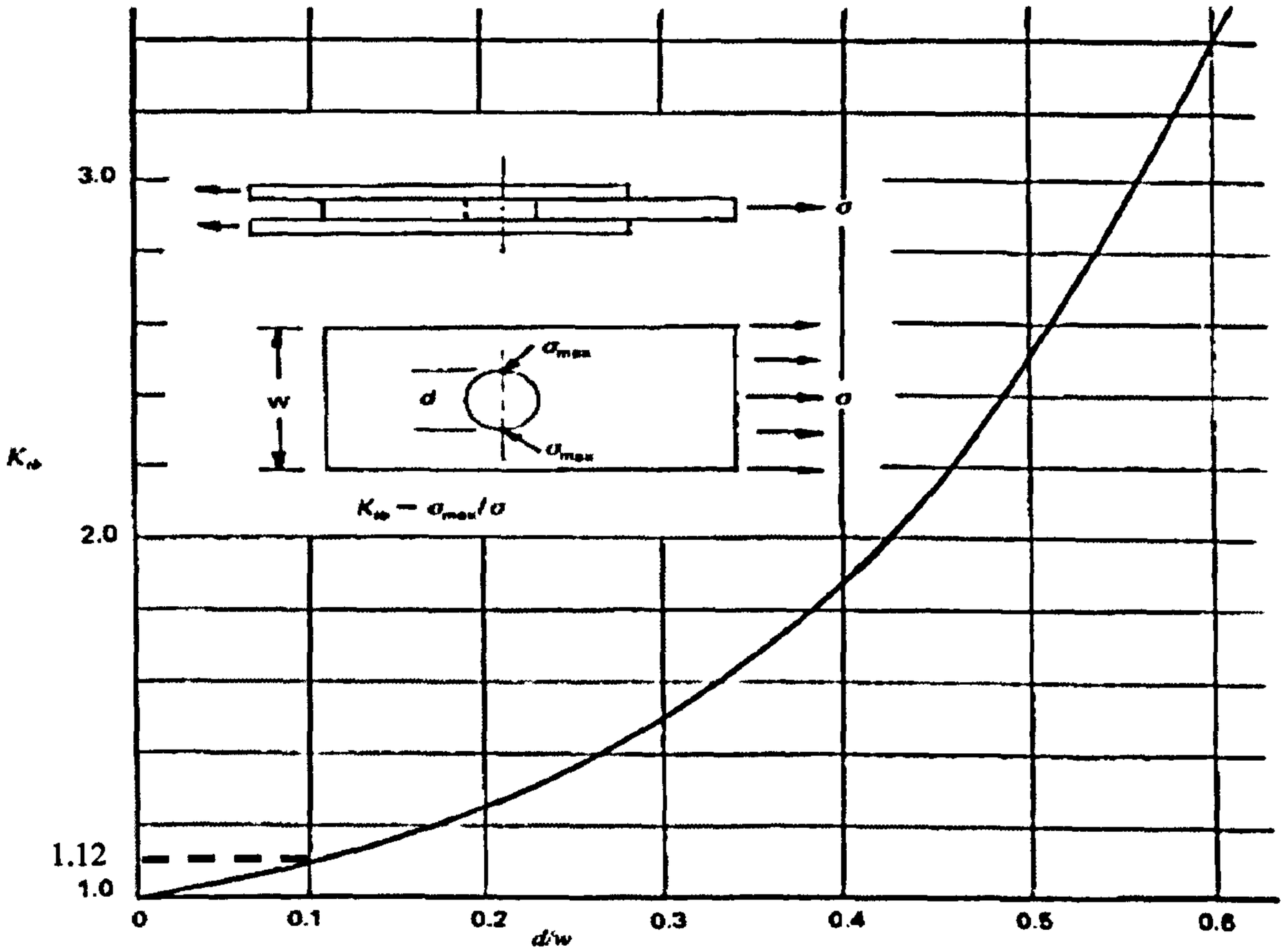

Figure B.1: Bearing stress concentration factor.

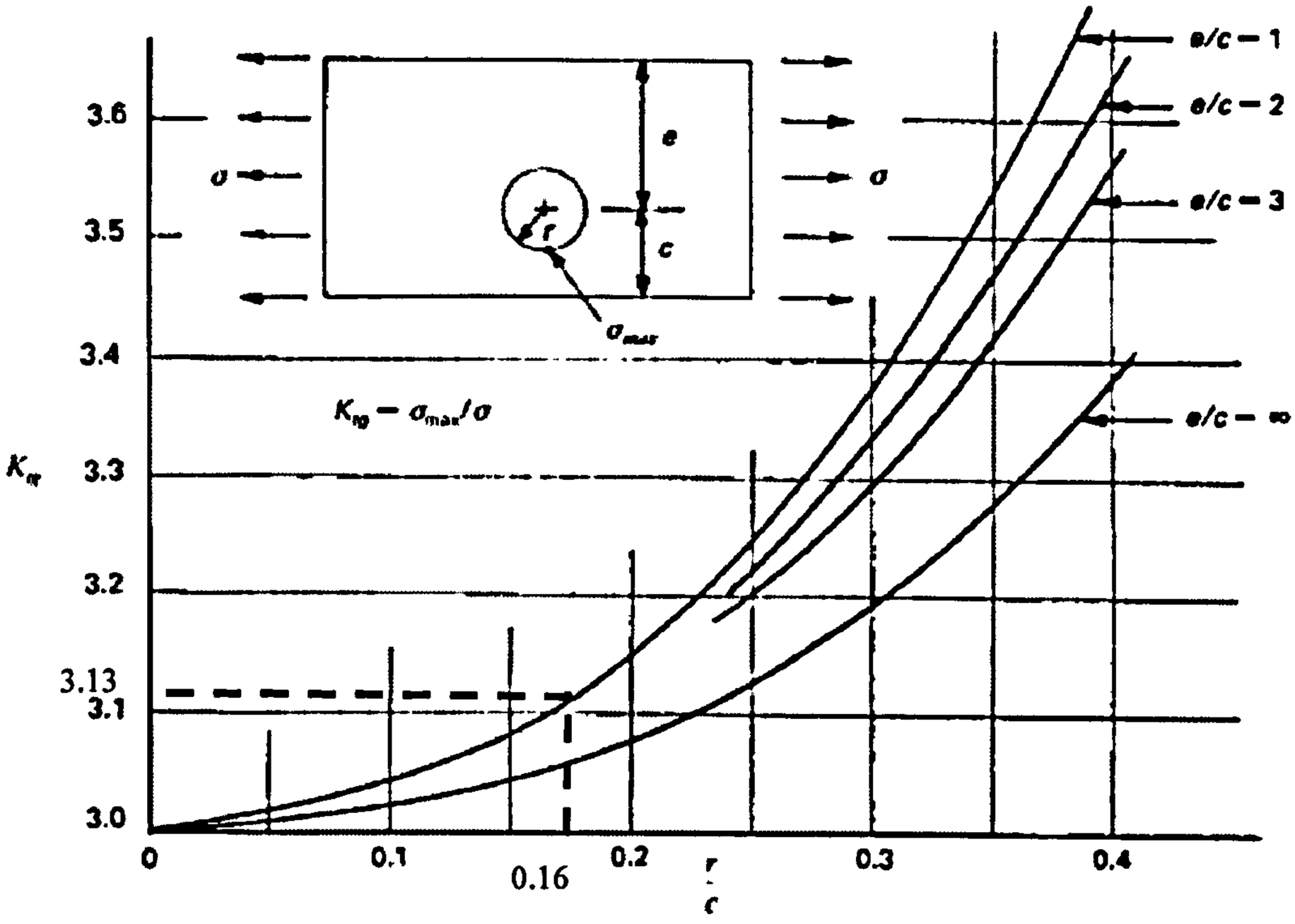

Figure B.2: Stress concentration factor.

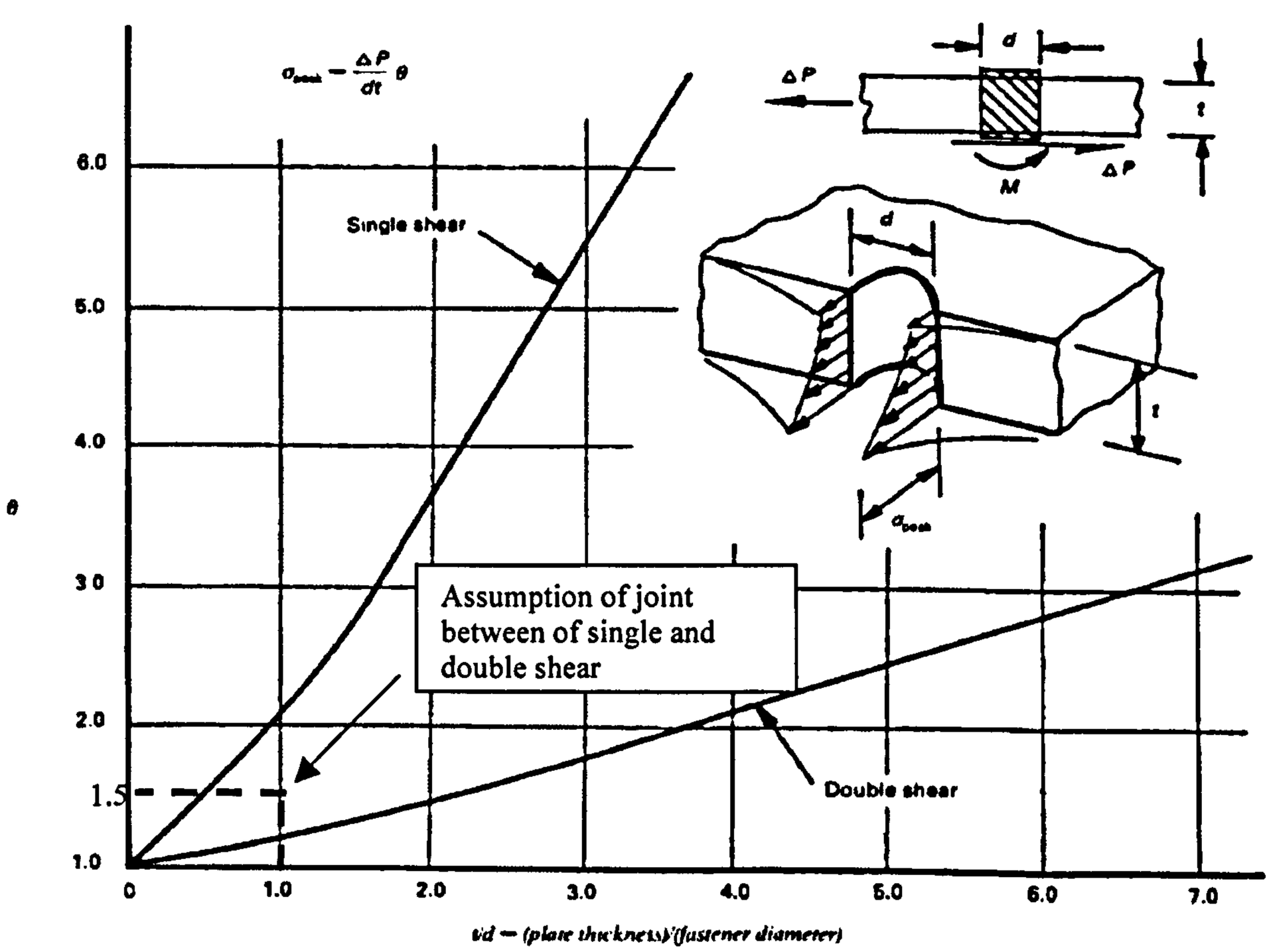

Figure B.3: Bearing distribution factor.

APPENDIX C

AFGROW AND ABAQUS MODELS

AFGROW INPUT/OUTPUT

STEP 1

The first step in setting up an AFGROW crack propagation analysis is the selection of a model. In this comparison between the available experimental curve and the AFGROW prediction the selected model is *Through-the-Thickness (User defined).* This model is used when a user has an existing stress intensity factor solution (in the form of a beta table) to input in AFGROW. The geometric beta values are not calculated by AFGROW, but are merely interpolated from the user defined table of beta values. This beta table is inserted into the AFGROW. In order to build this table the FE model for the parent coupon was used. For different crack length using the VCCT the SIF was calculated.

At this point a validation test can be performed since the FE model is a Crack Central Coupon (CCT) and there is an analytical solution available for the beta values as a function of the crack length in the literature [21] in the form of the following equation:

$$\beta = \sqrt{\sec\left(\frac{\pi\alpha}{W}\right)}$$

where, α is the half crack length in a CCT and W is the width of the coupon. The initial half crack length, width and thickness of the coupon were given to match the ones of the actual test specimen

Initial half crack length: α =1mm

Thickness of coupon: t = 7 mm

Half width of coupon: W =40 mm (due to symmetry, actual width is 80 mm)

STEP 2

In the next step the AFGROW software is being used. From the library NASGRO equation was chosen. This is because, this specific equation has the all the material constants which were calculated empirically from a series of experiments in a big range of aluminium alloys. But the main reason of selecting this material equation is because the crack closure effect is considered.

The NASGRO (Version 3.00) crack growth rate equations were developed by Forman and Newman at NASA, de Koning at NLR, and Henriksen at ESAb [59]. It has been implemented in AFGROW as follows:

$$\frac{da}{dN} = C\left[\left(\frac{1-f}{1-R}\right)\Delta K\right]^{n} \frac{\left(1-\frac{\Delta K_{th}}{\Delta K}\right)^{p}}{\left(1-\frac{K_{max}}{K_{crit}}\right)^{q}} \quad \text{(NASGRO EQUATION)}$$

where f is the parameter which controls the crack closure effect.

$$f = \frac{K_{op}}{K_{max}} = A_o + A_1 R + A_2 R^2 + A_3 R^3, \text{ for } R \geq 0$$

$$A_o = \left(0.825 - 0.34\alpha + 0.05\alpha^2\right)\left[\cos\left(\frac{\pi}{2} S_{max}/\sigma_o\right)\right]^{\frac{1}{\alpha}}$$

$$A_1 = \left(0.415 - 0.071\alpha\right) S_{max}/\sigma_o$$

$$A_2 = 1 - A_o - A_1 - A_3$$

$$A_3 = 2A_o + A_1 - 1$$

Here, a is the plane stress/strain constraint factor, and S_{max}/σ_o is the ratio of the maximum applied stress to the flow stress. These values are provided by the NASGRO material database for each material.

$$\Delta K_{th} = \Delta K_0 \left(\frac{\alpha}{\alpha + \alpha_0}\right)^{1/2} / \left(\frac{1-f}{(1-A_0)(1-R)}\right)^{(1+C_{th}R)}$$

where,

- ΔK_0 - threshold stress intensity range at R=0
- α - crack length (α or c in AFGROW)
- α_0 - intrinsic crack length (0.0015 inches or 0.0000381 meters)
- C_{th} - threshold coefficient

The values for ΔK_0 and C_{th} are provided by the NASGRO material database for each material. The used material in this application is Aluminium alloy 2024-T351.

The NASGRO equation accounts for thickness effects by the use of the critical stress intensity factor, Kcrit:

$$K_{crit} / K_{IC} = 1 + B_K e^{-\left(A_K t / t_0\right)^2}$$

where,

- K_{IC} - plane strain fracture toughness (Mode I)
- A_k - Fit Parameter
- B_k - Fit Parameter
- t - thickness
- t_0 - reference thickness (plane strain condition)

The plane strain condition is:

$$t_0 = 2.5\left(K_{IC}/\sigma_{ys}\right)^2$$

The values for K_{IC}, A_k, and B_k are provided by the NASGRO material database for each material. Although the plane strain thickness, t0, is defined by the equation shown above, Kcrit will asymptotically approach K_{IC} as the actual thickness gets larger than t_0.

Finally, Please note that AFGROW uses the plane strain (K_{IC}) and plane stress (Kc) fracture toughness values to interpolate a value for the critical stress intensity factor failure criterion. There is a difference between NASGRO and AFGROW in this regard. Therefore, the value (Kc) shown in the NASGRO dialog is really the value of Kcrit

determined by setting t=0 in the above equation for Kcrit /K_{IC}. This is done to provide a means of estimating the plane stress fracture toughness for a given material for use by AFGROW. Figures C.1 and C.2 shown all the applied parameters used in the NASGRO equation.

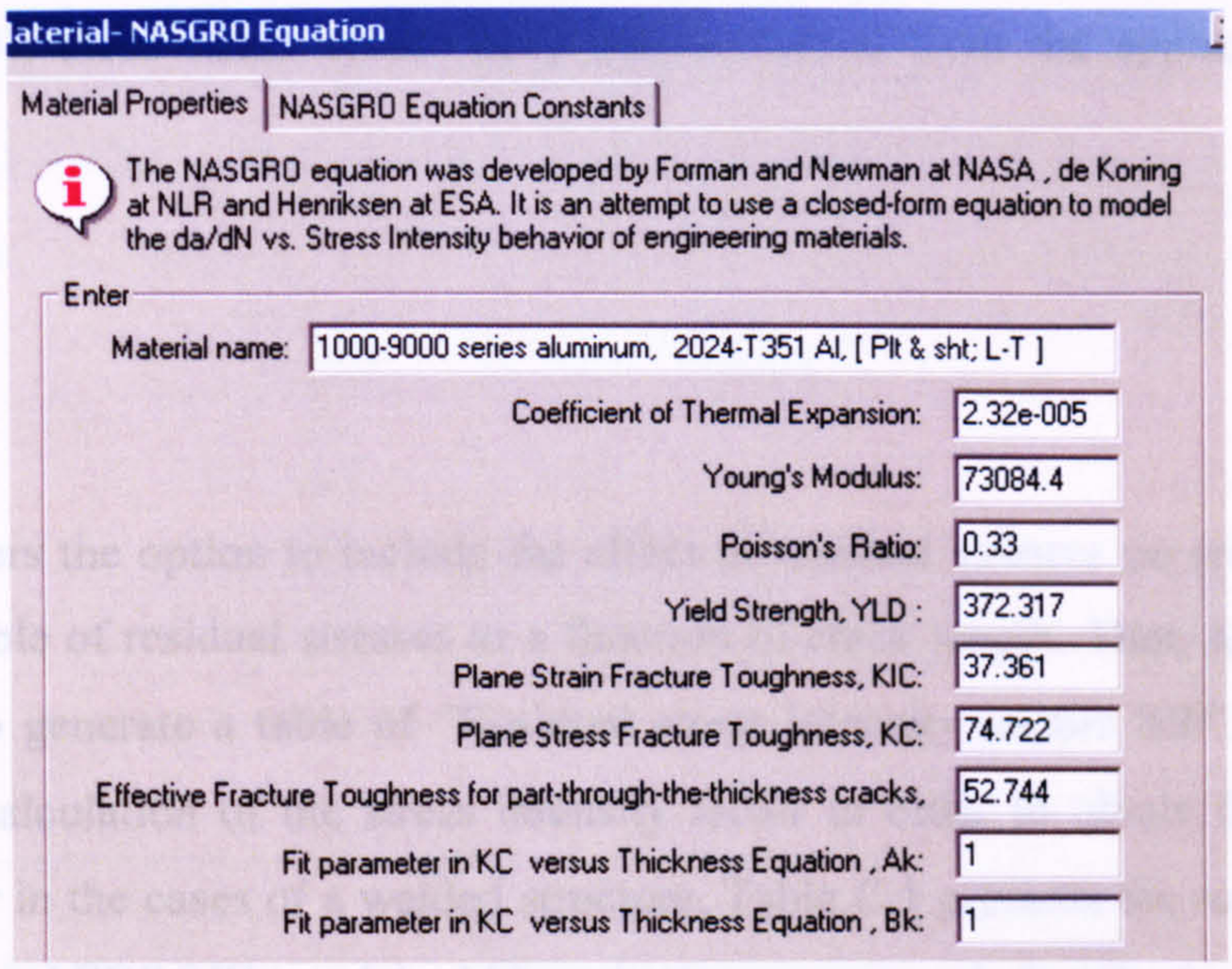

Figure C.1 Material properties of 2024-T351 in AFGROW database.

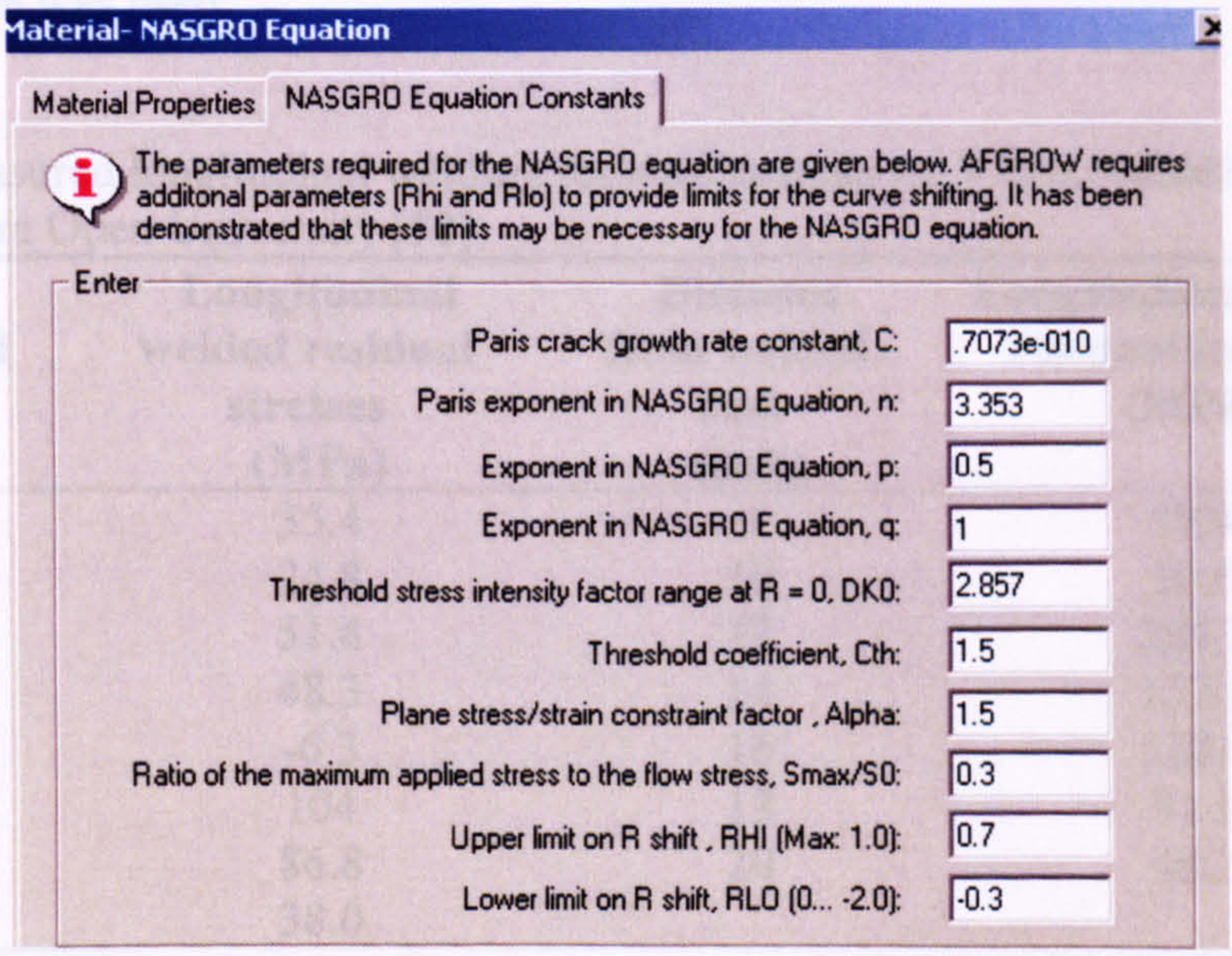

Figure C.2 Required parameters for the used NASGRO equation.

STEP 3

The applied spectrum for the prediction is the same with the applied spectrum in the available experiment in order to allow a comparison between the prediction and the experiment. A constant spectrum is applied with load ratio of R = 0.1 and S_{max} = 51.9 MPa as in [60]; these stress values have been obtained from the applied load in the experiment.

STEP 4

AFGROW offers the option to include the effect of residual stresses on crack growth by reading in a table of residual stresses as a function of crack length. Then AFGROW uses these values to generate a table of "Residual stress intensity factors SIF". This table is added to the calculation of the stress intensity factor in order to obtain the total stress intensity factor in the cases of a welded structure. Table C.1 presents the residual stresses inserted in the AFGROW model. Although three measured distributions of welding residual stresses were available from [58] as it is presented in Figure 4.35 only the longitudinal one was used.

Table C.1 Measured longitudinal welding residual stresses on VPPA welded coupons from Open University [58].

Distance from welded line (mm)	Longitudinal welded residual stresses (MPa)	Distance from welded line (mm)	Longitudinal welded residual stresses (MPa)
1	35.4	9	19.4
2	24.8	10	50.5
3	51.4	12	201.3
4	48.3	14	157.3
5	-6.3	16	138.6
6	104	18	91.3
7	86.8	20	48.2
8	38.0		

In Chapter 5 the following tables are corresponding to Figure 5.6. Tables C2 and C3 present the values of the welding residual stresses used for the life prediction at the two-stringer panel in Figures 5.9 and 5.10

Table C.2 Measured longitudinal welding residual stresses on VPPA welded 2-stringer panels for crack towards skin doubler; from Open University [58].

Distance from welded line (mm)	Longitudinal welded residual stresses (MPa)	Distance from welded line (mm)	Longitudinal welded residual stresses (MPa)
1	65	9	53
2	103	10	79
3	126	11	62.5
4	116	12	72
5	105	13	65
6	65	14	57
7	75	15	47
8	75		

Table C.3 Measured longitudinal welding residual stresses on VPPA welded 2-stringer panels for crack towards upper flange; from Open University [58].

Distance from welded line (mm)	Longitudinal welded residual stresses (MPa)	Distance from welded line (mm)	Longitudinal welded residual stresses (MPa)
2	92	24	23
4	123	26	-14
6	24	28	-33
8	-12	30	-50
10	49	32	-60
12	143	34	-69
14	135	36	-72
16	114	38	-82
18	87	40	-98
20	65	42	-99
22	48	44	-97

INVESTIGATION OF HARDENING EFFECT

In chapter 4, Figure 4.27: (The two plasticity models) illustrates the two different material behaviours. The *elastic-perfectly plastic (no strain hardening)* curve follows the assumption that after the initial yield stress there are no other yield stresses. The latter comply with the elastic-perfectly plastic assumption. More specifically, the Young's modulus for the used material 2024-T351 is 72 GPa. The initial and only one yield stress is 320 MPa. All the above are listed below in the ABAQUS format input file. The rest of the structure of the input file is not listed for simplicity since here the main concern is the material description.

```
TITLE
**NODES**
 **ELEMENTS**
*MATERIAL,NAME=ALUMINIUM
*ELASTIC
72E9,0.3
*PLASTIC
320E6,0.0
**SECTION PROPERTIES**
**BOUNDARY**
**STEP ANALYSIS**
APPLICATION OF LOAD
**END**
```

It is well known that metallic materials like steel and in this case aluminium exhibit some kind of hardening after it has yielded. In order to model the hardening of the material ABAQUS routines were used. Two kinematic hardening models are available in ABAQUS to model the cyclic loading of metals. The linear kinematic hardening model and the nonlinear isotropic/kinematic model. For this investigation the nonlinear isotropic/kinematic model (mixed model) was used to compare with the previous no hardening model. A schematic list of the used ABAQUS input file is listed below. Again only the details of material section are presented here.

```
TITLE
**NODES**
 **ELEMENTS**
*MATERIAL,NAME=ALUMINIUM
*ELASTIC
72E9,0.3
*PLASTIC,HARDENING=COMBINED,DATA TYPE=HALF CYCLE
320E6,0.0
325E6,3.53e-4
330e6,7.41e-4
335e6,1.17e-3
340e6,1.63e-3
345e6,2.15e-3
350e6,2.71e-3
355e6,3.33e-3
360e6,4.01e-3
365e6,4.76e-3
370e6,5.57e-3
375e6,6.47e-3
380e6,7.46e-3
385e6,8.54e-3
390e6,9.72e-3
395e6,1.1e-2
400e6,1.24e-2
405e6,1.4e-2
410e6,1.57e-2
415e6,1.75e-2
420e6,1.95e-2
425e6,2.17e-2
430e6,2.41e-2
```

435e6,2.67e-2
440e6,2.95e-2
445e6,3.26e-2
450e6,3.59e-2
455e6,3.95e-2
460e6,4.34e-2
480e6,1.0e-1
SECTION PROPERTIES

BOUNDARY

STEP ANALYSIS

APPLICATION OF LOAD

END

Note that the data of stress-strain in Al 2024-T351 were obtained from [60].